

Diss. ETH No. 20162

Transport experiments on p-GaAs quantum dots and point contacts

A dissertation submitted to the
ETH ZURICH

for the degree of
Doctor of Sciences

presented by

Yashar Komijani

Master. Electrical Eng. University of Tehran
born September 14, 1980 in Tehran, Iran
citizen of Iran

accepted on the recommendation of:

Prof. Dr. Klaus Ensslin, examiner
Prof. Dr. Wolfgang Belzig, co-examiner
Prof. Dr. Thomas Ihn, co-examiner

December 2011

The cover design by Maria Alexandrova

To my family

Abstract

In this thesis we have investigated low-temperature hole transport through p-type GaAs quantum point contacts and quantum dots. The interest in p-type GaAs nano-structures arises primarily from the fact that the Coulomb interaction and spin-orbit interaction are strong in these devices. The more pronounced carrier-carrier interactions in low-dimensional hole systems compared to their n-type counterparts make p-doped systems especially suitable for investigating many-body effects such as the 0.7 conductance anomaly in quantum point contacts (QPCs).

We have used the local anodic oxidation lithography by an atomic force microscope and shallow chemical etching in combination with top-gates in order to define highly tunable nano-structures in two-dimensional hole gases (2DHGs). Electronic functionality of these devices is demonstrated by studying the 0.7 anomaly and the g-factor anisotropy in QPCs and the observation of excited states and the time-resolved charge detection of hole tunnelling in p-type GaAs quantum dots (QDs).

Experiments on hole QPCs demonstrate a strong anisotropic modification of the Landé g-factor of holes due to the confinement. Therefore studying the 0.7 anomaly in hole QPCs enables examining the conjectured connection between the anomaly and the spin of the subbands. Furthermore we have employed magnetic fields up to $B_{\perp} = 13$ Tesla perpendicular to the plane of the 2DHG in order to exploit localization phenomena which are potentially linked to the 0.7 anomaly. These experiments suggest the presence of a quasi-bound state in the QPC and support the explanation of the 0.7 anomaly based on the Coulomb blockade and the Kondo physics. The role of impurities in the QPC channel on the conductance is discussed and it is shown the conductance anomaly in another QPC can be understood as being due to an impurity coupled to the intrinsic Kondo impurity of the 0.7 anomaly.

On quantum dots, we have demonstrated the observation of excited states in a small hole QD and deviations from the constant interaction model. Integration of a QPC in the vicinity of a dot and the capacitive coupling of the two enables the time-averaged as well as time-resolved charge detection of hole tunneling in the QD. The time resolution provides information about the dense spectrum of the QD. Moreover, the statistics of the charge transfer has been analyzed in the framework of full counting statistics (FCS). Ordinary and factorial cumulants have been calculated and the role of interactions in the dot and the reservoir is discussed.

Zusammenfassung

In dieser Dissertation wird der Transport von Löchern durch Quantenpunktkontakte (QPC) und Quantenpunkte (QD) in p-dotiertem GaAs bei tiefen Temperaturen untersucht. Der Grund für das Interesse an p-dotierten GaAs-Strukturen ist in erster Linie die starke Coulombwechselwirkung und Spin-Bahn-Kopplung in diesen Systemen. Die verglichen mit n-dotiertem GaAs erhöhte Wechselwirkung zwischen den Ladungsträgern in niedrig-dimensionalen Löcher-Systemen macht diese zu geeigneten Teststrukturen für Vielteilchen-Effekte wie die 0.7-Anomalie in der Leitfähigkeit von Quantenpunktkontakten. ‘ Mit Lithographie durch lokale Oxidation mit Hilfe einer Rasterkraft-Mikroskopspitze oder mit chemischem Oberflächen-Ätzen kombiniert mit metallischen Gattern haben wir Nanostrukturen in zweidimensionalen Löchergasen hergestellt. Auf diese Weise haben wir Quantenpunktkontakte, in denen wir die 0.7-Anomalie und die g-Faktor-Anisotropie untersucht haben, und Quantenpunkte, in denen wir angeregte Zustände sowie das zeit-aufgelöste Tunneln von Löchern beobachtet haben, definiert.

Das Einschränkungspotential in einem Quantenpunktkontakt verursacht eine stark anisotrope Modifikation des Landéschen g-Faktors der Löcher. Deshalb ermöglicht die Untersuchung der 0.7-Anomalie in Löcher-Quantenpunktkontakten Rückschlüsse auf den vorgeschlagenen Zusammenhang zwischen Spins und Subbändern. Zudem haben wir mit senkrechten Magnetfeldern von bis zu 13 T Lokalisierungsphänomene betrachtet, welche möglicherweise ebenfalls mit der 0.7-Anomalie in Verbindung stehen. Diese Experimente deuten auf quasi-gebundene Zustände in den Quantenpunktkontakten hin und unterstützen die Theorien zur Erklärung der 0.7-Anomalie, welche auf Coulombblockade und dem Kondo-Effekt beruhen. Wir diskutieren die Rolle von Störstellen im QPC-Kanal und zeigen, dass die 0.7-Anomalie als Störstelle betrachtet werden kann, die im Rahmen eines Kondo-Modells verstanden werden kann.

In einem kleinen Quantenpunkt haben wir angeregte Zustände ausgemessen und Abweichungen vom Modell der konstanten Wechselwirkung beobachtet. Durch das Platzieren eines Quantenpunktkontaktes neben einem QD können wir zeitgemitteltes sowie zeitaufgelöstes Tunneln von Löchern im QD detektieren. Die Zeitauflösung gibt Aufschluss über das dichte Spektrum im Quantenpunkt. Schliesslich haben wir die Statistik des Ladungstransfers im Sinne einer vollständigen Zähl-Statistik analysiert. Dazu haben wir normale und faktorielle Kumulanten berechnet

und die diesbezügliche Rolle von Wechselwirkungen im Quantenpunkt und in den Reservoirs diskutiert.

Contents

1	Introduction	1
2	Basic concepts and theoretical background	4
2.1	Valence band of GaAs	4
2.1.1	Spin-orbit interaction	5
2.1.2	Luttinger Hamiltonian	6
2.1.3	SO interaction in the effective mass approximation	7
2.1.4	2D Confinement	8
2.1.5	Spin-orbit interaction in 2D electron and hole gases	9
2.1.6	Hyperfine interaction	10
2.2	Interactions in hole gases	10
2.2.1	Relevant scales	11
2.2.2	Interaction strength as the fundamental parameter	12
2.2.3	Screening	12
2.2.4	Phase diagram	13
2.3	Magnetoresistance	14
2.3.1	Drude model and the Hall effect	14
2.3.2	Landau levels	15
2.3.3	Quantum Hall Effect	16
2.4	Semiconductor nano-structures	18
2.4.1	Conductance quantization in quantum point contacts	19
2.4.2	Coulomb blockade in quantum dots	21
3	Sample Fabrication and Measurement Setup	24
3.1	Sample Fabrication	24
3.1.1	Carbon doped p-type GaAs/AlGaAs heterostructures	24
3.1.2	Optical lithography	26
3.1.3	Ohmic contacts to two-dimensional hole gases	27

3.1.4	AFM oxidation lithography	28
3.1.5	Electron beam lithography	30
3.2	Metallic gates on two-dimensional hole gases	32
3.2.1	Insulating materials and density-mobility curves	32
3.2.2	Leakage characteristics	35
3.2.3	Top-gate stability and improved tunability	36
3.2.4	Patterned top-gate in combination with in-plane gates	37
3.3	Measurement Setup	38
3.3.1	Electrical setups for transport measurements	39
3.3.2	Noise in electrical circuits	40
3.3.3	Cryogenics	41
4	The 0.7 conductance anomaly: a short review	43
4.1	Introduction	43
4.2	0.7 Anomaly in linear conductance	44
4.2.1	In-plane magnetic field	44
4.2.2	Temperature dependence	45
4.3	Possible explanations	46
4.3.1	Spontaneous Spin polarization	47
4.3.2	Coulomb blockade and Kondo physics	48
4.4	Spin density functional theory calculations	49
4.5	Temperature scaling	50
4.5.1	Thermal activation	51
4.5.2	Kondo effect	51
4.6	Finite bias spectroscopy	52
4.6.1	Zero bias anomaly	53
4.6.2	The extra subband-line	54
4.7	Summary	55
5	The 0.7 anomaly in hole Quantum Point Contacts	56
5.1	Introduction	56
5.2	The 0.7-anomaly characterization	57
5.2.1	Temperature-dependence	57
5.2.2	Temperature scaling	57
5.2.3	Finite bias spectroscopy	59
5.2.4	Zero bias peak height and width	60
5.2.5	Splitting of ZBA with B-field	61

5.2.6	Transconductance	62
5.2.7	In-plane magnetic field-dependence	63
5.2.8	Perpendicular magnetic field-dependence	64
5.3	0.7-feature and localization	65
5.3.1	Lateral shift of the channel	66
5.3.2	Finite bias spectroscopy at finite magnetic field	69
5.3.3	Coulomb blockade as the origin of the 0.7 anomaly	69
5.3.4	Friedel oscillations	70
5.3.5	Coulomb peak fitting to the resonance line shape	71
5.3.6	Coulomb resonance in the quantum Hall regime	73
5.4	Summary	74
6	Impurities in the QPC	75
6.1	Introduction	75
6.2	Temperature-dependence	75
6.3	Magnetic field-dependence	76
6.4	Lateral shift of the channel	77
6.5	Finite bias spectroscopy	78
6.5.1	Zero bias anomaly	79
6.6	QPC Simulations	80
6.6.1	Ideal QPC: saddle point potential	81
6.6.2	QPC with an additional transmission resonance	84
6.6.3	QPC with a spurious charge impurity nearby	86
6.7	Possible explanation	86
6.8	Summary	90
7	Anisotropic Zeeman splitting of 1D states in p-GaAs QPCs	91
7.1	Introduction	91
7.1.1	Confinement Anisotropy: previous and present works	92
7.2	Transconductance	93
7.3	Calculation of lever arm	95
7.4	Zeeman splitting anisotropy	96
7.5	Possible explanations	98
7.6	Perpendicular magnetic field	99
7.7	Conclusion and future works	100
8	Excited states in a p-GaAs single quantum dot	102

8.1	Introduction	102
8.2	Coulomb resonances	104
8.3	Resonance peak shape and hole temperature	105
8.4	Coulomb diamonds	106
8.5	Excited states of the quantum dot	107
8.6	Conclusion	110
9	Time-resolved single-hole detection in quantum dots	111
9.1	Introduction	111
9.2	Charge detection in p-GaAs quantum dots	111
9.3	Time-resolved charge detection	112
9.3.1	The noise in the QPC current	113
9.3.2	Telegraph noise	114
9.3.3	Fermi distribution of the leads	115
9.3.4	Tunnel rates	117
9.3.5	Time histograms	118
9.3.6	Connection to the queueing theory	120
9.4	Fano factor	120
9.5	The excited state spectrum	122
9.5.1	Possible explanations	123
9.5.2	Complications arising due to QPC back-action	125
9.6	Rate equation simulation	126
9.6.1	Excited states just for Γ_{in}	126
9.6.2	Excited states for Γ_{in} and Γ_{out}	128
9.6.3	Energy-dependence of barriers	128
9.7	Summary and outlook	129
10	Statistics of hole transport	130
10.1	Introduction	130
10.2	Counting experiments	130
10.3	Theory of FCS in the weak coupling regime	133
10.3.1	Two-state system	135
10.3.2	Charge transfer distribution	136
10.4	Cumulants as non-Gaussian qualifiers	137
10.4.1	Cumulants	137
10.4.2	Correlation time	139
10.4.3	Bagrets-Nazarov distribution	139

10.4.4	Poisson and Gaussian distributions	140
10.5	Difficulties of measuring cumulants	140
10.5.1	The problem of limited bandwidth	140
10.5.2	The problem of limited signal to noise ratio	142
10.5.3	The problem of finite statistics	144
10.5.4	Universal oscillations of cumulants	146
10.6	Cumulants and interactions	146
10.6.1	Generalized Binomial distributions	147
10.6.2	Factorial cumulants	148
10.6.3	Measurement data	149
10.7	Summary and outlook	151
Appendices		152
A	List of samples	152
B	Pre-biased cool down of p-GaAs nano-structures	154
C	Correction procedure to eliminate the magnetic field-dependent resistance of the leads	157
D	Evolution of the finite bias differential conductance at large perpendicular magnetic fields	160
E	Another example of a QPC with 0.7-feature	161
F	Anisotropic Zeeman spin-splitting of hole QPCs	162
G	Three charge-state regime	163
H	Cumulants in the three charge-state regime	165
Publications		166
Bibliography		167
Acknowledgements		184
Curriculum Vitae		186

Lists of symbols

physical constants	explanation
a_B	Bohr radius
$-e < 0$	electron charge
ϵ	dielectric permittivity
ϵ_o	vacuum dielectric constant
$h = 2\pi\hbar$	Planck's constant
k_B	Boltzmann constant
μ_B	Bohr magneton

Abbreviation	Explanation
2DHG	two dimensional hole gas
AC	alternating current
AFM	atomic force microscope
CB	Coulomb blockade
CPD	conditional probability density
DC	direct current
DoS	density of states
FIRST	frontiers in research, space and time or simply our clean room
FWHM	full width at half maximum
LL	Landau level
MBE	molecular beam epitaxy
QD	quantum dot
QPC	quantum point contact
SdH	Shubnikov de Haas

Symbol	Explanation
L, W	system size (length, width)
B	magnetic field
\vec{A}	vector potential
C_Σ	self-capacitance of a quantum dot
E_C	constant interaction energy
α_G	gate lever arm
ε_N	single particle energy of the Nth level
Δ_{SO}	energy offset of the spin split-off valence band
Δ	mean level-spacing
E_F	Fermi energy
Q	charge
I	current
V	voltage
G	conductance
ρ	resistivity
\mathcal{D}	density of states
$\Gamma^{S,D}$	tunnel coupling
v_F	Fermi velocity
k_F	Fermi wavenumber
λ_F	Fermi wavelength
l_c	magnetic length
ℓ_e	elastic mean free path
τ_{tr}	transport scattering time
τ_q	quantum life time
m^*	effective mass of heavy holes in the valence band of GaAs
μ_e	electron mobility
N_s^{2D}	electron sheet density
ν	filling factor
ω_c	cyclotron frequency
R_c	classical cyclotron radius
ω_0	confinement strength of a harmonic potential
r_s	interaction strength
g^*	effective g-factor
σ	Pauli matrices
T	temperature

Chapter 1

Introduction

Quantum mechanics is certainly imposing. But an inner voice tells me that it is not yet the real thing. The theory says a lot, but does not really bring us any closer to the secret of the 'old one'. I, at any rate, am convinced that He does not throw dice.

Albert Einstein, Letter to Max Born, 1926

Wave-particle duality is at the heart of quantum mechanics. The wavefunctions follow a deterministic evolution given by the Schrödinger equation while the particle nature of the field emerges in the measurement process. Max Born's interpretation of the wavefunction as a probability amplitude relating the two, is still full of counter-intuitive surprises after about one century.

In this thesis we report on experiments in solid state systems that reveal both the wave and the particle nature of holes. On one hand we talk about conductance quantization of quantum point contacts and excited states in a quantum dot which are wave phenomena, very similar to what happens in a microwave wave-guide and resonator. On the other hand we count the same particles tunnelling one by one into or out of a quantum dot and talk about its statistics.

The GaAs environment, within which these experiments were realized, is a complex system, consisting of many ions, electrons and nuclei each with their own dynamics and complications. However, by working at low temperatures, low energies and low current and voltages, many of the afore-mentioned complications can be neglected while various parameters involved in the experiment remain tunable.

The particles we deal with are holes on top of the valence band, a band full of electrons, and they can be pictured as bubbles in a bottle full of water (in analogy with the electron liquid). While the only real charge carriers in solids are electrons, it is fascinating that the holes of a full band can be regarded as the 'real' particles. For example when we talk about the spin of a hole, we in fact refer to the total spin of an almost full band of electrons.

The dispersion relation of the GaAs valence band is such that the holes have

several times larger effective masses than the (conduction band) electrons. This leads to the fact that the interactions, such as Coulomb interaction, are much more significant among holes than electrons. This pronounced carrier-carrier interaction in low-dimensional hole systems make p-doped systems especially suitable for investigating many-body effects such as the 0.7 conductance anomaly in quantum point contacts. Moreover the heavy holes with which we deal here are spin-3/2 particles which are susceptible to strong spin-orbit interaction and this has an important impact on their orbital and spin dynamics. It leads for example to a strong modification of the Landé g-factor of holes due to confinement.

This large effective mass on the other hand has the disadvantage that typical energy spacings in hole nano-structures are quite small and therefore stronger confinement and lower temperatures are necessary in order to resolve individual quantum states. Besides, holes, due to their large effective mass, are generally more prone to disorder. Since phase-coherence and ballistic transport [1] are two main requirements for quantum transport experiments, very high quality heterostructures are desired for nano-structure realizations. The carbon-doped GaAs/AlGaAs heterostructures [2–5] employed here have proven to be a suitable platform for this purpose [6].

From a technological point of view, experimental studies of hole transport in nano-structures are notoriously challenging. This is reflected in the fact that even though two-dimensional hole gases have been available for a long time, very few groups worldwide have been or are working on this subject. Nonetheless thanks to the rich physics they promise, two-dimensional hole systems have been extensively investigated, including studies of fractional quantum Hall effect [7–9], g-factor anisotropy [10–12], weak anti-localization [13], metal-insulator [14–16] and other phase transitions in quantum hall regime [17, 18].

In nanostructures, demonstration of Coulomb blockade effects in single-hole transistors [19, 20], ballistic transport through one-dimensional hole systems [21–24], phase-coherent transport through quantum rings [25, 26] and the observation of 0.7 anomaly in hole nanowires [27–29] are achieved so far. However, further experimental investigations of these p-type GaAs nano-devices are obscured compare to their n-type counterparts due to technological difficulties in fabricating stable p-type GaAs nano-structures with conventional split-gate techniques. In order to overcome these difficulties we have explored in this thesis the use of Atomic Force Microscope lithography and shallow chemical etching in combination with top-gates to define highly tunable nano-structures in two-dimensional hole gases. The electronic functionality of these structures is demonstrated by our studies on 0.7-anomaly in quantum point contacts and the observation of excited states and time-resolved charge detection of hole tunnelling in p-type GaAs quantum dots for the first time.

Besides these, holes have a number of other properties that, if cultivated, can provide a promising potential for the quantum computation technology. Hyperfine interaction of the confined spin with the nuclear spins which is currently one of the main sources of decoherence in spin qubits is strongly suppressed. Moreover,

the strong spin-orbit interaction in these systems points to the feasibility of an all-electrical control of the spin. Due to their large effective mass, however, confined holes have a dense spectrum that requires strong confinements and very low temperatures in order to resolve the single particle energy levels, a pre-requisite for potential hole-based spin-qubit applications. The observation of the excited states and the demonstration of time-resolved charge detection reported in this thesis is therefore a step in this direction.

This thesis starts with a brief introduction to the main concepts and theoretical background required to understand the measurement results in chapter 2. We present our experimental techniques in chapter 3. This chapter contains a discussion on sample fabrication technology, noise in electronic setups, cryogenics and low temperature measurement techniques and a section on top-gate fabrication. Top-gates prove to be an important tool for increasing the tunability of hole nano-structures. The rest of the thesis can be divided to two parts. Chapters 4, 5, 6, 7 discuss the many-body effects and spin physics of quantum point contacts and chapters 8, 9, 10 are dedicated to transport experiments on quantum dots.

Chapter 4 contains a very short review of many-body conductance anomalies, especially the 0.7 feature, in quantum point contacts. We present our measurements of this feature in hole quantum point contacts in chapter 5, where we exploit the perpendicular magnetic field to study the effects of localization on 0.7 anomaly. These experiments suggest the presence of a quasi-bound state in quantum point contacts and support the idea that the 0.7 anomaly can be understood based on Coulomb blockade and Kondo physics. When it comes to conductance anomalies in quasi-ballistic systems, disorder is an inevitable part of the game. In chapter 6 we discuss the effect of the point contact impurities on transport and how they are distinguished from the 0.7 anomaly. Last but not least, holes confined to two dimension have the peculiar property that their spin is not influenced by an in-plane magnetic field if they pass through a constriction perpendicular to the field. In chapter 7 we report on the observation of this phenomenon and discuss the possible explanations.

Chapter 8 reports the observation of excited states of holes confined to a small quantum dot and deviations from the constant interaction model. In chapter 9 we demonstrate how the individual tunnelling events of holes into/out of a quantum dot can be detected in real-time with a nearby charge detector. This tool opens a new window to the nano-structure, by which the statistics of the hole tunnellings can be used to extract information about the dense spectrum of states in the dot and their coupling to the leads. Finally in the last chapter we look deeper into the statistics of hole transfer through the quantum dot. We show that this statistics is indeed non-Gaussian and introduce cumulants, a set of measures that quantify deviations of a probability distribution from the Gaussian statistics. The cumulants of charge transfer show oscillations as a function of any parameter of the dot including the time. We discuss the origin of these oscillations, and calculate the recently proposed factorial cumulants for our tunnelling statistics to probe the interactions.

Chapter 2

Basic concepts and theoretical background

This chapter is intended to serve as a theoretical introduction to the basic concepts used in the following chapters. It should be stressed that this is by no means a theoretical overview but merely a general framework based on which our experimental results are interpreted. The vast majority of the content is extracted from textbooks and articles to which we have referenced accordingly. Most of the materials are simplified in order to present an intuitive picture. Only basic concepts common to all chapters are discussed here. Each chapter will contain some sections introducing additional concepts specially required in that chapter.

2.1 Valence band of GaAs

The states at the bottom of the conduction band of a lattice are composed of atomic s-orbital $|S\rangle$ (orbital angular momentum $l = 0$) with spin up/down $\{|\uparrow\rangle, |\downarrow\rangle\}$ (spin $s = 1/2$), known as spin doublet. The spherical symmetry of these orbitals leads to the fact that in the spherical approximation (discussed below) the resulting conduction band at low energies is isotropic. States at the edge of the valence band on the other hand have the symmetry of atomic p-orbitals $\{|X\rangle, |Y\rangle, |Z\rangle\}$ (orbital angular momentum $l = 1$) with spin up/down ($s = 1/2$), a sextet of degenerate states in the absence of spin-orbit interaction. The anisotropic shape of p-orbitals leads to the fact that the bands made of them are not isotropic. This can be seen for example if we use a tight-binding model to make a band out of only $|X\rangle$ -orbitals in a 2D cubic lattice. The wavefunction overlap between orbitals at different sites, which is proportional to the tunnelling amplitude, would be different in x and y directions [30]. The degeneracy of the levels however is lifted thanks to relativity as we will see shortly.

2.1.1 Spin-orbit interaction

Spin-orbit (SO) interaction is a purely relativistic effect that enters into the Hamiltonian in atomic physics from a non-relativistic approximation to the Dirac equation [31]. Electrons moving in the potential of an ion feel an effective magnetic field in their rest frame which acts on the spin. The Hamiltonian is

$$\mathcal{H}_{SO} = -\frac{\hbar}{4m_0^2c^2}\hat{\sigma} \cdot \hat{\mathbf{p}} \times \nabla V_0 \quad (2.1)$$

where $\{\hat{\sigma}_i\}$ are the Pauli matrices. Noting that for a central-force atomic potential $\nabla V_0 = \hat{\mathbf{r}}dV_0/dr$ and the orbital and spin angular momenta are defined as $\hat{\mathbf{L}} = \mathbf{r} \times \hat{\mathbf{p}}$ and $\hat{\mathbf{S}} = \frac{1}{2}\hat{\sigma}$, we can rewrite this Hamiltonian as

$$\mathcal{H}_{SO} = -\frac{\hbar}{2m_0^2c^2}\frac{1}{r}\frac{dV_0}{dr}\hat{\mathbf{S}} \cdot \hat{\mathbf{L}} \quad (2.2)$$

and therefore orbital and spin angular momenta are coupled by SO interaction. Introducing the total angular momentum $\hat{\mathbf{J}} = \hat{\mathbf{L}} + \hat{\mathbf{S}}$, this coupling is written as

$$2\hat{\mathbf{L}} \cdot \hat{\mathbf{S}} = \hat{\mathbf{J}}^2 - \hat{\mathbf{L}}^2 - \hat{\mathbf{S}}^2 \quad (2.3)$$

Addition of $l = 1$ to $s = 1/2$ gives a quadruplet with $j = 3/2$ ($m_j = \pm 3/2, \pm 1/2$) and a doublet with $j = 1/2$ ($m_j = \pm 1/2$). It is obvious from Eq. 2.3 and 2.2 that these two sets will have a different energy. Hence the $j = 1/2$ doublet is lowered in energy with the corresponding band known as SO split-off band, separated by an amount Δ_{SO} which is about 0.34 eV in GaAs.¹ This is significant compared to the band-gap $E_g = 1.52$ eV in this material (Fig. 2.1a). A similar effect in atomic physics is responsible for the sodium D-line doublet.

Because of the SO interaction 2.2, the total angular momentum j and one of its components for example along the z -direction m_j are the only good quantum numbers, thus $|j, m_j\rangle$ is used as the basis for the atomic states. For the $j = 3/2$ quadruplet these states are related to the orbital and spin states as [31]

$$\begin{aligned} \left| \frac{3}{2}, \frac{3}{2} \right\rangle_{\text{HH}} &= \frac{-|X + iY\rangle |\uparrow\rangle}{\sqrt{2}} & \left| \frac{3}{2}, \frac{1}{2} \right\rangle_{\text{LH}} &= \frac{-|X + iY\rangle |\downarrow\rangle + 2|Z\rangle |\uparrow\rangle}{\sqrt{6}} \\ \left| \frac{3}{2}, -\frac{1}{2} \right\rangle_{\text{LH}} &= \frac{|X - iY\rangle |\uparrow\rangle + 2|Z\rangle |\downarrow\rangle}{\sqrt{6}} & \left| \frac{3}{2}, -\frac{3}{2} \right\rangle_{\text{HH}} &= \frac{|X - iY\rangle |\downarrow\rangle}{\sqrt{2}} \end{aligned} \quad (2.4)$$

Band diagram of crystals can be obtained by a number of different methods. In the so-called $\mathbf{k} \cdot \mathbf{p}$ method, the band edge states at the Γ point ($\mathbf{k} = 0$) are used as the basis for the expansion of Bloch states with non-zero wave vectors using perturbation theory in \mathbf{k} and SO interaction Eq. 2.1 [1, 31].

¹For III-V semiconductor compounds $\Delta_{SO}(\text{AB}) = 0.5(1 - f_i)\Delta_{SO}(\text{A}) + 0.5(1 + f_i)\Delta_{SO}(\text{B})$ [31]. For comparison Δ_{SO} in Si and Ge is equal to 0.044 eV and 0.296 eV while E_g is equal to 1.11 eV and 0.67 eV respectively.

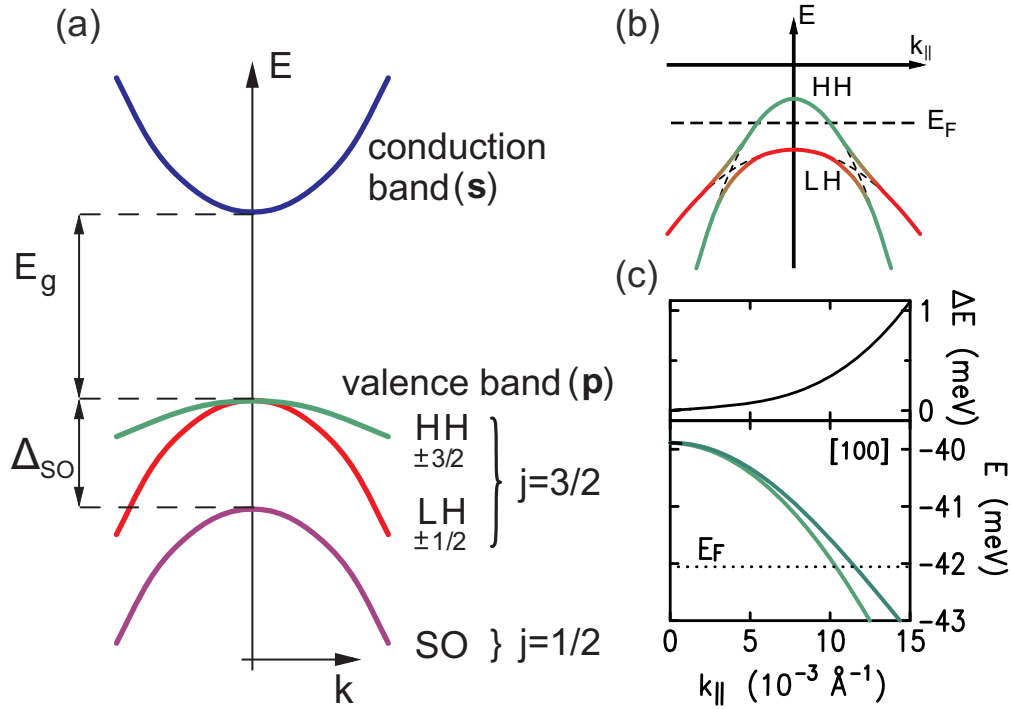


Figure 2.1: (a) Schematic of GaAs band structure in the so-called isotropic approximation with conduction band, heavy and light hole bands and SO split-off band shown. (b) Energy diagram of $j = 3/2$ bands vs. in-plane wavevector $k_{||}$ emphasizing the mass inversion. HH and LH bands crossing is lifted by HH-LH mixing. (c) Self-consistently calculated dispersions $E_{\pm}(\mathbf{k}_{||})$ of the lowest HH subband in a (100)-grown GaAs/AlGaAs heterostructure with a density of $2 \times 10^{15} \text{ m}^{-2}$ (lower figure) together with the spin-splitting $E_{+}(\mathbf{k}_{||}) - E_{-}(\mathbf{k}_{||})$. All figures adapted from [31].

2.1.2 Luttinger Hamiltonian

Bulk semiconductors with diamond structure like Si and Ge have the point group symmetry of a cube. GaAs, however, has a zinc blende structure and has the point group symmetry of a tetrahedron which is essentially the cubic symmetry without the inversion symmetry. It has been shown [31] that the total Hamiltonian of a zinc blende bulk material can be separated into a symmetry hierarchy

$$\mathcal{H}_{bulk} = \mathcal{H}_{spherical} + \mathcal{H}_{cubic} + \mathcal{H}_{tetrahedron} \quad (2.5)$$

in which terms with lower symmetry are smaller and smaller. Although it is necessary to include all these terms to make any realistic theoretical prediction, already some insight can be obtained by keeping only the first term known as the *spherical approximation*. The $\mathbf{k} \cdot \mathbf{p}$ Hamiltonian of a crystal at zero field in this approximation

is given by [32]²

$$\mathcal{H}_{spherical} \approx -\frac{\hbar^2}{2m_0} \left[(\gamma_1 + \frac{5}{2}\gamma_2)\mathbf{k}^2 - 2\bar{\gamma}(\mathbf{k} \cdot \mathbf{J})^2 \right] \quad (2.6)$$

which enjoys full rotational symmetry. The $j = 3/2$ block of this Hamiltonian, known as the Luttinger Hamiltonian, describes the $j = 3/2$ quadruplet and has a four-fold degeneracy at $\mathbf{k} = 0$. The parameters $\{\gamma_i\}$ are material-dependent positive numbers ($\gamma_1 > 2\gamma_2$) known as the Luttinger parameters.³ The terms beyond the spherical approximation in Eq. 2.5 mix different j -blocks relating the quadruplet valence bands to the conduction band, the SO split-off band and other remote bands. We neglect these couplings here for simplicity. Taking the z -direction as the direction of quantization of total angular momentum and writing the above Hamiltonian in the basis of \hat{J}_z with $m_j = \pm 3/2, \pm 1/2$ we have [31, 33]

$$\mathcal{H}_{spherical}^{4 \times 4} = \begin{pmatrix} \mathcal{H}^{HH} & c & b & 0 \\ c^\dagger & \mathcal{H}^{LH} & 0 & -b \\ b^\dagger & 0 & \mathcal{H}^{LH} & c \\ 0 & -b^\dagger & c^\dagger & \mathcal{H}^{HH} \end{pmatrix}. \quad (2.7)$$

The diagonal elements of this Hamiltonian known as the *diagonal approximation* are

$$\mathcal{H}_{diagonal}^{HH/LH} = -\frac{\hbar^2}{2m_0} [(\gamma_1 \pm \gamma_2)\mathbf{k}_{\parallel}^2 + (\gamma_1 \mp 2\gamma_2)k_z^2]. \quad (2.8)$$

It is clear from this Hamiltonian that the heavy holes (HH with $m_j = \pm 3/2$) and light holes (LH with $m_j = \pm 1/2$) have different effective masses along and perpendicular to the quantization axis. The names heavy and light refer to the former direction (Fig. 2.1a). The non-diagonal elements of (2.7) are

$$\begin{aligned} b &= \frac{\hbar^2}{2m_0} 2\sqrt{3}\gamma_3 k_z k_- \\ c &= \frac{\hbar^2}{2m_0} \sqrt{3}/2 [(\gamma_3 + \gamma_2)k_-^2 + (\gamma_3 - \gamma_2)k_+^2], \end{aligned} \quad (2.9)$$

with k_{\pm} defined as $k_{\pm} = k_x \pm ik_y$ and mix the HH and LH bands at any non-zero momentum in the bulk.

2.1.3 SO interaction in the effective mass approximation

The Hamiltonians described so far are not the bare Hamiltonian which includes the bare kinetic energy and the crystal potential but in fact the dispersion relations of the Bloch wave functions

$$\psi_{n\mathbf{k}}(\mathbf{r}) = e^{i\mathbf{k} \cdot \mathbf{r}} u_{n\mathbf{k}}(\mathbf{r}). \quad (2.10)$$

²Strictly speaking the Hamiltonian in the spherical approximation is more complicated than Eq. 2.6. The form given here assumes that $\gamma_2 = \gamma_3 = \bar{\gamma}$ [32]. The Hamiltonian in Eq. 2.7 does not make such assumption and is more accurate.

³In GaAs γ_1 , γ_2 and γ_3 are equal to 6.85, 2.10 and 2.90 respectively.

However in the so-called *envelope function approximation* they can be assumed to be the kinetic Hamiltonian of the nearly-free particles in the solid ($\hbar\mathbf{k} \rightarrow \hat{\mathbf{p}} = -i\hbar\nabla$). The expansion of the dispersion relation to second order ⁴ in \mathbf{k} gives the effective mass m^* . The atomic SO interaction in Eq. 2.1 can be written in the form

$$\mathcal{H}_{SO} = - \left[\frac{\hat{\mathbf{p}}}{m_0} \times \nabla \left(\frac{V}{2m_0c^2} \right) \right] \cdot \hbar\hat{\mathbf{S}} \quad (2.11)$$

which emphasizes its derivation from the Dirac equation. But do the nearly-free particles in a crystal feel any SO interaction? It is interesting that indeed a similar SO interaction term is inherited from the bare Hamiltonian by the envelope function approximation. This can be extracted from the 8×8 $\mathbf{k} \cdot \mathbf{p}$ Hamiltonian [31] by systematic block diagonalization and keeping only the desired band [31]. For the conduction band this procedure gives the simple expression of

$$\mathcal{H}_{SO} \sim -k_{SO} \left[\frac{\hat{\mathbf{p}}}{m_{c/v}^*} \times \nabla \left(\frac{V}{E_g} \right) \right] \cdot \hbar\hat{\mathbf{S}} \quad (2.12)$$

which is very similar to Eq. 2.11. As $E_g \approx 1$ eV compared to $2m_0c^2 \approx 1$ MeV, the spin-orbit effects are drastically enhanced in solids. ⁵ The coefficient k_{SO} is given by

$$k_{SO} = \frac{1}{6} \left[1 - \left(1 + \frac{\Delta_{SO}}{E_g} \right)^{-2} \right] \approx \frac{\Delta_{SO}}{3E_g} \quad (2.13)$$

and hence Δ_{SO}/E_g (≈ 0.22 in GaAs) is a measure of the SO interaction strength in solids.

The Zeeman energy is also affected by the dispersion relations. To first order in \mathbf{B} , this can be lumped into an effective Landé g-factor so that the Zeeman shift is

$$\mathcal{H}_Z = g^* \mu_B \mathbf{B} \cdot \hat{\mathbf{S}}. \quad (2.14)$$

This change of the g-factor in p-GaAs system will be discussed in Chapter 7.

2.1.4 2D Confinement

Confining holes to two dimension defines the direction normal to the plane of the 2DHG as the natural direction of quantization [31]. The heavy holes with higher effective mass in this direction are lowered in energy than light holes but at the same time have lower in-plane effective mass which means that these two subbands cross at some nonzero k_{\parallel} . This change of mass of the subbands is called *mass inversion*. The degeneracy at these points is lifted and the bands have an anti-crossing due to non-diagonal elements of the Hamiltonian in the total angular momentum basis

⁴Discarding the terms beyond second order is called effective mass approximation.

⁵However the field gradients in solids are much smaller than their atomic counterparts.

(Fig. 2.1b). Fortunately only the heavy hole band is occupied with typical values for the 2D density considered in this thesis and we do not need to be bothered either by the light holes or their mixing with the heavy holes in most of the thesis. However one has to bear in mind that at any non-zero k_{\parallel} they are slightly mixed. This becomes important when we discuss the anisotropy of g -factors in Chapter 7.

2.1.5 Spin-orbit interaction in 2D electron and hole gases

The heavy hole states in Eq. 2.4 described by the Hamiltonian 2.7 are spin degenerate in the absence of magnetic field. Generally the spin degeneracy of energy bands in solid state systems $E_{\mathbf{k}\uparrow} = E_{\mathbf{k}\downarrow}$, results from *time reversal symmetry* and *spatial inversion symmetry*. The former changes the direction of both momentum \mathbf{k} and spin, resulting in the so-called *Kramers degeneracy* $E_{\mathbf{k}\uparrow} = E_{-\mathbf{k}\downarrow}$ while the latter only changes the momentum direction, implying $E_{\mathbf{k}\uparrow} = E_{-\mathbf{k}\uparrow}$ and $E_{\mathbf{k}\downarrow} = E_{-\mathbf{k}\downarrow}$.

This degeneracy is broken if either a magnetic field is applied breaking the time reversal symmetry (known as the Zeeman shift discussed in Chapter 7) or if the Hamiltonian contains terms that break the inversion symmetry. The latter may have two origins: One is the so-called *bulk inversion asymmetry* (BIA), i.e. the presence of the term $\mathcal{H}_{tetrahedral}$ in the bulk Hamiltonian Eq. 2.5. In III-V semiconductor compounds with zinc blende structure this lack of spatial inversion symmetry results in the so-called Dresselhaus SO splitting [34]. Obviously this effect strongly depends on the crystallographic directions of the lattice. For conduction band electrons in a 2DEG grown on the [100]-plane and normal to the z -direction this interaction is described by

$$\mathcal{H}_D = \beta \langle k_z^2 \rangle (\sigma_x k_x - \sigma_y k_y), \quad (2.15)$$

where β is the Dresselhaus coefficient and depends on the band parameters of the host material. It follows that narrower quantum wells have larger Dresselhaus splitting. The other origin of the spin-splitting known as the *structure inversion asymmetry* (SIA) is the electric field due to the confinement potential, band offsets or the voltage applied to the surrounding gates ($\mathcal{H} = \mathcal{H}_{bulk} + V$) which induces the so-called Rashba spin splitting. For electrons confined in a 2DEG this interaction is given by

$$\mathcal{H}_R = \alpha \langle E_z \rangle (\sigma_x k_y - \sigma_y k_x) \quad (2.16)$$

and again α is called the Rashba SO coupling parameter. The quantity $\langle E_z \rangle$ is the average electric field perpendicular to the plane. Experimentally this electric field can be produced either by engineering the confinement potential in GaAs/AlGaAs heterostructures or an electric field produced by the top or back-gates. The latter method can be used to control the Rashba splitting as it was shown experimentally by Nitta et al. [35] and Engels et al. [36]. This electrical control of SO interaction is essential in many proposals, e.g. the Datta-Das transistor [37], that use the spin degree of freedom instead of the charge of carriers for information processing.

SO splitting in 2D heavy hole gases differs from that in 2D electron gases due to fact that the quantization axis in these systems is fixed in the growth direction. Thus the SO interactions that tends to orient the spin in the plane of 2DHG are cubic in wavevector [6, 31]. As this subject is not directly related to the experiments reported in the thesis we refrain from providing further details and refer the interested readers to Winkler [31], Habib et al. [38] and Zawadzki and Pfeffer [39]. The large effective mass of the holes enhances the effect of Rashba and Dresselhaus spin-splitting in p-type systems.⁶ Fig. 2.1c shows the energy of heavy hole (HH) bands as a function of the in-plane wavevector and the spin-splitting between the two spin-subbands.

2.1.6 Hyperfine interaction

Confined spins in solid state environments are promising candidates for future quantum information processing and computation science and technology [40]. However it has been found that the excessive number of degrees of freedom in these systems results in fast relaxation and decoherence of the spins, inhibiting scalable applications. Hyperfine interaction between the confined spin \mathbf{S} and the host nuclear spins $\{\mathbf{I}_n\}$ has been identified as the main origin of this decoherence [41–43]. It has been argued that the hyperfine interaction, proportional to the wavefunction of the confined particle at the position of the nuclear spin, is expected to vanish for valence band holes due to p-type symmetry of the atomic orbitals which has a node at the nucleus. It was recently predicted [44] that even though the hyperfine interaction vanishes the dipole-dipole coupling between two spins is still present giving rise to an Ising-like Hamiltonian in quasi-two-dimensional systems (e.g. lateral quantum dots) and a coupling strength on the order of $10 \mu\text{eV}$, one order of magnitude smaller than the hyperfine coupling for electrons. This coupling strength indeed has been measured recently by optical pump and probe technique in self-assembled p-doped InGaAs quantum dots [45].

2.2 Interactions in hole gases

Most of the experiments in this thesis were performed at low temperatures where the vibrational degrees of freedom of the crystal lattice are ‘frozen’.⁷ In this regime

⁶Note that the effective mass in Eq. 2.12 is sort of an average effective mass of the two bands. Therefore the carriers in the band with a larger effective mass still experience stronger SO interaction compared to their kinetic energy.

⁷Nevertheless electron-phonon interaction is usually kept in Eq. 2.17 since it is responsible for relaxation and decoherence. Here we do not consider these effects.

the Hamiltonian for a spinless system in the effective mass approximation is [46]⁸

$$\mathcal{H} = \sum_{i=1}^N \left(\frac{\hat{\mathbf{p}}_i^2}{2m^*} + \frac{1}{2} \sum_{j \neq i}^N \frac{e^2/4\pi\epsilon}{|\mathbf{r}_i - \mathbf{r}_j|} + eV(\mathbf{r}_i) \right) \quad (2.17)$$

The first two terms are the kinetic energy and the Coulomb interaction between the particles⁹. The last term is the potential energy felt by the particles due to presence of impurities and the voltage on gates¹⁰. m^* is the effective mass ($\overline{m^*} = 0.43m_e$ for holes) and $\epsilon = \epsilon_0\epsilon_r$ is the permittivity with $\epsilon_r = 12.9$ in GaAs.

2.2.1 Relevant scales

A number of energy and length scales are associated with a hole gas. An important length scale from the atomic physics is the effective Bohr radius defined as

$$a_B^* = \frac{\hbar^2}{m^*e^2/4\pi\epsilon} \quad (2.18)$$

which is about $a_B^* \approx 1.6$ nm in our system. The physical significance of this quantity becomes clear in a moment. At low temperatures all the states below the Fermi energy E_F are occupied. Assuming a parabolic dispersion relation, the density of states (DoS) is constant in 2D [1] and for n particles per unit area we can write

$$\mathcal{D}_{2D}(E) = \frac{m^*}{\pi\hbar^2} \quad n = \int_0^{E_F} \mathcal{D}(E)dE = E_F\mathcal{D}_{2D} \quad (2.19)$$

and therefore the Fermi energy is linear with density. Defining the Fermi momentum p_F and the Fermi wavelength λ_F through $E_F = p_F^2/2m^*$ and $p_F = h/\lambda_F$, we get

$$\lambda_F^{2D} = \sqrt{\frac{2\pi}{n}} \quad (2.20)$$

$E_F \approx 2$ meV and $\lambda_F \approx 40$ nm for the typical 2D density of $4 \times 10^{15} \text{ m}^{-2}$ studied here. Confinement effects become important if the size of the nano-structure is of the order of the Fermi wavelength λ_F .

⁸Even in the simple case of the so-called Jellium model two other terms responsible for the the bulk-bulk and bulk-electron interactions $\mathcal{H}_{e-b} + \mathcal{H}_{b-b}$ are necessary in order to fulfil the charge stability of the system [47, 48]. Here we do not consider these technicalities.

⁹we take $e = |e|$ as the electric charge of holes.

¹⁰The presence of the gates can modify the interaction term in this Hamiltonian due to screening. we neglect these effect here.

2.2.2 Interaction strength as the fundamental parameter

The Fermi wavelength is proportional to the (average) distance between particles. This distance counted in units of a_B^* is denoted by r_s and can be calculated from

$$\frac{1}{n} = \begin{cases} \frac{4\pi}{3}(r_s a_B^*)^3 & \text{3D} \\ \pi(r_s a_B^*)^2 & \text{2D} \\ 2(r_s a_B^*) & \text{1D} \end{cases} \quad (2.21)$$

If we take the distance between particles as our unit length using the new tilde variables defined by $\mathbf{r} \rightarrow (r_s a_B^*)\tilde{\mathbf{r}}$ and $\hat{\mathbf{p}} \rightarrow \hat{\tilde{\mathbf{p}}}/(r_s a_B^*)$, the Hamiltonian 2.17 becomes [48]

$$\mathcal{H}_0/Ry^* = \frac{1}{r_s^2} \sum_{i=1}^N \hat{\tilde{\mathbf{p}}}_i^2 + \frac{1}{r_s} \sum_{i=1}^N \left(\sum_{j \neq i} \frac{1}{|\tilde{\mathbf{r}}_i - \tilde{\mathbf{r}}_j|} \right) + \sum_{i=1}^N \tilde{V}(\tilde{\mathbf{r}}_i) \quad (2.22)$$

The first two terms are universal; apart from r_s no material-dependent parameter is involved in a homogeneous system. The potential energy, however, does depend on material parameters through $\tilde{V}(\tilde{\mathbf{r}}) = eV(r_s a_B^* \tilde{\mathbf{r}})/Ry^*$ but it usually has a series expansion that involves no powers of r_s less than -1 at any point in space. Note that $r_s a_B^* \propto \lambda_F$ sets the scale of the confinement as mentioned before. The Hamiltonian here is in units of effective Rydberg energy defined as

$$Ry^* = \frac{e^2/4\pi\epsilon}{2a_B^*} \quad (2.23)$$

which is about 450 meV in our system. In the Hamiltonian 2.22 the kinetic energy and the Coulomb interaction are divided by the first and second powers of r_s and therefore this parameter sets the relative measure of these two energies. r_s can also be expressed as the ratio between Coulomb interaction and the Fermi energy ¹¹

$$r_s = \frac{e^2/4\pi\epsilon(r_s a_B^*)}{E_F} \quad (2.24)$$

and hence it is usually called the *interaction strength* which is about $r_s \approx 5.6$ in our two-dimensional hole system for typical densities of $4 \times 10^{15} \text{ m}^{-2}$.

2.2.3 Screening

In order to develop some intuition about the solutions of the many-body problem described by the Hamiltonians 2.17 and 2.22 it is desirable to have some approximate solutions. Especially single-particle approximations are preferred in which different phenomenological effects motivated by Eq. 2.17 are added one by one in a mean-field sense into an effective potential felt by the particles. One of these effects is the

¹¹Generally average Coulomb interaction and average kinetic energy must be used for the numerator and denominator here. However the same expression would be obtained for the 2D case.

linear screening [1] of a potential by other carriers. The external potential $V_{\text{ext}}(\mathbf{r})$ is modified by the presence of the other particles so that the Fourier transform of the total potential $V_{\text{tot}}(\mathbf{q})$ is given by [1]

$$\langle V_{\text{tot}}(\mathbf{q}) \rangle = \frac{\langle V_{\text{ext}}(\mathbf{q}) \rangle}{\epsilon(q, E_F, T)} \quad (2.25)$$

The Lindhard's dielectric function $\epsilon(q, E_F, T)$ is a monotonic functional of the DoS $\mathcal{D}(E)$. In the simple case of Thomas-Fermi approximation [1]

$$\epsilon_{\text{TF}}(\mathbf{q}) = 1 + \frac{2}{qa_B^*} \quad (2.26)$$

and again the effective Bohr radius sets the length scale of the screening $\lambda_{\text{TF}} = \pi a_B^*$. External potentials are thus expected to be screened on a length scale of about $\lambda_{\text{TF}} \approx 5$ nm in our system (much shorter than corresponding scale for electrons), resulting in a hard wall potential confinement. On one hand this makes it difficult to hit the right size for a constriction to be still tunable by the gates, but on the other hand it has the advantage that if 'enough' holes are around, the potential is perfectly screened. This might be responsible for rather clean conductance plateaus in our QPCs.

2.2.4 Phase diagram

An electron gas described by Eq. 2.22 has a very rich phase diagram [48]. Here we only sketch a simplified qualitative picture. At large densities $r_s \rightarrow 0$ the first term is dominant due to Pauli exclusion principle requiring no double occupancy of the energy levels. At intermediate values of r_s the second term gets dominant. The main contribution of this term is usually due to so-called Hartree interaction which for a homogeneous system is cancelled by the background. The screening effect discussed above is a result of Hartree interaction in an inhomogeneous system. The other contribution which is the so-called exchange effect becomes important at lower densities [46] resulting in an exchange-induced ferro-magnetism (for spinful particles). This effect will be discussed again in Chapter 4 in connection to the so-called 0.7 anomaly. At yet lower densities (higher r_s) in a disordered system the last term gets dominant and the carriers have to obey the potential energy to minimize the Hamiltonian. This results in a sudden drop of conductivity known as the *mobility edge* which limits the density tunability (see Chapter 3). In a clean system when second and third terms compete a transition to a solid called *Wigner crystal* is predicted.

The interaction strength scales linearly with the effective mass m^* . Thanks to their large effective mass, *holes tend to localize* in local potential minima. This can be better seen in the original Hamiltonian 2.17 if we neglect the Coulomb interaction.

2.3 Magnetoresistance

Magnetoresistance measurements are an essential tool in transport experiments and are involved in a number of measurements reported in this thesis. Typically a perpendicular magnetic field is applied that acts not only on the spin of the charge carriers but also on their orbital motion. At low fields this can be captured by the Hall effect within the framework of the Drude model. At larger fields quantum effects become considerable, the orbital motion is quantized and the evolution of the constant zero-field density of states (DoS) of holes into Landau levels at finite B leads to Shubnikov-de Haas oscillations of the magnetoresistance. At even higher fields we enter the regime of the quantum Hall effect (QHE) where the transport is dominated by the edge states. In the following we will give a brief introduction to these effects. For an in-depth introduction we refer the interested readers to Ihn [1].

2.3.1 Drude model and the Hall effect

The low-field magnetoresistance is used in this thesis to characterize the density and mobility of carriers in two-dimensional hole gases (2DHG). Typically a sample with Hall bar geometry (shown in Fig. 2.2d) is measured at low temperature using standard four-terminal technique. The longitudinal ρ_{XX} and Hall resistivity ρ_{XY} are related to the applied current and the measured voltages through

$$\rho_{XY} = \frac{V_Y}{I_X} \quad \rho_{XX} = \frac{W}{L} \frac{V_X}{I_X} \quad (2.27)$$

where W and L are the width and the length of the Hall bar respectively. In a two-dimensional system at low magnetic fields from the Drude model we have [1]

$$\rho_{XY} = \frac{B}{ne} \quad \rho_{XX} = \frac{1}{ne\mu} \quad (2.28)$$

where n is the sheet carrier density and μ the mobility. From Eq. 2.28 density and mobility are obtained by

$$n = \frac{1}{e d \rho_{XY}/dB|_{B=0}} \quad \mu = \frac{d\rho_{XY}/dB|_{B=0}}{\rho_{XX}(B=0)} \quad (2.29)$$

According to the Drude model the mobility is related to the mean scattering time τ_e by $\mu = e\tau_e/m^*$. The appearance of the effective mass in the denominator indicates that hole systems with comparable scattering times have much lower mobility than electron systems. Furthermore, the scattering rate is proportional to the effective mass via the density of states. For equal carrier density and type of scatterers the scattering rate is therefore enhanced by the larger mass. An important length scale for transport physics is the elastic mean free path $l_e = v_F\tau_e$ which is the distance

the carriers travel between two scattering. Mean free path can be calculated from density and mobility using the formula

$$l_e = \frac{h}{e} \mu \sqrt{\frac{n}{2\pi}} \quad (2.30)$$

A magnetic field perpendicular to the plane of 2DHG forces the charge carriers to have a cyclotron motion while their orbit center drifts with a velocity $v_D = E/B$ normal to both electric and magnetic fields ($\mathbf{E} \times \mathbf{B}$ -drift) [1]. This motion is characterized by the cyclotron frequency $\omega_c = eB/m^*$ ($\approx 270 \mu\text{eV}/\text{Tesla}$ here) and the classical cyclotron radius $R_c = p_F/eB$ ($\approx 100 \text{ nm} \times \text{Tesla}$ here). Initially the charge carriers drift normal to the applied electric field towards the edge of the Hall bar. But as soon as the electric field built up by the accumulated charges gets dominant, the carriers drift along the Hall bar. Different magnetoresistance regimes are characterized by the parameter $\omega_c \tau$. For $\omega_c \tau = B\mu \ll 1$ the classical Hall effect and the Drude model provide a sufficient description of the transport. At higher values of this parameter quantum effects become important which are discussed in the next section.

2.3.2 Landau levels

A magnetic field can be incorporated in the Hamiltonian of Eq. 2.17 by minimal coupling $\hat{\mathbf{p}} \rightarrow \hat{\boldsymbol{\Pi}} = \hat{\mathbf{p}} - e\mathbf{A}$ (we take $q=|e|=e$ as the charge of holes). \mathbf{A} is the vector potential satisfying $\mathbf{B} = \nabla \times \mathbf{A}$ which is $\mathbf{A} = \frac{1}{2}\mathbf{r} \times \mathbf{B}$ in the symmetric gauge. With this transformation for $\mathbf{B} = \hat{z}B$, the kinetic part of the Hamiltonian becomes

$$\mathcal{H}_K = \frac{1}{2m^*} \left(\hat{\Pi}_x^2 + \hat{\Pi}_y^2 \right) + \frac{\hat{p}_z^2}{2m^*} \quad (2.31)$$

The new twist is that the momentum components do not commute any more, i.e.,

$$\left[\hat{\Pi}_x, \hat{\Pi}_y \right] = i\hbar eB. \quad (2.32)$$

Defining two new operators

$$\hat{a} = \frac{l_c}{\sqrt{2\hbar}} \left(\hat{\Pi}_x + i\hat{\Pi}_y \right) \quad \hat{a}^\dagger = \frac{l_c}{\sqrt{2\hbar}} \left(\hat{\Pi}_x - i\hat{\Pi}_y \right) \quad (2.33)$$

where $l_c = \sqrt{\hbar/eB}$ ($\approx 25 \text{ nm}/\sqrt{\text{Tesla}}$) is the magnetic length, it can be seen that \hat{a} and \hat{a}^\dagger satisfy $[\hat{a}, \hat{a}^\dagger] = 1$ and other bosonic commutation relations. If additionally we neglect the z -dependent part of the Hamiltonian as it merely gives an energy offset due to separation of variables and 2D confinement, the kinetic part Eq. 2.31 becomes

$$\mathcal{H}_K = \hbar\omega_c \left(\hat{a}^\dagger \hat{a} + \frac{1}{2} \right) + E_0 \quad (2.34)$$

which is a 1D harmonic oscillator. $\omega_c = eB/m^*$ is the cyclotron frequency introduced before. Fig. 2.2b depicts the spatial extent of the wave functions. The wavefunction of the m th-state has the width $l_c^{(m)} = \sqrt{2m+1}l_c$ [1]. The operator $\hat{\Pi}$ is related to *cyclotron motion* of the particles. Having a 1D harmonic oscillator for a 2D system means that there are a lot of degeneracies. Indeed it can be shown that a set of new operators defined as $\hat{\Lambda} = \hat{\mathbf{p}} + e\mathbf{A}$ commute with the Hamiltonian, resulting in this extra degeneracy and are related to the *guiding center coordinates* [31, 48, 49].

Fig. 2.2a shows the so-called Landau levels (LLs), the set of energy levels separated by $\hbar\omega_c$ mentioned here, in the density of states. The plot also shows how the constant zero-field DoS of holes in 2D given by Eq. 2.19 transforms to these discrete levels which are broadened by impurity scattering. At low fields (but still large enough to satisfy $B > \mu^{-1}$) the presence of this oscillating density of states creates the so-called Shubnikov-de Haas oscillations of the resistance. These oscillations can be seen in the longitudinal resistivity ρ_{XX} shown in the inset of Fig. 2.2e. The density difference between two spin subbands resulting from SO interaction (Fig. 2.1c) is the origin of the complex beating pattern in these oscillations [6] and can be extracted from the data by Fourier transformation [8, 38].

For a sample with the area A , the degeneracy of the Landau levels $N_L = n_L A$ is given by the ratio between total flux through the sample $\Phi = BA$ and the flux quantum $\Phi_0 = h/e$ so that the area underneath $\mathcal{D}_0(E)$ and $\mathcal{D}_B(E)$ over a full $\hbar\omega_c$ period is the same, i.e.,

$$n_L = eB/h. \quad (2.35)$$

The filling factor $\nu = n/n_L$ is defined as the number of occupied Landau levels and therefore it depends on both magnetic field and the 2D density n

$$\nu B = nh/e. \quad (2.36)$$

2.3.3 Quantum Hall Effect

When the potential energy is added to the Hamiltonian 2.34, the Landau levels depicted in Fig. 2.2a are broadened due to short-range potential disorder [1]. This potential disorder divides each Landau level into a set of localized states and extended states indicated in this figure. The extended states percolate throughout the sample and a mobility edge arises at the transition between extended and localized states [1]. Furthermore, the local density of states basically follow the long-range background potential as illustrated in Fig. 2.2c. Assuming a form $\psi \propto \phi(y)e^{ik_x x}$ for the carriers, the Hamiltonian 2.31 couples the \tilde{y} position of center coordinate to the wave vector k_x and therefore either of the two can be used for the x axis in Fig. 2.2c.

At low temperature and low bias carrier transport happens at the Fermi energy, thus close to the red points in Fig. 2.2c that mark the crossing of the energy levels with the Fermi level. At these points in addition to the normal magnetic field, the particles feel an electric potential due to the boundaries of the sample and therefore have a so-called $\mathbf{E} \times \mathbf{B}$ -drift [1] along the sample boundary (Fig. 2.2d). Having only

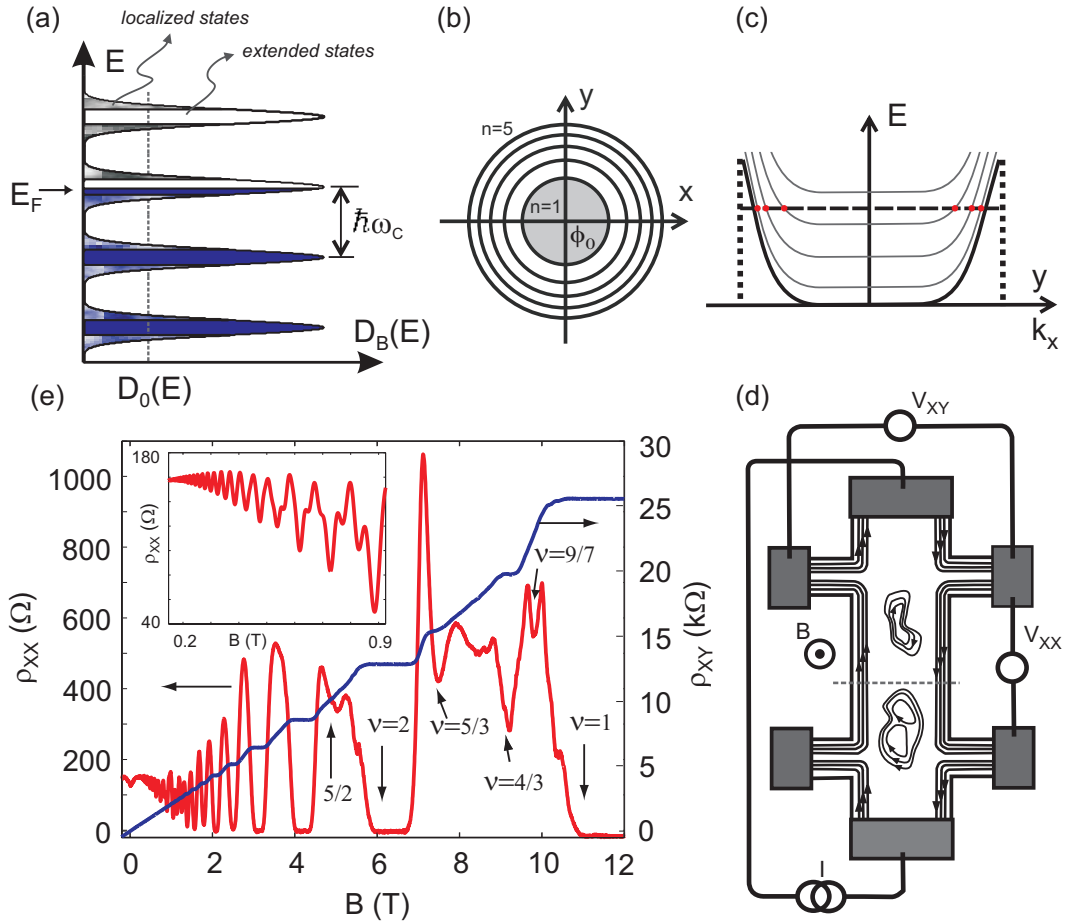


Figure 2.2: (a) The zero-field density of states $\mathcal{D}_0(E)$ transforms to a set of Landau levels separated by $\hbar\omega_c$ at finite fields (Zeeman shift is neglected here). The localized and extended states are indicated in the figure. (b) (taken from [1]) Quantized cyclotron orbits in real space. The smallest orbit encloses exactly one flux quantum Φ_0 . (c) The energies of LLs as a function of the guiding center coordinate y (along the dashed cut in (d)) or the wavevector k_x which is proportional to the center coordinate y . Note that at the sample edge the energy levels have a finite derivative and hence the carriers feel an electric field. At low temperature the current is carried at the Fermi energy (red dots) by $\mathbf{E} \times \mathbf{B}$ -drift. (d) Schematic of a magnetoresistance measurement in a sample with Hallbar geometry. The current is transferred through chiral states at the edge of the sample in the QHE regime (E_F is between the LLs here). Note that edge states also encircle the hills in the disordered potential. (e) (taken from [6]) Longitudinal (red) and Hall (blue) resistivity at $T=70$ mK in a 100 nm deep 2DHG (Bochum1282). Zeros in ρ_{XX} and plateaus in ρ_{XY} are observed in the QHE regime whenever the Fermi energy is between Landau levels. The filling factor is indicated for a number of integer and fractional QHE states. Inset shows highly resolved Shubnikov-de Haas oscillations which exhibit a beating pattern due to SO-induced density difference between spin subbands.

half of a parabola for the dispersion relation at each side of the Hall bar means that the edge states are in fact *chiral*.

Therefore when the Fermi energy is inside a gap the transport is through unidirectional 1D channels at the boundary. According to Landauer-Büttiker theory [1] each channel contributes e^2/h to the two-terminal conductance. As a result of this chirality there is a macroscopic spatial separation between transport in the two directions which significantly suppresses backscattering. Therefore if the Fermi energy is in between two Landau levels the edge channels perfectly transmit and the four-terminal resistance V_X/I_X is zero. Using the Landauer formalism discussed later it can be shown that at these points the Hall resistance $R_{XY} = V_Y/I_X$ is constant with plateaus at

$$R_{XY} = \frac{h}{\nu e^2}. \quad (2.37)$$

Note that the classical Hall resistance B/ne , which crosses the plateaus in the middle, gives the above value for integer ν from Eq. 2.36. Magnetoresistance measurements on a 2DHG Hallbar from the PhD thesis of B. Grbić [6] is shown in Fig. 2.2d. Longitudinal resistivity drops to zero and plateaus develop on the Hall resistivity when the Fermi energy is between two Landau levels as expected. The values of the filling factor ν are indicated at some of the plateaus. The precision of quantization given by Eq. 2.37 is found to be within 1 part of a million in very precise experiments. This is striking given the amount of disorder in the system. It turns out that the rigidity of QHE is protected by topology. The discovery of the QHE by Klaus von Klitzing was one of the hallmarks of the new physics for which he was awarded the Nobel prize in physics in 1985.

Some values indicated for ν in the measurement of Fig. 2.2e take rational numbers whereas only integer numbers would be expected for the integer quantum Hall effect. It turns out from Eq. 2.34 that at low filling factors, the kinetic energy in Eq. 2.17 is just a constant which is the same for all the occupied states and thus irrelevant. Therefore the system enters into a new regime in which interaction effects play a very important role. Within the composite fermion description of the fractional quantum Hall effect, some of flux quantas are joined with the charge carriers to make composite fermions in this regime which act as the new carriers [1]. The discovery of fractional quantum Hall effect (FQHE) was also praised by a Nobel prize in physics in 1998.

2.4 Semiconductor nano-structures

So far we have discussed the holes in bulk GaAs and how they are affected by 2D confinement and perpendicular magnetic field. Additional confinement results in more interesting physics, conductance quantization and Coulomb blockade are the two prominent examples. The former arises as the carriers are confined to one dimension and the latter happens when they are confined in all directions. Since

these topics are discussed in detail within the thesis, here we only introduce briefly the main concepts. The technology used to realize these settings in p-type hole systems will be described in the next chapter.

2.4.1 Conductance quantization in quantum point contacts

A quantum point contact (QPC) is a narrow constriction defined in a 2D electron/hole gas whose width W is of the order of the Fermi wavelength λ_F and much smaller than the mean free path, so that electron transport is in the ballistic regime. Varying the width of the constriction continuously, its conductance is found to change between some quantized values rather than following the channel-width continuously as expected from the classical diffusive transport. The observation of this fact was one of the hallmarks of mesoscopic physics. Conductance quantization in QPCs was discovered by van Wees et al. [50] (shown in Fig. 2.3a) and Wharam et al. [51]. The constrictions in these experiments were realized by depositing metallic gates on top of a heterostructure containing a 2DEG. Applying a negative voltage to the gates depleted the electron gas underneath and shrunk the constriction width continuously (upper left inset of Fig. 2.3a). Shortly after its discovery conductance quantization has been reproduced in constrictions and even nano-wires fabricated with different techniques on different material systems, establishing its place as a universal effect.

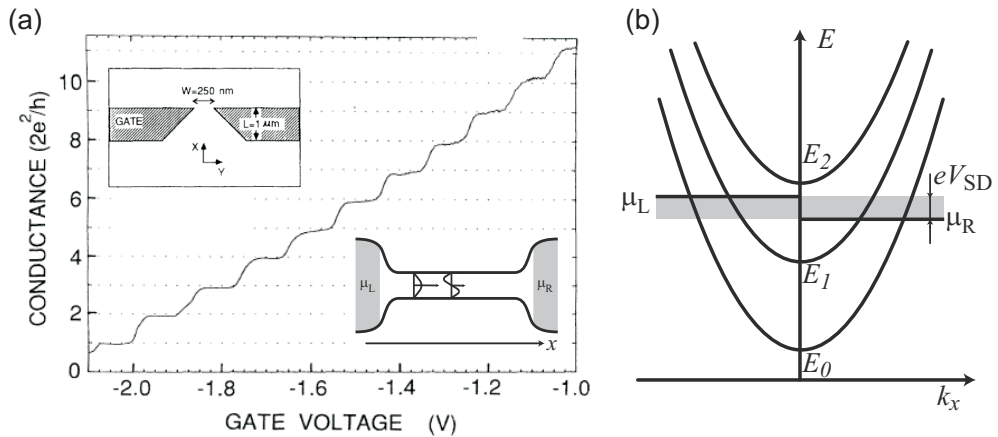


Figure 2.3: (a) The first measurement of conductance quantization in a QPC. The upper inset shows the split-gate constriction on top a 2DEG used for the measured. (taken from [50, 52]) The lower inset (taken from [1]) shows schematically how lateral quantization results in independent transverse channels (subbands) in a 1D structure, very much like a photon microwave waveguide. (b) (taken from [1]) Parabolic dispersion diagram for the subbands with the energy offset E_n indicated for each subband. Electrochemical potential of the left and right leads, μ_L and μ_R , define an energy window within which the carriers in the two directions are not compensated and a net current flows through the constriction.

In a 1D system the lateral quantization of the wave vector (schematically represented in the lower right inset of Fig. 2.3a) results in a number of subbands each having a parabolic dispersion¹² relation

$$E_n(k_x) = E_n^0 + \frac{\hbar^2 k_x^2}{2m^*} \quad (2.38)$$

as sketched in Fig. 2.3b. The charge carriers move with the group velocity $\mathbf{v}_n = \hat{\mathbf{x}}v_n$

$$v_n(k_x) = \frac{1}{\hbar} \frac{dE_n(k_x)}{dk_x} \quad (2.39)$$

Therefore positive- k_x branch originates from the left lead moving to the right¹³ and negative- k_x branch comes from the right lead and moves to the left. Considering the classical relation $\mathbf{j} = en\mathbf{v}$, (n is the density) the total current can be written as

$$\begin{aligned} I &= \frac{e}{L} \sum_{\{n,k_x\}}^{\text{occupied}} v_n(k_x) \\ &= \frac{e}{2\pi} \sum_n \int_{-\infty}^{+\infty} dk_x v_n(k_x) [\theta(k_x) f_\beta(E_n(k_x) - \mu_L) + \theta(-k_x) f_\beta(E_n(k_x) - \mu_R)] \end{aligned}$$

Note that the summation in the first row is only over occupied k_x states. This is ensured by the terms in the brackets in the second row. The unit step function $\theta(x)$ is used because the population of right movers is controlled by the left lead and vice versa. $\beta = 1/k_B T$ and $f_\beta(E) = (1 + e^{\beta E})^{-1}$ is the Fermi-Dirac distribution function. Combining the above relation with Eq. 2.39 gives

$$I = \frac{e}{h} \sum_n \int_{E_n^0}^{+\infty} dE [f_\beta(E - \mu_L) - f_\beta(E - \mu_R)] \quad (2.40)$$

At low source-drain bias ($\mu_{L/R} = E_F \pm \frac{1}{2}eV_{SD}$ and $V_{SD} \ll 1$) the integrand becomes

$$-eV_{SD} \frac{\partial f_\beta(E - E_F)}{\partial E} \xrightarrow{\beta \rightarrow \infty} eV_{SD} \delta(E - E_F) \quad (2.41)$$

Therefore at the limit of low temperatures the current is $I = GV_{SD}$ where the linear conductance $G = \nu e^2/h$ is equal to the number of (partially) occupied subbands ν times e^2/h . Opening up the constriction decreases the subband offsets E_n^0 and makes a step in the conductance each time a subband edge passes the Fermi energy. Conductance measurements (like the one in Fig. 2.3a) typically show steps in units of $2e^2/h$ because the 1D subbands are spin-degenerate.

¹²The assumption of a parabolic dispersion is not really essential here.

¹³ $\psi(x) = L^{-1/2} \exp(ik_x x)$ is the wave function of carriers.

So far we have assumed that each subband is perfectly transmitted. In the so-called *Landauer theory* an energy-dependent transmission probability $T_n(E) \in [0, 1]$ is included in the integrand of Eq. 2.40 to account for the back-scattering

$$I = \frac{e}{h} \sum_n \int_{-\infty}^{+\infty} dE T_n(E) [f_\beta(E - \mu_L) - f_\beta(E - \mu_R)] \quad (2.42)$$

Note that $T_n(E)$ contains the subband edge and therefore the lower limit of the integral is sent to minus infinity. For low source-drain biases, Eq. 2.41 and its low temperature limit can also be used in this formula. Landauer theory and its multi-terminal generalization known as Landauer-Büttiker formalism [1] are frequently used in this thesis.

2.4.2 Coulomb blockade in quantum dots

Quantum dots are small conducting islands that have a tunable number of confined charge carriers. Due to this spatial confinement in all three directions, the energy spectrum of the confined carriers is discrete. The main characteristic energy scales are the charging energy E_C which represents the energy necessary to add one more charge carrier to the dot and is inversely proportional to its size and the quantum mechanical confinement energy ΔE . Transport measurements on quantum dots are possible if the dot is coupled to some charge carrier reservoirs (source and drain) enabling charge tunnelling between the quantum dot and the reservoir. The energy distribution of carriers in the reservoirs in equilibrium follows the Fermi-Dirac distribution which brings about another energy scale $k_B T$, the thermal excitation energy of the carriers. If the size of the dot and therefore its electrostatic capacitance is small enough, then the charging energy E_C necessary to add one more charge carrier to the dot is larger than $k_B T$, and the carriers in the dot can have a fixed number. In this case the current through the dot is blocked, an effect known as *Coulomb blockade*.

Fig. 2.4a shows a schematic of a quantum dot (QD) coupled to its source and drain leads. The number of charge carriers in the dot can be controlled by the voltage V_G applied to the gate which is capacitively coupled to the dot. The signature of Coulomb blockade in transport is that a set of separated *Coulomb resonances* in the current shown in Fig. 2.4b is observed if a very low bias is applied between source and drain ($\mu_S \simeq \mu_D$). This current flows due to *sequential tunnelling* of single particles from source to dot and dot to drain when two consecutive charge configurations of the dot become degenerate by the voltage applied to the gate. To see this, note the m th excited states of a N -hole charge state of the QD is equal to

$$U_m(N, V_G) = \frac{(Ne - C_G V_G)^2}{2C_\Sigma} + E_m \quad (2.43)$$

which can be tuned continuously by the voltage V_G applied to the gate. C_Σ is the total capacitance of the dot and besides C_G includes its capacitance to the

source and drain and all stray capacitances. It must be emphasized that a QD is a strongly interacting particle system (most of the interaction is however Hartree) and in principle the Hamiltonian 2.17 must be diagonalized to get the energy eigenvalues of a QD. The assumption that the interaction between particles can be lumped into a fixed charging energy (associated with the dot capacitance) with a set of single-particle excited states independent of the total particle number is an approximation called the *constant interaction model* [53, 54]. The electrochemical potential μ_{mn} is defined as the energy required to add one more charge carrier to the QD (with n and m the old and new occupied single-particle energies)

$$\begin{aligned}\mu_{mn}(N, V_G) &= U_m(N, V_G) - U_n(N-1, V_G) \\ &= \frac{e^2}{C_\Sigma} \left(N - \frac{1}{2} \right) - e\alpha V_G + \Delta E_{mn}\end{aligned}\tag{2.44}$$

where $\Delta E_{mn} = E_m - E_n$ and $\alpha = C_G/C_\Sigma$ is the gate lever arm. If we neglect the confinement energy ΔE , the distance between the Coulomb peaks can be calculated by the change in V_G so that two consecutive charge states in the dot have the equal electrochemical potential $\mu(N+1, V_{G1}) = \mu(N, V_{G2})$. From this we obtain

$$\Delta V_G = \frac{1}{e\alpha} \frac{e^2}{C_\Sigma}.\tag{2.45}$$

The tunnelling current between source and drain through a QD can be used as a spectroscopic tool to gain information about the energy spectrum of the carriers in the dot. This is achieved by the so-called *Coulomb blockade diamond* measurement (Fig. 2.4c). These measurements typically exhibit a charge stability diagram, the parameter regime at which a given charge configuration is stable. A sufficiently large source-drain bias voltage can lift the Coulomb blockade. This is shown in Fig. 2.4c,d. Therefore charging energy can be read in this plot as the largest source-drain bias at which Coulomb blockade can still happen. If $\Delta E \gg k_B T$ the dot is in the so-called single-particle regime, and transport occurs via single quantum level. Each state in the quantum dot acts like a channel for current flow. The current through the QD thus increases as soon as an excited states enters the bias window. In this case information about the spectrum of the dot can be extracted by the steps in the current outside the Coulomb blockade regime parallel to the diamond edge as shown in Fig. 2.4c. The electrochemical potential due to excited states are not shown in Fig. 2.4d. On the other side for $\Delta E \ll k_B T$, the dot is in the multi-level transport regime and the transport occurs via many single-particle levels. For steep potential wells with an area A , the mean single-particle level spacing can be calculated from $\langle \Delta \rangle = 1/DA$. Using the 2D DoS (Eq. 2.19) this gives $\langle \Delta \rangle = \pi \hbar^2 / m^* A$. Since the holes in 2D systems have much larger effective mass than electrons, $\langle \Delta \rangle$ is much smaller in the case of hole quantum dots and therefore harder to resolve. This is discussed extensively in Chapters 8 and 9.

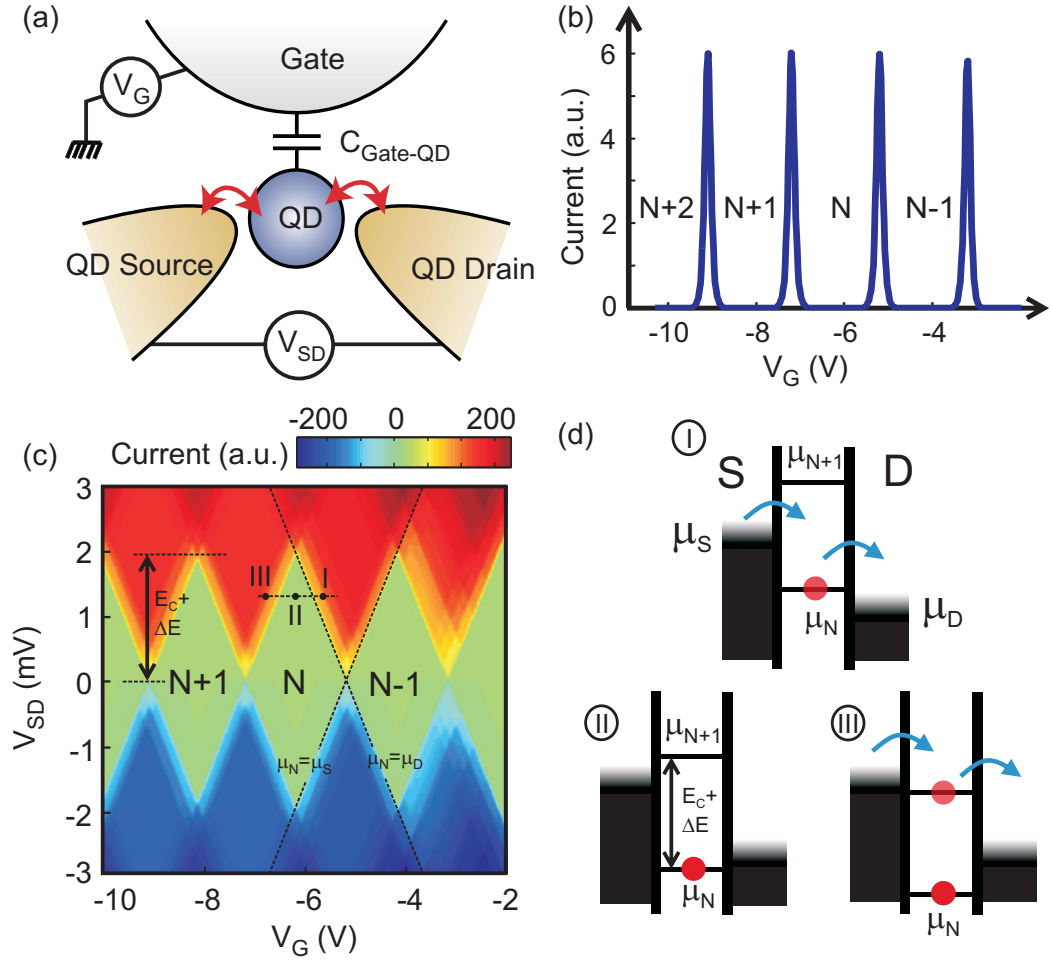


Figure 2.4: (a) (adapted from [55]) Schematic of a single quantum dot tunnel coupled to the source and drain. The capacitive coupling to the gate enables the number of charges within the dot to be tuned by the V_G as depicted in b. (b) Calculated Coulomb peaks in the current for low source-drain bias: a current flows between source and drain at the charge degeneracy points. (c) A calculated colormap of source-drain current as a function of applied bias and the gate voltage exhibiting Coulomb diamonds. The edge of the diamonds are related to the configuration where the electrochemical potentials of the dot are aligned with that of source and drain. The charging energy can be read directly as the extension in bias direction. The lines outside diamonds parallel to the edge are caused by the excited states. (d) Energy diagram of the dot at the three configurations marked with I, II and III in c. I and III both have one dot level in the bias window and a current flows from source to drain. In II the current is blocked due to the gapped spectrum of the dot or Coulomb blockade.

Chapter 3

Sample Fabrication and Measurement Setup

3.1 Sample Fabrication

Roughly speaking more than half of the time of this thesis was spent on sample fabrication and therefore this step was the most crucial part of the project. The starting point in fabrication were p-type GaAs/AlGaAs heterostructures containing a two-dimensional hole gas (2DHG) grown by the group of Prof. Wieck, University of Bochum. After producing Hall bars and mesas from these wafers and making low resistivity Ohmic contacts to them in order to access the 2DHG, they were characterized by standard low temperature magneto-transport measurements. Conventional semiconductor nano-devices are usually created using split-gate technique which are metallic Schottky gates evaporated on top of the heterostructure surface. While these split-gate devices fabricated on n-type GaAs/AlGaAs heterostructures show excellent electronic properties, they exhibit significant leakage and gate instabilities on p-GaAs/AlGaAs heterostructures [6, 56, 57] most probably due to the low Schottky barrier [58] and the fact that in order to deplete the 2DHG and create the nano-devices, the resulting diode must be forward biased. Therefore in this thesis atomic force microscope (AFM) and electron beam (e-beam) lithography was used to pattern the 2DHG into a main channel and several in-plane gates.

3.1.1 Carbon doped p-type GaAs/AlGaAs heterostructures

Fig. 3.1 shows the schematics of the heterostructure used to fabricate the nano-structures studied in this thesis. The host heterostructure consists of a 5 nm undoped GaAs cap layer, followed by a 15 nm thick, homogeneously C-doped layer of AlGaAs, which is separated from the two-dimensional hole gas (2DHG) by a 25 nm thick, undoped AlGaAs spacer layer [2]. It is to be noted that Carbon acts as an acceptor on the (100) plane [3], and thus the anisotropy in the 2DHG formed in this plane is significantly reduced compared to the case of Si doped (311) heterostruc-

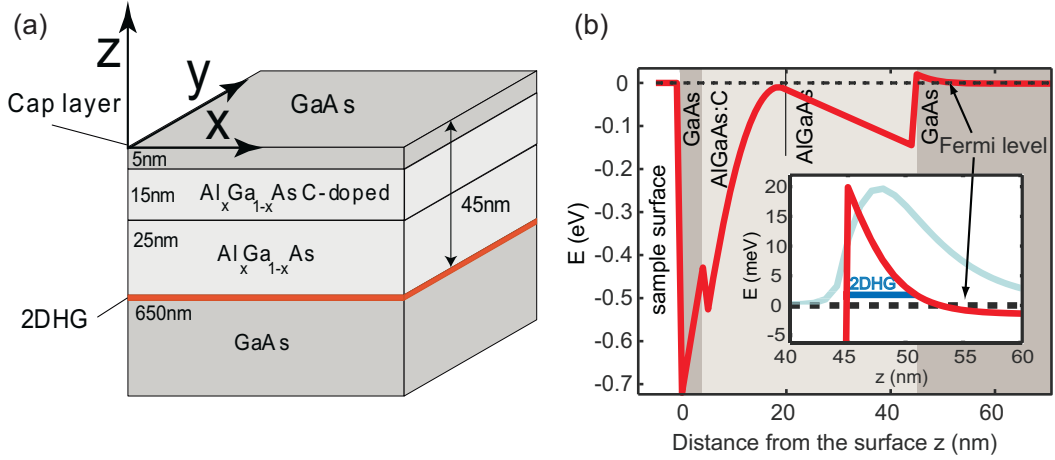


Figure 3.1: (adapted from [6]) (a) The schematic of the heterostructure used in this thesis to fabricate the nano-devices. (b) Valence band energy profile along the growth direction (red line) with the designated position of the Fermi energy (dashed line) calculated from a self-consistent Poisson-Schrödinger solver. Inset: Magnified confining potential of a 2DHG (red line) with the quantized level of a 2DHG (dark blue line). The light blue line shows the spatial profile of the charge density.

tures. The functionality of devices patterned on C-doped GaAs wafers as well as the interpretation of the transport experiments in these devices are therefore expected to be independent of the particular orientation of the device with respect to the wafer. The nanostructures were fabricated from 3 almost identically grown heterostructures: *A2*(Bochum12029), *A3-4*(Bochum13127) and *A10*(Bochum20122). Fig. 3.1 illustrates the heterostructure, different layers and the thickness of each layer. The main nominal difference between the three wafers is the doping concentration and the variation of the Aluminium content in the $\text{Al}_x\text{Ga}_{1-x}\text{As}$ alloy x , which was 0.35, 0.36 and 0.34 in the three wafers respectively. A word about the notation is in order here. In reference to a sample e.g. *A2.1.2*, the first two characters identify the wafer while the rest are indices that refer to a particular position in the wafer from which the sample was fabricated. The list of all the samples discussed in this thesis is shown in Appendix A. Prior to sample fabrication the quality of the 2DHG was characterized by standard magnetotransport measurements at 4.2K and the values obtained for the hole density p and mobility μ are listed in table 3.1.1. The mean-free-path $\ell_e = \frac{\hbar}{e}\mu\sqrt{2\pi n}$ is also shown in this table for the three wafers. The Fermi wavelength λ_F depends only on the density and is about 40 nm similar to electron systems. Valence band heavy holes in 2DHG formed at the interface of GaAs/AlGaAs heterostructures are susceptible to strong Rashba [59] and Dresselhaus [34] spin-orbit interactions. These interactions modify the dispersion relation and lift the degeneracy of the two spin-degenerate subbands that are referred to as the *Kramers doublets* due to lack of a constant quantization axis. Assuming a cubic k -dependence of the heavy-hole subband splitting $\Delta E_{SO} = 2\beta k_{\parallel}^3$ [31] results in band

wafer	x	$p(10^{15}m^{-2})$	$\mu(cm^2/Vs)$	$\ell_e(\mu m)$
<i>A2</i>	0.35	3.8	120,000	1.2
<i>A3-4</i>	0.36	4	200,000	2
<i>A10</i>	0.34	2.7	60,000	0.5

Table 3.1: The Aluminium content x , density n and mobility μ of the three GaAs/AlGaAs heterostructures used in this thesis. The values were obtained by standard Hall bar measurements at a temperature of 4.2 K in the dark.

non-parabolicity and a difference in the effective masses and the Fermi wave vectors of the two Kramers doublets. The in-plane effective masses of the two spin-split subbands in *A2* are $m_1 = 0.34 m_e$ and $m_2 = 0.53 m_e$ measured by our group from the temperature dependence of the Shubnikov-de Haas oscillations [8].¹ With these effective masses and the 2D density of states of a single non-degenerate band given by $\mathcal{D}_i = m_i^*/2\pi\hbar^2$ we obtain $E_F = N/(\mathcal{D}_1 + \mathcal{D}_2) \approx 2$ meV for the typical density of $N = 4 \times 10^{15} m^{-2}$. This value of the Fermi energy is much less than the splitting between heavy and light holes (due to quantum well confinement) identifying the former as the main carriers of the two dimensional hole gas. We assume that the average effective mass obtained from this study on *A2* holds also for the other similar C-doped GaAs heterostructures studied in this thesis. Note that this Fermi energy is about 7 times smaller than typical Fermi energies in n-type systems with similar carrier density. With this effective mass and density, typical values for the interaction parameter are estimated to be $r_s \geq 5$. The difference in the effective mass of the two spin-subbands results in a density mismatch of about $\Delta N/N = 0.29$ measured from the beating of the Shubnikov-de Haas oscillations, suggesting a spin-orbit interaction energy of $\Delta E_{SO} = 0.85$ meV and a significant relative spin-orbit strength of $\Delta E_{SO}/E_F \approx 33\%$. The decoherence length for the wafer *A2* was calculated by Boris Grbić [6] from the temperature dependence of the Aharonov-Bohm oscillations in quantum rings fabricated in this wafer [26] to be $\ell_\phi = 2 \mu m$. This value agreed with the value extracted from weak anti-localization measurements in a Hall bar made of the same heterostructure [13]².

3.1.2 Optical lithography

Optical lithography was used in this thesis for the fabrication of Hall bars and $20 \times 20 \mu m^2$ mesa structures, which serve as platforms for AFM and e-beam lithography, as well as for defining the Ohmic contacts. The scheme of a standard photolithography process is shown in Fig. 3.2 and further details about the process and

¹Slightly higher values were obtained in a similar experiment by Habib et al. [38].

²It was also found from these measurements that in a 100 nm deep 2DHG (Bochum1282), spin-orbit scattering time τ_{SO} can be as low as 3 ps (compared to $\tau_\phi = 120$ ps for the phase decoherence time in that 2DHG) giving rise to a $\ell_{SO} = 100$ nm compared to $\ell_\phi = 5 \mu m$ in this material.

parameters can be found in [6]. The heterostructures received from the growers were initially covered with a thick layer of photo-resist in order to protect the surface. After cutting to the desired size, removing the protective layer and cleaning the wafer with acetone and isopropanol, the sample was first dried and then covered with a positive photoresist and exposed to the UV light through a mask containing the desired pattern. The resolution of optical lithography is limited by the wavelength of the UV light used in the exposure and the distance between the mask and the sample surface and is usually around $1 \mu\text{m}$. After development, the photoresist exposed to the UV is removed and the wafer outside the desired pattern is then etched down by 60-100 nm with a solution of $\text{H}_2\text{O} : \text{H}_2\text{SO}_4 : \text{H}_2\text{O}_2$, thus removing the 2DHG outside the desired region. In the second photo-lithography step, used to define the Ohmic contacts, a negative photo-resist is spun on the sample surface and a different mask with contact patterns is aligned with respect to the predefined mesa structure. After exposure and development of the photoresist similar to the first step, instead of etching this time Au/In/Zn is evaporated as the contact and standard lift-off process is followed.

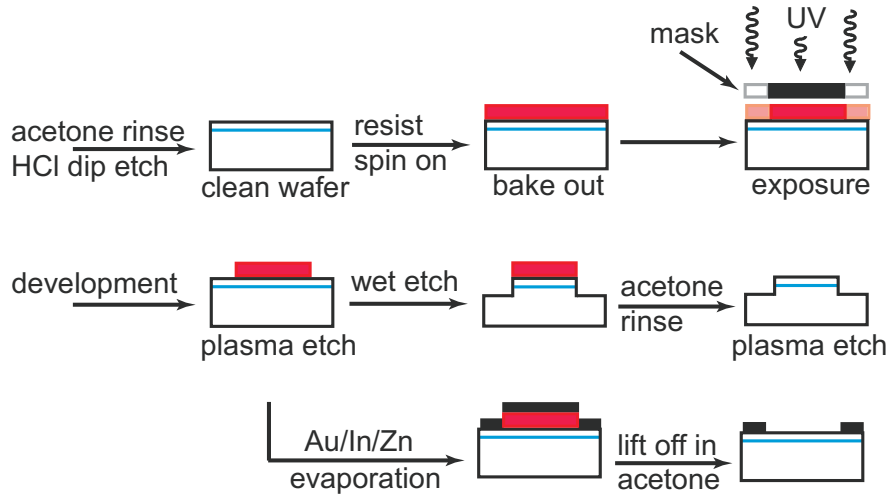


Figure 3.2: (taken from [60]) Schematic of the optical lithography process used to define the mesa and the Ohmic contacts.

3.1.3 Ohmic contacts to two-dimensional hole gases

Low resistance Ohmic contacts are necessary for low-noise transport measurements of semiconductor nano-structures. While the technology of making good Ohmic contacts to n-type GaAs/AlGaAs heterostructures are well-established, the fabrication of good contacts to p-type GaAs wafers are proven to be more difficult [6]. Typically AuZn, AuBe or InZn metalizations are used for Ohmic contacts to p-type GaAs [61]. Note that Be is preferentially avoided because of its poisonousness and In is very diffusive and therefore has to be evaporated in a separate evaporating system to

avoid cross-contamination risks. Here we provide the recipe developed by Grbić [6] to make such contacts to C-doped heterostructures with shallow 2DHG using an alloy of Au/In/Zn evaporated on top of the sample which was used extensively in this thesis.

Before evaporation, the sample is cleaned for 2 minutes with plasma ashing using O₂ gas with 200 W power. It is then immediately placed in the evaporation machine and a sequence of Au(2 nm), Zn(40 nm), In(40 nm) and Au(200 nm) is evaporated on the sample. The first Au layer serves as the sticking layer. The key component of the alloy is Zn while In serves to facilitate Zn diffusion through the heterostructure. The last Au layer is evaporated to make the wire contact. Using In for the contact metallization has the disadvantage that it alloys with the last Au layer, resulting in soft contacts which are difficult to contact using the wire bonder. Most of the wire bonding in this thesis was therefore performed manually. After evaporation, the resist is removed by a standard lift-off process in warm Acetone or NMP (N-Methyl-2-Pyrrolidone). The samples were then annealed for 2 minutes at 130°C (to remove water and humidity) and then 2 minutes at 500°C in the formier gas made of 95% N₂ and 5% H₂. While the duration of the annealing is not so important and it can get longer, the temperature was found to be crucial. With this recipe contact resistances (resistance of one contact to all the other contacts grounded) between 5-20 kΩ were obtained reproducibly at the temperature of 4.2 K. Enhancement of the room temperature values of the (dark) contact resistance to about 100 kΩ due to presence of oxide lines or etched trenches can be used as a quick test of their insulating behavior at low temperatures.

3.1.4 AFM oxidation lithography

Local anodic oxidation lithography [62–64] was used extensively to pattern the nanostructures on 2DHG in this thesis. The basic mechanism is illustrated in Fig. 3.3a. A charged tip of an atomic force microscope (AFM) is brought close to the semiconductor surface in a humid environment. This setting is very similar to anodic oxidation in which the conducting tip of the AFM, the semiconductor surface and the water film are anode, cathode and electrolyte [65]. Applying a negative voltage to the tip with respect to the semiconductor results in reduction of the tip and local oxidation of the semiconductor surface. Initially, AFM oxidation has been performed with a constant dc voltage being applied to the AFM tip [63], but it was shown by Graf et al. [66] that the application of a square ac-modulated voltage to the AFM tip leads to better reproducibility of the oxidation process and also enhances the aspect ratio of the oxide lines which improves their insulating behavior. Therefore the structures in this thesis were formed by applying a square ac-modulation with a peak-to-peak amplitude V_{ac} of 10-25 V superimposed on a dc offset V_{dc} of -5 to -15 V with a frequency of modulation of about 1000 Hz. A Ti/N cantilever covered with Au coating was used for the lithography and the humidity was kept in the range of 40-45% during lithography. The set point was in the range of 0.03-0.1, much

smaller than typical set point values during scanning (about 0.7-0.8) which means that in the writing mode the tip was approaching the surface much more than in the scanning mode [6].

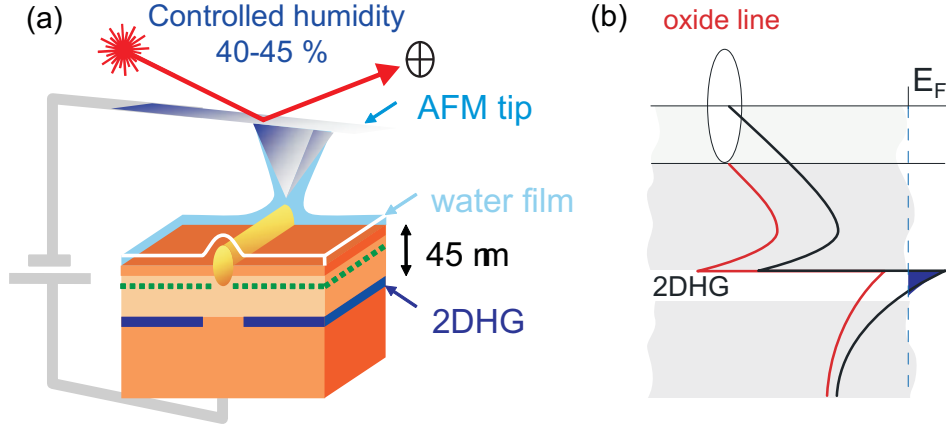


Figure 3.3: (adapted from [6]) (a) Scheme of AFM oxidation lithography. (b) Simple schematic of how local depletion of 2DHG underneath the oxide line is achieved by shifting the band above the Fermi level.

Fig. 3.4a shows an example of a double dot created by local anodic oxidation lithography. Oxide lines as high as 15 nm are able to locally deplete the 2DHG situated 45 nm below the surface separating the 2DHG into laterally disconnected regions which are individually connected to metallic leads. Voltages in the range of $[-200 \text{ mV}, +200 \text{ mV}]$ can be applied between separated regions without any significant leakage current across the oxide line (see e.g. Fig. 8.1b in Chapter 8).

Fig. 3.3b explains why surface oxidation results in the depletion of the 2DHG. The oxide has almost twice the volume as GaAs and it is accompanied by an equal amount of oxide below the surface [65]. This can be easily checked by exposing the sample to a dilute (1:9) solution of Hydrochloric acid ($\text{HCl}:\text{H}_2\text{O}$) which removes the oxide and leaves the GaAs untouched as shown in Fig. 3.4b. The trenches left have similar electronic properties as those before HCl-dipping. When the wafer is slightly etched down, the sample surface is effectively brought closer to the 2DHG. Since the position of the valence band edge at the surface has to remain at the same position below the Fermi level, due to Fermi level pinning, the valence band is pushed down in energy (Fig. 3.3b), and the 2DHG gets depleted below the oxide line [6].

HCl-dipping also eliminates the native oxide of GaAs. Although this oxide is expected to form again with further water rinsing and exposure to the ambient atmosphere, higher oxide height and better quality of lines is obtained after HCl-dipping of the sample. Therefore this technique was often used in this thesis. Sample A3.10.2 discussed in Chapter 6 is an example in which the oxides forming the quantum dot were removed by subsequent HCl-dipping. The advantage of AFM oxidation lithography over other techniques is that once the sample is placed in the AFM chamber one can, with the same tip, inspect the sample surface, write the structure at a de-

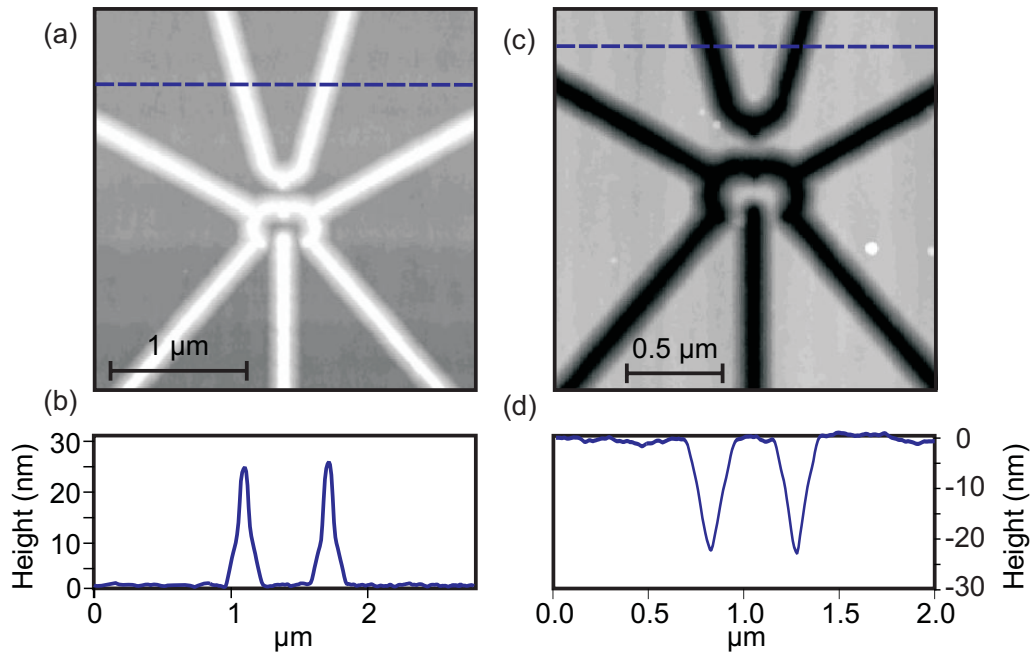


Figure 3.4: (a) AFM defined double quantum dot with the height profile shown in (b). Oxide lines are as high as 25 nm. (c) Same sample after HCl-dipping. The oxide lines are removed and the left trenches are more than 20 nm deep which is more or less the initial height of the oxide line. Note that the scales are different and the AFM tip does not reach the bottom of the trench in (d).

sired location and finally check the topography of the written structure and correct for possible errors after measurement. A detailed explanation of the technique and relevant parameters for AFM lithography on p-type GaAs/AlGaAs heterostructures can be found in [6].

3.1.5 Electron beam lithography

AFM oxidation lithography is a flexible method for nano-fabrication however its performance depends on two main parameters: the microscopic details of the tip, and the sample surface, which are both difficult to control thus limiting the fabrication yield. Motivated by the fact that it is the trench and not the oxide that depletes the 2DHG underneath the oxide line, we used electron beam (e-beam) lithography to define trenches on PMMA and then chemical etching to produce shallow trenches on top of the surface. A (1:1) solution of 950K PMMA in ethylactate was used as the e-beam resist. The crucial step is the chemical etching which again depends on the surface details and it will be discussed in the following.

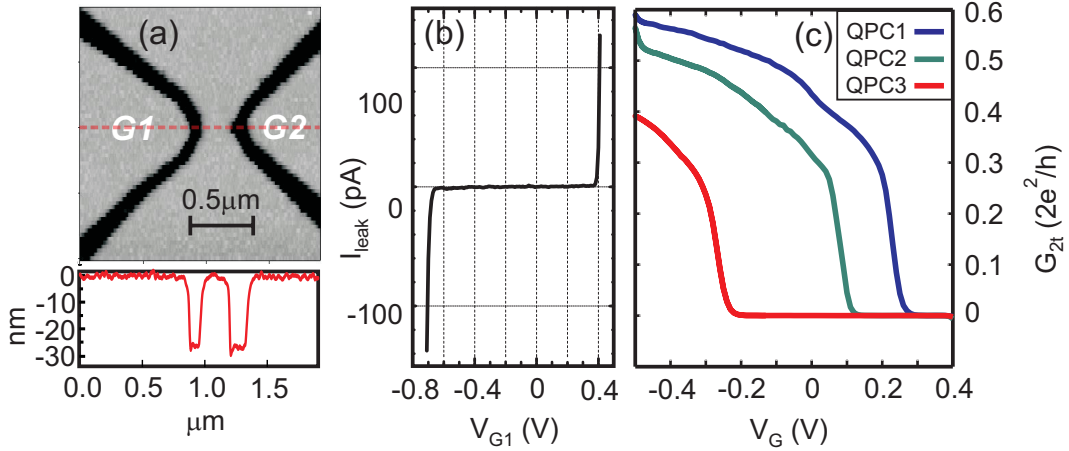


Figure 3.5: AFM micrograph of (a) a QPC defined with e-beam lithography followed by shallow chemical etching. (b) Representative breakdown characteristics of the etched lines at $T=4.2$ K shown for the in-plane gate G_1 . (c) Two-terminal linear conductance of three QPCs with different channel widths measured at $T=4.2$ K. The lithographical sizes are 230, 210 and 190 nm for QPC1, QPC2 and QPC3 respectively.

Shallow chemical etching

After e-beam exposure and development, the sample was post-baked at 120°C for 2 minutes followed by 33 seconds plasma ashing at 200 W with O_2 (Plasma ashing removes about 10 nm of PMMA from the top and widens the lines about 20 nm. This is necessary in order to remove residual PMMA from the exposed areas). This recipe proved to be crucial in order to get narrow and smooth trenches after etching. The sample was etched in a fresh dilute (500:3:1) solution of acid ($\text{H}_2\text{O}:\text{H}_2\text{SO}_4:\text{H}_2\text{O}_2$) for about 60 seconds and rinsed in DI water immediately afterwards. The PMMA was then removed in acetone and isopropanol and the depth of the trenches was measured afterwards with AFM to be about 20 nm. As the etching rate was changing each time depending on sample surface and other parameters it was necessary to make an etch test on the mesa arm before the final e-beam lithography step in the mesa center. Fig. 3.5a shows an example of a nano-structure fabricated with this technique. The topographical height profile of the sample shows that the trenches as deep as 20 nm with a width of 100 nm can be created similar to AFM oxidation lithography. It has to be emphasized that in order to reproduce deep and clean trenches, it is crucial that the PMMA exposed to the e-beam is removed completely. If this condition is not met, the etched line defining the nano-structure is cut at several points. Fig. 3.5c shows the breakdown voltage characteristic for the gate G_1 in Fig. 3.5a which is typical for the etched lines. Fig. 3.5d shows the two-terminal conductance vs. gate voltage for three different QPCs fabricated on a different sample (A2.1.2) with lithographical channel widths of 230, 210 and 190 nm. The voltage threshold for opening up the channels in the three QPCs correlate very nicely

with the lithographical channel widths. This sample was used later on to study the influence of pre-biased cooling with and without a top-gate (see Appendix B).

3.2 Metallic gates on two-dimensional hole gases

The in-plane gates created by AFM and e-beam lithography are in the same plane as the channel and therefore their tunability is limited due to the geometry. In this section we discuss how this limited tunability can be improved using a global top-gate or a set of top-gate fingers. Metallic gates directly on top of the two-dimensional holes gases are leaky as stated in the introduction. This is most probably due to limited height of the Schottky barrier [58] and the fact that in order to deplete the 2DHG and create the nano-devices, the resulting diode must be forward biased. Therefore several materials have been tried as a gate insulator between GaAs wafer and the metallic top-gate in this thesis.

3.2.1 Insulating materials and density-mobility curves

Three main criteria are involved in the choice of the insulating material. 1) it has to have a large dielectric constant k . The total capacitance $C^{-1} = C_k^{-1} + C_{2DHG}^{-1}$ is the series combination of the insulator capacitance C_k and the heterostructure capacitance C_{2DHG} . The higher the dielectric constant, the higher the total capacitance and density tunability of the top-gate. 2) The breakdown voltage of the material must be high enough to provide the desired density tunability. In homogeneous materials, the breakdown limit is expressed in terms of a maximum electric field (e.g. 1.6 V/nm for HfO₂) however in practice the breakdown voltage of a thin film does not scale linearly with the film thickness due to the presence of defects. The film quality is therefore the main parameter that determines the breakdown voltage for a given thickness or the required thickness for the desired breakdown voltage. 3) The band gap and the band offset [67]. The conduction and valence bands of the insulator must be far from corresponding bands of the GaAs to prohibit charge tunnelling to the insulator and surface charge accumulation at the interface. A good insulator for n-type GaAs can have undesirable (enhanced noise or depletion) effects on p-type GaAs nano-structures or vice versa. Although these parameters are well-studied and tabulated for various insulators on Silicon, not much information is available for GaAs-based heterostructures especially in the presence of the native oxide of the semiconductor.³ In this section we discuss the applicability of Hafnium and Aluminium oxides grown by atomic layer deposition (ALD) [68, 69] in a Picosun Sunale RR-150B system on the tunability of p-type GaAs nano-structures.

³We observed that the mere deposition of an insulator like HfO₂ tends to decrease the ungated density in the 2DHG.

HfO₂

Hafnium oxide (HfO₂) is a high dielectric constant ($k \approx 25$) material [67, 70] that is used as the gate insulator for Field Effect Transistors (FET) and dielectric in DRAM capacitors. It can be deposited using tetrakis (ethylmethyamido) hafnium (TEMAH) as the precursor in ALD system. A linear growth rate of 0.08 nm per pulse cycle has been found at a reaction chamber temperature of 250°C and at a source temperature of 90°C. The structural quality of a 20 nm thick layer of the resulting polycrystalline HfO₂ have been investigated by scanning electron microscopy (SEM) on freshly cleaved GaAs wafers as illustrated in Fig. 3.6(a). The surface roughness determined by AFM is found to be 4 nm rms, independent of the layer thickness.

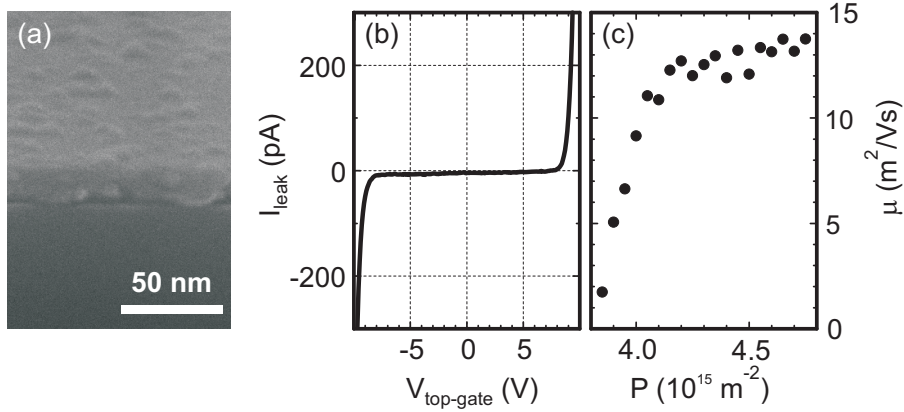


Figure 3.6: (a) SEM image of a freshly cleaved GaAs wafer covered with a 20 nm thick HfO₂ layer. (b) Breakdown characteristics of the top gate at $T=4.2$ K (c) Hole mobility μ as a function of the hole density P in the 2DHG in a Hall bar from *A3* wafer in the range of $-8\text{V} < V_{\text{top-gate}} < 8\text{V}$ at 4.2 K.

The electronic properties of the oxide layer as well as the tunability of the host 2DHG by the top-gate were tested separately at $T = 4.2$ K on a 100 μm wide Hall-bar device. The breakdown characteristics of the 20 nm thick oxide layer on top of the sample *A3.25.2* shows no trace of leakage currents in the $-8\text{ V} < V_{\text{tg}} < 8\text{ V}$ top-gate voltage regime and is reproducible as long as the high voltage leakage current is kept below 0.5 nA as shown in Fig. 3.6(b). The hole density P and mobility μ of the 2DHG were determined by conventional four-terminal longitudinal and Hall resistance measurements performed at low magnetic fields up to 0.1 T. The tunability of P in the 2DHG is however limited to about 20-25% within the leakage free top-gate voltage regime [Fig. 3.6(c)]. This is in contrast to the estimated depletion voltage of $V_{\text{tg}} \approx 0.5\text{ V}$ based on a plate capacitor model taking the thicknesses and the dielectric constants of the layers into account. This is presumably due to the screening effect of the low mobility charges residing in the doping layer and at the interface between the insulator and the semiconductor. The mobility edge arising from the background potential roughness of the 2DHG is close to the density of the ungated sample $P \approx 4 \times 10^{11}\text{ cm}^{-2}$.

Al_2O_3

Atomic layer deposition of Aluminium oxide (Al_2O_3) is the most well developed [67] and uses Trimethylaluminium (TMA) as the precursor. Al_2O_3 has a dielectric constant between 7-9 depending on the oxide quality and it is frequently used as the gate insulator in semiconductor and graphene-based nano-electronics. Fig. 3.7 shows the mobility of five Hall bars covered with Al_2O_3 as a gate insulator as a function of hole density varied by the top-gate voltage. The density at each $V_{top-gate}$ value was measured by standard Hall effect. The nominal thickness of the alumina layer was 70 nm except the sample *A2.1.4* which had an oxide layer with nominal thickness of 50 nm. The reaction chamber temperature during deposition was 300°C except the oxide on sample *A3.3.1* which was grown at 200°C.

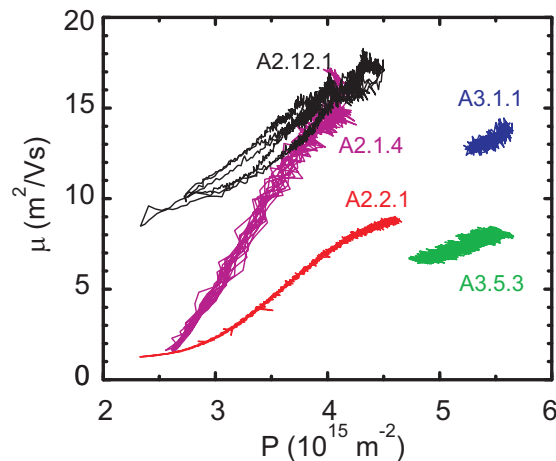


Figure 3.7: The hole mobility vs. hole density curves for five Hall bars fabricated from the wafers *A2* and *A3* using 50-70 nm thick layer of Al_2O_3 as a gate insulator. While the density in *A2* can be changed with a factor of two and the mobility increases monotonically with density, the density in wafer *A3* can hardly be tuned within the breakdown voltage range of the top-gate.

The samples fabricated from similar wafers have different density-mobility characteristics presumably due to slightly different surface treatment during processing. Furthermore, while the density of samples from the wafer *A2* can be tuned with a factor of two, the density in the wafer *A3* is not tunable. This observation together with the fact that the wafer *A3* has a parallel conductance of about 200 k Ω (see Appendix C), suggests that the parallel conducting layer due to low mobility charges in the doping layer in this wafer gives rise to the enhanced screening effect. Although the bulk density is not tunable in these wafers, it is very interesting that the density in nano-structures can be perfectly tuned with a top-gate.

3.2.2 Leakage characteristics

The presence of the top-gate also influences the breakdown characteristics of oxide lines or etched trenches separating in-plane gates from the channel. In order to illustrate this effect we look at the leakage of the gate G_1 in sample $A4.2.2$ shown in Fig. 3.5a. The breakdown characteristics of this gate, before putting a top-gate, was shown in Fig. 3.5b. Later on this sample was covered with a 20 nm thick layer of HfO_2 and 10/90 nm of Ti/Au metallization as the top-gate. Figure 3.8(a) shows the absolute value of the leakage current across the separating line in the leakage free gate configuration regime defined as $|I_{\text{leak}}| < 0.1$ nA when both the top-gate $V_{\text{top-gate}}$ and one of the in-plane gate voltages [shown for V_{G_1} in Fig. 3.8(a)] are varied. The overall broadening of the leakage free domain in V_{G_1} with respect to the $I_{\text{leak}}(V_{G_1})$ trace recorded in the absence of the top-gate [Fig. 3.5(b)] can be understood as the screening effect of the top-gate. The further broadening towards higher $V_{\text{top-gate}}$ reveals the variation of the hole density in the 2DHG, i.e., a decrease in electrochemical potential with respect to the in-plane gate barriers. The hole density measured *in situ* on this sample using standard Hall effect for different $V_{\text{top-gate}}$ values, illustrated in Fig. 3.8b, confirms a monotonic decrease in density with the variation of the top-gate voltage. The asymmetry in the position of the border lines [also visible in Fig. 3.5(b)] reflects the asymmetry in the applied in-plane gate biases as one side of the separating lines was always kept at ground. The asymmetry in the curvature of the border lines is attributed to the nonlinearities in the tunneling probability across the barrier under asymmetric in-plane gate biases.

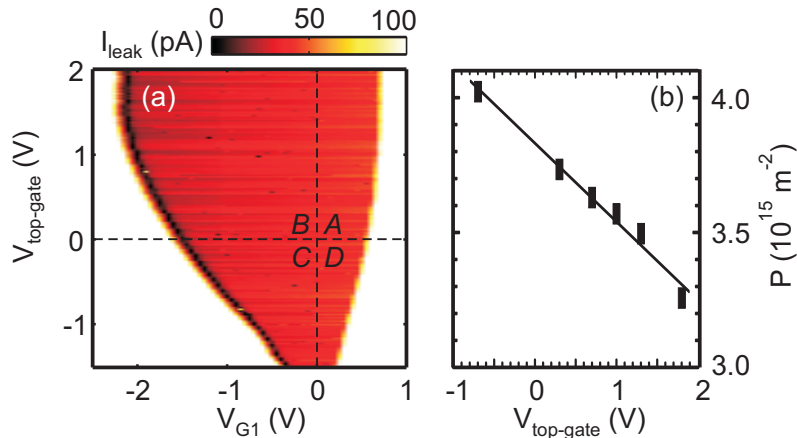


Figure 3.8: (a) Leakage current I_{leak} across the in-plane barrier of gate G_1 in the QPC of Fig. 3.5a as a function of the $V_{\text{top-gate}}$ voltage and the V_{G_1} in-plane gate voltage at $T = 100$ mK. The colored area shows the magnitude of I_{leak} in the leakage free domain defined as $I_{\text{leak}} < 0.1$ nA. (b) Variation of the hole density with the top-gate voltage $V_{\text{top-gate}}$, measured on the same sample using two independent contacts.

The parameter space in Fig. 3.8a is divided into four quarters. For negative in-plane gates ($V_{G_1} < 0$) in quarters B and C the channel and other in-plane gates (all

grounded) act as a gate to deplete $G1$. In regions A and B , the positive top-gate also acts to deplete the in-plane gate $G1$. Therefore the depletion length between the gate and the channel in region B is enhanced compared to the other quarters, explaining the extension of leakage free regime in this case.

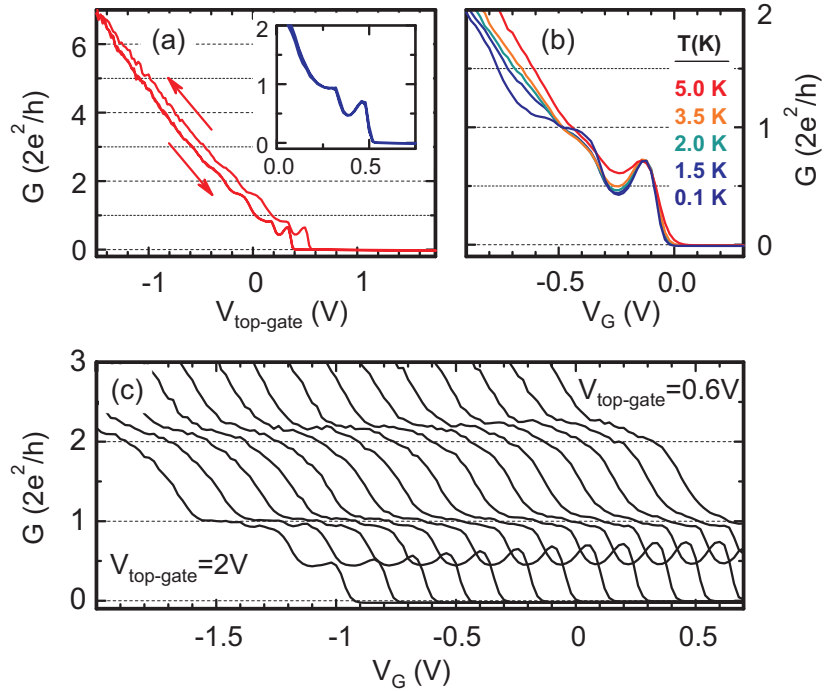


Figure 3.9: (a) QPC conductance G as a function of $V_{top-gate}$ at $T=100$ mK while V_G is kept at a constant value of 0.5 V. The arrows indicate the direction of the consecutive $V_{top-gate}$ sweeps. The inset shows a hysteresis-free top-gate sweep in a limited $V_{top-gate}$ regime. (b) G as a function of V_G at various temperatures between $T=5$ K and 100 mK at $V_{top-gate} = 1.4$ V. (c) G as a function of V_G recorded at different top-gate voltages ranging from $V_{top-gate} = 2$ V (leftmost trace) to $V_{top-gate} = 0.6$ V (rightmost trace). V_G is the symmetric voltage applied to in-plane gates.

3.2.3 Top-gate stability and improved tunability

The stability of the conductance traces upon different top-gate sweeps is illustrated in Fig. 3.9a. Sweeping $V_{top-gate}$ over the extended regime of Fig. 3.8a at a fixed in-plane gate V_G value results in a hysteretic behavior due to the charging of the defect sites in the doping as well as in the oxide layer. On the other hand, a top-gate sweep performed in the limited voltage range displayed in the inset of Fig. 3.9a yields to hysteresis-free, stable conductance traces. The tunability of the QPC by the in-plane gates at various $V_{top-gate}$ values is shown in Fig. 3.9c. It demonstrates that while the overall shape of the individual conductance curves is slightly affected, the range of tunability by means of V_G can be optimized by the proper choice of the

additional control parameter $V_{top-gate}$. Moreover, our experience shows that QPCs which were not tunable prior to top-gate deposition due to a large misalignment between the electrochemical potential and the first QPC subband become tunable by changing $V_{top-gate}$.

At more positive $V_{top-gate}$ the density in the leads is lower and the opening of the QPC requires more negative voltages on the in-plane gates corresponding to a broader lateral confinement. At the same time, the length of the observed quantized plateaus slightly increases in agreement with the saddle-point potential model [71]. Based on the temperature dependence shown in Fig. 3.9b along with further criteria for the associated zero bias anomaly discussed in Chapter 5 we attribute the resonant feature on the rise of the $2e^2/h$ plateau to a transmission resonance arising from the interaction with an impurity state inside the QPC. The effect of this impurity resonance on the transmission becomes more pronounced towards narrower QPC confinements set by less positive $V_{top-gate}$ top-gate voltages. It has to be added that the majority of the hole QPCs exhibit a different conductance feature below the $2e^2/h$ plateau with a markedly different temperature dependence which we attribute to the so-called 0.7 anomaly and is the topic of next Chapter.

3.2.4 Patterned top-gate in combination with in-plane gates

Measuring the spectrum of a few-hole quantum dot can provide very interesting information about the effects of spin-orbit and exchange interactions on the energy levels of the hole dot. However, due to the larger effective mass of the holes compared to electrons a stronger confinement and therefore larger dot charging energy is required in order to resolve the individual states. While charging energies as large as 2-3 meV were obtained using only in-plane gates in this thesis, it would be definitely interesting to get smaller dots with fewer confined holes in future. Further confinement using in-plane gates is limited due to cross capacitance of different constriction gates on each other.

The way to overcome this problem is to implement separate top-gate fingers with local influence to control individual constrictions. Defining the dot using only split-gates on top of insulating layer requires large voltages on the gates and is not practical given the gate hysteresis and inability to tune the density in the 2DHG. Fig. 3.10 shows two different approaches to this problem in a quantum dot. In both cases after defining the quantum dot using electron beam lithography followed by shallow chemical etching, the sample surface was covered by a 40-60 nm thick HfO_2 as the gate insulator. In (a) a 5 nm thin layer of Ti was then deposited on the surface and AFM lithography technique was used to oxidise this thin metal film in order to create mutually insulated top-gate patches over the constrictions. The thickness of the Ti layer is very crucial and is controlled by monitoring the sheet resistance to be between 5-15 k Ω prior to AFM lithography. A too thin layer is not a good top-gate because it is not conducting and a too thick layer can not be totally oxidized by the AFM lithography [72, 73]. This method can be used in combination

with either AFM or e-beam lithography for the first layer and requires a certain quality and thickness for the insulating oxide layer. If the AFM oxide lines with the height of 20 nm are used to define the dot, they are still visible (and the alignment is possible) under the oxide layers as thick as 60 nm. The roughness of the oxide layer must be below 5 nm in order for the second AFM lithography step to work. If the dot is defined by e-beam lithography, AFM lithography on the second layer across the etched trenches usually results in a discharge marked with the black arrow in Fig. 3.10a.

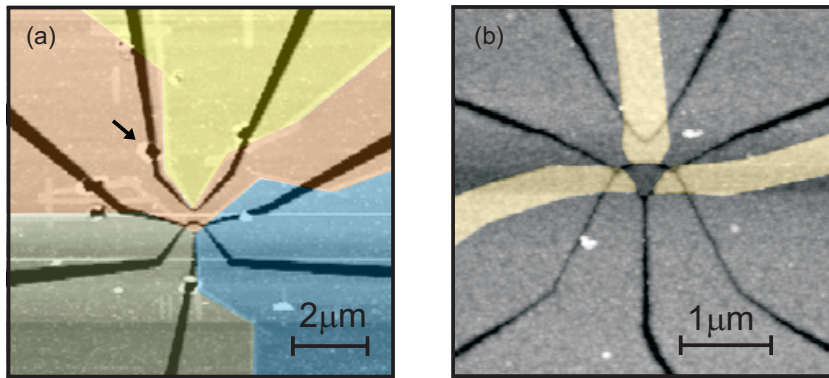


Figure 3.10: False color AFM micrograph of two samples showing double-layer lithography. After e-beam lithography and shallow etching, the samples surface were covered by 40 nm thick layer of HfO_2 . The sample in (a) was then covered with ≈ 5 nm Ti and AFM lithography was used to separate the global gate to a set of independent patches. Different patches are shown in different colors. For the sample shown in (b) a second e-beam lithography followed by Ti/Au evaporation and standard lift-off process was used to create the top-gate fingers on the constrictions.

The second method is to define the top-gate fingers by electron beam lithography followed by Ti/Au evaporation and standard lift-off technique. The result is shown in Fig. 3.10b. In order to align the two e-beam lithography steps, 150 nm large alignment markers were used. This alignment markers buried under a 60 nm thick layer of HfO_2 were visible in the SEM. Note that due to thin top-gate layers these double-layer structures are more sensitive to electrostatic discharge (ESD) than their corresponding single-layer counterparts.

3.3 Measurement Setup

The ultimate goal in transport experiments is to measure resistances accurately and draw conclusions from them about the underlying microscopic physical processes. The measurement is achieved by applying a voltage across an electrical channel (controlled by a set of gates) and measuring the current or vice versa. Large currents and voltages are too invasive and therefore low-noise amplifiers are used for low-level current and voltage measurements. This brings up the issue of noise and various

techniques that are used to overcome it. Moreover, in order to observe various quantum phenomena in semiconductor nano-devices, the characteristic energy scales of the system must be larger than the thermal energy $k_B T$. Therefore electronic transport experiments are usually performed at very low temperatures. In this section we briefly discuss how this low-temperature is achieved in the experiment, the electrical setups that are used for low-level measurements in this thesis and various sources of noise in these electrical setup.

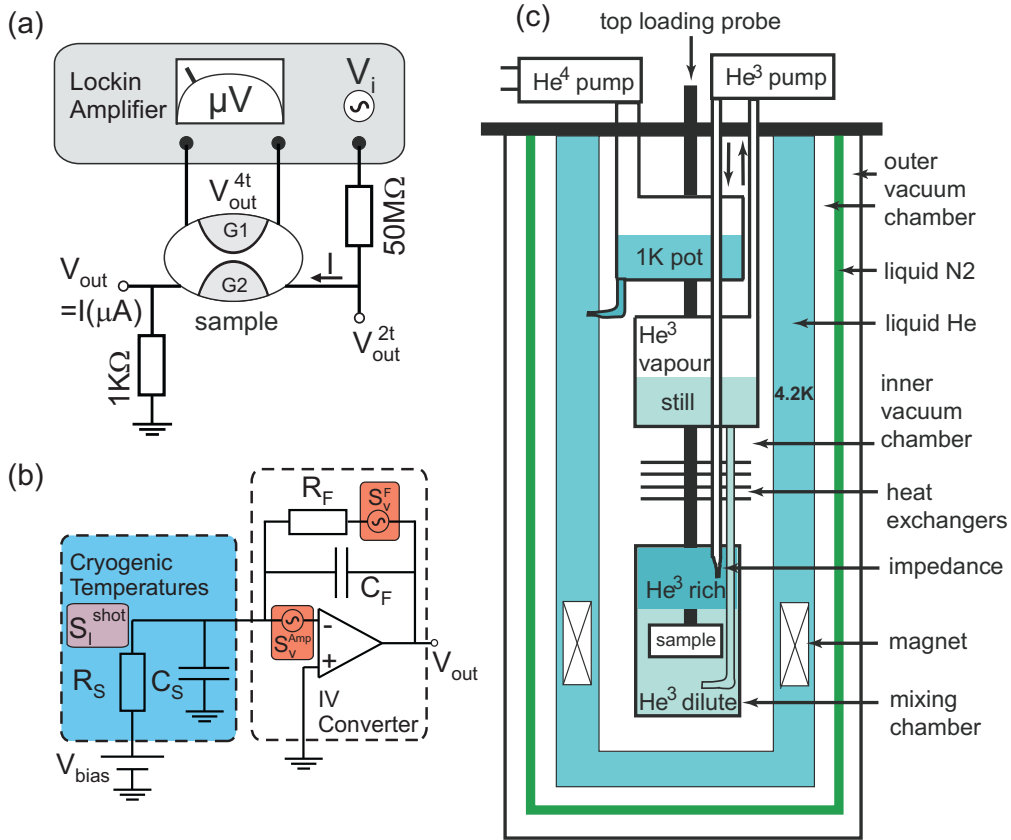


Figure 3.11: (a) (adapted from [60]) Scheme of the four-terminal resistance measurement setup for a QPC using a lock-in amplifier. (b) (adapted from [55]) Scheme of the two-terminal conductance measurement using an IV converter. The measured sample is modelled by the resistor R_S while C_S stands for the total cable and parasitic capacitances. The circuit model of an IV converter is also shown in the figure and various internal and external noise sources are identified. (c) (taken from [60]) Scheme of a top loading $^3He/^4He$ dilution refrigerator.

3.3.1 Electrical setups for transport measurements

Depending on the resistance of the sample, two different setups are used to measure the resistance. [74]. Low impedance measurements ($R \leq h/e^2$) are usually done by

passing a current through the system and measuring the voltage drop. Using two independent probes for the voltage has the advantage that the cable and contact resistances are excluded. Fig. 3.11a shows the scheme for the four-terminal conductance measurement of a sample which is a QPC in this case. A low ac bias voltage at the frequency of 31 Hz is applied using a Stanford SRS 830 lock-in amplifier to a large resistor (50 M Ω here) in series with the sample. This provides a constant current of about 1-10 nA through the sample as long as the sample resistance is small compared to this series resistance. This current can be also passed through a small resistance (1 k Ω here), the voltage drop across which, is used to monitor the current. The four-terminal and two-terminal voltage drops are indicated in the figure. Divided by the current they give the measured four-terminal and two-terminal resistances.

For high impedance samples ($R \gg h/e^2$), two-terminal measurements of the sample conductance were performed using a home-built IV converter. The IV converter consists of an operational amplifier (OPA627) with a differential gain of 10^8 - 10^9 and a feedback resistor R_F in the range of 1-100 M Ω as shown in Fig. 3.11b. The capacitive gain of the IV converter can be modelled with a capacitance C_F on the order of 2 pF. A low dc or ac bias voltage is applied symmetrically or asymmetrically across the sample and the current through the sample is measured with the IV converter. In Fig. 3.11b the sample is modelled with the resistance R_S . The cable and parasitic capacitances C_S on the order of 1 nF are the main parameters that limit the measurement bandwidth. All measurements were automatized with LabVIEW computer program [55].

3.3.2 Noise in electrical circuits

Various noise sources are indicated in the setup of Fig. 3.11b. These include the thermal noise, the amplifier noise and the current shot noise in the sample. Noise is usually characterized by power spectral density $S(\omega)$ defined as the Fourier transform of the correlation function ⁴

$$S(\omega) = \int dt e^{i\omega t} \langle\langle V(0)I(t) \rangle\rangle \quad (3.1)$$

For an Ohmic resistor $V(t) = RI(t)$ or generalized Ohmic impedance $V(\omega) = Z(\omega)I(\omega)$ this expression can be written in terms of current-current correlation which is the form one frequently encounters with. Noise power (in units of Watts) is calculated by integrating this quantity over the measurement bandwidth. For measurement purposes it is more convenient to express the noise in terms of power spectral densities of voltage S_V or current S_I (in units of V/ $\sqrt{\text{Hz}}$ or A/ $\sqrt{\text{Hz}}$) defined by

$$S(\omega) = Z S_I^2(\omega) = \frac{1}{Z} S_V^2(\omega) \quad (3.2)$$

⁴In case of current and voltage operators this expression must be symmetrized to give real numbers [75]. For a definition of cumulant average $\langle\langle X \rangle\rangle$ see Chapter 10.

Thermal fluctuations of the charges in the conductors produce a noise which is flat for $\hbar\omega \ll k_B T$ with voltage spectral density of $S_V = \sqrt{4k_B T R}$ known as the *Johnson-Nyquist noise* where T and R stand for temperature and the conductor resistance. Since the sample is at cryogenic temperatures during measurement, its thermal noise is negligible. The feedback resistance R_F however is at room temperature and has a contribution on the order of $S_V^F \approx 0.4 \mu\text{V}/\sqrt{\text{Hz}}$ for 10 M Ω .

The operational amplifier is also a source of current and voltage noise that appear in its input. While the current noise is usually negligible ($S_I=1.6 \text{ fA}/\sqrt{\text{Hz}}$ for OPA627), the voltage noise $S_V^{Amp} \approx 5 \text{ nV}/\sqrt{\text{Hz}}$ is significant, especially because it produces a current through the sample that is multiplied by the feedback resistor in the output. Therefore the output voltage noise of the amplifier is proportional to Z_F/Z_S and is higher for low-impedance samples. Different noise sources add up incoherently and we have

$$S_V^{n,ext}(f) = \sqrt{(V_F^n)^2 + (V_{Amp}^n)^2(1 + Z_F/Z_S)^2} \quad (3.3)$$

The choice of feedback resistance is therefore adjusted with the sample resistance to minimize the noise. The signal however has a gain of Z_F/Z_S which limits the bandwidth by the amplifier pole $Z_F = (1/R_F + iC_F\omega)^{-1}$ and the sample zero $Z_S = (1/R_S + iC_S\omega)^{-1}$. Apart from these external noise sources, the fact that current is carried by discrete charged particles and each get randomly transmitted or reflected through a nano-structure also produces the so-called *Shot noise*. In a QPC with a single degenerate channel this noise is given by $S_I^{shot} = \sqrt{eIF}$ (see section 9.4) where $F = 1 - D$ is the Fano factor with D the transmission probability of the QPC. For a current on the order of 10 nA through a QPC at 50 k Ω ($V_{bias} \approx 500 \mu\text{V}$) the shot noise is about 40 fA/ $\sqrt{\text{Hz}}$. With the same parameters and assuming 10 M Ω for the feedback resistor, the external noise is equivalent to a current noise of 110 fA/ $\sqrt{\text{Hz}}$ which is only a factor of 3 higher than the intrinsic noise of the QPC. The total noise must be again calculated using incoherent sum of intrinsic and extrinsic noises.

Above we discussed about inevitable sources of noise in transport measurements. There are also a number of other sources of noise like the Flicker noise, due to charged fluctuators in the solid-state environment, or the 50 Hz noise from power supplies that can be eliminated by avoiding ground loops in the measurement setup.

3.3.3 Cryogenics

Three type of refrigeration systems have been used in the experiments presented in this thesis. The first system is a simple dewar filled with liquid helium (^4He) which cools the sample to 4.2 K equipped with a 5 Tesla magnet. The second system is a ^4He system with a variable temperature insert (VTI) which is used to continuously pump the liquid helium down to ^4He vapour pressure of around 10 mbar. This system is equipped with a 9 Tesla magnet and can achieve temperatures down to 1.2 K. These two systems were used mostly for the basic characterization of the samples.

A measure of the relevant energy scales in a quantum system is the quantum confinement energy spacing which is inversely proportional to the effective mass. Since holes in p-GaAs have effective masses m^* that are about 5-8 times higher than electrons in n-GaAs, measuring at very low temperatures is essential for studying the hole transport. Most of the measurements presented in this thesis were therefore performed in a $^3\text{He}/^4\text{He}$ dilution refrigerator equipped with a 13 Tesla magnetic which is commonly used to cool down samples to temperatures below 60 mK [76]. Fig. 3.11c shows the scheme of this system. The fridge is composed of two nearly independent He flow circuits that are isolated from the ambient temperature by outer vacuum chamber (OVC), liquid nitrogen N_2 shield, main liquid He bath and inner vacuum chamber (IVC). The first circuit composed of a ^4He 1K pot and the ^4He rotary pump, is very similar to a VTI in which pumping on a liquid ^4He vapour is used to cool down the pot to about 1.2 K. The second circuit is a circulation circuit in which a mixture of $^3\text{He}/^4\text{He}$ mixture is circulated by a ^3He rotary pump. The sample loaded from the top of the fridge is kept in the mixing chamber where at temperatures below 700 mK, the mixture undergoes a phase transition to a ^3He -rich and a ^3He -dilute phase. The dilute phase extends up to a container called still where it is pumped continuously using the ^3He pump and is kept at temperature around 700 mK. At this temperature the ^3He has higher vapour pressure than the ^4He . Therefore mostly ^3He gas is pumped and circulated by the ^3He pump to a condenser located in the 1K pot (this is why 1K pot has to be cold) and after passing heat exchangers it is fed back to the ^3He rich phase. The transfer of ^3He atoms from the rich phase to the dilute phase, due to the difference in enthalpy because of different quantum zero-point motion of the two isotopes, provides the cooling power at the interface between the two phases where the sample is located. A detailed explanation of the working principles of the dilution refrigerator can be found in [76].

Chapter 4

The 0.7 conductance anomaly: a short review

4.1 Introduction

Since its discovery in 1988 [50, 51] conductance quantization in ballistic quantum point contacts (QPCs) has become one of the hallmarks of mesoscopic physics. The experimental observation of this effect in many different systems and materials has established its universality. From a theory point of view the conductance of a non-interacting 1D wire is given by the Landauer formula (Eq. 2.42) namely the number of transmitting channels times $2e^2/h$ (2 to take into account the spin-degeneracy). This result is obtained because in 1D, independent of the details of the dispersion relation, the energy-dependence of density of states (DoS) cancels out exactly with the group velocity of the carriers.

Coulomb interactions can significantly alter this picture. In 2D and 3D Fermi liquid theory states that the role of particles is replaced with non-interacting pseudo-particles that have a renormalized mass. This theory is not applicable in 1D and the interactions cannot be renormalized there due to the fact that DoS is discrete at the Fermi energy. Fortunately many-body systems in 1D have an exact solution known as the Tomonaga-Luttinger liquid. This liquid has qualitatively different properties than the non-interacting systems. For example it was predicted by Kane and Fisher [77] that transport properties of a clean 1D interacting electron gas have power law dependence on temperature and voltage. However it has been argued [78] that the finite resistance of a finite ballistic wire is due to the contact resistance and comes entirely from processes that take place outside the wire, where electrons are not in the Luttinger-liquid state. Maslov and Stone [78] have shown that the conductance of a single channel is still given by the non-interacting Landauer formula. In spite of this the question of to what extent interactions play an essential role in 1D transport is still far from being clear.

From an experimental point of view the conductance of quantum point contacts and quantum wires show deviations from the single-particle picture provided by the

Landauer formula, the most prominent one being known as the 0.7 anomaly. A clear understanding of these anomalies is still debated in spite of extensive investigations.

In the following we will give a short review of the 0.7 anomaly in n-GaAs quantum point contacts. This is by no means intended to be a complete review of the topic. The 0.7 anomaly has a very rich literature including many essential experimental and theoretical studies during almost 20 years based upon which our current, yet incomplete, understanding is built. Only few experiments that we believe to be directly related to our measurements are discussed here. A complete set of data from each experiment is not presented here. Rather we have chosen to pick a particular data set from each experiment in order to build a general picture which reflects the diversity of the phenomenon. The goal is to set the stage to introduce the measurement results on our hole QPCs in the next chapters and to be able to compare them to electron QPCs. Interested readers are referred to a recent comprehensive review of this field by Micolich [79]. *

4.2 0.7 Anomaly in linear conductance

The 0.7 anomaly is usually referred to the observation of an anomalous plateau at the conductance value of about $0.7(2e^2/h)$. However it is not the precise conductance of this plateau but rather a set of qualitative features that are associated with the anomaly. In the following we will introduce these qualitative features. The plateau itself has been experimentally observed to have conductance values between 0.6 to $0.8(2e^2/h)$.

4.2.1 In-plane magnetic field

Fig. 4.1a shows a typical measurement of linear conductance vs. gate voltage for an n-GaAs quantum wire adapted from the PhD thesis of Abi Graham [80]. The figure shows how the linear conductance is affected by the application of an in-plane magnetic field. Linear conductance traces taken for different magnetic fields are shifted horizontally for clarity. The leftmost curve exhibits quantization of the conductance in units of $2e^2/h$ at zero magnetic field. This changes with magnetic field. However, most of the observed features can be understood in a single particle picture. The conductance is given by the Landauer formula and different modes are separated in energy due to lateral confinement which gives rise to a conductance staircase in units of $2e^2/h$. By applying an in-plane magnetic field the spin degeneracy is lifted and the steps are seen in units of e^2/h as expected.

What defies a single-particle understanding though, is the small plateau-like shoulder (red arrow) around $0.8(2e^2/h)$ on the rise of the first plateau in the leftmost curve known as the 0.7 anomaly. This anomalous feature is less universal than the

*Valuable discussions with Y.Meir, A.R.Hamilton, F.Sfigakis, B.R.Bulka, J.Folk and I.Zozoulenko is appreciated.

conductance quantization, but it has also been widely observed in point contacts made of different materials and fabricated with different techniques. Despite its observation in the first conductance quantization discovery (Fig. 2.3a), it took eight years before it was taken seriously by the community [81]. By the application of an in-plane magnetic field, the conductance of the anomalous feature decreases and it is gradually transformed to the first spin-split subband. This smooth transition suggests connection between the 0.7 anomaly and the spin of the electron.

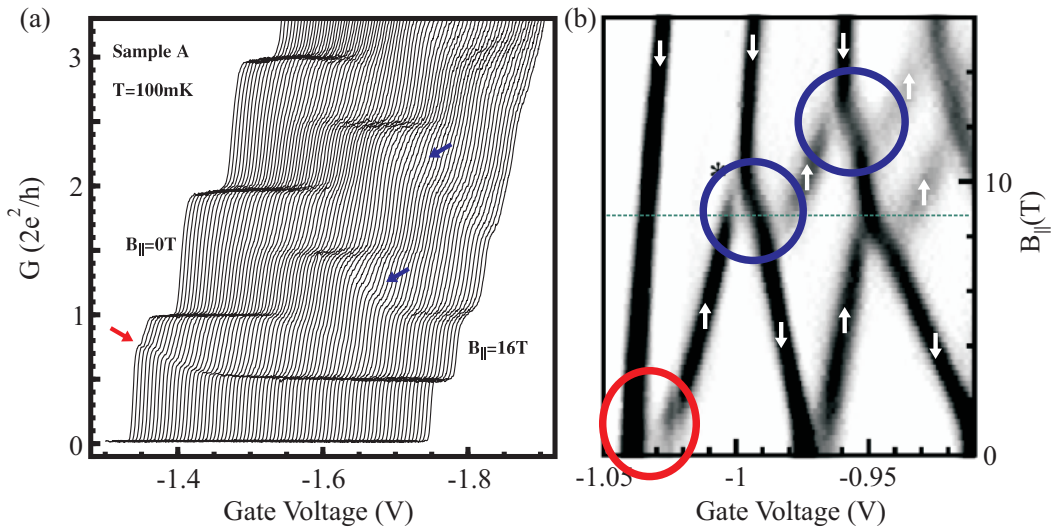


Figure 4.1: (a) Linear conductance and (b) Transconductance of a n-GaAs nanowire as a function of gate voltage and in-plane magnetic field adapted from PhD thesis of Graham [80]. The smooth transition of the 0.7-feature to a half-plateau by application of in-plane magnetic field is in contrast to the Zeeman splitting of other subbands. At zero field there is a finite energy gap between the two spin-split subbands marked with the red circle. The blue circles mark the energy jump in the crossing of spin-split subbands at larger magnetic fields.

The data shown in Fig. 4.1a can also be represented as the gray-scale colormap of Fig. 4.1b which shows the transconductance (derivative of linear conductance vs. gate voltage) as a function of the gate voltage and the magnetic field. The Zeeman splitting of the first subband by an in-plane magnetic field can be seen in this figure, however there is a finite energy gap left at zero field between the two subbands marked with the red circle. This gap is the manifestation of the 0.7 anomaly.

4.2.2 Temperature dependence

The peculiar temperature-dependence of the linear conductance is one of the main features of the 0.7 anomaly. This is shown for two n-GaAs QPCs in Fig. 4.2. In Fig. 4.2a from Kristensen et al. [82], no anomalous feature is observed at the lowest temperature (solid line). Increasing the temperature from 0.3 K to 5.1 K smears out the conductance but a small kink at elevated conductance of about $0.7(2e^2/h)$ is

visible in the plot. In Fig. 4.2b from Cronenwett et al. [83] a more obvious feature, like a short plateau at about $0.7(2e^2/h)$, develops as the temperature is increased from 80 mK to 4.1 K. At the lowest temperature the remnant of the 0.7 feature is left as a shoulder-like feature on the linear conductance.

In a single-particle picture the temperature dependence is expected to be given by the Landauer formula Eq. 2.42 and 2.41. Increasing the temperature smears out the conductance. In a so-called saddle point potential model of the QPC discussed in Chapter 5, the conductance of two temperature-invariant points [84], one in the middle of each plateau and another one in the middle of the rise between plateaus are expected to be unaffected. These points are indicated in Fig. 4.2b with black arrows. The temperature-invariance of the point close to the pinch-off is usually influenced by self-consistent screening effects at low temperatures. However, at sufficiently large temperatures this point can be clearly identified.

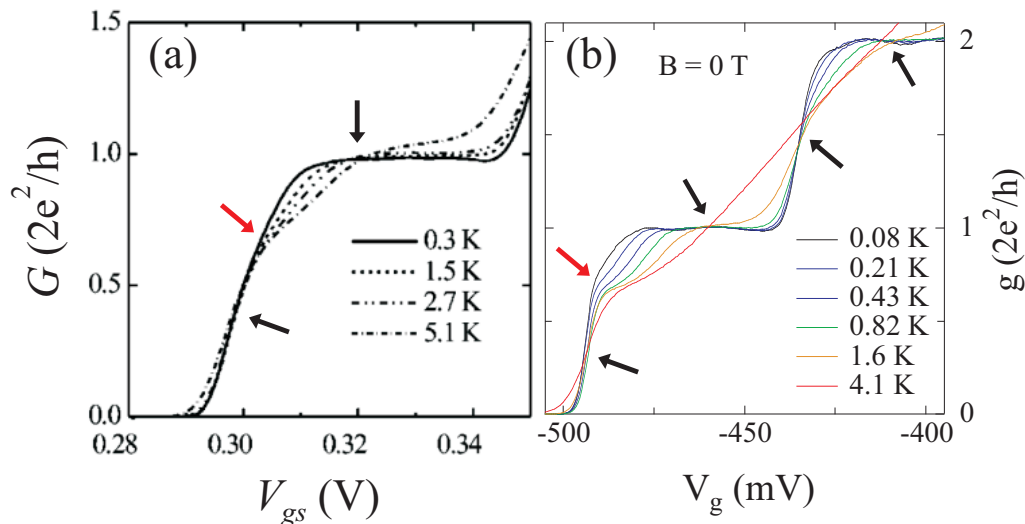


Figure 4.2: The peculiar temperature dependence of the linear conductance for two n-GaAs quantum point contacts (a) taken from Kristensen et al. [82] and (b) taken from Cronenwett et al. [83]. Black arrows point to the temperature invariant points. Red arrows point to the 0.7 conductance anomaly.

4.3 Possible explanations

It must be emphasized at this point that there is no general consensus on the origin of the 0.7 anomaly to this date. What is agreed upon however is that many-body phenomena, spin physics and strong interactions are certainly the main ingredients. Many theoretical works to date have focused on different many-body explanations for the anomaly, such as separation of singlet and triplet channels [85], spin and charge channels in a Wigner crystal at low densities [86], non momentum-conserving electron-electron scattering [87] and phonon back-scattering [88] to name a few. In

the rest of this section we will focus on the two most promising explanations of the anomaly, namely the spontaneous spin polarization and the quasi-bound state model.

4.3.1 Spontaneous Spin polarization

To introduce the spontaneous spin polarization model we have to get back to the Zeeman splittings in the transconductance data presented in Fig. 4.1b. The spin direction of the subbands are also indicated in this figure. At the positions where two opposite spin-subbands meet (marked with blue circles) a crossing is expected in the plot (no anti-crossing is expected since the quantum numbers differ). However what is observed in the experiment is neither a crossing and nor an anti-crossing. Rather there is a kink in the evolution of spin- \downarrow subband and a discontinuity in the energy of the spin- \uparrow subband at the points of degeneracy.

Theoretical calculations by Berggren et al. [89] using Kohn-Sham spin density functional theory (SDFT) reproduce these discontinuities remarkably well. These calculations have shown that the kinks and the change of slopes at the crossing points can be taken into account by a Hartree approximation. Furthermore if the exchange and correlation effects are included it is possible to reproduce the jumps.

Therefore the discontinuities in Fig. 4.1b can be understood in terms of the van Hove singularity of 1D DoS [46] and the exchange effects introduced in Chapter 7. Imagine crossing one of the blue circles by increasing the gate voltage (or the electron density in the constriction) at about 9 T along the green dashed line. At about $V_g = -1$ V the $1\uparrow$ -subband is lower in energy than $2\downarrow$ and therefore this subband has a lot of electrons. As the $2\downarrow$ -subband crosses the Fermi energy it gets quickly filled with spin- \downarrow electrons. These newcomers start to act back (via exchange interaction favouring parallel spins)¹ on spin- \uparrow electrons (in $1\uparrow$ -subband) shifting their energy up and eventually emptying the subband. Therefore due to exchange interaction these two subbands never get stable degeneracy. There is a finite gap and a density mismatch (finite spin polarization) close to degeneracy.

The blue circles in Fig. 4.1b have a signature in the conductance (Fig. 4.1b) that is marked with the blue arrows. At these points there are anomalous plateaus that have a gradual drop in conductance very similar to the gradual transformation of the 0.7 anomaly to the spin-split subband (red arrow). This similarity suggests that a finite energy gap between the spins and a spontaneous spin polarization may also be responsible for the 0.7 anomaly. It was shown that by Graham et al. [90] that features marked with blue arrows, known as the ‘0.7 analogue’ structures, have similar conductance behavior as the 0.7 anomaly.

Motivated by the above discussion, the 0.7 gap in the transconductance has been interpreted to be similar to a residual field due to a spontaneous spin polarization of the low-density electrons close to the pinch off [22, 81, 82, 91–93]. This suggestion has remained controversial in connection with the exact theory forbidding a ferro-

¹Note that the electrons with the same spin do not have exchange interaction.

magnetic ground state in 1D [94, 95]. However it must be mentioned that the setting in typical experiments does not exactly fit into this theory due to the presence of 2D reservoirs that contact the 1D region [96].

4.3.2 Coulomb blockade and Kondo physics

An alternative explanation, motivated by the physics of quantum dots, suggests that the Coulomb blockade-like physics could be responsible for the zero-field energy gap observed at zero field [97]. Since any possible confined state in the QPC is strongly coupled to the leads, higher-order processes and especially the Kondo effect are invoked by this model.

The presence of Coulomb blockade and Kondo physics in open systems like quantum point contacts and quantum wires is highly controversial [98, 99] but the proposed picture is that the screened effective potential landscape of the quantum point contact may support the formation of a strongly-coupled quasi-bound state close to the Fermi energy, based on which the system can be described by an Anderson-like Hamiltonian [100].

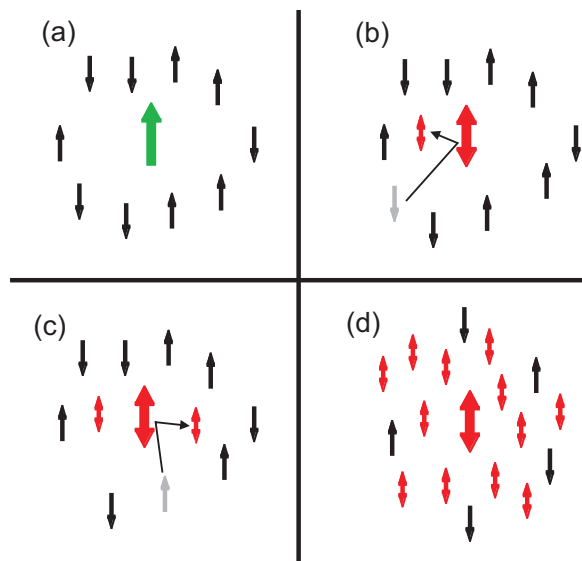


Figure 4.3: (adapted from [101]) A simple picture of Kondo cloud formation in metals. (a) A single magnetic impurity is surrounded by conduction electrons (b) One electron scatters off the impurity with the possibility of flipping (or not) of its spin and that of the impurity. These particles are now entangled (red). (c) A second electron scatters off the impurity, thus becoming entangled with both impurity and the previous scattered electron. (d) Continued scattering events build up a state where a large number of conduction electrons are correlated with the localized impurity. This many-body singlet state, known as the Kondo cloud, has a lower energy than (a) (defining a temperature scale) and is the new ground state.

This quasi-bound state can be occupied by one electron while double occupancy of the state by opposite-spin electrons (singlet) is forbidden due to on site Coulomb repulsion.² The two spin-channels propagating through the QPC thus get correlated so that while one electron is momentarily trapped in the quasi-bound state the propagation of the opposite spin electron is blocked essentially due to Coulomb blockade [97].³ At high temperatures the trapped electron thermally fluctuates between two spin-degenerate states but at temperatures lower than the so-called *Kondo temperature* T_K , it is frozen. While sequential tunnelling is momentarily blocked, provided that the coupling to the leads is sufficiently large, higher-order co-tunnelling processes set in. Those co-tunnelling processes that involve spin-flip of the electron in the quasi-bound state entangle this spin with the electrons in the leads while reducing the energy by forming a many-body spin-singlet (Fig. 4.3) [97]. Moreover they create a narrow peak in the density of states (DoS) of the quasi-bound state at the electrochemical potential of the leads that enhances the conductance.

4.4 Spin density functional theory calculations

Rejec and Meir [102] calculated the effective potential of a quantum point contact using spin density functional theory (SDFT) [48]. By careful self-consistent accounting for the effect of remote dopants and the gates used to define the QPC, they found that the effective Kohn-Sham potential [103] of the QPC, that includes the effects of screening and many-body interactions in a mean-field level (every spin up/down electron experiences the same Hartree/exchange potential) is qualitatively different from the saddle-point potential that is often assumed.

This effective potential that is density (and thus gate) dependent is shown as white dashed curves in Fig. 4.4a,b for two different gate voltage values. The color map shows the local density of states (LDOS) as a function of energy and longitudinal position along the QPC axis. At low densities the Fermi energy is below the top of the effective barrier (Fig. 4.4a). As the density is increased by changing the gate voltage, the Kohn-Sham potential changes to a double-barrier potential that has a resonance below Fermi energy and therefore supports a quasi-bound state (Fig. 4.4b). This is mainly due to Friedel oscillations of the density which lead to oscillating screening behavior. Fig. 4.4c shows the energies of the symmetric (red) and anti-symmetric (blue) solutions of the SDFT calculation (with respect to the unpolarized solution) as a function of the gate voltage and compares it to the conductance of the QPC calculated using Landauer-Buttiker formalism and Kohn-Sham wavefunctions of the unpolarized solution. The data suggests that the symmetric solution shown in Fig. 4.4d is the ground state of the system within the gate range

²This is a good assumption provided that the overlap of the quasi-bound state with the electrons in the leads is sufficiently weak.

³Simultaneous occupation of the resonant level with two carriers with the same spin is assumed to be forbidden due to Pauli principle.

of the anomaly. Spin densities of spin- \uparrow (left) and spin- \downarrow (right) electrons are shown in Fig. 4.4d at various gate voltages A, B and C marked in the linear conductance plot of Fig. 4.4c. Based on this, Rejec and Meir [102] suggested that at point C the system can be described by an Anderson Hamiltonian from which the conductance is suppressed as the Coulomb blockade through the quasi-bound state correlates the two spin channels. They also mention that the quasi-bound state formation is very sensitive on the length of the QPC as it requires that half of the local Fermi wavelength fit along the QPC. No quasi-bound state is expected for short QPCs.

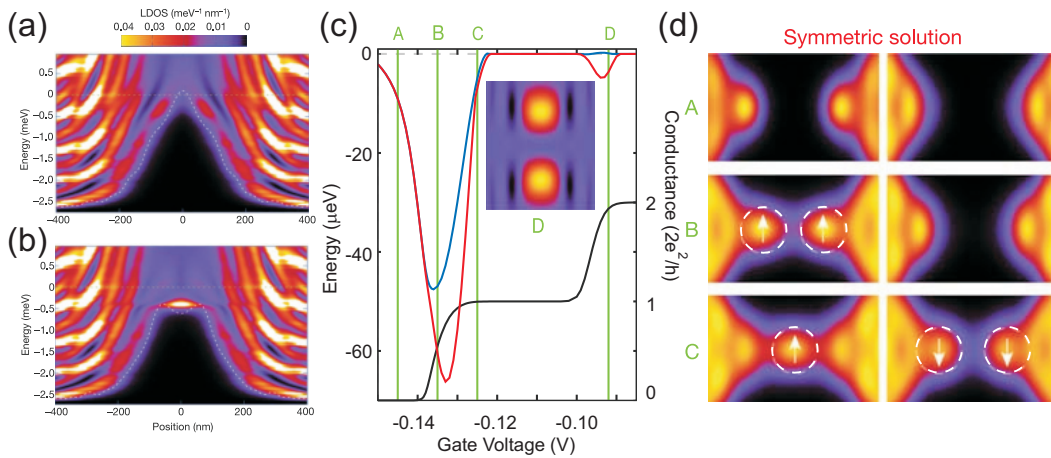


Figure 4.4: SDFT calculations of a QPC adapted from [102]. (a) and (b) show the LDOS vs. energy and longitudinal position for the Fermi energy above and below the top of the barrier. The white dashed curve shows the Kohn-Sham potential that is different in two cases. (c) Linear conductance (black), the energy of symmetric (red) and anti-symmetric solutions of SDFT with respect to unpolarized solution as a function of the gate voltage. The symmetric solution is the ground state within the gate voltage range relevant for the 0.7 anomaly. (d) shows the density of spin-up (left) and spin-down (right) electrons vs. longitudinal and lateral positions at various gate voltages in figure (c). A small in-plane magnetic field is assumed that favours spin-up population.

4.5 Temperature scaling

In order to understand the physics of the 0.7-feature it is important to quantify the temperature scale at which conductance exhibits the maximum change. This scale obviously depends on other configuration parameters like the gate voltage. However it is speculated that if the temperature-dependence at each gate voltage is scaled with its corresponding temperature scale we may get to a universal behavior that sheds light on the physical phenomena behind the anomaly.

4.5.1 Thermal activation

Kristensen et al. [82] were the first to study the possibility of a temperature scaling of the anomaly. They showed that the conductance vs. temperature of Fig. 4.2b fits to an Arrhenius-type (exponential) behavior, $G_0 - G(T) \propto e^{-E_A/k_B T}$ that supports activated transport phenomenon with E_A as the activation energy. In their notation

$$G_{Activated} = G_0 [1 - C e^{-T_A/T}] \quad (4.1)$$

where $G_0 = 2e^2/h$ is the conductance quantum, T_A is the scaling parameter and C is a constant fit to the data. The extracted T_A scaled exponentially with the gate voltage or density. This conclusion inspired several phenomenological theories of the 0.7-anomaly [93, 104–106], including the one by D. Reilly in which a density-dependent energy gap between two spin-subbands is assumed to explain most of the experimentally observed features [79].

Despite theoretical support for the spontaneous spin polarization in the QPC, the mean-field theories have failed to account for the density-dependent energy gap assumed in this model and thus the observed temperature-dependence [96, 107, 108].

4.5.2 Kondo effect

Another type of temperature scaling that is common in quantum dots is due to the Kondo effect [1, 109] where an unpaired trapped spin is screened by the electrons in the leads (Fig. 4.3) and the conductance follows a temperature-dependence of the form

$$G_{Kondo} = G_0 [1 + (2^{1/s} - 1)(T/T_K)^2]^{-s} \quad (4.2)$$

The parameter s is obtained from numerical renormalization group (NRG) calculations and is around 0.22 for spin-1/2 systems [83, 109].

Quantum point contacts typically show a peak in their dI/dV around zero bias voltage, known as *zero bias anomaly* (ZBA), which can be regarded as a signature of the DoS peak created by the Kondo effect. Motivated by the presence of ZBA, Cronenwett et al. [83] studied the possibility of a Kondo-like fit to the conductance. However the Coulomb blockade by a quasi-bound state is dynamical (in contrast to quantum dots in which an electron/hole can block the current forever) and so is the Kondo effect and therefore it is highly non-trivial to know how much sequential tunnelling and how much co-tunnelling contribute to the current. In contrast to the Kondo effect in quantum dots, the conductance does not go to zero at high temperatures and part of the current is carried by sequential tunnelling whose contribution is not easy to estimate. Therefore the authors in [83] tried the empirical formula of

$$G_{Modified\ Kondo} = G_0/2 + G_{Kondo}/2 \quad (4.3)$$

which assumes that the conductance above e^2/h is of Kondo origin.

Fig. 4.5a shows the result of this scaling. The temperature dependence at each gate voltage, if scaled with a gate-dependent Kondo temperature, falls on the black

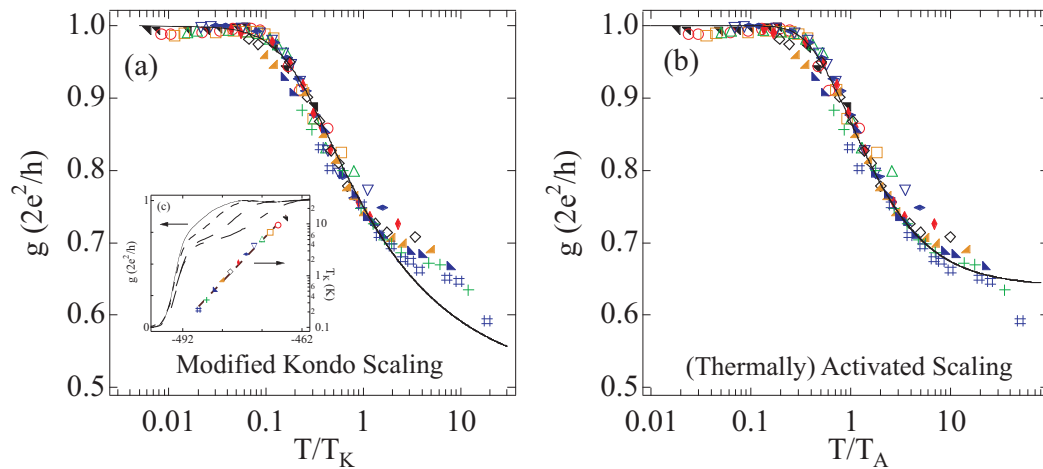


Figure 4.5: (taken from [101]) Conductance vs. the scaled temperature calculated from the data of Fig. 4.2b for the two models (a) Modified Kondo model (b) Thermally activated model. Note that both models fit nicely to the data. The inset in (a) shows again the temperature dependence of linear conductance vs. gate voltage along with the temperature scales extracted from the fitting. The temperature scale increases exponentially with the gate voltage.

curve given by Eq. 4.3. The inset shows the temperature-dependence of the linear conductance together with the extracted Kondo temperatures that show an exponential gate-dependence. Based on this fit the authors suggested the Kondo effect as the origin of the peculiar temperature-dependence of the 0.7 feature. Although not shown in the original paper [83], the authors mentioned that the thermally activated fit is equally good. Fig. 4.5b from the PhD thesis of S. Cronenwett [101] shows that a thermally activated fit to the data based on Eq. 4.1 is, if not better, as good as the Kondo scaling.

To conclude this section, the temperature scaling of the linear conductance to different models has initiated various theories for the 0.7-feature, however the procedure is not very reliable and cannot distinguish between the thermally activated transport and the Kondo model. The latter has the additional complication that the precise contribution of the Kondo effect in the conductance is difficult to estimate.

4.6 Finite bias spectroscopy

It is common to investigate the density of states in the QPC by finite bias spectroscopy i.e. measuring dI/dV of the nano-structure as a function of applied bias voltage. Fig. 4.6a from [83] shows the non-linear differential conductance g of the QPC, whose temperature dependence was shown in Fig. 4.2b, as a function of the applied bias voltage for different gate configurations. Each curve in this figure corresponds to a specific gate voltage and the plateaus in $G(V_g)$ appear as the accumulation of the individual g traces corresponding to different V_g gate voltages. The

differential conductance data of Fig. 4.6a can be alternatively plotted as the color map of Fig. 4.6b. This plot shows the transconductance which is the derivative of the differential conductance with respect to the gate voltage.

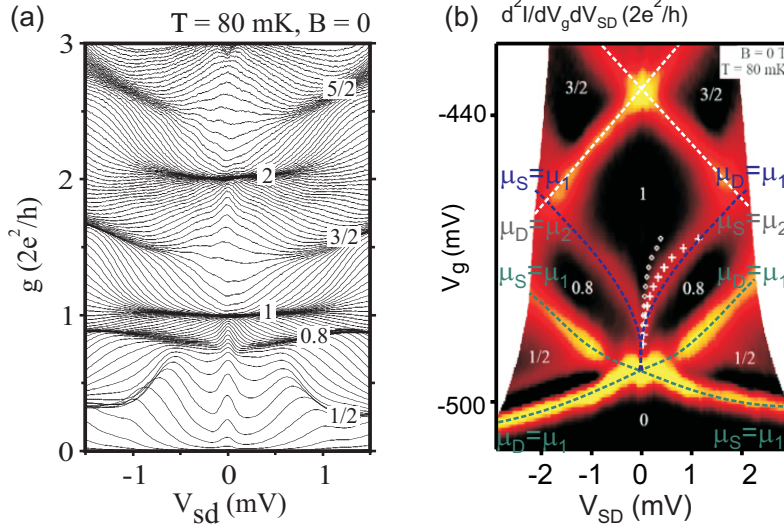


Figure 4.6: (adapted from [101]) (a) Nonlinear differential conductance vs. source-drain bias for several gate voltages at $T = 80$ mK. Plateaus in linear conductance correspond to the accumulation of dI/dV curves here, whose conductance is indicated. ZBA is the peak around zero bias below first plateau. (b) Color map of transconductance (numerical derivative of g with respect to gate voltage). Dark areas correspond to plateaus and the bright regions the transition between plateaus. The crossings of the subbands with μ_S and μ_L are indicated by the dashed lines. The blue and green dashed lines both correspond to the first subband. For the white plus and circle marks see the text below.

4.6.1 Zero bias anomaly

The peak around $V_{sd} \approx 0$ for $g < 1(2e^2/h)$ in Fig. 4.6a is the zero bias anomaly discussed before.⁴ A zero bias peak in the differential conductance can have different origins, some of which are discussed in Chapter 6. For example some theoretical and experimental studies indicate that ZBA can even show up in a clean 2D electron gas [111, 112].

In a Kondo model a peak emerges in the density of the state of the QPC at the Fermi energy and a ZBA naturally arises in dI/dV as a result. This Kondo peak in the density of states has the special feature that it is locked at the Fermi energy (the energy at which the unpaired electron is screened by those in the leads) and therefore it splits to two peaks if there is a finite bias between source and drain. The current in a two terminal system however depends on both density of

⁴There is a similar but weaker peak at higher conductance $g \in (1.5, 2)(2e^2/h)$.

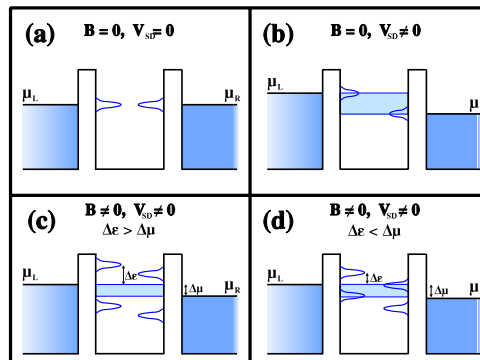


Figure 4.7: (taken from [80]) (a) DoS of a dot with large coupling to the leads at low temperatures has peaks at the left/right electrochemical potentials due to Kondo effect. (b) At finite bias the peaks are suppressed [110] and separated in energy. (c) Finite magnetic field causes Zeeman splitting and suppression of DoS peaks [110]. For $\Delta\epsilon > \Delta\mu$ the DoS peaks leave the bias window and conductance enhancement vanishes. (d) For $\Delta\epsilon < \Delta\mu$ Kondo enhancement of the conductance still exist. The maximum current happens for $\Delta\mu = 2\Delta\epsilon$ implying that the splitting of ZBA is twice the Zeeman splitting.

states and therefore shows only one peak [110] (see Fig. 4.7a,b). On the other hand applying a finite magnetic field splits each of these two peaks and therefore results in a splitting of ZBA at finite magnetic field. As a matter of fact a ZBA does split by the magnetic field [83]. The splitting obtained [83] however was equal to Zeeman splitting, while twice splitting would be expected for a Kondo DoS-peak with a more careful consideration (Fig. 4.7c,d).

The ZBA however does not fit into a spontaneous spin polarization model of the anomaly. Therefore some proposals have suggested that the spontaneous spin polarization can co-exist together with the Kondo effect or set-in at temperatures above the Kondo temperature [93, 105]. The correlation between these criteria and the 0.7-feature is also debated [113–117]. These works have shown by measuring the splitting of ZBA vs. magnetic field and/or density (gate voltage) that ZBA, especially at low conductances, does not fit to a Kondo model and have suggested that the ZBA and the 0.7 anomaly may have different origins.

4.6.2 The extra subband-line

The transconductance shown in Fig. 4.6b is very similar to the typical Coulomb diamond measurements in quantum dots enabling the quantized subband structure of QPC to be easily followed. Various subbands and their alignment with the source and drain electrochemical potentials are marked in the figure. The white dashed lines mark the evolution of the second subband with the bias and the gate voltage. The first subband however has an anomalous subband structure.

The blue dashed lines that cut through the first plateau together with the green

dashed lines define the first subband. A constant bias cut through this plot, for example with $V_{sd} > 0$, reveals that as the density is increased in the QPC, only one subband crosses the source while two subbands cross the drain. In spontaneous spin polarization models this observation [79] has been interpreted as a sign of an energy gap opening up between the two spin subbands as they cross the Fermi energy. The suggested picture is that as soon as the spin-degenerate subband crosses μ_S , one of the spin subbands gets pinned at μ_S (thus kept under-populated) while the other spin subband enters the bias window and continues to go down in energy and get populated. Cronenwett [101] superimposed the temperature scales $k_B T_A/e$ extracted from the thermal activation fitting of Fig. 4.5b on the transconductance plot. These are marked with small open white circles in Fig. 4.6b.

In Coulomb blockade-like physics from a quasi-bound state model a suppression of current is expected at low density regions of the first plateau. It is expected that if the gate voltage is increased (the subband is pulled further below the Fermi energy), Coulomb blockade is eventually overcome and the conductance gets back to its normal value of $1(2e^2/h)$. The blocked region is thus the stripe in energy (or gate voltage) between green and blue dashed lines with the reduced conductance at $0.8(2e^2/h)$. Around $V_{sd} \approx 0$ the blue lines bend down, cutting this region, connecting to the green line. This connection bridge which is due to ZBA is interpreted as a sign of Kondo effect. The white plus signs in Fig. 4.6b correspond to the temperature scales extracted from the modified Kondo model. These signs fit better to the blue lines suggesting that the Kondo effect is as robust against the applied bias as against the temperature.

4.7 Summary

Conductance measurements on quantum point contacts and quantum wires typically show an anomalous plateau-like feature at the conductance of about $0.7(2e^2/h)$ which cannot be understood within a single particle theory. Some of the main experimental signatures of the anomaly in n-type quantum point contacts and quantum wires are introduced. Many theoretical models have been put forward as an explanation, none of which can fully account for the experimentally observed features. Two of these theoretical models, the spontaneous spin polarization model and the Coulomb blockade model, are explained and discussed in connection to experiments.

Chapter 5

The 0.7 anomaly in hole Quantum Point Contacts

5.1 Introduction

The more pronounced carrier-carrier interactions in low-dimensional hole systems compared to their n-type counterparts make p-doped systems especially suitable for investigating many-body effects such as the 0.7 anomaly [27, 118]. Moreover holes strong susceptibility to spin-orbit interaction leads to the peculiar property that their g-factor is influenced by the lateral confinement (see Chapter 7). Therefore studying the anomaly in hole quantum point contacts (QPCs) provides a possibility to examine the conjectured connection between the anomaly and the spin of the subbands [118]. For example, the strong exchange-enhancement of the g-factor for small subband indices in electron QPCs was initially put forward as a support for the explanation of the 0.7 anomaly based on a spontaneous spin polarization model [81]. Whereas our p-type QPCs generally exhibit a very pronounced 0.7 anomaly, no clear evidence for exchange-enhancement of the 1D g-factor is available in these systems.

In this chapter we explore these effects in a hole QPC exhibiting an exceptionally strong 0.7 anomaly. The quality of the data presented is remarkable not only among the very few observations of this feature in hole systems [22, 27, 29, 118] but also compared to the typical reports of the anomaly in n-type quantum point contacts. We start the chapter first by presenting the standard characterization of the anomaly in our QPC. Then we investigate the effects of a magnetic field perpendicular to the 2DHG, showing that localization effects induced by the magnetic field can reveal information about the presence of a quasi-bound state in the point contact.

The sample presented in this chapter has the label *A3.24.1* and is shown in the inset of Fig. 5.1. This sample was fabricated by electron beam lithography followed by shallow etching. The 2DHG is depleted under the etched black regions thus $G1$ and $G2$ can be used as in-plane gates to tune the electrical confinement of the QPC which has a lithographical width of 200 nm. Throughout this chapter, the measurement results of this sample will be compared with those of the sample

A4.10.1/QPC1-10 whose complete data set is presented in Appendix E. *

5.2 The 0.7-anomaly characterization

Measurements of the linear conductance were carried out by the application of an ac current of 2 nA at the frequency of 31 Hz through the QPC in series with a 10 k Ω resistor and simultaneously measuring the voltage drop across the sample using two independent voltage contacts. This voltage drop was below 200 μ V and 50 μ V during pinch off and around 0.7 anomaly respectively. The voltage drop across the 10 k Ω resistor was used to measure the exact current passed through the QPC.

5.2.1 Temperature-dependence

Fig. 5.1 shows the linear conductance of our hole QPC as a function of the gate voltage for different temperatures. At the base temperature first plateau and the pinch-off regime can be identified. The wiggles on top of the first plateau has been associated to the deviations from saddle-point potential [119]. By increasing the temperature the first plateau smears out but a strong plateau at $0.7(2e^2/h)$ appears which is the so-called 0.7 feature discussed before. Note that there is no trace of this feature on the conductance at low temperatures. For non-interacting carriers we expect to have two temperature-invariant points in this figure: one in the middle of the first plateau and the other one in the middle of the conductance rise. However only one of this points is seen in the measurements and the conductance threshold is pinned at certain gate voltage due to self-consistent screening effects. According to Landauer formula (see Eq. 5.2) resonances in the linear conductance are expected to be smeared out by increasing the temperature. The peculiar temperature-dependence of the 0.7 anomaly, which differs from this expectation, testifies on its many-body origin.

5.2.2 Temperature scaling

To see if the temperature-dependence of our hole QPC presented in Fig. 5.1 favors a particular temperature scaling model, it is preferable to demonstrate these data in the form of Fig. 5.2a where each curve displays the effect of temperature on the conductance at constant gate voltage. A word of caution is in order here; the temperature-dependent measurements of the linear conductance discussed here were performed by constantly sweeping the gate voltage up and down and measuring the conductance while starting the circulation in the dilution refrigerator. Therefore the temperature changes slightly during each gate sweep. The values reported here correspond to the average of the temperatures read from the mixing chamber sensor during each sweep.

*Valuable discussions with Y. Meir and J. Folk is appreciated.

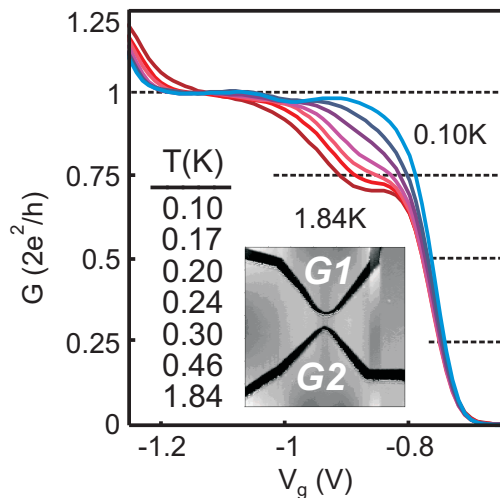


Figure 5.1: (a) Linear conductance G as a function of the gate voltage V_g at $B = 0$ for temperatures between $T = 1.84$ K and 100 mK. The inset shows the AFM micrograph of the QPC.

Here we try fitting the data to the two temperature scaling models explained in previous chapter. To which model the data fits best strongly depends on the choice of the temperature range and the gate voltage range over which the scaling procedure is attempted. The fact that the curves below e^2/h exhibit qualitatively similar temperature-dependence as those above, implies that a fit to Eq. 4.3 is not possible.

Fig. 5.2b illustrates the temperature scaling procedure for different models as a function of the scaled temperature $T/T_{K,A}$. The red curves depict the activated transport model for different values of the parameter C in Eq. 4.1. The blue curves present the Kondo model of Eq. 4.2 for different values of s and the green curves show the modified Kondo model of Eq. 4.3 for the same values of s . The temperature-dependence data on the left side of the vertical dashed line of Fig. 5.2a are shown in black at their actual temperatures ($T_{K,A} = 1$) in Fig. 5.2b. Since the plot is logarithmic the choice of the temperature scale corresponds to a shift of the black data curves horizontally by the amount of $-\log T_{K,A}$ to align them to a particular model (this is shown in the figure for few data curves). As mentioned before the conductances below e^2/h cannot be fit to the modified Kondo model. The triangular conductance dependence of the distance between the black curves and those of the model demonstrates that the temperature scale grows almost exponentially with the conductance. The blue curves representing Eq. 4.2 with $s = 0.22$ and different Kondo temperatures are super imposed as thin lines on Fig. 5.2a.

It is evident from these comparison and Fig. 5.2 that the temperature-dependent results from our hole QPC does not fit to the modified Kondo model suggested in [83]. A similar result is obtained on the QPC presented in Appendix E.

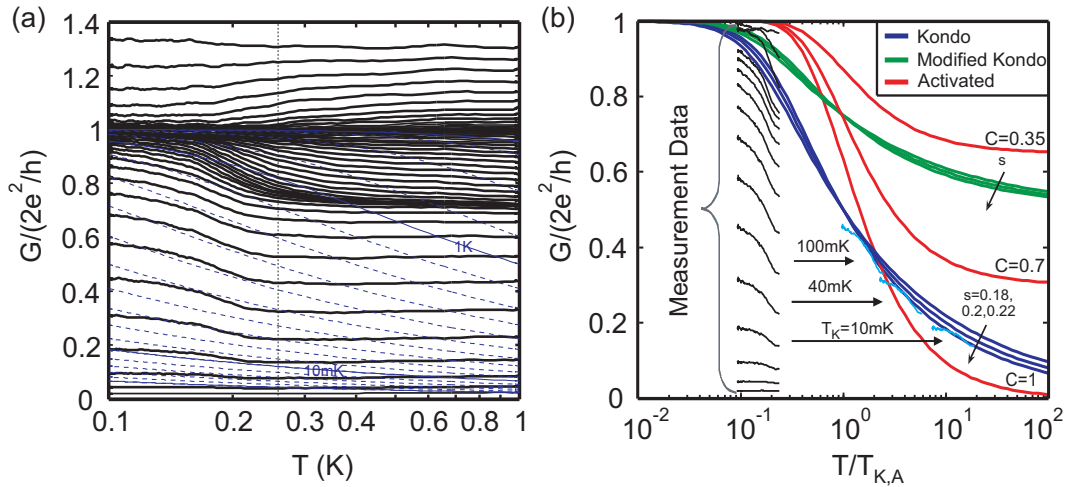


Figure 5.2: (a) Constant-gate conductance traces vs. temperature from the data of Fig. 5.1. The data between 0.1 K and 0.25 K (vertical dotted line) is used for the scaling procedure. (b) Conductance as a function of scaled temperature for the measurement data and both thermally activated (Eq. 4.3), Kondo (Eq. 4.2) and modified Kondo (Eq. 4.3) models for different parameters. Since the temperature axis is logarithmic, the scaling temperature is determined by horizontally shifting the measured data to fit it with the models. Modified Kondo model is obviously not the right choice. Kondo model fits the best to the data and is represented by faint blue solid-dashed lines in a.

5.2.3 Finite bias spectroscopy

Fig. 5.3 shows the non-linear differential conductance $g = dI(V_{sd}, V_g)/dV$ of the QPC as a function of the applied bias voltage for different gate configurations. Measurements of the differential conductance were carried out by the simultaneous application of an ac excitation with an amplitude of $20 \mu\text{V}$ at 31 Hz lock-in frequency, and a dc bias V_{sd} of up to ± 6 mV between source and drain. The voltage drop V_{sd} across the QPC was measured using two independent leads. The extent of the plateau in the bias axis suggests the subband energy spacing of the QPC to be about 0.6 meV.¹

The comparison of the non-linear differential conductance recorded at $T = 800$ mK and 100 mK shown in Fig. 5.3a,b highlights the intimate relation of the 0.7 anomaly observed in G to the ZBA, the narrow peak arising in g around $V_{sd} = 0$ at low temperature. This representation emphasizes the role of the ZBA in the low temperature recovery of the $2e^2/h$ unitary conductance from the 0.7 plateau. The ZBA which seems to be responsible for the temperature dependence of the 0.7 anomaly is

¹However it must be emphasized that due to the anomalous subband structure of the first plateau it is difficult to extract a clear value of subband spacing. The value given here corresponds to the crossing between the blue and white dashed lines in Fig. 5.6c (see also (Fig. 4.6b)) while the crossing between white and green dashed lines are at $V_{sd} > 1$ mV which is outside the range of the bias voltage explored here.

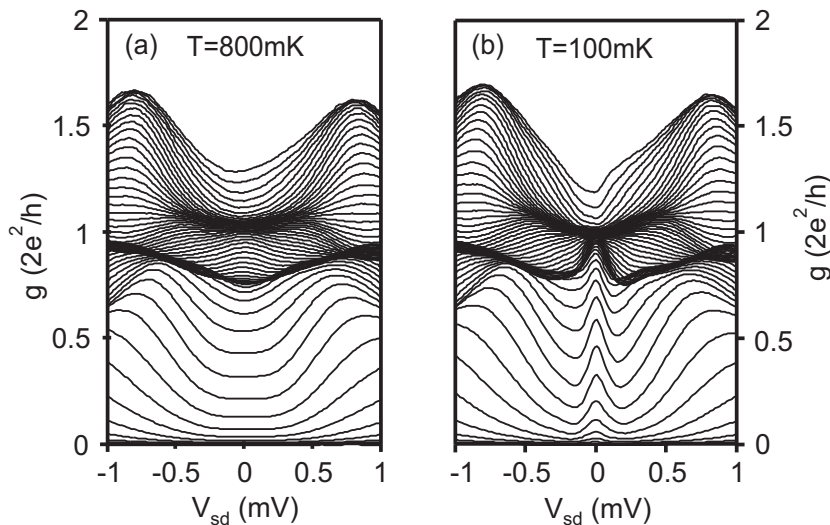


Figure 5.3: (a) and (b) Nonlinear differential conductance g at $B = 0$ as a function of V_{sd} taken at $T = 800$ mK and 100 mK respectively. Each trace correspond to different gate voltages V_g . Plateaus in G appear as accumulation of the individual curves in g . The extra plateau around $V_{sd} = 0$ with $g \approx 0.7(2e^2/h)$ is only present at $T = 800$ mK. With decreasing temperature a gradually emerging zero-bias peak restores the conductance at $2e^2/h$.

also observed at conductances well below $0.7(2e^2/h)$ down to pinch-off in agreement with the temperature-dependence data shown in Fig. 5.2b. Also note that the 0.7 plateau in Fig. 5.3 moves to higher conductances of about $\sim 0.9(2e^2/h)$ as the bias is increased at both low and high temperatures.

5.2.4 Zero bias peak height and width

In order to closely investigate the connection between the temperature-dependence data of Fig. 5.1 and the emergence of ZBA with lowering temperature in Fig. 5.3b, the (peak to valley) height and the (valley to valley) width of ZBA measured at $T = 100$ mK as a function of the gate voltage together with the linear conductance for different temperatures is demonstrated in Fig. 5.4. The ZBA height shows a double peak characteristic, only one of which (the high conductance one or the HC-peak) seems to be responsible for the temperature evolution of the 0.7 anomaly. The width of this peak increases with density (or lowering the gate voltage). As this width corresponds to the Kondo temperature in the Kondo model, this increase is consistent with the temperature scaling discussed before. The other low conductance peak or the LC-peak, located on the rise of the plateau, does not seem to be correlated with the 0.7 anomaly and has a width that is constant in gate voltage. Similar results is recently reported in n-GaAs QPCs [116].

The demonstrated correlation between ZBA and the temperature-dependence of the linear conductance supports a (Coulomb blockade plus) Kondo model of the 0.7

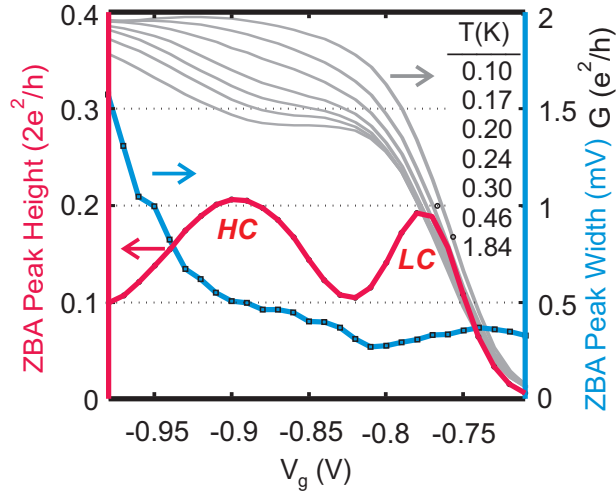


Figure 5.4: The height (red) and width (blue) of the zero bias anomaly as a function of the gate voltage at $T=100$ mK. The two peaks of the zero bias anomaly are denoted as high conductance (HC) peak and low conductance (LC) peak. On the same plot the temperature dependence of the linear conductance is shown (gray).

anomaly and suggests that the ZBA (HC-peak) originates from a peak in the density of states at the point A in Fig. 4.4c. It has been suggested that the LC-peak might also be connected to the ferromagnetic coupling of the two spins at the point B in Fig. 4.4c [102, 120].

5.2.5 Splitting of ZBA with B-field

Fig. 5.5a-f displays the splitting of the ZBA by application of moderate magnetic fields perpendicular to the 2DHG plane. A series resistance due to Shubnikov-de Haas (SdH) oscillations is subtracted from the data to keep the 1st plateau at $2e^2/h$. This technique is introduced in details in Appendix C. The splitting of the ZBA is visible already at $B_{\perp} = 0.5$ T. The splitting seems to be dependent on density (gate voltage) at this field in agreement with the recent results of Sarkozy et al. [114] in n-GaAs QPCs. At higher fields the splitting transforms to the Zeeman-split subband formed at e^2/h level. The 1st plateau shows an asymmetric bias-dependent feature at $V_{sd} = 0$ whose sign alternates in Fig. 5.5a-f. This alternation agrees with the maxima/minima of SdH oscillations in the two-terminal resistance of the 2DHG outside the QPC shown in Fig. 5.5g and it is most probably related to the leads.

We observe the splitting of both HC-peak (at $B=0.5$ T) and LC-peak (at $B=0.75$ T) in Fig. 5.5. However it is not straightforward to distinguish between a ZBA splitting and the Zeeman splitting of 1D spin subbands. Fig. 5.5h shows the gate-dependent linear increase of the splitting with the magnetic field. The quantitative comparison of this splitting with the expected spin splitting for a Kondo bound-state is however obscured in 2DHG systems by additional complication that confinements in hole

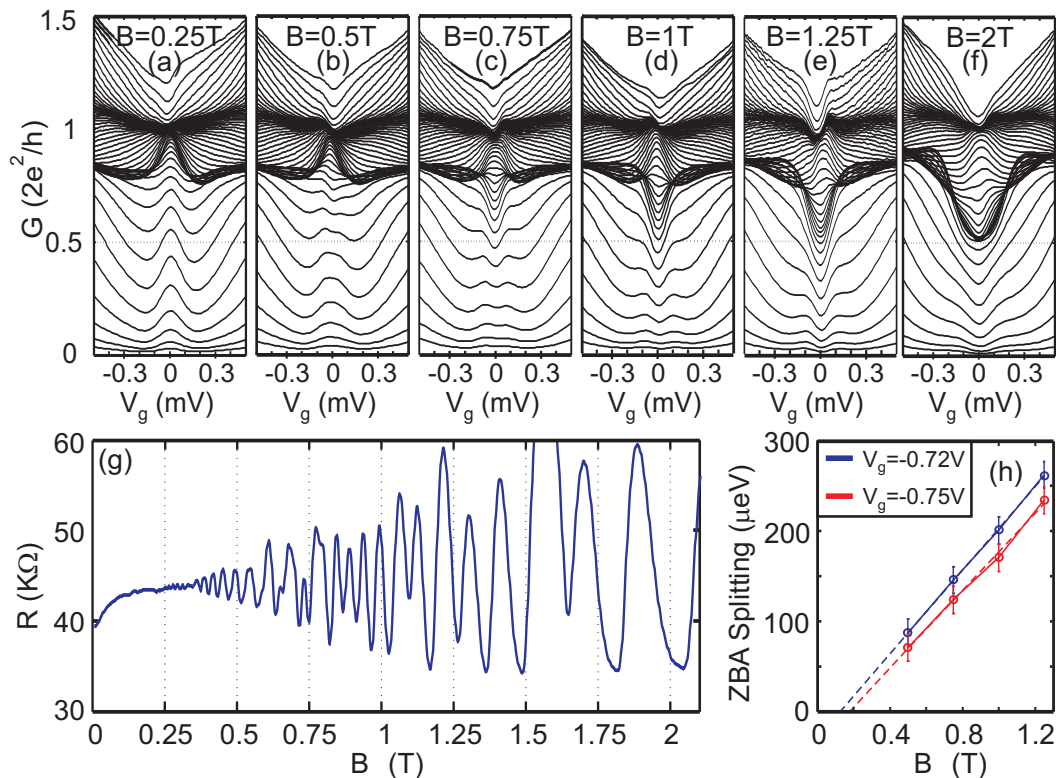


Figure 5.5: Splitting of the ZBA by application of perpendicular magnetic field (a-f). (g) the two terminal resistance of the 2DHG vs. perpendicular magnetic field suggest that the asymmetric shape of the dI/dV at $V_{sd} = 0$ on the 1st plateau in (a-f) is probably connected to the density of states of the leads. (h) ZBA splitting vs. magnetic field at two different gate voltages. Note that the linear fit does not cross zero and therefore the splitting is non-linear.

systems result in mixing the heavy hole and light hole bands and therefore the effective Zeeman splitting strongly depends on the geometry. As a result, the Landé g -factor in 2D, 1D and 0D are very different (see Chapter 7). Nevertheless a splitting of about $200 \mu\text{eV}$ can be read from Fig. 5.5h while the Zeeman splitting due to magnetic field perpendicular to the 2DHG is expected to be about $400\text{-}600 \mu\text{eV/T}$ as discussed in Chapter 7. Unfortunately the splitting of the ZBA with an in-plane magnetic field was not explored on this QPC because of experimental limitations. The observation of such splittings in another hole QPC is reported in Chapter 6.

5.2.6 Transconductance

The non-linear differential conductance of the QPC presented in Fig. 5.3b can be alternatively drawn as a function of V_{sd} and V_g in the color map plot of Fig. 5.6a which clearly demonstrates the subband structure of the constriction. The ZBA can be seen as a high conductance ridge around $V_{sd} = 0$. The dashed line marks

the border between HC and LC-peaks. The derivative with respect to the gate voltage, gives the transconductance plotted in Fig. 5.6b. Dark regions of the color map correspond to plateaus in g with the plateau values indicated in units of $2e^2/h$. The bright areas represent the transitions between adjacent plateaus. Note that the trench in between the finite bias 0.8 plateaus and the cusp-like feature at the low conductance side of this trench are the manifestation of the ZBA. The similarity between the hole QPC data of Fig. 5.6b to the n-type QPC data of Fig. 4.6b testifies the structural and electronic quality of the sample. However the form of the ZBA is different. It is a distinct feature of the 0.7 anomaly in holes that its extension in gate voltage is comparable to the extension of the 1st plateau (presumably due to the small subband energy spacing). This can also be seen in Fig. E.6c where the differential conductance of the QPC from Appendix E shows an extended ridge pointing to a strong 0.7 anomaly.

Fig. 5.6c shows the transconductance map at a higher temperature of 800 mK. The anomalous subband structure of the first subband is marked with green and blue dashed lines while the white dashed line is used for higher subbands. Note that while the ZBA has disappeared at this temperature, the anomalous subband structure persists and a clear (dark-color) gap characterizing the 0.7 plateau exist between the pinch off and the first plateau.

5.2.7 In-plane magnetic field-dependence

The in-plane g-factor of heavy holes in [001]-plane grown quantum wells is supposed to be zero [31]. Lateral confinement mixes heavy and light hole and results in a finite anisotropic g-factor. In Chapter 7 we will see that the g-factor in a QPC depends on the direction of the in-plane magnetic field with respect to the current. If they are perpendicular, the in-plane g-factor is the same as in 2D, i.e. zero.

The linear conductance of the QPC for different in-plane (and perpendicular to the current) magnetic fields from 0 to 13 T (with 0.5 T steps) measured at the base temperature of 100 mK is plotted in Fig. 5.7a. The 0.7 plateau is not present at low temperature and low magnetic fields up to about 5T. For higher fields a step splits from the 1st plateau and moves toward lower conductances but it starts to get faint at about 8T. Fig. 5.7b shows the same measurement performed at a higher temperature of 800 mK. Here the 0.7 plateau is present at low fields and for magnetic fields above 5T it lower its conductance and transforms to a small peak.

No subband spin-splitting is observed up to 13T for this direction of in-plane magnetic field. This can be seen in transconductance data presented in Appendix F. The fact that an in-plane magnetic field affects the 0.7 anomaly while it does not split the 1D subband questions a direct connection between the two effects. However, the spin-splitting of the 0D bound state can be very different than that of the observed 1D subbands.

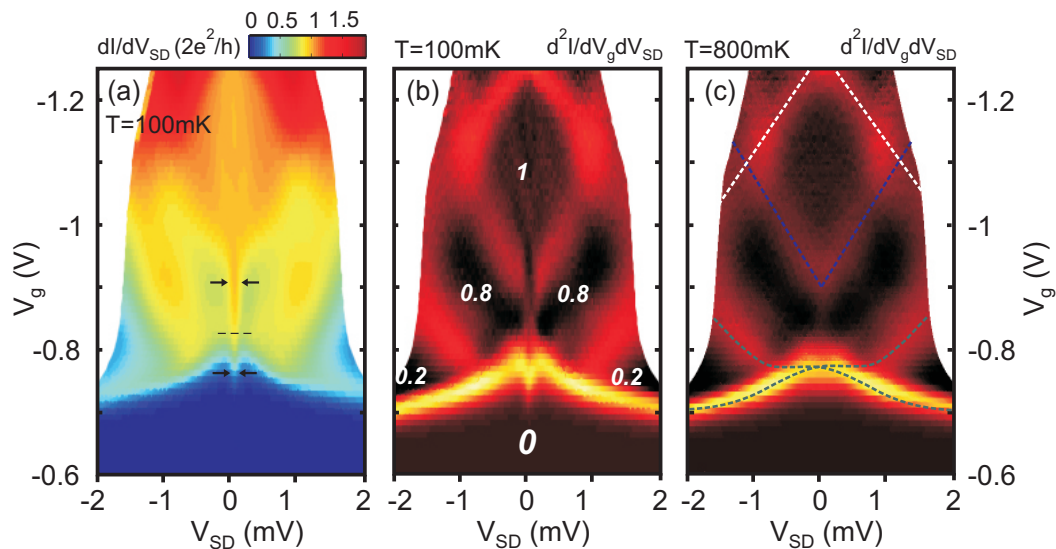


Figure 5.6: Finite bias spectroscopy of the QPC. (a) Differential conductance ($g = dI/dV_{SD}$) as a function of source-drain bias and the gate voltage at $T = 100$ mK. The arrows point to the extension of the zero bias anomaly in bias. (b) Transconductance (numerical derivative of g with respect to the gate voltage) at $T = 100$ mK. Dark areas are the plateaus in the conductance, whose conductance in units of $2e^2/h$ is indicated in the figure, and the bright regions are the transitions between plateaus. The zero bias wedge at the opening of the QPC and the gap that connects it to the first plateau are the signatures of ZBA in transconductance. (c) Transconductance at $T = 800$ mK without a sign of ZBA. The white dashed lines mark the normal second subband. The blue and green dashed lines mark the anomalous first subband.

5.2.8 Perpendicular magnetic field-dependence

Because of the small in-plane g -factor of heavy holes, the spin-degeneracy of the subbands is best lifted by applying the magnetic field perpendicular to the plane of the 2DHG. Fig. 5.8 shows the effect of such a magnetic field on the linear conductance of the QPC. Studies of the 0.7 anomaly in this particular magnetic field orientation are rarely reported [121]. This is mainly because the magnetic field perpendicular to the 2DHG acts on both spin and orbital degrees of freedom, obscuring the interpretation of the result. Within the QPC, the magnetic field results in Zeeman and diamagnetic shifts and in the leads, it causes the formation of the Landau levels which result in Shubnikov-de Haas oscillations of the resistance at low fields and relevance of quantum Hall physics at high fields. Here we employ magnetic fields up to $B_{\perp} = 13$ T in order to exploit localization phenomena which are potentially linked to the 0.7 anomaly.

These effects can be seen in the two-terminal and four-terminal conductances of the QPC at representative perpendicular magnetic fields of 0, 4, 7, 9 and 11 Tesla at a temperature of 800 mK in Fig. 5.8a,b. The conductance of the open QPC fluctuates wildly for different perpendicular magnetic fields. Most of these fluctuations come

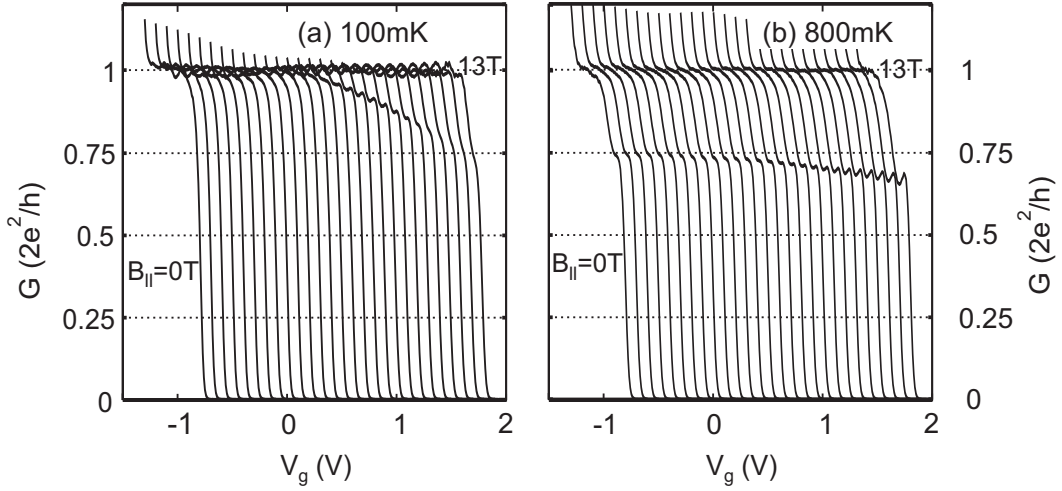


Figure 5.7: Effect of in-plane magnetic field (from 0 to 13 T with 0.5 T steps) on the linear conductance of the QPC at (a) $T = 100$ mK and (b) $T = 800$ mK. In both cases the conductance of the anomaly drops for the fields beyond about 5 T.

from the Shubnikov-de Haas oscillations in the resistance of the leads. These effects can be corrected for by subtracting a separately measured field dependent serial resistance from the total resistance after which the resulting conductance looks like the one shown in Fig. 5.8c,d. The agreement between the final result from the two-terminal and four-terminal measurements confirms the correction procedure and suggests that the observed conductance vs. gate result is related to the physics of the QPC and its connection with the leads. In the following we discuss the implications of these results. The correction procedure employed here is discussed in details in Appendix C.

5.3 0.7-feature and localization

Fig. 5.9 shows the corrected linear conductance for perpendicular magnetic fields from 0 to 13 Tesla and at temperatures of 100 and 800 mK. The Zeeman splitting of the spin-down subband can be seen in this figure as the shift of the conductance rise between 0.5 to $1(2e^2/h)$ toward higher energies (lower gate voltages) with increasing the perpendicular (to the plane) magnetic field. The anomalous 0.7 plateau in Fig. 5.9a,c gradually transforms to a region of suppressed conductance close to and after the first subband rise and a pronounced conductance peak emerges. Same development can be seen in the linear conductance at the lower temperature of 100 mK (Fig. 5.9b,d) however the 0.7 anomaly is lifted to the first plateau at zero field consistent with the temperature-dependence of the linear conductance (Fig. 5.1).

The similarity between the conductance peak at large magnetic field in these results and a Coulomb resonance in quantum dots suggests that perhaps the conductance peak at the rise of the half-plateau is a Coulomb resonance and conductance

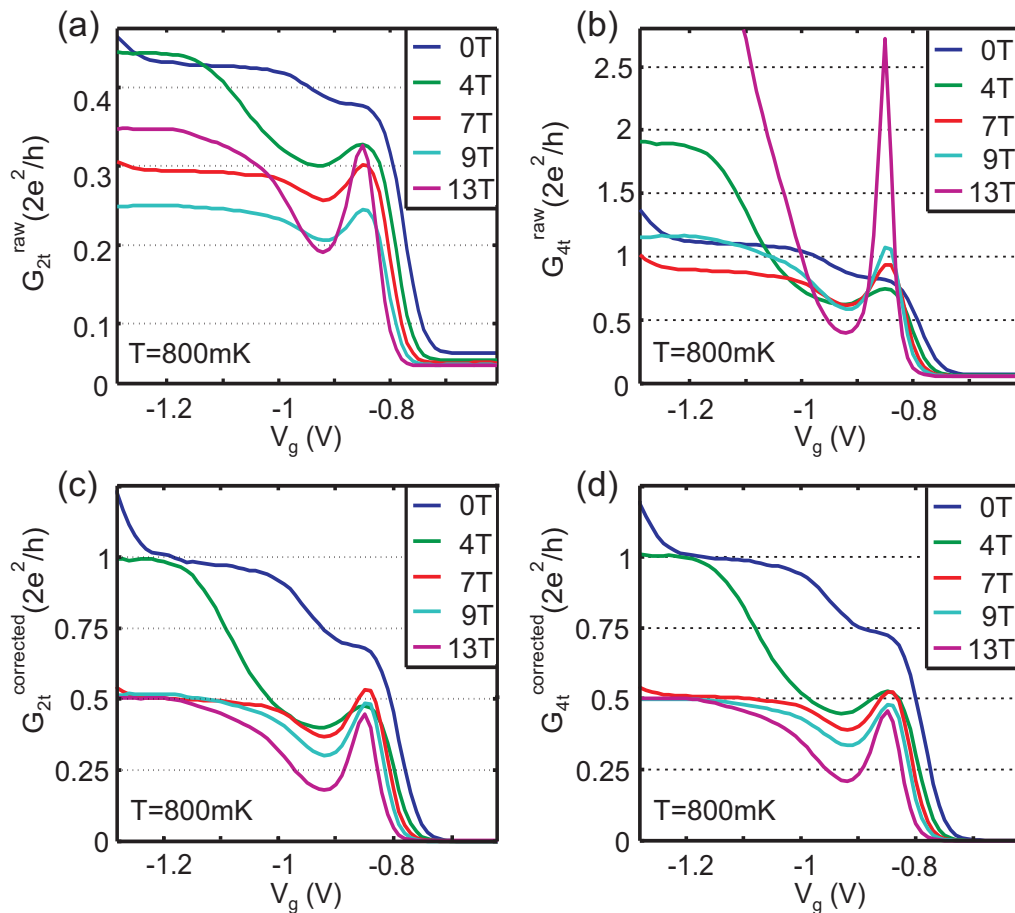


Figure 5.8: Linear conductance of the QPC vs. gate voltage for different magnetic fields at the temperature of 800 mK. (a) two-terminal and (b) four-terminal raw measurement results. (c) and (d) show the corresponding *corrected* result after accounting for the SdH oscillations in the leads.

suppression after opening of the channel is due to Coulomb blockade. A similar gradual transformation of the 0.7-feature to a conductance peak can be seen for another p-GaAs QPC in Appendix E.

5.3.1 Lateral shift of the channel

A resonance in the rise of the linear conductance, especially at large perpendicular (to the plane) magnetic fields, can have many different origins [56, 122, 123]. Such resonances usually arise from impurities in the QPC channel or deviations from a saddle point potential due to disorder. We will see in Chapter 6 that the lateral shift of the QPC channel is a powerful tool to distinguish between the generic effects of the QPC and those that strongly depend on the potential boundary and the impurity configurations. This lateral shift is achieved by applying asymmetric voltages to the two gates surrounding the channel.

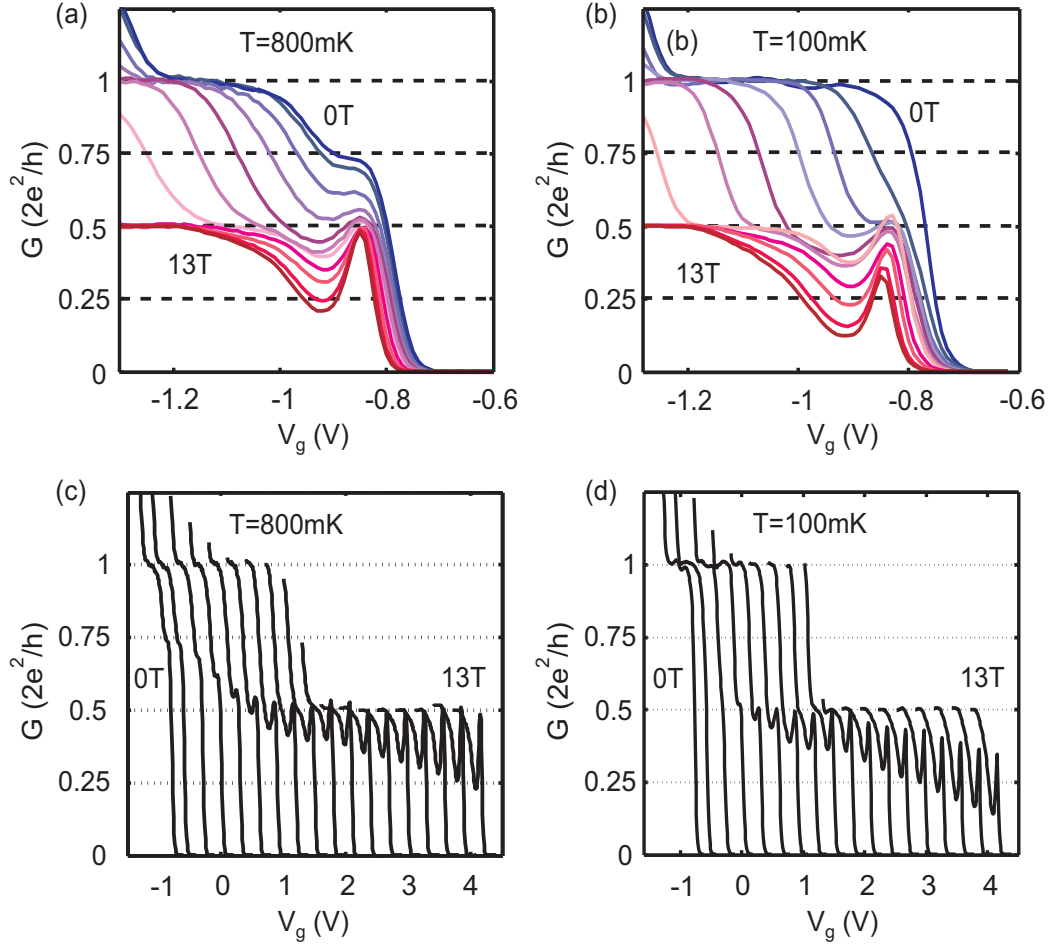


Figure 5.9: Linear conductance vs. gate voltage for different perpendicular magnetic fields at temperatures of (a) 800 mK and (b) 100 mK. The Zeeman splitting of the spin subbands can be seen as the gradual shift of the half-plateau toward higher energy (lower gate voltage) as the field is increased. The 0.7 anomaly in (a) transforms to a region of suppressed current, resulting in a conductance peak as the field is enhanced. (b) shows similar behavior but the 0.7-feature is masked at low temperature. (c) and (d) show the same data but the conductances are shifted horizontally for clarity. The peak clearly emerges from the 0.7 plateau in (c). The conductance traces are cut because of limited gate regime to avoid leakage.

Fig. 5.10a shows a colormap of the linear conductance of the QPC as function of the in-plane gates at a temperature of 1.7 K. Two new axes ΔV and V_g are defined in this figure as the symmetric and asymmetric combination of the two gate voltages by a rotation of axes.

$$\begin{pmatrix} \Delta V \\ V_g \end{pmatrix} = \begin{pmatrix} \cos \theta & -\sin \theta \\ \sin \theta & \cos \theta \end{pmatrix} \begin{pmatrix} V_{G1} \\ V_{G2} \end{pmatrix} \quad (5.1)$$

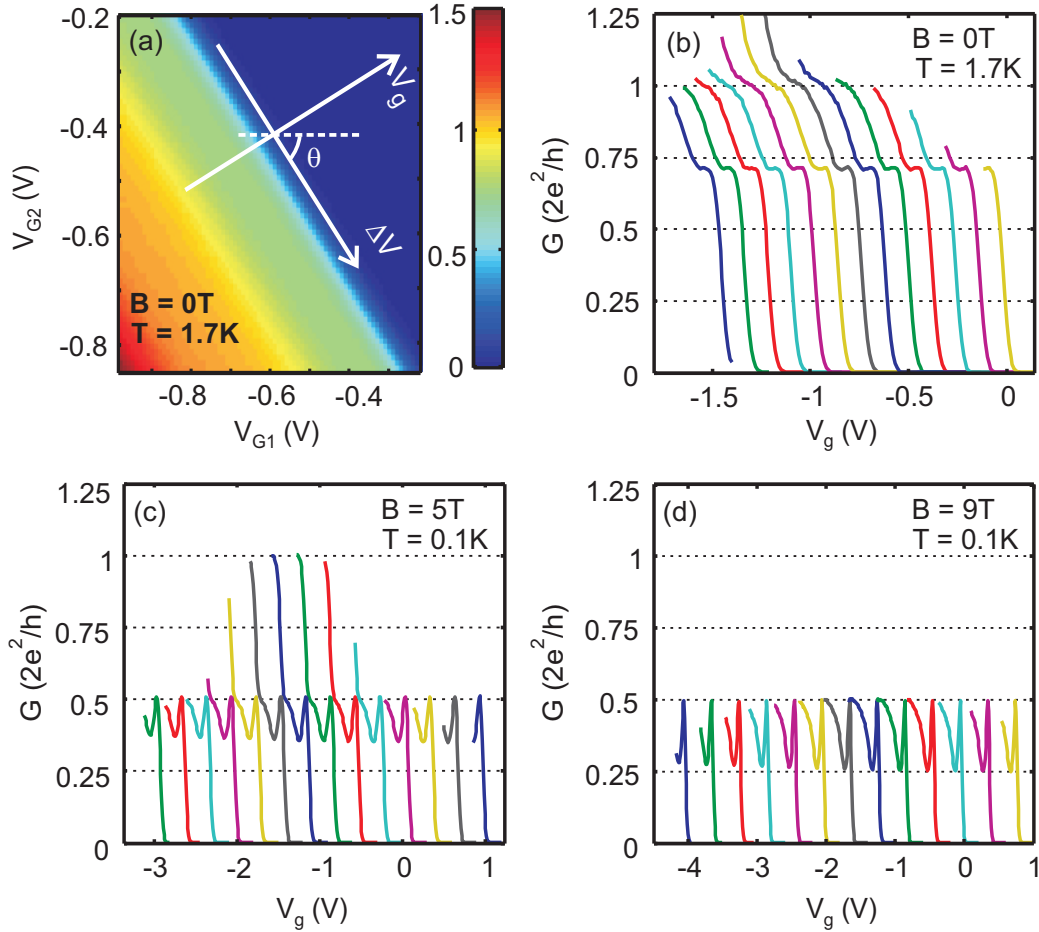


Figure 5.10: (a) Linear conductance of the QPC in unit of $2e^2/h$ as a function V_{G1} and V_{G2} . The two new axes of V_g and ΔV are defined as the symmetric and anti-symmetric combination of the two gate voltages along and perpendicular to equi-conductance lines. (b)-(d) Linear conductance G as a function of V_g at selected magnetic fields of $B = 0$ T, $B = 5$ T and $B = 9$ T, respectively. The temperature is $T = 1.7$ K for $B = 0$ T and $T = 100$ mK for the finite field data. Each conductance curve corresponds to a different ΔV value ranging from $\Delta V = -0.35$ V (leftmost trace) to $\Delta V = 0.37$ V (rightmost trace) on panel (b), from $\Delta V = -0.35$ V to $\Delta V = 0.3$ V for (c) and from $\Delta V = -0.4$ V to $\Delta V = 0.2$ V on panel (d). The individual traces are horizontally shifted for clarity. Note that the accessible conductance regime is limited due to leakage to the side gates.

The density of carriers in the channel can be tuned by V_g , while ΔV is responsible for the lateral shift of the channel perpendicular to the current direction. From the geometry of the sample this lateral shift is estimated to be around 8-10 nm/V [124]. As the effective Bohr radius a_B^* which is an estimate of the size of impurities is in the order of 1-2 nm in p-GaAs, this range covers a sufficiently large region to exclude impurity resonance effects.

Fig. 5.10b shows the linear conductance vs. V_g for different ΔV at zero field and a high temperature of 1.7 K. Fig. 5.10c,d shows similar measurements at the base temperature of 100 mK with the perpendicular magnetic fields of 5 and 9 Tesla respectively. Both zero field 0.7 plateau in b and high field conductance peak in c and d are robust against lateral shift of the channel. The smooth transition of the $0.7(2e^2/h)$ plateau into a Coulomb resonance peak with increasing magnetic field has been found to be also robust against thermal cycling. Therefore we conclude that the conductance peak is a generic feature of the QPC and is not related to any impurity or potential imperfection in the sample.

5.3.2 Finite bias spectroscopy at finite magnetic field

Further support for the mentioned hypothesis about the origin of the conductance resonance comes from finite bias measurements of the differential conductance. The evolution of the differential conductance by varying the perpendicular magnetic field is demonstrated in Appendix D. The ZBA visible in Fig. 5.6a disappears quickly with increasing B_\perp -field and transforms to a diamond-like region of suppressed conductance above 8 Tesla as shown in Fig. 5.11b. Note that the resonance has a lever arm with both source and drain and therefore it is located between the two. The diamond-like region of suppressed conductance has a striking similarity to a Coulomb diamond in a quantum dot. A similar Coulomb diamond-like shape in the large field differential conductance can be seen in Appendix E for another QPC.

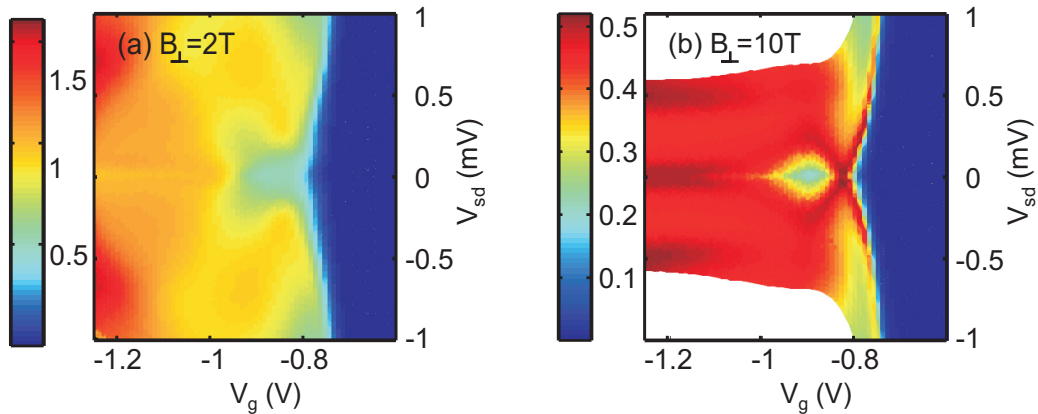


Figure 5.11: Finite bias spectroscopy at finite perpendicular magnetic field for (a) $B_\perp = 2$ T and (b) $B_\perp = 10$ T. Note that these plots are turned 90° with respect to Fig. 5.6a to facilitate the comparison with linear conductances in Fig. 5.9.

5.3.3 Coulomb blockade as the origin of the 0.7 anomaly

The evidences that are provided so far suggest that the conductance resonance developed at large perpendicular magnetic field can have a Coulomb blockade origin. The

smooth evolution of the 0.7 plateau to this resonance over a large range of magnetic fields (and filling factors in the leads) and on the same gate voltage range implies that a common origin must be involved for both of these phenomena. Therefore the suppression of the zero-field conductance of a QPC from $2e^2/h$ to $0.7(2e^2/h)$ is probably due to Coulomb blockade-like effects by a quasi-bound state. Having established this picture, a Kondo model naturally arises at low temperatures since the mentioned quasi-bound state has a strong coupling to the leads. This is an important result as the quasi-bound state assumed in Kondo-model explanations of the 0.7 anomaly has never been directly observed in the experiment.

In the following we speculate on the transition between the zero-field anomalous 0.7-feature and the conductance resonance at large perpendicular magnetic fields. First we point out that the SDFT calculations (presented in section 4.4) suggest that Friedel oscillations are responsible for the formation of the quasi-bound state. These oscillations are shown to be modified due to orbital effects of a perpendicular magnetic fields. As a result the coupling of the quasi-bound state with the leads is expected to decrease by increasing the magnetic field. This coupling in our data is extracted by a coupling-broadened Coulomb resonance fit to the conductance traces measured at large magnetic fields. In the end we provide a possible picture of the origin of the Coulomb resonance in the quantum Hall regime.

5.3.4 Friedel oscillations

The motion of particles in a hole liquid is highly correlated. On a mean-field level the bare potential of the quantum point contact is modified due to screening, exchange and correlation effects of the other holes. This was discussed in section 4.4 and it was pointed out that according to SDFT calculations, Friedel oscillations in a 2DEG can change the bare saddle point potential to support a resonant quasi-bound state [97, 102]. The amplitude of the Friedel oscillations around a test impurity is modified at large perpendicular magnetic fields as shown in Fig. 5.12 [125]. The nearest oscillation is largely enhanced with decreasing the filling factor (the Landau levels occupancy) in expense of oscillations further apart. This can be understood since at large magnetic fields the wavelength distribution of the holes is reduced to the magnetic length and its multiples depending on the filling factor. Holes can contribute to screening only at these specific wavelengths leading to larger oscillations independent of the dimensionality. For the quasi-bound state, a perpendicular magnetic field acts not only on the spin degree of freedom but also on the orbital part of the resonant wavefunction, shrinking it as the magnetic length decreases with $\propto 1/\sqrt{B}$. Due to this combined orbital effect and the enhanced Friedel oscillations, the coupling of the quasi-localized state to the source and drain is expected to decrease and the localization of the holes in the lower-lying spin subband becomes more prominent. It is noteworthy that according to Rensink [125] the amplitude of the Friedel oscillations is proportional to the effective mass of the screening carriers and stronger localization is expected for holes with an 8 times larger effective mass

compared to electrons.

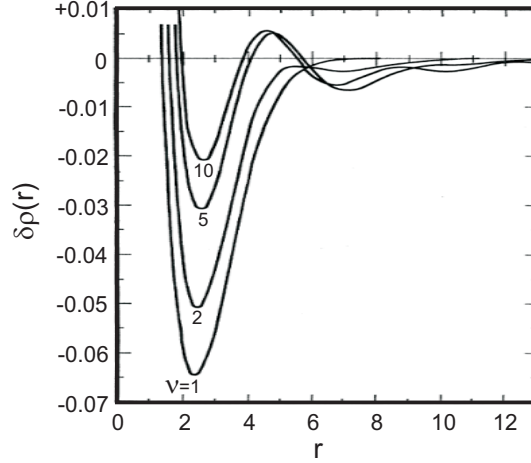


Figure 5.12: The electron density modulation near an impurity vs. distance from the impurity for different filling factors in the bulk adapted from [125]. The first dip in the density oscillations is enhanced at lower filling factors in expense of the other oscillations.

5.3.5 Coulomb peak fitting to the resonance line shape

The suppression of coupling of the bound state to the leads can be quantified by a simple empirical model. Here we show that the linear conductance traces at large perpendicular magnetic fields can be fit with a Lorentzian peak superimposed on a saddle point potential background. Based on Landauer formula (Eq. 2.42) the linear conductance can be calculated using

$$G(\mu, V_g) = e^2/h \int_{-\infty}^{+\infty} T(E, V_g) \left(-\frac{\partial f_{\beta}(E - \mu)}{\partial E} \right) dE \quad (5.2)$$

The transmission $T = T_{saddle} + T_{Fano}$ is assumed to be composed of two parts

$$T_{saddle}(\epsilon_s) = \frac{1}{1 + \exp(-2\pi\epsilon_s)} \quad (5.3)$$

$$T_{Fano}(\epsilon_p) = \frac{1}{1 + q^2} \frac{(q + \epsilon_p)^2}{1 + \epsilon_p^2} \quad (5.4)$$

The first part gives the transmission of a saddle-point potential [71] of the form $V(x, y) = V_0 - 1/2m\omega_x^2x^2 + 1/2m\omega_y^2y^2$ and the second part is the transmission of an asymmetric resonant line shape. This type of line shape can appear due to the so-called Fano effect which is the interference between two channels, one with a continuous spectrum and the other one with a discrete spectrum [1]. The parameter $q = -\cot \phi_F$ with ϕ_F being the phase difference between the two paths controls

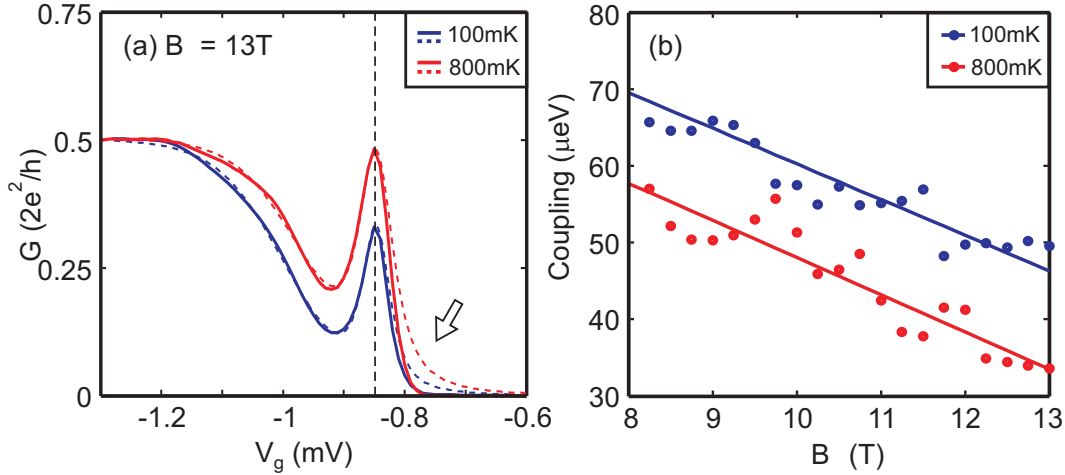


Figure 5.13: (a) Linear conductance measurement (solid) and the fit (dashed) at 13 T at the temperatures of 100 and 800 mK. Note that the peak is asymmetric around the vertical dashed line. The white arrow points to the part where the peak shows deviation from Lorentzian line shape. (b) The coupling constant extracted from the fits like the one in (a) as a function of magnetic field for 100 and 800 mK. The coupling decreases with increasing magnetic field. The solid lines have slopes of $d\Gamma/dB = -4.6$ and $-4.8 \mu\text{eV}/\text{T}$ for blue and red respectively.

the asymmetry of the lineshape. The energy and gate voltage dependence of the transmissions T_{saddle} and T_{Fano} is contained in $\epsilon_s = (E - E_s(V_g))/\hbar\omega_x$ and $\epsilon_p = (E - E_p(V_g))/\hbar\Gamma$ respectively. The parameter Γ is the coupling broadening of the resonant peak that we wish to extract. Both energies E_p and $E_s = V_0 + \hbar\omega_y(n + 0.5)$, for the first spin-split subband ($n = 0$), are assumed to be linearly dependent on the gate voltage

$$E_{s,p}(V_g) = E_{s,p}^0 + C_{s,p}V_g \quad (5.5)$$

Fig. 5.13a shows two examples of the fitting to the measured linear conductances at 13 Tesla. The Fano parameter q was found consistently larger than 100 resulting in a very symmetric Lorentzian line shape [1] of the form $T_{Fano} = (1 + \epsilon_p^2)^{-1}$. This is reassuring since if transport is through a generic Coulomb blocked resonance we expect no parallel channel for the current. It must be mentioned that with the parameters left, there are several redundancies in the model. The width of the saddle point conductance rise vs. gate voltage is given with both ω_x and C_s and the width of the Lorentzian peak is given by both Γ and C_p . The capacitances can be approximately extracted from zero field and large field finite bias spectroscopy data. The temperature was plugged in from the measurement and Γ and ω_x were extracted from the fitting.

Overall the fitting works quite well, apart from the fact that the measured peak is very asymmetric with respect to the dashed symmetry axis shown in the figure. The white arrow points to the deviation between the model and the data. Such an asym-

metry may arise however due to the self-consistent nature of the quasi-bound state that is probed. Fig. 5.13b shows the coupling constant of the impurity extracted from the fit. The coupling decreases by increasing the perpendicular magnetic field (the peak gets narrower) as expected. Also please note that the coupling seems to be temperature-dependent, possibly due to a temperature-dependent screening.

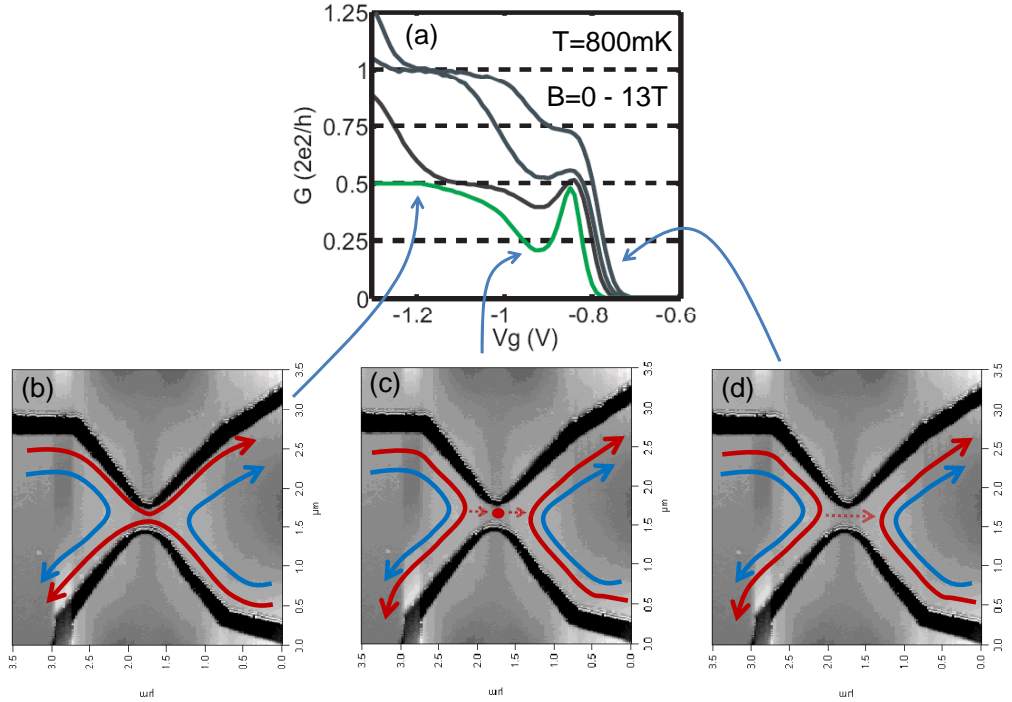


Figure 5.14: (a) The evolution of the 0.7 anomaly in linear conductance to a conductance peak with perpendicular magnetic field (b-d) Schematic of edge states at different gate voltages.

5.3.6 Coulomb resonance in the quantum Hall regime

At large perpendicular B-field the holes are forced to propagate along edge states. When the QPC is closed, the edge states do not percolate and are decoupled in the source and drain, the only current being due to the tunnelling between outermost edge states in two sides (Fig. 5.14d). As the gate voltage is lowered, the edge states penetrate inside the potential hill of the QPC from the two sides. Therefore the density increases in the QPC and the Fermi wavelength is decreased until half of the Fermi wavelength fits inside the QPC. This happens presumably at the apex of the peak in the linear conductance (the green curve in Fig. 5.14a). Since the Fermi wavelength is a measure of separation of the holes, at this point the intra-channel interaction starts to dominate over the kinetic energy and further tunnelling of the holes is blocked due to Coulomb blockade (Fig. 5.14c). Coulomb blockade is the

main reason for the region of suppressed conductance after the peak. Note that in the QHE regime the leads can play the role of reservoirs for the localized state. As the gate voltage is further decreased, Coulomb energy is overcome, the continuum of states at higher energy are reached, the edge states merge together, and current flows through the QPC (Fig. 5.14b). This scenario suggests a different picture on the two sides of the conductance peak apex and therefore supports the observed asymmetry mentioned in the previous section.

5.4 Summary

Transport measurements on a high quality p-GaAs QPC exhibiting a strong 0.7 anomaly are presented. The 0.7 anomaly is investigated in detail using linear conductance and finite bias spectroscopy at different field orientations. It is shown that the 0.7 plateau gradually transforms to a strong resonance peak in the linear conductance by applying a magnetic field perpendicular to the 2DHG. This resonance is accompanied by a diamond-like region of suppressed finite bias differential conductance very similar to a Coulomb diamond in quantum dots. Coulomb blockade-like effect by a quasi-bound state is therefore suggested as the origin of this conductance peak and the 0.7 anomaly which is its low-field precursor. Possible explanations for the emergence of the peak at large perpendicular magnetic field are discussed.

The experiment results presented in this chapter suggest the presence of a quasi-bound state in quantum point contacts and support the idea that the 0.7 anomaly can be understood based on Coulomb blockade and Kondo physics. It would be interesting to repeat this experiment in electron QPCs in n-type GaAs systems to see if perpendicular magnetic field leads to a similar effect.

Chapter 6

Impurities in the QPC

6.1 Introduction

We saw in chapter 4 that the 0.7 anomaly is associated with a number of qualitative features in linear and non-linear conductance. In the last chapter we introduced a generic effect in a QPC exhibiting a standard 0.7 anomaly which has been observed in many other hole QPCs. In this chapter we study another hole quantum point contact in sample *A3.10.2* which also exhibits a very clear conductance anomaly, however a closer investigation of its properties especially the temperature dependence of the linear conductance differs from a standard 0.7 anomaly. Moreover by comparing the signatures of the anomaly with a number of toy-models we are able to understand the origin of the observed anomalies and find qualitative agreement with measurements. What is interesting here and what makes it of general relevance is that this is one of the rare cases where such an understanding and thereby differentiation of the anomalies is possible. And it points to the difficulties of distinguishing between channel imperfections and the generic 0.7 anomaly. Furthermore, the results presented here suggests both the coexistence and the interplay between the impurity and the 0.7 anomaly in this sample and testifies the local origin of the zero bias anomaly. This sample has been cooled down 5 times and the features discussed in this chapter have always been qualitatively reproduced. *

6.2 Temperature-dependence

Fig. 6.1 shows the linear conductance of the QPC as a function of the symmetric voltage applied to the surrounding gates measured at temperatures from 100 mK to 600 mK. In contrast to the QPC discussed in the previous chapter (and similar to the QPC shown in Appendix E), here there is an anomalous plateau at $0.75(2e^2/h)$ visible even at the base temperature. By increasing the temperature the conductance of the plateau decreases to around $0.65(2e^2/h)$ in accordance with the corresponding

*Valuable discussions with Y. Meir and S. Ulloa are appreciated.

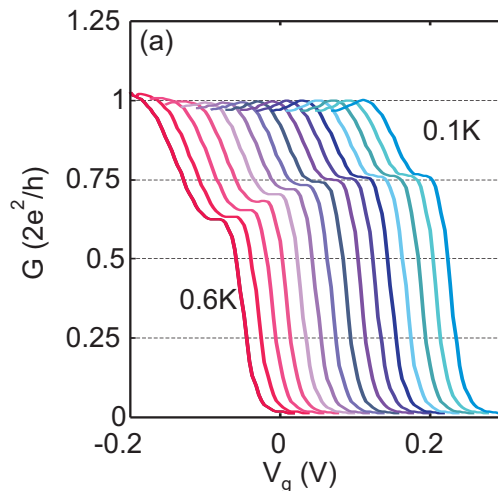


Figure 6.1: Temperature-dependence of the conductance anomaly from 0.1 K (right) to 0.6 K (left). The conductance of the anomaly decreases with increasing the temperature but it does not get stronger. The measurement was performed at $\Delta V = +113$ mV (see Fig. 6.3a). Curves are shifted horizontally for clarity.

data in the literature [83]. The full length of the first plateau cannot be seen in the figure as the gate voltage range is limited by the leakage.

6.3 Magnetic field-dependence

Fig. 6.2a,b shows the effect of in-plane and perpendicular magnetic fields respectively on this anomaly. The effect of perpendicular magnetic field is qualitatively different than the one discussed in previous chapter.¹ As the field increases, the conductance of the anomalous feature gradually decreases but instead of transforming to a half-plateau it crosses $0.5(2e^2/h)$ and saturates around $0.4(2e^2/h)$. At higher fields of around 4 Tesla a separate and seemingly independent plateau appears at $0.5(2e^2/h)$. We have paid extra attention to make sure that the precise value of the large-field conductance of the anomalous plateau does not come from our resistance subtraction method. Furthermore similar result can be seen in Fig. 6.2a under the influence of an in-plane magnetic field, applied perpendicular to the current direction.² As a reminder the g-factor of holes in 1D structures in this particular direction is strongly suppressed as will be discussed in chapter 7 (see also [126]). The difference between Fig. 6.2a and b arises due to the lower value of the in-plane g-factor but the essence of the effect, the fact that the anomalous feature crosses the conductance of the half-plateau, can be seen in both. The features that are present for an in-plane

¹Here also a field-dependent series resistance is subtracted from the measured data which was confirmed to be consistent with the Shubnikov-de Haas (SdH) oscillations in the leads.

²In order to do measurements with in-plane magnetic field the sample was warmed up and cooled down with the new orientation.

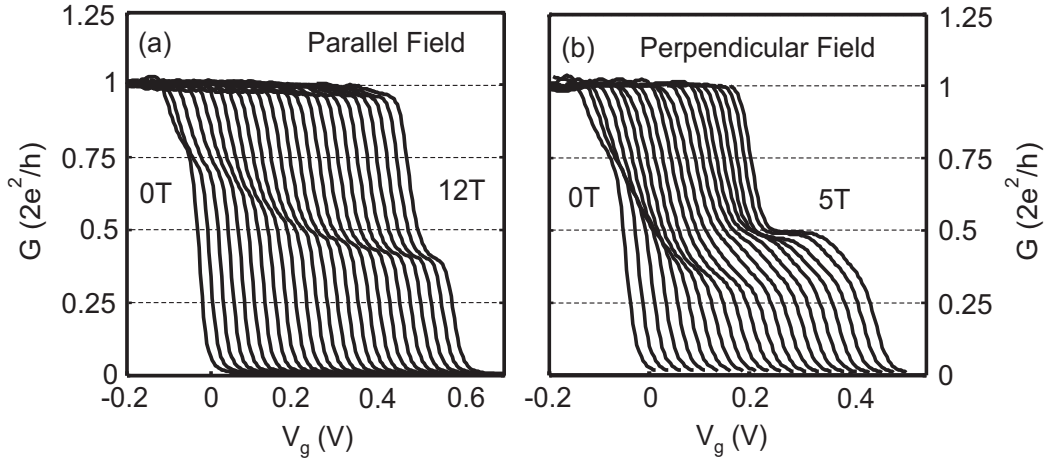


Figure 6.2: Effect of (a) in-plane and (b) perpendicular-to-the-plane magnetic field on the linear conductance of the QPC. The steps in the two cases are 0.5 and 0.25 Tesla respectively. The curves are shifted horizontally for clarity. For perpendicular case a gate-independent and field-dependent series resistance is subtracted which was checked to be due to the SdH oscillations in the leads as discussed in details in previous chapter. (Both measurements are with $\Delta V = +113$ mV)

field of 12 Tesla, are already developed at the perpendicular field of about 2.5 Tesla. From this we estimate a ratio of ≈ 5 for the two corresponding g -factors. Therefore in order to study this effect we will focus on the perpendicular magnetic field from now on.

6.4 Lateral shift of the channel

By employing an asymmetric combination of the voltages applied to the two gates it is possible to shift the quantum point contact laterally as discussed in chapter 5. Fig. 6.3a shows the linear conductance of the QPC as a function of the voltages applied to $G1$ and $G2$. There are two charge re-arrangements induced by the gate $G2$ shown in the figure by black arrows. Two new axes of V_g and ΔV are introduced as the symmetric and asymmetric combination of $G1$ and $G2$ with a rotation of axes as introduced before. The edge of the anomalous plateau is marked with dashed green line and is not parallel to the conductance edge. Therefore this plateau strongly depends on ΔV . This can be seen on the left-most curve of Fig. 6.3b-d where the zero-field conductance of the QPC is shown for different asymmetric voltages ΔV . While the anomalous feature at $0.75(2e^2/h)$ is present for positive ΔV in b and c it is absent for negative ΔV in d. The effect of perpendicular magnetic field for these three asymmetric gate configurations confirms that while b and c are very similar to Fig. 6.2b discussed before, the half-plateau in d appears suddenly at fields of around 4 Tesla independent of the asymmetric gate configuration.

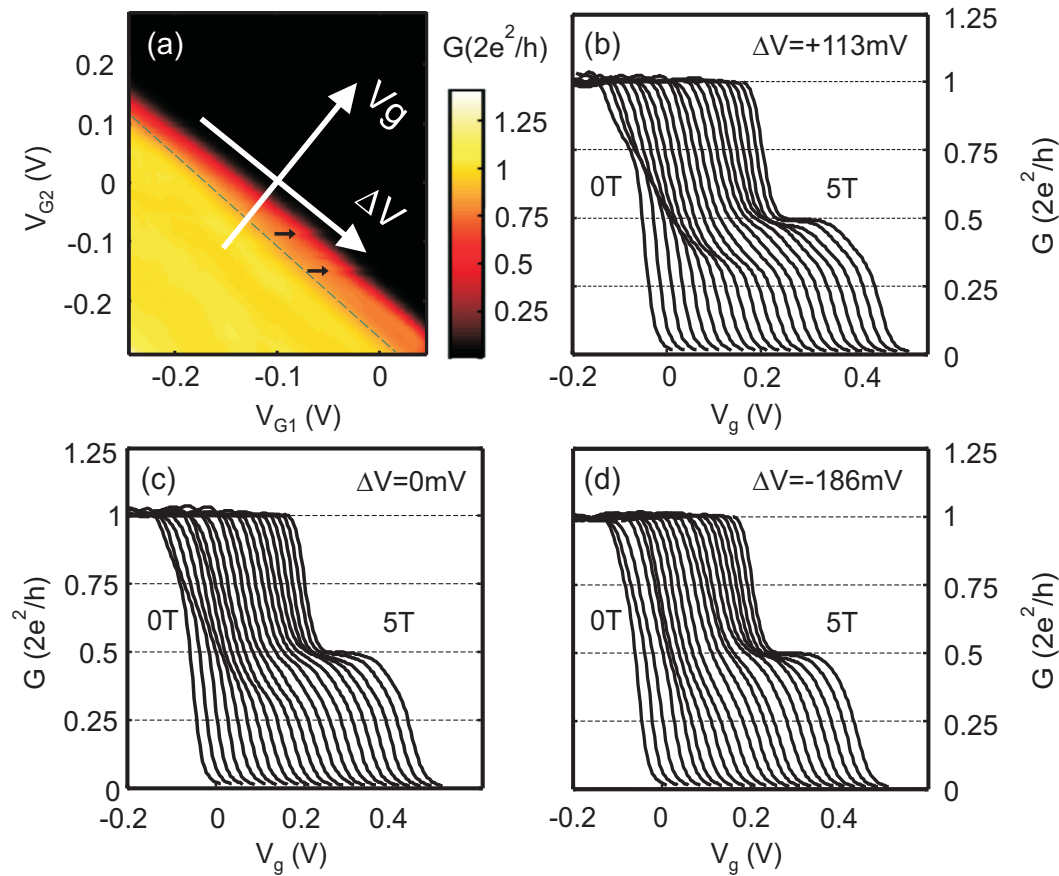


Figure 6.3: Effect of lateral shift of the channel on the linear conductance. (a) Linear conductance as a function of the voltage applied to G_1 and G_2 at $T=100$ mK. Two new axes of V_g and ΔV are defined as the symmetric and asymmetric combination of these voltages and make an angle $\theta = 35^\circ$ with the old axes (see Eq. 5.1). The anomalous plateau is marked with a green dashed line. Two charge re-arrangements induced by V_{G_2} are marked with arrows. (b)-(d) Linear conductance vs. V_g for different voltage asymmetries $\Delta V = +113, 0$ and -186 mV. Each plot shows the effect of perpendicular magnetic field for 0 to 5 Tesla. Curves are shifted for clarity.

This measurement imply that the anomalous feature observed in this QPC has a strong dependence on the lateral position of the channel and therefore seems to be due to impurities and/or potential imperfections in the channel.

6.5 Finite bias spectroscopy

The non-linear differential conductance dI/dV of the quantum point contact is shown in Fig. 6.4a,b at 600 and 100 mK respectively. These two measurements were performed along different directions of the gate configuration: the former along $\Delta V = 0$ and the latter along $V_{G_1} = V_{G_2}$. They both have the distinct feature that

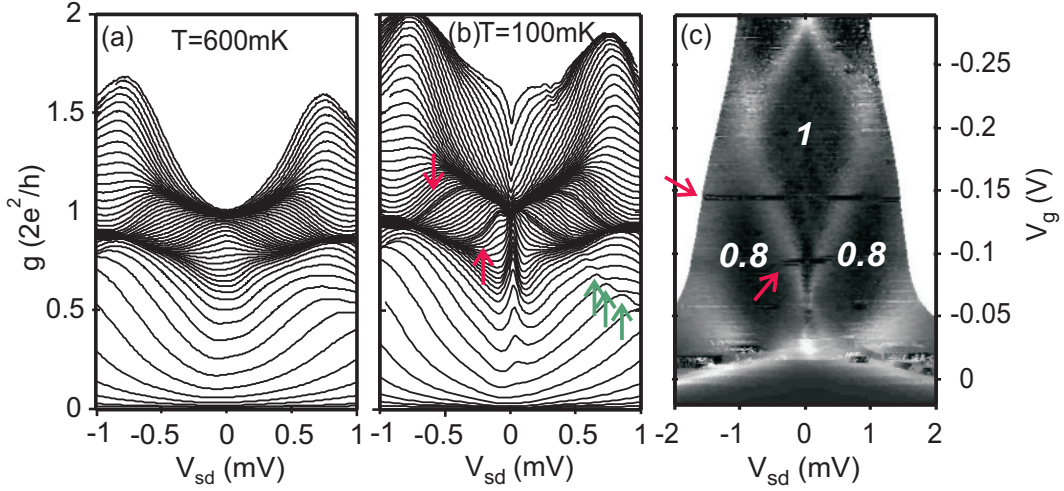


Figure 6.4: (a) and (b) Non-linear differential conductance $g = dI/dV$ as a function of bias voltage for different gate voltages at 600 mK and 100 mK. The first plateau has an upward slope with V_{SD} in both cases. In (b) this upward slope is more extreme and linear and a peak at zero bias is also evident. The dI/dV have a clear accumulation, called bunching here, around two gate voltages shown with red arrows. These bunchings are also visible in the transconductance, numerical derivative of g with respect to the gate voltage $d^2I/dVdV_g$ shown in (c). (a) and (b) were measured along $\Delta V = 0$ and $V_{G1} = V_{G2}$ respectively. This means that ΔV was changed 64 mV during the gate sweep in the later case.

the first plateau shifts to higher conductances by increasing the bias. This upward shift is more extreme and becomes a linear bias dependence at the base temperature (b). The emergence of an asymmetric zero bias anomaly (ZBA) at the base temperature challenges our conclusion in previous section about the connection of the anomalous feature with the 0.7 anomaly. Numerical differentiation of dI/dV_{SD} in Fig. 6.4b with respect to the gate voltage gives the transconductance plotted in a gray-scale color map in Fig. 6.4c. The transconductance confirms the subband structure of the point contact confirming the ballistic transport through the QPC. Two charge re-arrangements marked with red arrows, visible in this figure are also seen in the differential conductance of Fig. 6.4b (again marked with red arrows). However these re-arrangements happen on the first plateau and do not affect the conductance anomaly discussed here.

6.5.1 Zero bias anomaly

As expected the shape of the ZBA³ also depends on ΔV and changes by the lateral shift of the channel. Fig. 6.5 shows a zoom into low bias part of the differential conductance for various values of ΔV . While for negative ΔV (Fig. 6.5a) a clean

³Only one ZBA was observed for this QPC and the width and amplitude of this ZBA was monotonic with gate voltage.

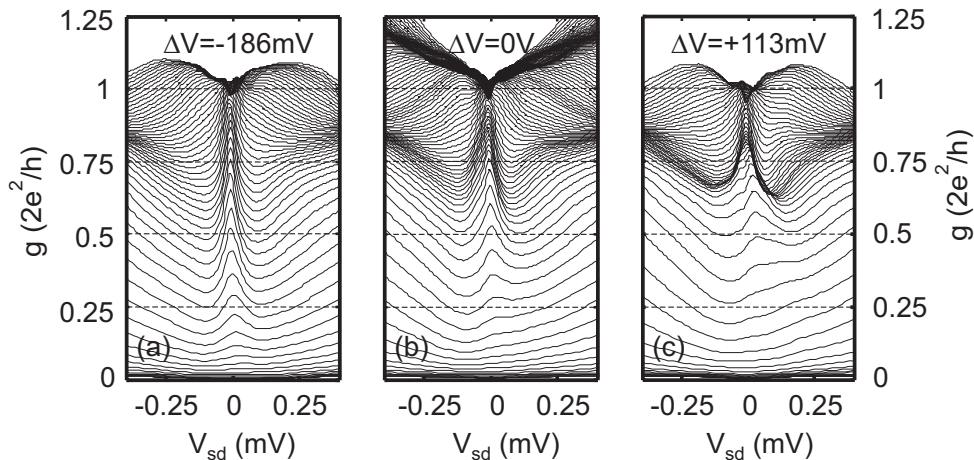


Figure 6.5: Effect of lateral shift of the channel on the ZBA. A zoom into low-bias ZBA at $\Delta V =$ (a) -186 mV, (b) 0 and (c) $+113$ mV. The ZBA is symmetric in (a), it gets asymmetric in (b) and splits in (c). A bunching of several dI/dV -curves develops around the ZBA toward positive ΔV .

and isolated zero bias anomaly is observed from pinch-off to the first plateau, it becomes slightly asymmetric for $\Delta V = 0$. At the same time several dI/dV -curves at different gate voltages get closer in the conductance. At positive asymmetric of $\Delta V = +113$ mV the ZBA is split into two peaks and a bunch of dI/dV curves have approached together and created a plateau-like structure that follows the shape of a zero bias peak. Note that the ZBA is more symmetric above the plateau.

As discussed before and will be shown in more details later, a zero bias peak can have non-Kondo origin. To see whether the ZBA observed here is related to the Kondo effect, we investigate the effect of an in-plane magnetic field on the splitting of the peak in Fig. 6.6a,b. Here negative ΔV is chosen for which the ZBA is symmetric. The single peak at zero field splits at $B_{\parallel} = 2$ T and the splitting grows further at $B_{\parallel} = 4$ T. The peaks are marked with small red arrows. This splitting of the ZBA can be compared to the Zeeman splitting of the subbands extracted from the width of the half-plateaus as discussed in chapter 7. The latter shown in Fig. 6.6c shows a factor of 4 between the in-plane and perpendicular to the plane g-factors which more or less agrees with our estimation before. The splitting of the ZBA is clearly gate dependent but it approximately agrees with the in-plane (perpendicular to the current) g-factor of the 1D subband.

6.6 QPC Simulations

The measurement results presented in this chapter bring about the following puzzle: There is an anomalous plateau at the opening of the first subband at the conductance of about $0.75(2e^2/h)$. This feature has a temperature dependent behavior that is generic of the typical 0.7 anomaly reported in the literature [81–83]. The feature is

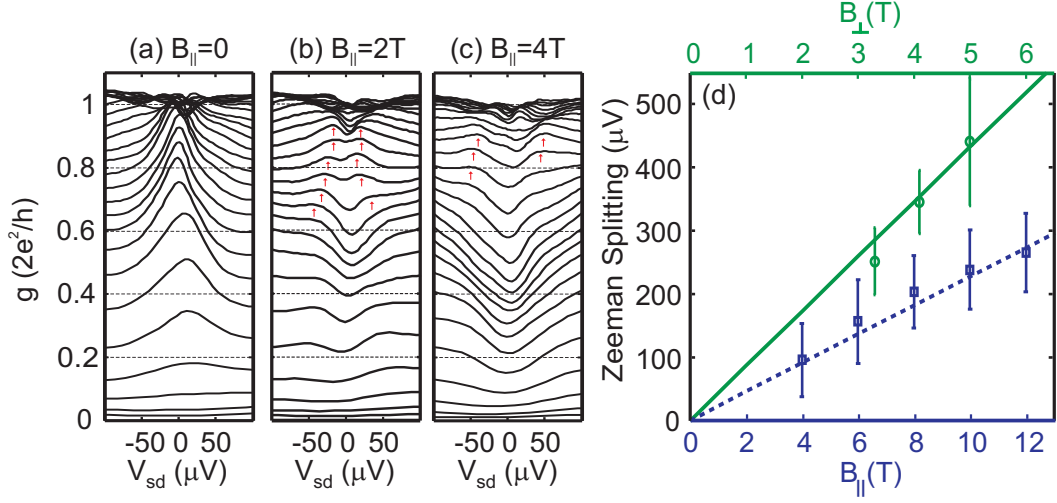


Figure 6.6: (a)-(c) The ZBA splits by application of an in-plane magnetic field (perpendicular to the current direction). The split peaks are marked with red arrows. The splitting depends on the gate voltage. (d) A comparison of 1D subband splitting due to in-plane and perpendicular-to-the-plane magnetic fields in this sample.

accompanied by a zero bias peak in dI/dV that disappears at high temperature and splits with increasing in-plane magnetic field. These are all signatures of a classical 0.7 anomaly. However there are two discrepancies compared to common 0.7 anomalies: first, by applying an in-plane magnetic field our anomalous feature gradually falls in conductance, crosses the $0.5(2e^2/h)$ and saturates around $0.4(2e^2/h)$. At larger fields the seemingly independent half plateau emerges due to Zeeman splitting of spin-degenerate subbands. Were we confident about the 0.7 anomaly, this could have suggested that the 0.7 anomaly and the subband spins are *independent*. But the fact that the anomalous plateau can get turned on and off by tuning ΔV and lateral shift of the channel, suggests that it is not an intrinsic effect of the QPC and depends on the details of the channel potential. To resolve this puzzle we have performed simple simulations of the effect of different impurities and potential imperfections on the QPC characteristic using Landauer-Buttiker formalism.

6.6.1 Ideal QPC: saddle point potential

The transport properties of an ideal QPC is reproduced here from Landauer-Büttiker theory [71, 127, 128]. According to this theory the current in the low-bias regime is given by Eq. 5.2 discussed before. In the non-linear case the current is given by

$$I = e/h \sum_n \int_{-\infty}^{+\infty} dE T_n(E) [f_{\beta}(E - \mu_L) - f_{\beta}(E - \mu_R)] \quad (6.1)$$

Assuming a symmetric voltage bias, the electrochemical potentials of the leads are given by $\mu_L - E_F = -\mu_R + E_F = eV_{SD}/2$ and in the case of low bias ($V_{SD} \ll 1$) this

formula reduces back to Eq. 5.2. $T_n(E)$ is the transmission of channel n . Hereafter we take into account only two spin-degenerate subbands and assume that apart from a (possible) shift in energy, the transmission is the same for all the channels. This is of course not true, because once a channel is open it acts to modify the potential felt by the other channels through screening but we neglect these interaction effects. Differential conductance $g = dI/dV$ can be calculated readily from Eq. 6.1

$$g(V_{SD}, V_g) = \frac{e^2}{2h} \sum_n \int dE T_n(E + E_F) [-f'_\beta(E - V_{SD}/2) - f'_\beta(E + V_{SD}/2)] \quad (6.2)$$

where we have shifted $E \rightarrow E + E_F$. Note that g is symmetric in bias as it should be. The derivative of the Fermi function is $-f'_\beta(E) = (\beta/4)/\cosh^2(\beta E/2)$ with $\beta = 1/k_B T$ and it approaches to delta function at zero temperature $\lim_{\beta \rightarrow \infty} -f'_\beta(E) = \delta(E)$. Therefore the second part of the integrand causes both shift and smearing out of the transmission. With this introduction we plug in the transmission of an ideal QPC with a saddle point potential from Eq. 5.3 into the linear conductance formula, Eq. 5.2, and differential conductance formula, Eq. 6.2. We take $\epsilon_s = (E - E_F - E_s)/\hbar\omega_x$ with s as the spin-index of the degenerate subband. The energy threshold of the band E_s changes linearly with the gate voltage similar to section 5.3.5. Fig. 6.8a,b show the energy-dependence of the transmission and the linear conductance vs. gate voltage for different temperatures calculated from Eq. 5.2 for this transmission. Higher temperature only smears out the data. Fig. 6.8c shows the non-linear differential conductance calculated from Eq. 6.2.

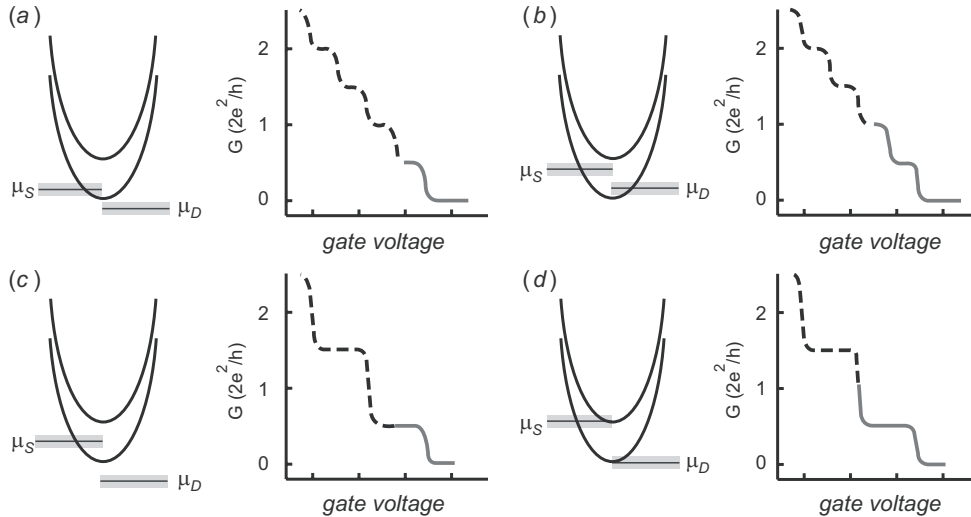


Figure 6.7: Schematic of feeding two 1D channels with parabolic dispersion by source-drain bias and how it influences the gate-dependence of the conductance. (a)-(b) bias voltage is half of the subband energy spacing $V_{SD} = \Delta E/2$, difference is only the gate voltage. (c)-(d) bias voltage is equal to subband spacing $V_{SD} = \Delta E$, again difference being the gate voltage. Adapted from Berggren and Pepper [129].

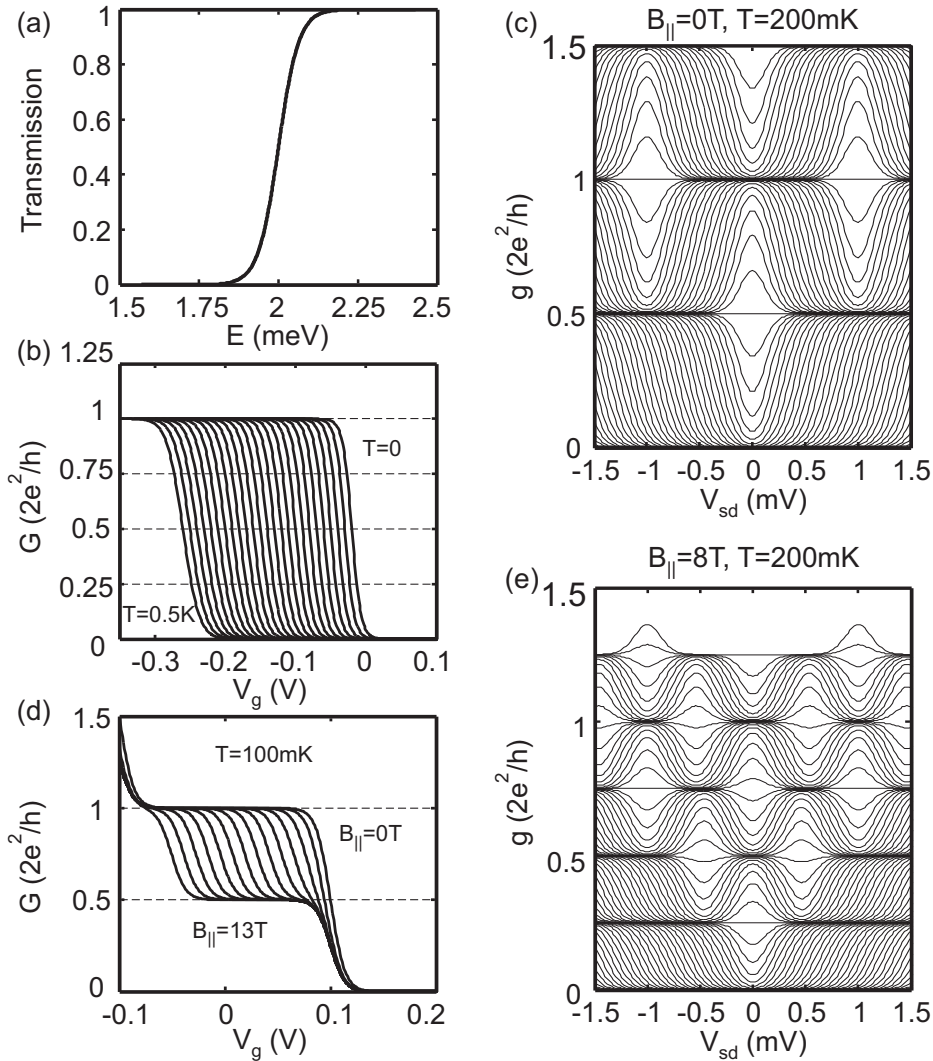


Figure 6.8: Characteristics of an ideal quantum point contact with saddle-point potential. (a) transmission vs. energy. (b) temperature-dependence (horizontally shifted) and (d) in-plane magnetic field dependence of the linear conductance. (c)-(e) differential conductance at zero and finite (8 T) field.

Fig. 6.7 shows the energy diagram of a 1D system with two subbands. According to differential conductance formula, Eq. 6.2, source and drain have separate contributions to $g(V_{SD}, V_g)$ (all the terms are positive) and each time a non-degenerate subband edge is lowered than the electrochemical potentials of source and/or drain, a contribution of $0.25(2e^2/h)$ is added to the differential conductance. It is easy to convince oneself that with the energy diagram given in Fig. 6.7 and the conductance vs. gate voltage shown there for different bias voltages, the non-linear differential conductance of Fig. 6.8c can be completely understood. According to this picture, the plateaus in the differential conductance are parallel to the bias axis in agreement with Fig. 6.8c. In reality however, all the plateaus have a bias dependent

conductance due to Coulomb interactions. This effect can be taken into account by assuming a non-linear drop of the potential between the source and the bottleneck of the constriction [128]. In this case the potential drop across the QPC can be phenomenologically written as $U_0(V_{SD}) = U_0 - \alpha e V_{SD} + \gamma e V_{SD}^2/2$ and this quantity must be inserted in Eq. 6.1 and the second derivative of the Fermi-Dirac distribution also taken into account. Here we neglect these effects. An important observation is that the ZBA does not appear in a saddle point potential. Using a phenomenological model similar to here, Chen et al. [115] have shown that the zero-bias anomaly can occur in 1D whenever the subband energy rises slightly with increasing dc bias, irrespective of the precise functional form of this rise in energy. Here we assume that the subband energy is constant with bias and only depends on the gate voltage.

Applying an in-plane magnetic field results in Zeeman splitting of the subbands as shown in Fig. 6.8d. Here we assume that the energy of the spin-up subband is pinned to certain gate voltages due to self-consistent screening effects as is usually seen in the experiment. The differential conductance at finite magnetic field shows more dense plateaus due to spin-degeneracy lifted subbands.

6.6.2 QPC with an additional transmission resonance

The transmission probability can be calculated using Fermi golden rule in the lowest approximation [1, 47] and it contains the density of states of source and drain and the matrix element of tunnelling between different states of the leads. All these can be phenomenologically lumped into an energy-dependence of the transmission. Here we make a simple model of these potential imperfections by assuming the transmission to be a Lorentzian resonance superimposed on top of the transmission of a saddle point potential, shown in Fig. 6.9a which is very similar to the model used to fit the large-magnetic field conductance peak in section 5.3.5. The temperature-dependence shown in Fig. 6.9b confirms that such transmission resonances disappear quickly by increasing the temperature. It is interesting though that the resonances leads to a zero bias peak in the differential conductance, shown in Fig. 6.9c, that again disappears by increasing the temperature. The assumption that the transmission is the same for all the subbands results in appearance of the zero bias peak at all the three rises of the differential conductance shown in the figure. Had we taken into account the screening effects, the higher zero bias peaks would have been suppressed. Note that there are also curves with split zero bias peaks in the zero-field differential conductance.

Application of an in-plane magnetic field splits the subbands but as we have assumed equal transmission for spin-split subbands the resonance appears in both subbands as shown in Fig. 6.9d. The finite bias spectroscopy at finite magnetic field shows similar pattern as the zero-field one, but here the split zero bias peaks are even more evident.

To summarize this section, we conclude that the zero bias peak can appear in g due to a transmission resonance, get suppressed by increasing the temperature

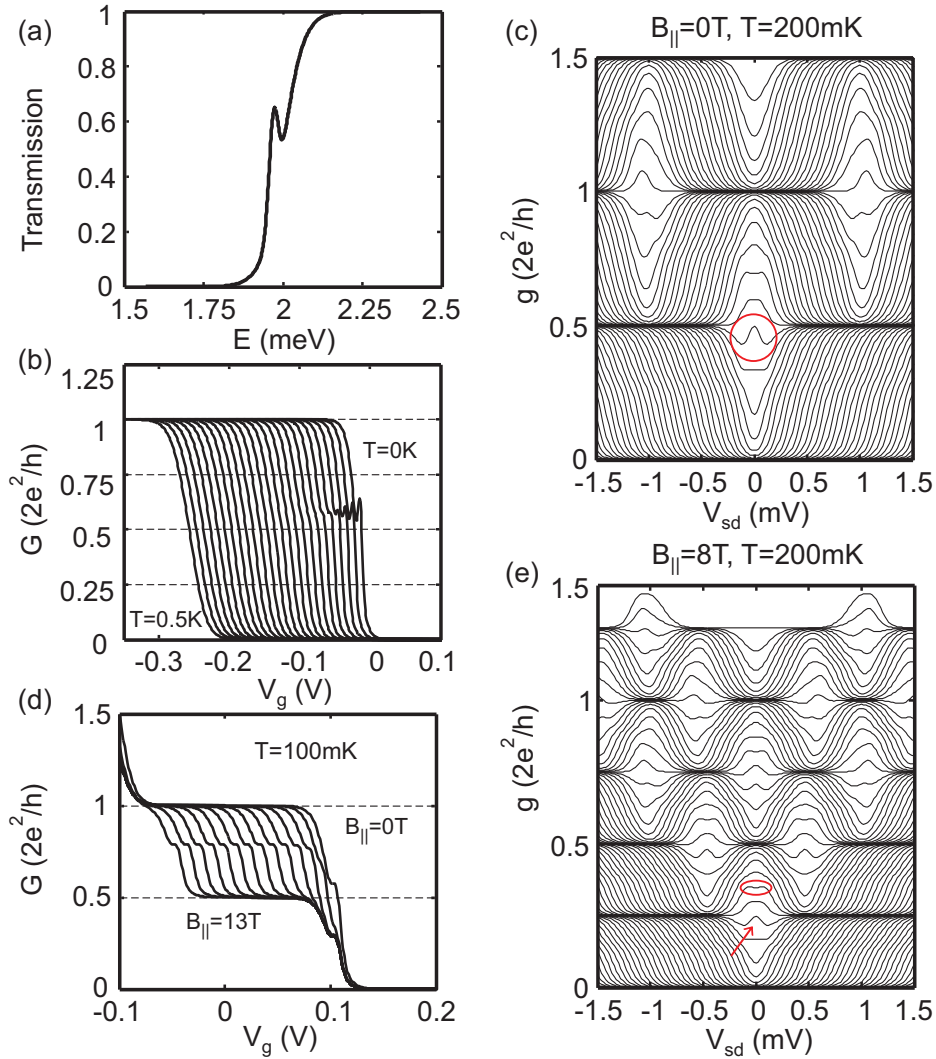


Figure 6.9: Characteristics of an quantum point contact with a resonance in the transmission (a). (see Fig. 6.8 for explanations). The resonances disappears by increasing the temperature (b). It is observable on both spin-split subbands (d). It gives rise to a zero bias peak (c)-(d) for the narrow gate regime corresponding to the anomaly, marked with red circle and arrow. The zero bias peak is even split at a certain gate voltage marked in red ellipse in (e).

and split by application of an in-plane magnetic field. In contrast to the commonly observed ZBA in QPCs, this peak appears at a certain gate voltage and splits at slightly higher conductances. It would be very interesting to know what are the effects of screening on this result if it is included even in a simple phenomenological modification of the transmission.

6.6.3 QPC with a spurious charge impurity nearby

Another type of imperfections that we consider is capacitive coupling of the channel bottom to a potential well or impurity that can get filled at a certain gate voltage. The QPC has a saddle-point transmission but the potential of the nano-structure shown in Fig. 6.10a has a minima with a certain state that can get filled by an electron/hole from either the channel or the leads. We assume that this state is weakly coupled to outside and its occupancy is given by a Fermi-Dirac distribution. Upon filling at a certain gate voltage the conductance trace of the QPC is shifted horizontally proportional to the capacitive coupling between them and a feature appears in the linear conductance as shown in Fig. 6.10b. Increasing the temperature has two effects: first, it decreases the conductance of the QPC at this gate voltage and therefore the feature also gradually decreases in conductance, very similar to the standard 0.7-feature behavior. Second, it extends the width of the feature by broadening the occupation profile of the impurity in the gate voltage. This occupation profile is given by the depth of the potential well and the temperature. For temperatures above the ionization energy of the impurity the anomaly is expected to vanish (not taken into account here).

Fig. 6.10c shows the differential conductance data which looks very similar to a corresponding one from an ideal QPC (Fig. 6.8c). The only difference is the bunching of several dI/dV curves at the the gate voltages of the filling of the impurity. This feature is very similar to the measurements performed on the QPC presented in Fig. 6.4b. Note that in contrast the model assumed here does not produce any zero bias peak. Perhaps the most interesting feature of this model is that application of an in-plane magnetic field, shown in Fig. 6.10b, results in very similar measurement features presented earlier in this chapter. Apart from Zeeman splitting of the subband, one can also imagine a g-factor for the impurity state however, here we assume this g-factor to be zero. As the spin-degenerate subband splits gradually only one subband is affected by the impurity filling. Starting from $0.75(2e^2/h)$ the conductance anomaly crosses $0.5(2e^2/h)$, saturates at $0.4(2e^2/h)$ and seemingly independent half-plateau appears at higher fields, all very consistent with the measurements on this QPC. Finite-field differential conductance in Fig. 6.10e has nothing new for us except same dI/dV bunching discussed before.

6.7 Possible explanation

After reviewing some of the effects of impurities on the characteristics of QPCs, we suggest the following picture. It is plausible that since the anomalous feature can appear/disappear by lateral shift of the channel, some impurity or potential imperfections of the QPC must be involved. The model of a QPC with a nearby charge impurity fits quite well to the temperature-dependent and magnetic field-dependent data. The effect of lateral shift of the channel can be due to a ΔV -dependence of the capacitive coupling of the impurity to the bottom of the channel

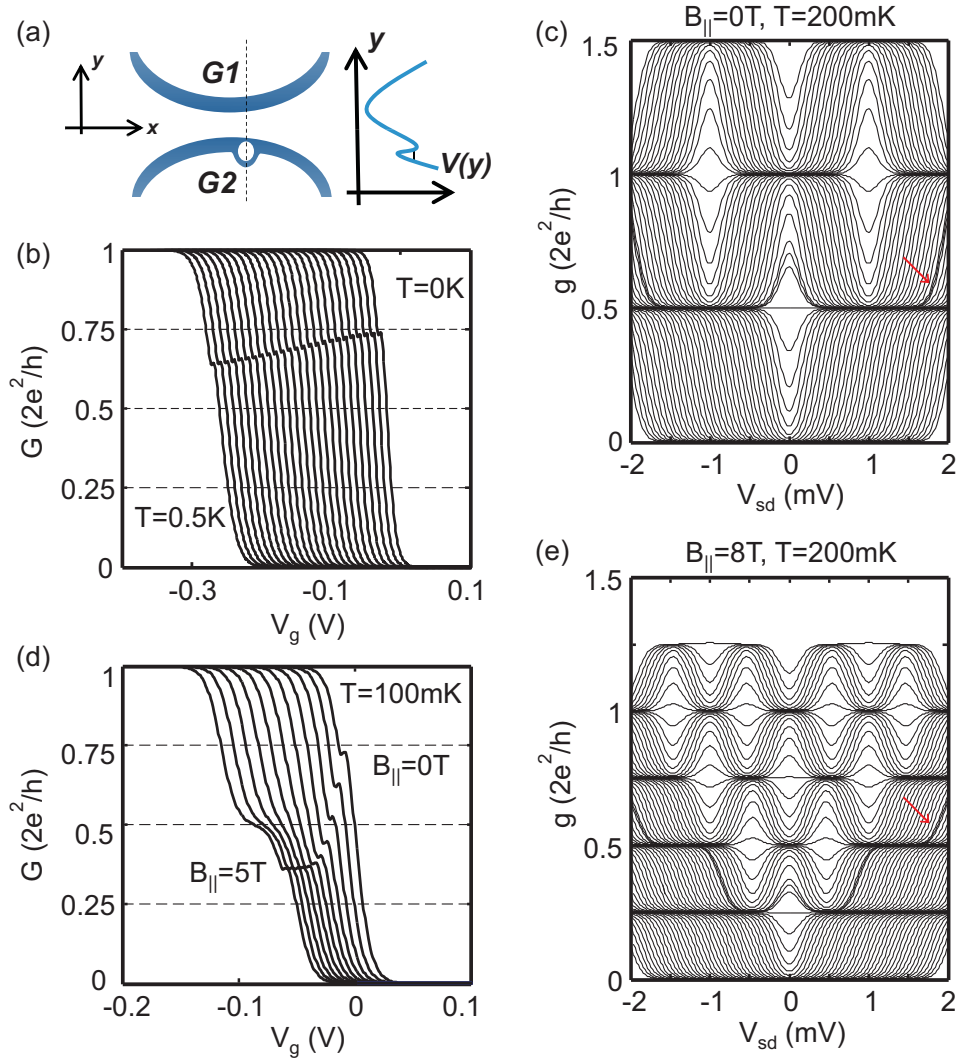


Figure 6.10: Characteristics of an quantum point contact with a nearby charge impurity. (a) schematic of the potential of the point contact, supporting an impurity state. Blue depleted regions separate the in-plane gates from the channel. (b) the feature survives higher temperatures and drops in conductance. (d) the feature drops in conductance and appears only in the rise of one spin-split subband by applying an in-plane field. (c)-(e) bunching of several dI/dV -curves (marked with red arrow).

which is conceivable. Based on the measurement shown in Fig. 6.3, we conclude that the impurity is located near gate $G2$. With positive ΔV the channel is pushed toward the impurity and with negative ΔV the channel is pulled back. However, the main measurement feature that defies this simple model is the presence of a strong ZBA within a large gate voltage range. Motivated with the measurements on the ZBA in section 6.5.1, we assume that it has different origins as the anomalous conductance feature discussed here. If the ZBA is due to Kondo effect, as suggested extensively in the literature [83, 97, 100] and the splitting with in-plane magnetic

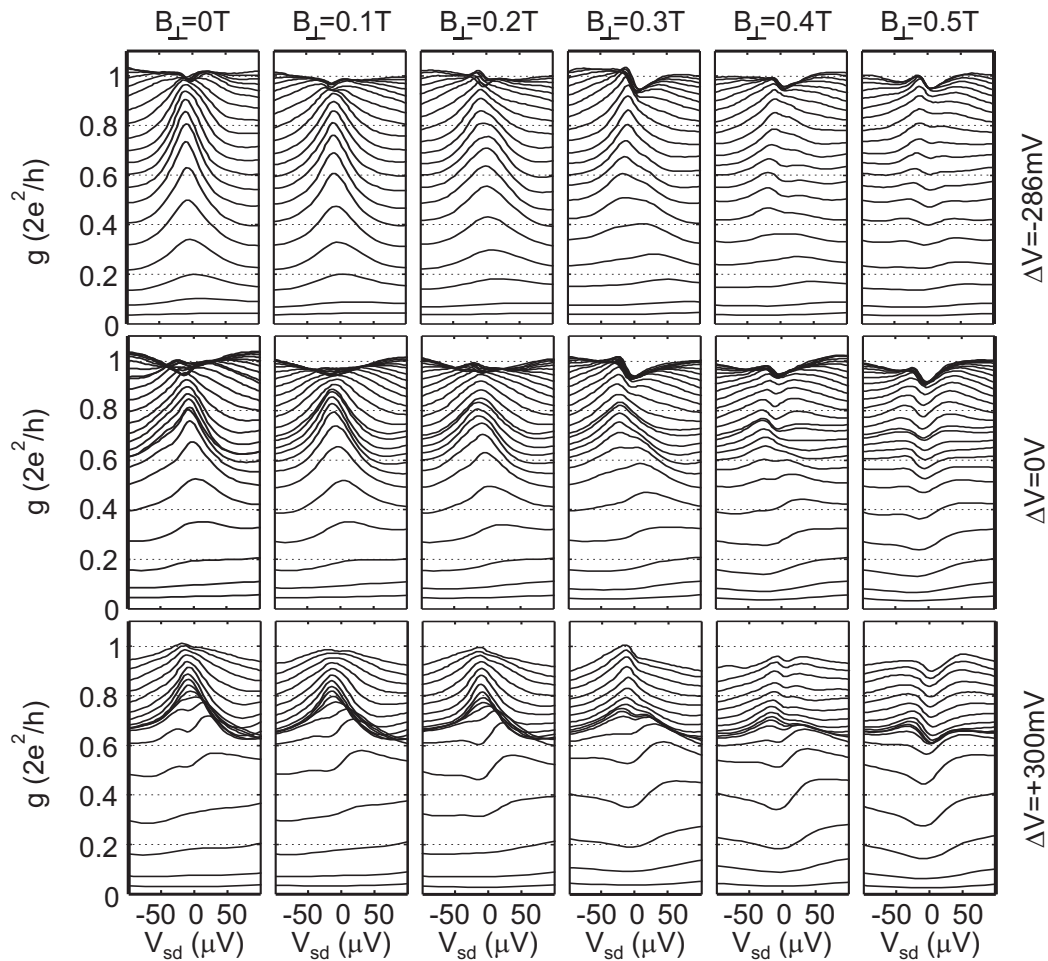


Figure 6.11: Evolution of the ZBA with perpendicular magnetic field B_{\perp} and the gate asymmetry ΔV . A field-dependent series resistance is subtracted to keep the first plateau at $2e^2/h$.

field suggests [110], it is not due to the impurity. Fig. 6.5 suggests that as the channel is pushed toward the impurity, the ZBA tends to get asymmetric and eventually split to two peaks. These data is presented in further details in Fig. 6.11 where the effect of perpendicular magnetic field (after subtracting a series resistance) on the ZBA is also shown in addition to the ΔV -dependence.

The first row with $\Delta V = -286$ mV with channel far from the impurity shows a symmetric ZBA that with increasing magnetic field starts to split around $B_{\perp} = 0.4$ T. As the channel is pushed toward the impurity, some of the dI/dV curves are bunched together. This is the onset of the occupation of the impurity. For the conductances below these bunching (more positive gate voltage) the state is above the electrochemical potential of the leads and it is empty. For the conductances above these bunching the state is filled. When the channel is very close to the impurity in the third line with $\Delta V = +300$ mV, the ZBA is split even at zero field. It is very interest-

ing that this zero-field splitting of the ZBA happens only when the impurity state is empty (conductances below the bunching). Above that the ZBA is symmetric and single peaked. By applying the magnetic field the splitting of the ZBA grows even further. At about $B_{\perp} = 0.4$ T, the unoccupied state-ZBA starts to split very similar to the first row and this splitting grows further by increasing the magnetic field.

Several publications have associated the ZBA with the leads and not with the QPC [111, 112]. Notwithstanding the questions about the origin of the ZBA, the zero-field splitting reported here supports a local origin of the ZBA with a position located inside or around the QPC. Furthermore, apart from the controversial origin of the Kondo effect in QPCs, the system investigated here is very similar to the extensively theoretically investigated settings of Kondo effect in a parallel double-dot [130–135] or in a single dot side-coupled to another dot [136, 137]. Except Wang [134] that assumes only contact interaction between the dots, the others assume a tunnel coupling between the two dots. The ZBA splits as a result of the hybridization between the two dots as experimentally observed here, supporting the idea that there is a ΔV -dependent tunnel coupling between the channel and the impurity in our case. The parallel double dot system, accidentally formed here, is a very interesting system to study two-channel Kondo effect [138].

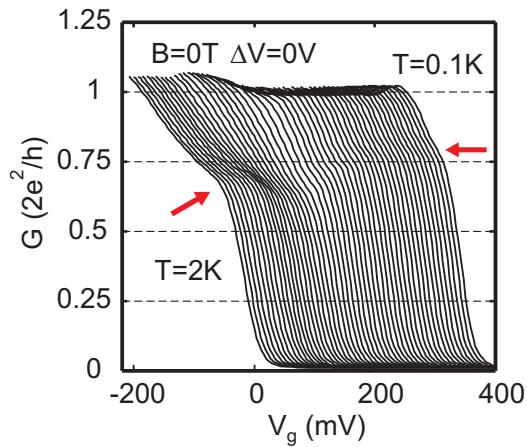


Figure 6.12: Temperature-dependence of the linear conductance at $\Delta V = 0$. The rightmost and leftmost curves have temperatures of 100 mK and 2 K respectively and the steps are not equidistant. The low-temperature conductance anomaly marked with the red arrow on the right drops in conductance and smears out and a new anomaly appears at higher temperature (marked with the red arrow on the left).

The Kondo theories of the 0.7-feature predict that the ZBA is a signature of the Kondo screening of an unpaired spin occupied the quasi-bound state of the QPC. At very high temperatures the Kondo effect is suppressed, the impurity is ionized and the 0.7-feature is expected to show up if the channel is not pushed too much to the impurity (for not too positive ΔV). Fig. 6.12 shows the temperature dependence of the linear conductance at $\Delta V = 0$ and up to a temperature of 2 K. The weak

anomaly originally at $0.75(2e^2/h)$ decreases in conductance to about $0.6(2e^2/h)$ and at even higher temperature the 0.7-feature emerges as expected.

6.8 Summary

A conductance anomaly in a hole QPC is experimentally investigated in detail. It is shown using simple toy-models that seemingly paradoxical features in the conductance arise due to a charge impurity nearby the QPC. However, the QPC exhibits a zero bias peak in the differential conductance that appears to have a different origin and is affected when the channel is pushed toward the impurity using asymmetric gate voltages. The splitting of this peak by in-plane and perpendicular magnetic fields suggests a Kondo origin for the ZBA and the tunnel coupling to the impurity results in a zero-field splitting of the ZBA. The result is consistent with the Kondo picture of the 0.7-anomaly and supports a local origin of the ZBA located at the QPC. The difference with common 0.7 anomaly therefore seems to be caused by an impurity in the channel.

Chapter 7

Anisotropic Zeeman splitting of 1D states in p-GaAs QPCs

7.1 Introduction

A magnetic field changes the energy of a system by coupling to its magnetic moment, an effect known as the Zeeman shift. For a free electron the only contribution to the magnetic moment is from the spin \mathbf{S} and the energy difference between spin-up and down is given by $\Delta E = g_s \mu_B B$ with $g_s = 2$. For electrons in atoms the orbital angular momentum \mathbf{L} also contributes to the magnetic moment which due to spin-orbit interactions is mixed with the spin. The g-factor is modified, and the z-component of spin and orbital angular momenta are no longer good quantum numbers and the Zeeman shift depends on the total angular momentum $\mathbf{J} = \mathbf{L} + \mathbf{S}$ which is the only conserved parameter (together with L^2 , S^2 and J^2).

In a solid-state environment the spin-orbit interaction can be much stronger than in free space and strongly modifies the proportionality constant in the Zeeman shift formula [46, 139] so that for electrons in bulk GaAs, the g-factor is given by $g_{n-\text{GaAs}}^* = -0.44$. This value is valid even in electron systems confined to two or one dimension provided that the carrier density is high enough. Only as the number of 1D subbands decreases below 20 propagating channels, Daneshvar et al. [57] found deviations due to exchange enhancement of the g-factor which has also been observed in 2D systems in the quantum Hall regime [140].

Much richer spin physics is expected in hole systems [31]. In two-dimensional hole gases the growth direction becomes the preferred direction of quantization for heavy holes due to quantum confinement [31]. As a result Zeeman splitting is significant perpendicular to the plane and zero for in-plane magnetic fields in quantum wells (QWs) grown on high-symmetry (100) and (111) surfaces [12, 38]. For other surfaces however a B_{\parallel} -linear splitting is obtained the magnitude of which depends on the in-plane orientation of B_{\parallel} relative to the crystal axes [12]. While the g-factor measurements in 2D rely on the involved technique of analyzing commensurability effects in Shubnikov-de Haas oscillations at different angles, in lower dimensions

the subband structure of the system provides direct information about the Zeeman spin-splitting of the carriers. *

7.1.1 Confinement Anisotropy: previous and present works

The interesting feature of valence band compared to the conduction band is that any finite in-plane k_{\parallel} mixes the heavy holes with the light holes which have a non-zero g-factor. In particular any further confinement results in such a mixing in the confinement direction, modifying the isotropy of the in-plane Zeeman splitting. This effect was first studied by Danneau et al. [141] on quantum wires made in a 2DHG on (311)A surface. On this surface the two main in-plane crystallographic directions $[0\bar{1}1]$ and $[\bar{2}33]$ have different two dimensional g-factors which are equal to 0.2 and 0.6 respectively [31]. In their 1D system aligned along $[\bar{2}33]$, Danneau et al. observed a clear lifting of the spin degeneracy and crossings of the subbands when the in-plane magnetic field B was applied parallel to the wire. The effective g-factor was found to be decreasing with the subband index toward the 2D limit of 0.6. When B was oriented perpendicular to the wire, no spin splitting was discernible up to $B = 8.8$ T. The authors associated this result with the importance of quantum confinement in spin-3/2 systems.

Motivated by this work, Koduvayur et al. [23] studied QPCs made by AFM lithography along both $[0\bar{1}1]$ and $[\bar{2}33]$ directions on (311)A surface and concluded that the anisotropy of the 1D hole spin-splitting was primarily due to the crystallographic anisotropy of the spin-orbit interaction rather than the 1D confinement. They reported that the effective g-factor does not depend on 1D energy level number N for $B \parallel [0\bar{1}1]$ but has a strong N dependence for $B \parallel [\bar{2}33]$. This was in contrast to Klochan et al. [126] who repeated this experiment on quantum wires made along both $[0\bar{1}1]$ and $[\bar{2}33]$ directions in a 2DHG on (311)A surface and found that in spite of two-dimensional anisotropy of the Zeeman splitting, the g-factor is significantly altered from these values with a subband-dependent value for in-plane magnetic field B parallel to the wires while for B perpendicular to the wires in both directions, the result is essentially equal to the anisotropic 2D limits mentioned before.

These experiments suggest that perhaps the role of confinement anisotropy is different in quantum wires compared to quantum point contacts motivating more experiments to resolve the puzzle. This is conceivable as the lateral confinement is probably more pronounced in long quantum wires compared to point contacts making them more alike one-dimensional systems. Moreover it would be desirable to perform these experiment on nano-structures made from high symmetry QWs where the crystallographic anisotropy does not play any role. Recently Chen et al. [142] did similar experiments on quantum wires fabricated along $[011]$ and $[0\bar{1}\bar{1}]$ crystallographic axes of a high-mobility undoped (100)-oriented heterostructure and reported similar confinement anisotropy of the hole g-factor.¹ Moreover they re-

*Valuable discussions with U. Zulicke and O. Klochan is appreciated.

¹We had already observed this effect in a number of quantum point contacts (see Appendix F)

ported a monotonic increase of the g-factors with the subband index approaching $g^* = 0.5$ for $N > 4$ subbands even though a value of zero in 2D limit is expected.

We have measured the Zeeman splitting in eight quantum point contacts made with both AFM and e-beam lithography along two different directions of $[011]$ and $[01\bar{1}]$ on (100)-plane of p-GaAs in this thesis. No dependence with respect to the angle between QPC axis and the crystallographic directions were observed as expected. The g-factors extracted from our experiments agree qualitatively with those reported in [126, 141, 142]. We observe clear spin-splitting if the in-plane magnetic field B is applied parallel to the QPC axis while no spin-splitting was observed when B is perpendicular to the QPC axis. Since the QPCs measured in this thesis have lithographical lengths comparable to their widths, it is striking to observe such a significant effect due to their lateral confinement. As a consequence the zero in-plane g-factor of holes becomes finite once the carriers are confined in one direction. In other words the holes do not ‘feel’ any in-plane magnetic field when they pass a constriction perpendicular to the field. This finding highlights the difference between spin-3/2 holes compared to the electrons and can have important implications for future nanotechnology devices that wish to exploit the spin of the carriers besides their charge.

In this chapter we study three similar quantum point contacts fabricated with e-beam lithography on the same chip *A4.10.1* in three different directions. These QPCs called *QPC1*, *QPC2*, *QPC3* are in 45° , 0° and 90° with respect to the in-plane field. The standard linear and finite bias differential conductance measurements were performed at base temperature in a dilution refrigerator with in-plane magnetic field up to 13 Tesla in a fixed direction. The field angle with respect to the plane was less than 2 degree. Unless explicitly mentioned B stands for in-plane magnetic field in this chapter. As the role of confinement anisotropy in hole quantum wires is best summarized in [142] and it is the only reported experiment on (100)-plane, in the following we will compare our results on hole quantum point contacts to those reported in this paper. While our measurements are in qualitative agreement with these result, a number of quantitative differences must be highlighted. We obtain larger values of the g-factor compared to those reported in [142]. This might be because the strong confinement in our case results in subband splittings that are larger than the quantum wires studied by Chen et al. [142] implying that exchange enhancement of g-factor in hole systems, not observed to date, may play a role.

7.2 Transconductance

The signature of spin-splitting is shown in the transconductance plots shown in Fig. 7.1, where the high transconductance regimes shown in blue indicate the subbands while the yellow, orange and red areas indicate the plateaus between these subbands. The transconductance was obtained from a numerical derivative of the

when this paper first appeared.

measured linear conductance with respect to the gate voltage. A clear Zeeman splitting is observed for *QPC1* (Fig. 7.1a) and *QPC2* (Fig. 7.1b) while for *QPC3* in which the current flows perpendicular to the magnetic field, no spin-splitting is discernible up to 13 T (Fig. 7.1c). Similar effects on five other QPCs are shown in Appendix F. Two features of these data are worth mentioning here. First, *QPC2* which is oriented parallel to the B field, seems to have a larger splitting compared to *QPC1* which has a 45° angle with the field. The other interesting feature of the data is that although the first subband does not split in *QPC2*, consistent with the data from other QPCs parallel to the field in Appendix F and in agreement with those reported in [142], it does split for *QPC1*.

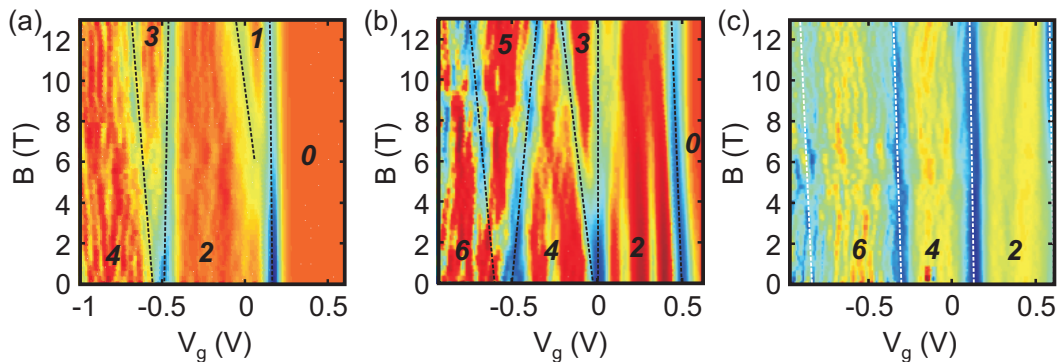


Figure 7.1: Transconductance (numerical derivative with respect to the gate voltage) with arbitrary unit as a function of gate voltage and in-plane magnetic field measured at $T = 100$ mK. (a) *QPC1* (45° with respect to magnetic field) (b) *QPC2* (parallel to magnetic field) (c) *QPC3* (perpendicular to magnetic field). The (blue) high transconductance regimes highlighted with dashed lines indicate the subbands. The linear conductance values in units of e^2/h are indicated on each plateau.

There are two ways to calculate the g-factor in one-dimensional systems. The common approach is to calculate it from the source-drain bias at which the 1D subbands cross, divided by the magnetic field at which spin-split subband crossings occur [23, 27, 126, 142]. In our quantum point contacts however the subband splitting is so large (a factor of 2-6 larger than the figures reported in these references) that no spin-split crossing happens up to magnetic field of 13 T. Therefore we use the second approach which requires independent determination of gate lever arm from finite bias spectroscopy, to transform the x-axes in Fig. 7.1 to an energy axis.

Table 7.2 quantifies the splitting of spin subbands in Fig. 7.1. The width of the lines is the main source of error. For the first subband in *QPC2* and the subbands of *QPC3* a maximum splitting is reported based on the width of these lines.

	<i>QPC1</i>	<i>QPC2</i>	<i>QPC3</i>
$dV_g(1)/dB$	0.013(± 0.001)	<0.001	
$dV_g(2)/dB$	0.013(± 0.001)	0.017(± 0.002)	<0.001
$dV_g(3)/dB$		0.024(± 0.002)	<0.002
$dV_g(4)/dB$			<0.002

Table 7.1: Spin-splitting of subbands per Tesla measured in the gate voltage for the data presented in Fig. 7.1. The numbers in parentheses are the errors. A maximum splitting is indicated for the cases where a clear spin-splitting is not observed.

7.3 Calculation of lever arm

The gate lever arm can be calculated from the finite bias differential conductance plots shown in Fig. 7.2. Bright areas in this plot are the plateaus with conductances indicated in the figure in units of e^2/h . The dark regions highlighted with dashed lines are transitions between the plateaus due to subbands entering or leaving the bias window. Some of these transitions are noted in Fig. 7.2c. The white dashed lines mark the alignment of the subbands with the electrochemical potential of source and drain. The blue and green dashed lines show the evolution of the first subband with the applied bias which is anomalous (only one subband crosses the source while two subbands cross drain) due to the presence of 0.7 feature as discussed in previous chapters. It is noteworthy that the gray dashed lines crossing the 2nd conductance plateau very similar to the blue dashed lines that cut the 1st conductance plateau, are probably signatures of a ‘0.7 Analogue’ [90]. Therefore we do not consider the first subband and the gray dashed line in our analysis in this chapter. Only the white dashed lines are taken into account in the following.

Vertical dashed lines in Fig. 7.2 evaluate the bias at which the electrochemical potential of source and drain are aligned against two subsequent subbands and therefore give the subband splittings in eV. As a general trend the subband splitting gets smaller as the constriction opens up toward more negative gate voltage. The same effect also causes the change in the slope of the white dashed lines as one moves toward more negative gate voltage. The first subband is again more complicated as discussed before. Table 7.3 summarizes the subband splittings and gate lever arms $\alpha_n = 0.5dV_{SD}(n)/dV_g(n)$ obtained from the slope of white dashed lines for different subbands averaged between the source and the drain lines. The errors are again due to extended width of the lines in Fig. 7.2.

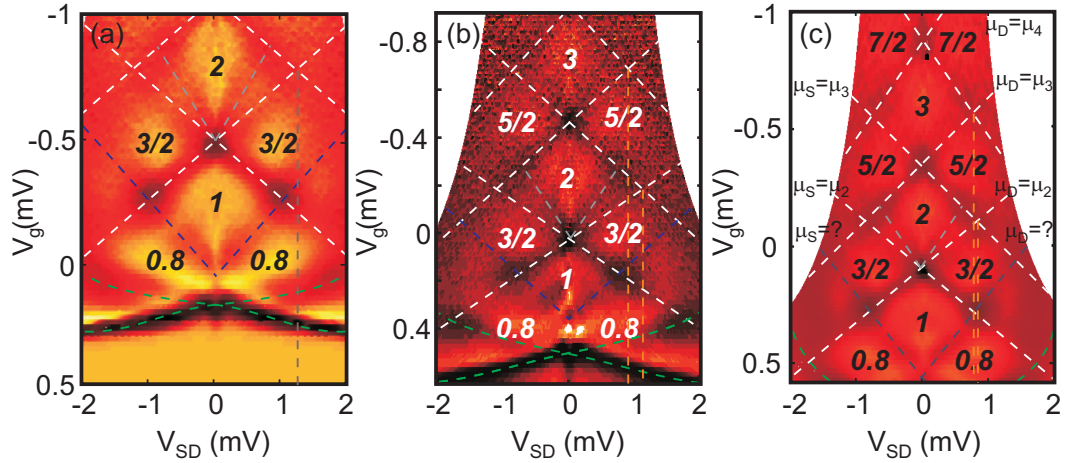


Figure 7.2: Transconductance (numerical derivative with respect to the gate voltage) with arbitrary unit as a function of this time gate voltage and source-drain bias measured at $T = 100$ mK. (a) *QPC1* (45° with respect to magnetic field) (b) *QPC2* (parallel to magnetic field) (c) *QPC3* (perpendicular to magnetic field). Bright areas are plateaus whose conductance is indicated in the figure. Dashed lines mark when subbands are aligned with the electrochemical potential of source/drain.

	<i>QPC1</i>	<i>QPC2</i>	<i>QPC3</i>
$\Delta E_{2,3}$ (meV)	$1.32(\pm 0.05)$	$1.14(\pm 0.05)$	$0.89(\pm 0.02)$
$\Delta E_{3,4}$ (meV)		$0.89(\pm 0.05)$	$0.77(\pm 0.03)$
α_2 (meV/V)	$2.6(\pm 0.2)$	$2.6(\pm 0.3)$	$2.5(\pm 0.2)$
α_3 (meV/V)	$1.8(\pm 0.1)$	$1.9(\pm 0.2)$	$1.7(\pm 0.1)$
α_4 (meV/V)		$1.7(\pm 0.2)$	$1.4(\pm 0.1)$

Table 7.2: The energy spacing between consecutive subbands $\Delta E_{n,n+1}$, measured from the position of the vertical dashed lines and the gate lever arm α_n on subband n , calculated from the slopes of the white dashed lines in Fig. 7.2. The numbers in parentheses are the errors.

7.4 Zeeman splitting anisotropy

The above results can be combined to give the Zeeman spin-splitting energies per Tesla listed in Table. 7.4. In this table the results from two samples *A4.2.1* and *A4.2.2*, measured parallel to the magnetic field as discussed in Appendix F, are also included. The numerical value of splitting for the first subband is not clear due to ambiguity in assigning the lever arm. Nevertheless it is clear from Fig. 7.1 that the first subband in *QPC1* has a non-zero spin-splitting. The ratio between spin-splittings of the 2nd subband in *QPC2* and *QPC1* agrees with the factor of $\sqrt{2}$ expected from the miss-alignment of the latter with respect to the field.

	<i>QPC1</i>	<i>QPC2</i>	<i>QPC3</i>	<i>A4.2.1</i>	<i>A4.2.2</i>
$\Delta E_1(\mu\text{eV/T})$	>0	0(?)			0(?)
$\Delta E_2(\mu\text{eV/T})$	33(± 3)	44(± 7)	<3	25(± 5)	36(± 5)
$\Delta E_3(\mu\text{eV/T})$		46(± 6)	<4	37(± 6)	28(± 4)
$\Delta E_4(\mu\text{eV/T})$			<3	56(± 6)	

Table 7.3: Zeeman spin-splitting of the subbands. The numbers in parentheses are the errors.

From these data we can calculate the g -factor. In order to be consistent with the literature we adapt the following definition of the effective Landé g -factor in which the spin of holes is included in the g -factor

$$\Delta E = g^* \mu_B B \quad (7.1)$$

This is plausible since confinement mixes the heavy and light holes, hence opposing a clear spin assignment to the subbands. Note that $\mu_B = \hbar e/2m_e \approx 58 \mu\text{eV/T}$ is the Bohr magneton with m_e the free electron mass. With this definition g^* is obtained from

$$g_n^* = \frac{\alpha_n}{\mu_B} \frac{dV_g(n)}{dB} \quad (7.2)$$

The g -factors are listed in Table 7.4. Only the absolute value of the g -factor are stated here as its sign cannot be deduced from our experiment. The same result is obtained by extrapolating the spin-splitting lines in Fig. 7.1 to find the crossing field $B > 13$ T outside the plots and divide the subband splitting by this crossing field to get the Zeeman shift as is commonly performed in the 1D spin-splitting literature [23, 27, 126, 142]. We stress that the values obtained here are a factor of 2-3 higher than those reported in the literature [23, 27, 126, 142]. This might be connected to the fact that the subband splitting in our QPCs are a factor of 2-6 higher than those reported in previous works indicating a stronger confinement. This large subband spacing and leakage-limited gate voltage range is probably the reason that only few subbands are observed in our quantum point contacts.

	<i>QPC1</i> $B \angle 45^\circ I$	<i>QPC2</i> $B \parallel I$	<i>QPC3</i> $B \perp I$	<i>A4.2.1</i> $B \parallel I$	<i>A4.2.2</i> $B \parallel I$
g_1	>0	0(?)			0(?)
g_2	0.55(± 0.05)	0.75(± 0.1)	<0.05	0.45(± 0.1)	0.6(± 0.1)
g_3		0.8(± 0.1)	<0.05	0.65(± 0.1)	0.4(± 0.05)
g_4			<0.05	0.95(± 0.1)	

Table 7.4: g -factor of the 1D subbands. The numbers in parentheses are the errors.

7.5 Possible explanations

As discussed in the introduction the anisotropy terms cubic in \vec{k}_{\parallel} that would result in a linear in B_{\parallel} spin-splitting are absent for (100) oriented quantum wells, however a substantial linear spin-splitting can be achieved because of heavy and light hole (HH-LH) mixing at $\vec{k}_{\parallel} = (k_x, k_y) \neq 0$ [31, 142]. To linear order in B_{\parallel} (page 174 of [31])

$$\begin{aligned} \mathcal{H}_{[100]}^{HH} = & z_{51}^{7h7h} (B_x k_x^2 \sigma_x - B_y k_y^2 \sigma_y) + z_{52}^{7h7h} (B_x k_y^2 \sigma_x - B_y k_x^2 \sigma_y) \\ & + z_{53}^{7h7h} \{k_x, k_y\} (B_x k_x^2 \sigma_x - B_y k_y^2 \sigma_y) + \mathcal{O}(B_{\parallel}^3) \end{aligned} \quad (7.3)$$

The z^{7h7h} parameters (related to \mathcal{Z} parameters introduced later) are constants that contain the HH-LH mixing. $\hbar \vec{k} = -i\hbar \vec{\nabla}$ is the momentum operator. In 2D the Zeeman splitting is the average of the above expression over the whole Fermi circle [142]. In 1D systems the transverse quantization of wavevector amplifies one of the k_x or k_y on the expense of the other, thus boosting up corresponding terms in the above Hamiltonian. However this anisotropy due of wavevector quantization does not explain the anisotropy observed here and reported in the literature. For example ² if the current is in x -direction with $\psi \propto \phi_n(y) e^{ik_x x}$, an order of magnitude estimate of the transverse wavevector k_y can be calculated from the zero field subband splittings using $E_n = \hbar^2 k_{y,n}^2 / 2m^*$ while $k_x \approx 0$ in linear conductance measurements. With this substitution only the following terms are left which contribute to the spin-splitting

$$\mathcal{H}_{[100]}^{HH} \rightarrow g_{xx}^* B_x \sigma_x + g_{yy}^* B_y \sigma_y \quad (7.4)$$

where the effective g-factors are given by

$$\begin{aligned} g_{xx}^* &= 3\gamma_2 k_{y,n}^2 (0.5\kappa \mathcal{Z}_1 - \gamma_3 \mathcal{Z}_2) \\ g_{yy}^* &= 3\gamma_2 k_{y,n}^2 (0.5\kappa \mathcal{Z}_1 - \gamma_3^2 \mathcal{Z}_2 / \gamma_2) \end{aligned} \quad (7.5)$$

parameters $\gamma_1, \gamma_2, \gamma_3$ are the Luttinger parameters [31] which are respectively equal to 6.85, 2.10 and 2.90 in GaAs and $\kappa = 1.2$ is the (valence-band) bulk g-factor. Parameters \mathcal{Z}_1 and \mathcal{Z}_2 , responsible for HH-LH mixing, depend on the precise confinement potential of the two dimensional hole gas by the quantum well (for a 15 nm wide rectangular QW $\mathcal{Z}_2 / \mathcal{Z}_1 \approx -2$ [31]).

Confinement enhancement of the g-factor

Equation 7.5 emphasizes the role of confinement on the Zeeman splitting. The g-factor in this formula is proportional to (the expectation value of) $k_{y,n}^2$ which is by itself proportional to the subband spacing. This can explain why the value of g-factors in our measurements are larger than those reported in the literature approximately proportional to the ratio of corresponding subband spacings.

²No dependence on crystallographic directions is assumed.

The origin of confinement anisotropy is however more intricate because it does not come out of the above 2D considerations as it was discussed by Chen et al. [142]. In the context of the above 2D theory, our experimental observation of $g_{xx} \gg g_{yy}$ requires either $\gamma_3/\gamma_2 = 1.4$ be much less than one which is not correct or that the sign of the above formula is different (only the absolute value of the g-factor is measured in our experiment) and the values of \mathcal{Z}_1 and \mathcal{Z}_2 are substantially altered from the above values due to triangular confinement. More theoretical work, perhaps in the framework of a quasi-1D theory [143, 144], is necessary in order to resolve this problem.

Exchange interaction

Another possible origin of the large measured g-factors is the Coulomb interaction. Strong confinement increases the overlap between the wavefunctions of the particles, strengthening the exchange interaction. The exchange interaction on the other hand can enhance the spin-splitting as it has been observed in 2D [145] and 1D systems [57, 146]. This effect can be explained as follows. In short, neglecting the spin-orbit interaction, the density mismatch between particles with spin- \uparrow and spin- \downarrow can increase the particle-particle interactions felt by low population subband (spin- \uparrow) as they mainly feel the particles with opposite spin (high-population spin- \downarrow). This is because the interaction between particles with the same spin is suppressed anyway due to Pauli exclusion principle. The extra particle-particle interaction can create an energy difference in the form of $\mathcal{J}(n_{\downarrow} - n_{\uparrow})$ which further increases the spin splitting [145].

In two-dimensional hole systems no sign of exchange enhancement of the g-factor has been observed up to the interaction parameter of $r_s < 15$ [10]. While the interaction parameter is lower in the leads of our QPCs $r_s \approx 5$, it is expected to be higher inside QPCs because of lower density and get enhanced due to confinement. If this were true we would expect that the g-factor scales inversely with the subband index which is certainly not the case. Therefore we believe that the exchange interaction is irrelevant for the measurements reported here.

7.6 Perpendicular magnetic field

For the sake of completeness here we shortly discuss the Zeeman splitting for the magnetic field perpendicular to the plane. Fig. 7.3 shows the transconductance of *QPC1* measured in this particular field direction. The filling factors on different plateaus are indicated in the figure. A clear diamagnetic shift as a result of the magnetic field in addition to the Zeeman spin-splitting of subbands is clear in this data. However it is not straightforward to transform the gate voltage axis of Fig. 7.3 to an energy axis. The classical cyclotron radius and the magnetic length in our system are 100 nm/Tesla, meaning that already at few Tesla the wavefunctions are

strongly influence by the field and the zero-field lever arms extracted from Fig. 7.2a are not valid anymore. Nevertheless reading the spin-splitting of $dV_g(2)/dB \approx 0.11$ for the 2nd subband from the low field $B_\perp < 3T$ part of Fig. 7.3 and using the zero-field lever arm $\alpha_2 \approx 2.6$ from Table. 7.3 gives a perpendicular g-factor of $g_\perp \approx 5$. This

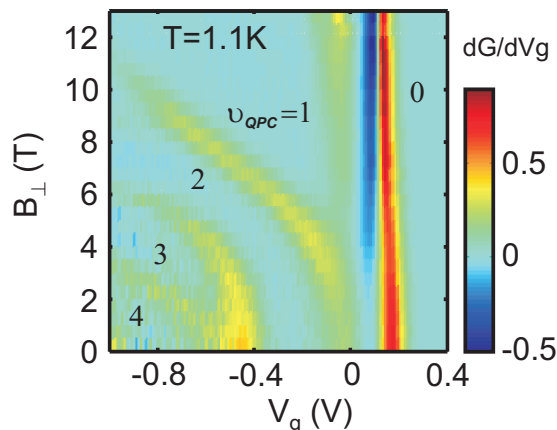


Figure 7.3: Transconductance (numerical derivative with respect to the gate voltage) of *QPC1* with arbitrary unit as a function of gate voltage and magnetic field perpendicular to the plane measured at $T = 1.1$ K. Blue areas are plateaus whose filling factor are indicated in the figure. Red and yellow lines are transitions between these plateaus as the subbands pass the Fermi energy. The blue stripe parallel to the red subband edge is the signature of a high-field conductance peak due to 0.7 anomaly discussed in Chapter 5. More information about the 0.7 anomaly in this QPC is shown in Appendix E

value must be treated with some care. For comparison the theoretical perpendicular g-factor of holes in 2D is $g_\perp^{HH} = 6\kappa \approx 7.2$ [31] which agrees with the optically measured values in the literature [147, 148].

7.7 Conclusion and future works

In this chapter we have explored the role of confinement on the in-plane anisotropy of the Zeeman spin-splitting of our hole quantum point contacts. It has been shown that the g-factor is zero if the in-plane magnetic field is applied perpendicular to the current direction. This means that the holes experience no magnetic field if they pass a constriction perpendicular to the field. The results presented here are in qualitative agreement with the works presented in [27, 126, 142]. The values for the g-factor are however higher than the figures reported in previous works. The role of confinement and exchange interaction on the enhancement of the g-factor is discussed and it is shown that the although 2D theory [31] can correctly account for this enhancement, it does not provide an explanation of the observed anisotropy. A clear experimental demonstration of exchange enhancement of the g-factor in 1D

hole systems is still elusive in spite of the fact that these interactions are supposedly stronger in these systems.

Chapter 8

Excited states in a p-GaAs single quantum dot

8.1 Introduction

Quantum dots implemented in GaAs heterostructures are promising candidates for the experimental realization of quantum computation [40], as well as various spintronic devices [149]. However, research based on electronic transport through such small conducting islands has been, so far, almost exclusively focused on electron quantum dots on n-type GaAs heterostructures [150–153]. The recently emerging interest in low-dimensional hole-doped systems arises primarily from the fact that spin-orbit as well as carrier-carrier Coulomb interaction (E_{int}) effects are more pronounced in such systems compared to the more established n-doped systems. The main reason for this is that holes have a much higher effective mass than electrons, and thus a smaller Fermi energy E_F . This enables the investigation of novel regimes with much higher interaction parameter $r_s = E_{\text{int}}/E_F$. In a confined system like a quantum dot the interaction is characterized by the ratio of charging energy and confinement energy $\lambda = E_{\text{int}}/\Delta$ [154]. While the former is given by the dot geometry and the dielectric constant, the latter depends on geometry and the effective mass. For a parabolic potential this is equal to

$$\lambda = \frac{e^2}{4\pi\epsilon l_0 \hbar\omega} = \frac{l_0}{a_B^*} \propto m^* l_0 \quad (8.1)$$

where $l_0 = \sqrt{\hbar/m^*\omega}$ is a measure of the size of the dot. For the same size of quantum dots, the interactions are thus stronger in hole quantum dots compared to electron dots due to the larger effective mass.

Stronger spin-orbit interactions in bulk two-dimensional hole-doped systems are expected to lead to significantly reduced spin relaxation times. On the other hand, it was also shown [155] that spin relaxation of holes confined into quantum wells is much slower than in the bulk case, but still several orders of magnitude faster than electron spin relaxation. This was one of the main reasons why p-type systems

received little attention in efforts to utilize the carriers' spin in quantum information technologies. However, it was recently predicted [156] that further confinement of holes into quantum dots can significantly increase the relaxation time T_1 of hole spins, so that it can be comparable, or even larger than the one of the electron spins as it was tested by optical pumping experiments in self-assembled p-doped InGaAs quantum dots [157]. The other interesting time scale is the spin decoherence time which besides spin-orbit interaction is governed by the hyperfine interaction between the electron and the bath of nuclear spins [41–43]. The hyperfine interaction however is suppressed in p-GaAs due to p-type orbital symmetry of holes [44] as it was experimentally confirmed recently [45] and longer decoherence times T_2 are expected. It has been predicted that for all spin-orbit mechanisms the spin decoherence times in quantum dots are as large as the spin relaxation times ($T_2 = 2T_1$) [158].

In this chapter the results of Coulomb blockade measurements in such a single-hole transistor defined on a p-type carbon doped GaAs heterostructure is presented. The area occupied by the confined holes in the investigated device turns out to be much smaller than in previously reported p-type quantum dots [19]. Thus the single-level regime becomes accessible for characterization via electrical transport experiments for the first time.

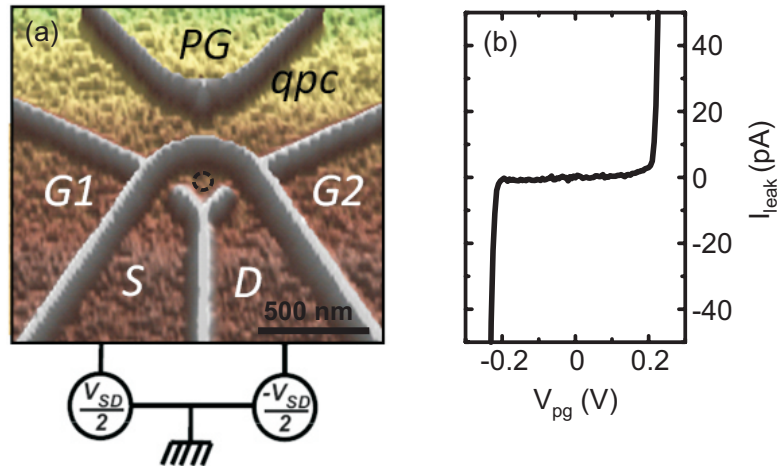


Figure 8.1: (a) AFM image of the sample topology. The 15 nm high oxide lines are prepared by local anodic oxidation and create insulating barriers in the underlying 2DHG separating it into electrically disconnected areas. The dashed circle indicates the location of the QD which is connected to source and drain contacts by two constrictions. The couplings of the dot to the leads are tuned individually by the in-plane gates G1 and G2 while the electrochemical potential of the dot can be varied by applying a background voltage on the nearby QPC (plunger gate). (b) Typical breakdown characteristics of the oxide lines at 60 mK base temperature.

The sample shown in Fig. 8.1 was patterned in the 2DHG by AFM lithography [63, 64] as described in chapter 3. Voltages in the range of [-200 mV, +200 mV] can be applied between separated regions without any significant leakage current

across the oxide line, as illustrated in Fig. 8.1(b). A small quantum dot is formed between the source (S) and drain (D) leads. The coupling of the dot to S and D through two constrictions can be tuned individually by applying voltages on the nearby in-plane gates $G1$ and $G2$. The background voltage applied to the qpc is used to align the electrochemical potential and thus the number of the confined holes in the dot with respect to the electrochemical potentials in S and D . Therefore this gate will be called plunger gate throughout this chapter. It is to be noted that qpc can serve also as a non-destructive detector for sensing the charge state of the dot as will be discussed in the next chapter.

The transport experiments were carried out at 60 mK base temperature of a standard $^3\text{He}/^4\text{He}$ dilution refrigerator. The two-terminal electrical conductance was measured by the simultaneous application of a symmetrical ac bias with an amplitude of $20 \mu\text{V}$ at 31 Hz lock-in frequency and dc biases up to 2 mV between S and D . The resolution of the current detection was better than 20 fA at 0.5 Hz bandwidth.

8.2 Coulomb resonances

From Coulomb diamond measurements it is found that the dot is symmetrically coupled to the S and D leads when the control gates of the nominally 140 nm wide constrictions are tuned according to $V_{G2} = V_{G1} - 115 \text{ mV}$ within the $[-200 \text{ mV}, +200 \text{ mV}]$ insulating regime of the oxide lines. In order to explore Coulomb blockaded transport the differential conductance of the dot was measured as a function of the V_{qpc} gate voltage at zero dc bias. The pronounced conductance resonances observed at different gate configurations are illustrated in Fig. 8.2. The fact that the dot closes with increasing V_{qpc} confirms that the electrical transport is maintained by holes. At the two gate configurations selected in Fig. 8.2 the peak positions were stable through several consecutive gate sweeps on a time scale of a day with an accuracy of 0.1 mV. However, at some particular gate configurations sudden rearrangements of the background charges made reproducible measurements difficult. From the relative shift of the resonances at different V_{G1} and V_{G2} voltages it is also clearly visible that the plunger gate not only tunes the number of holes in the dot but it also acts on the two constrictions leading to a change in the coupling strength of the dot to S and D . The latter effect can be compensated by accordingly changing the voltages on the two side gates $G1$ and $G2$ as it is indicated in Fig. 8.2.

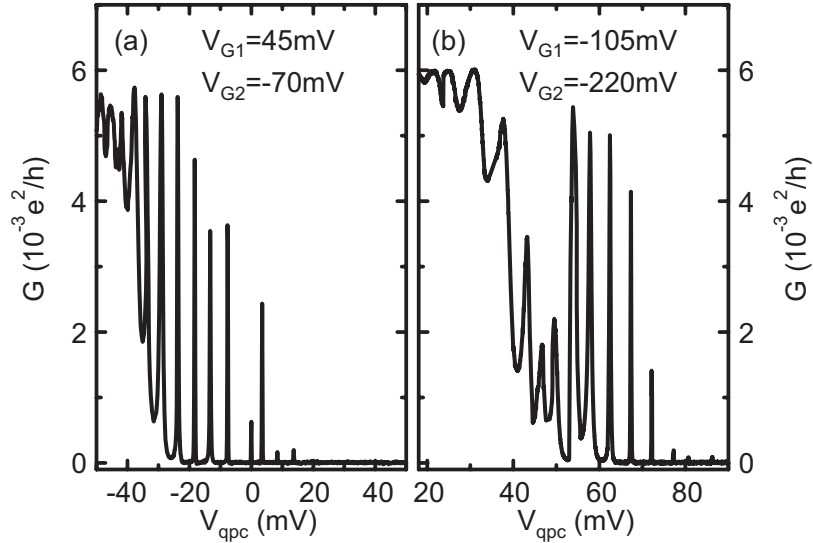


Figure 8.2: Zero bias differential conductance through the dot measured at 60mK base temperature as a function of the plunger gate voltage at two different gate configurations (a) [$V_{G1} = 45$ mV, $V_{G2} = -70$ mV] and (b) [$V_{G1} = -105$ mV, $V_{G2} = -220$ mV], both in the symmetric coupling regime.

8.3 Resonance peak shape and hole temperature

In the weak coupling regime each resonance line has been fitted with an expression for a thermally broadened Coulomb blockade peak in the multi-level as well as in the single-level transport regime according to [159]

$$G = G_{\max} \cdot \cosh^{-2} \left[\frac{\alpha e (V_{\text{qpc}} - V_0)}{\nu k_B T_{\text{hole}}} \right], \quad (8.2)$$

where G_{\max} and V_0 are the amplitude and the position of the Coulomb peak, respectively. The lever arm α of the plunger gate can be determined from Coulomb diamond measurements, as will be discussed later. The coefficient ν in the denominator of the cosh function equals 2 in the single-level regime while it is roughly 2.5 in case of multi-level transport [159]. For comparison a coupling broadened Lorentzian function was also fitted to each resonance [159].

The magnified view of a representative peak at $V_{\text{qpc}} = 67.3$ mV in Fig. 8.2(b) as well as the fitted curves are shown in Fig. 8.3. In all cases the thermally broadened resonance fits significantly better to the data than the coupling broadened resonance, confirming that the dot is indeed in the weak coupling regime and that the peak broadening is determined by temperature rather than by the coupling to the leads. From Coulomb diamond measurements (see below) it can also be concluded that $k_B T_{\text{hole}} \approx \Delta \ll E_C$, where Δ and E_C are the mean single-particle level spacing and the charging energy of the dot, respectively. This indicates that the dot is in the single-level transport regime and $\nu = 2$ applies in Eq. 8.2. As a fitting parameter we

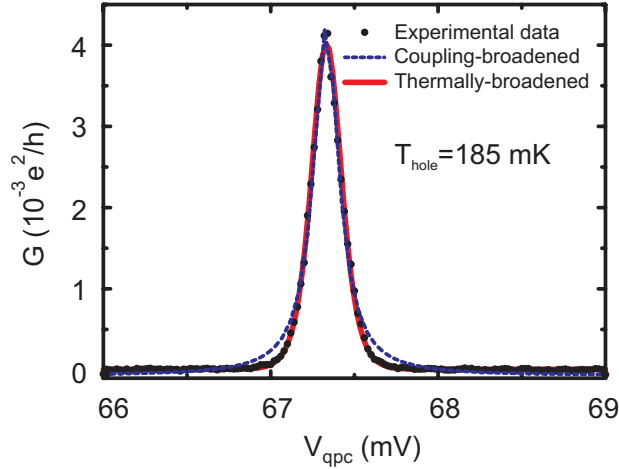


Figure 8.3: Magnified view of the Coulomb peak at $V_{\text{qpc}} = 67.3$ mV, $V_{\text{G1}} = -105$ mV, $V_{\text{G2}} = -220$ mV in Fig. 8.2(b). The experimental data (dots) are fitted to a thermally broadened (solid line) as well as to a coupling broadened resonance lineshape (dashed line). The thermally broadened model reveals a hole temperature of $T_{\text{hole}} = 185$ mK.

obtain typical hole temperatures in the range of $T_{\text{hole}} = 160 - 190$ mK. In case of symmetric coupling to the leads it is straightforward to evaluate the $\Gamma_{\text{S}} \approx \Gamma_{\text{D}} = \Gamma$ coupling strength from the $G_{\text{max}} = e^2\Gamma/(8\hbar k_{\text{B}}T_{\text{hole}})$ single-level transport formula for the resonance amplitude. Using the fitted values of T_{hole} we obtain $\Gamma \sim 1 \mu\text{eV}$ in agreement with the condition of the thermally broadened model.

8.4 Coulomb diamonds

Coulomb diamond measurements, i.e., measurements of the differential conductance as a function of bias voltage V_{bias} and plunger gate voltage V_{qpc} , were performed in the weak coupling regime. The result of an overall voltage scan is shown in Fig. 8.4. The size of the diamonds clearly increases towards higher V_{qpc} values which indicates the reduction of the electrostatic size of the dot, a phenomenon, that is characteristic to quantum dots with a small number of confined particles. From the extent of the last well resolvable diamonds in bias direction measured in the $-30 \text{ mV} < V_{\text{qpc}} < 20$ mV regime the value of $E_{\text{C}} \approx 2\text{meV}$ is estimated for the charging energy, while the lever-arm of the plunger gate is $\alpha \approx 0.28$. This charging energy corresponds to a capacitance of the dot $C = e^2/E_{\text{C}} \approx 8 \times 10^{-17}\text{F}$. Attributing a disk-like shape to the dot, the capacitance is given by $C = 8\epsilon_0\epsilon_r r$, where r is the radius of the dot and $\epsilon_r = 12.9$ for GaAs. This enables the rough estimation of the electronic diameter of the dot to be ≈ 170 nm, which is in good agreement with the lithographic dimensions of the sample and indicates an upper limit of ≈ 90 for the number of holes stored in the dot.

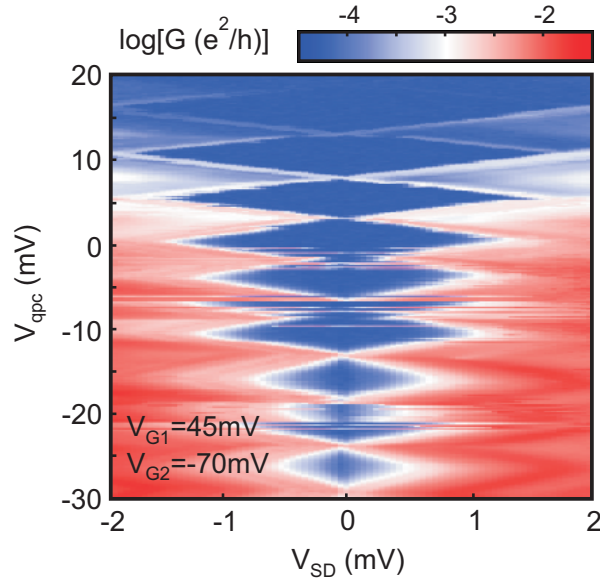


Figure 8.4: Logarithmic color map of the Coulomb diamonds observed in the finite bias differential conductance of the dot (dark regions represent low conductance). The charging energy associated with the size of the diamonds is clearly enhanced at higher plunger gate voltages. The measurement was performed at $V_{G1} = 45$ mV and $V_{G2} = -70$ mV gate configuration at 60 mK base temperature.

It is also visible in Fig. 8.4 that in certain dot configurations like at $V_{qpc} = -7$ mV and -21 mV, low-frequency switching noise due to charge rearrangements in the sample becomes quite expressed. Since these switching events may occur on a time scale of one day, a reasonable resolution of the consequent Coulomb diamond measurements is determined by the size of the scanned area in the $[V_{bias}, V_{qpc}]$ parameter space. Therefore, in order to resolve conductivity peaks outside the Coulomb diamonds which are related to excited states, the high resolution conductance scans are focused to a smaller regime in Fig. 8.4.

8.5 Excited states of the quantum dot

In case of a quantum dot with steep potential walls, the mean single-particle level spacing can be calculated as $\Delta = 2\pi\hbar^2/gm^*A$, where g is the degeneracy of hole states and A is the electronic area of the dot. Taking into account the electrostatic size of the dot as deduced from the charging energy and assuming an effective mass of $0.53 m_e$, the mean single-particle level spacing is estimated to be $\Delta \approx 20 \mu\text{eV}$. Due to the large effective mass of holes this is one order of magnitude smaller than typical values in electron quantum dots, but still comparable to $k_B T_{\text{hole}}$. An accordingly refined Coulomb diamond scan was performed at the same gate configuration as for the data presented in Fig. 8.4, and the result is displayed in Fig. 8.5. Apart from a small displacement due to a background charge rearrangement at $V_{qpc} \approx 4.5$ meV the

three diamonds in Fig. 8.5 can be directly mapped to Fig. 8.4. Outside the diamonds, parallel to the edges, lines of higher differential conductance are visible. The presence of the lines is further visualized in Fig. 8.6(a) by displaying various cross sections of the uppermost diamond along the V_{bias} axis. Apart from the missing left side counterpart of the right hand side line at $\approx 380 \mu\text{eV}$ which reveals the weak coupling of the excited states to the leads, the well visible left-right symmetry of the line distribution excludes an alternative explanation in terms of resonances in the random potential landscape of the leads. One can, therefore, unambiguously attribute these lines to elastic sequential tunnelling through the single-level excited states of the dot. The weak coupling of the excited states made the simultaneous detection of second order current steps in the Coulomb blocked region, characteristic to inelastic co-tunnelling [160] via the excited states difficult. However, a faint contrast in the middle of the Coulomb diamonds was found in the strongly coupled regime where the connecting excited state lines outside the diamonds were no longer resolvable.

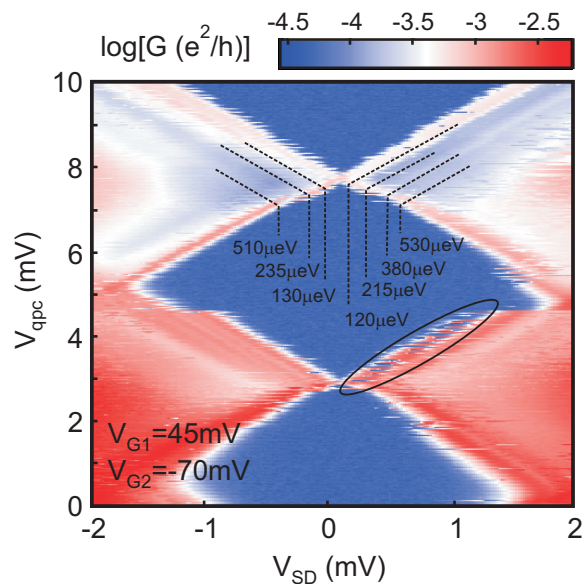


Figure 8.5: (a) High resolution scan of the Coulomb diamonds displayed in Fig. 8.4 in the $0 < V_{qpc} < 10$ mV regime. The parallel lines of higher conductivity outside the diamonds are attributed to sequential elastic tunneling through single-particle excited states of the dot. The corresponding excitation energies of the levels are also indicated. The black oval marks the fluctuations due to charge noise in the system.

While the broadening of the observed lines clearly exceeds both $k_B T_{\text{hole}}$ and the estimated $\Delta = 20 \mu\text{eV}$, the energy of the lowest well distinguishable excited state is found to be $120 \pm 10 \mu\text{eV}$. According to the above estimation this corresponds to an electronic dot diameter of ≈ 50 nm which implies an electronic area that is smaller by one order of magnitude compared to the value deduced from the charging energy and indicates a hole occupation number of $N \leq 10$. Beside the inaccuracy of the applied simple models this discrepancy may reflect the general breakdown of the

constant interaction model as well as the pronounced role of the strong hole-hole interactions at small occupation numbers. It is also to be noted that the value of the effective mass used for the estimation of the single-level spacing is taken from measurements of the extended 2DHG. It is conceivable that the effective mass of the carriers confined in the dot is different.

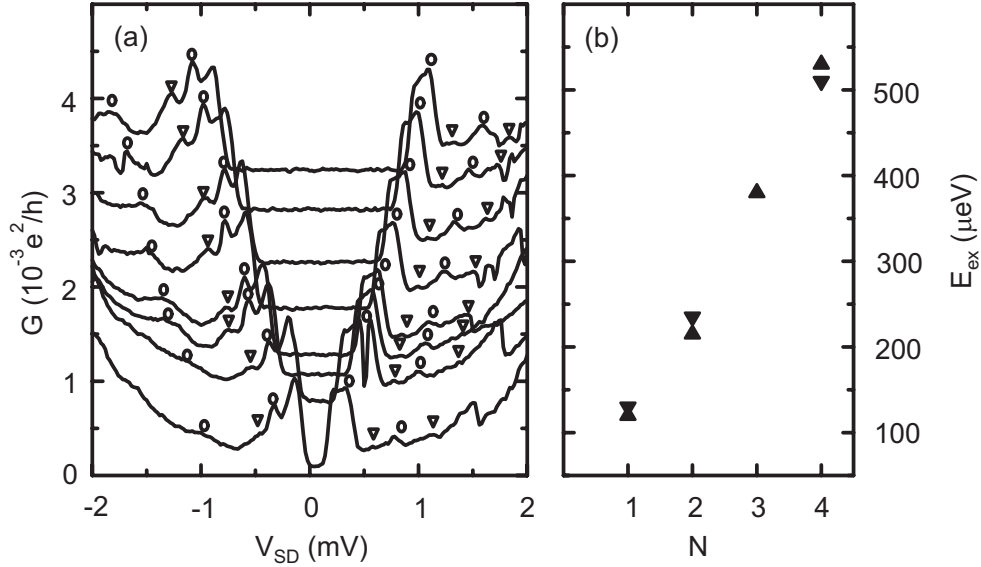


Figure 8.6: (a) Individual differential conductance traces recorded at various plunger gate voltages between $V_{\text{qpc}} = 8$ and 10 mV indicated by the horizontal lines on the right hand side of panel Fig. 8.5. Each curve is vertically shifted for better visibility by an offset which is proportional to the corresponding V_{qpc} value. The open circles and triangles indicate the local maxima which line up with the different excited state lines highlighted in the upper panel. (b) Excited state energies deduced from the lines at the right (\blacktriangle) and left (\blacktriangledown) sides in Fig. 8.5.

In the following the consequences of a small hole occupation number on the shape of the dot potential and on the spatial extension of the dot is briefly discussed. Due to their large effective mass compared to electrons, valence band holes can screen the confining potential more efficiently which results in an effective hard wall potential. Depending on the dot geometry this leads to a single-particle level spacing that generally increases with $\propto N^2$. In contrast, the observed equidistant distribution of the excited state levels displayed in Fig. 8.6(b) recalls a parabolic two-dimensional confining potential which reveals weak screening, providing further experimental evidence for the small number of holes stored in the dot. Although the actual potential landscape of the dot is not known, a quantitative analysis of a two-dimensional harmonic potential characterized by a $\Delta = \hbar\omega = 120 \mu\text{eV}$ single-particle level spacing and a hole effective mass of $m^* = 0.53 m_e$ also predicts a 50-110 nm spatial extension of the wavefunction for $N = 1-10$ holes. This is in good numerical agreement with the dot size determined directly from the observed

single-particle level spacing and a two-dimensional density of states and supports our argument about the break-down of the constant interaction model in the small N regime. In order to be able to determine the exact number of holes in the dot and thus explore the effects of hole-hole correlations experimentally, it is desirable to implement additional low noise QPC charge detection measurements in the close vicinity of the dot and work towards smaller dot sizes. While the former will be discussed in the next chapter, the latter is experimentally challenging due to the strong cross-capacitance of $G1$ and $G2$ in-plane gates on the opposite constrictions that prohibits independent tuning of the tunnel barriers. A set of top-gate fingers separated from the heterostructure by an insulating layer as described in section 3.2.4 would therefore be necessary to achieve stronger confinement.

8.6 Conclusion

We fabricated a quantum dot on a p-type GaAs/AlGaAs heterostructure by AFM oxidation lithography. Clear and reproducible Coulomb resonances were observed at weak couplings to the leads. From the Coulomb diamond measurements a charging energy with a magnitude up to ~ 2 meV was found at elevated plunger gate voltages indicating a small number of the confined holes. Lines of higher conductivity in the charge stability diagram outside the Coulomb blockaded region of the dot are resolved for the first time. They are attributed to sequential tunneling through single-hole excited states which may open new routes to the electrical manipulation of the individual hole spins.

Chapter 9

Time-resolved single-hole detection in quantum dots

9.1 Introduction

In the last chapter we saw how in-plane gates can be used in order to tune the number of holes in the quantum dot. This tunability is achieved as a result of capacitive coupling of these in-plane gates to the quantum dot. It is a fascinating experimental observation that the same capacitance coupling provides the possibility of measuring the charge of the quantum dot with a precision of a small fraction of an electron's charge using a nearby quantum point contact. The conductance of the point contact changes as a function of the average charge population in the quantum dot [161]. In this chapter we report on the observation of this phenomenon in a p-GaAs quantum dot system. Looking at the noise of the current through the point contacts provides much more information than just the average current. We will see that the telegraph noise of current enables time-resolved detection of the single-particle charging and de-charging of the nearby quantum dot [162–164]. This on the other hand reveals more information about the spectrum of the quantum dot, the relaxation of excited states to the ground state and their coupling to the leads. *

9.2 Charge detection in p-GaAs quantum dots

The sample and the measurement set-up are shown in Fig. 9.1a. The sample consists of a quantum dot (QD) together with a nearby quantum point contact (QPC). The charging energy of the QD is 2 meV which corresponds to a total capacitance of $C_{\Sigma} \approx 80aF$. If we assume a disk-like shape for the dot then $C = 8\epsilon_0\epsilon_r r$, where r is the dot radius and $\epsilon_r = 12.9$ for GaAs. This provides an (upper) estimate of ≈ 170 nm for the electronic diameter of the dot, giving an upper limit of 90 on the number of holes in the quantum dot. With this diameter the mean single-particle

*Valuable discussions with B. Küng is appreciated.

level spacing can be calculated as $\Delta = \pi\hbar^2/m^*A$ which is around $\Delta \approx 20 \mu\text{V}$.

The overall potential of the QPC is used to control the electrochemical potential of the dot, while the plunger gate is used to tune the QPC. The in-plane gates G1 and G2 are used to tune the tunnel coupling between the dot and source (S) and drain (D) but they also have a significant lever arm on the dot.

Fig. 9.1b shows simultaneous measurements of QPC and QD current as a function of the voltage applied to the G1 at the temperature of $\sim 1.2\text{K}$. As the gate voltage is increased, the holes are unloaded from the dot one by one. The dot current shows clear Coulomb peaks at the charge degeneracy points where the charge state of the dot changes by one electron charge. This can be clearly seen as a 30 pA-height step in the QPC current ($\approx 4\%$) at the position of the Coulomb peaks. Note that the average QPC current decreases as a function of G2 due to the corresponding lever arm since no electrostatic compensation was performed here. This was because it was realized that changing V_{qpc} or V_{pg} activates other fluctuators in the sample, therefore these voltages were kept constant during the experiment.

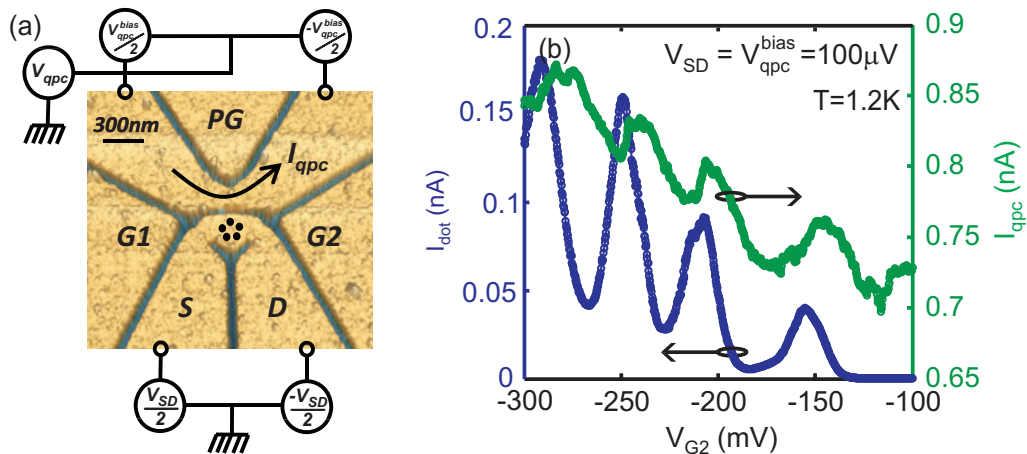


Figure 9.1: (a) AFM micrograph of the single dot with a QPC as an integrated charge read-out used for this experiment. The lines are defined by eBeam lithography technique followed by shallow etching described in chapter 2 and are 20nm deep. The applied bias voltages are shown on the same figure. The dot bias and the QPC bias are both symmetric. (b) The dot current (blue) and QPC current (green) as a function of G2 measured at the temperature of 1.2 K. The same bias of $100\mu\text{V}$ is applied to both quantum dot and the QPC and both currents were measured with an I-V converter with $R_f = 100\text{M}\Omega$ feedback resistance.

9.3 Time-resolved charge detection

When the bandwidth of the detector circuit Γ_D is low, the QPC only responds to the average charge population of the dot. Individual charging events are too fast to be followed when the dot current is measurable. With the bandwidth of about 3 KHz

due to the IV-converter, time-resolved charge detection becomes possible only when the dot current is below 0.5 fA which requires much more closed tunnel barriers.

9.3.1 The noise in the QPC current

The sample in Fig. 9.1a was later cooled down in a dilution refrigerator with a base temperature of 100 mK. In order to facilitate the search for the proper regime, the detector current noise is plotted in Fig. 9.2a as a function of the in-plane gates G1 and G2, while a bias voltage of $700\mu\text{V}$ was applied to the dot. The voltage bias on QPC will be always $250\mu\text{V}$ from now on unless explicitly mentioned in the text. The noise in the detector current increases along diagonal stripes in G1-G2 plane, indicating charge tunnelling effects.

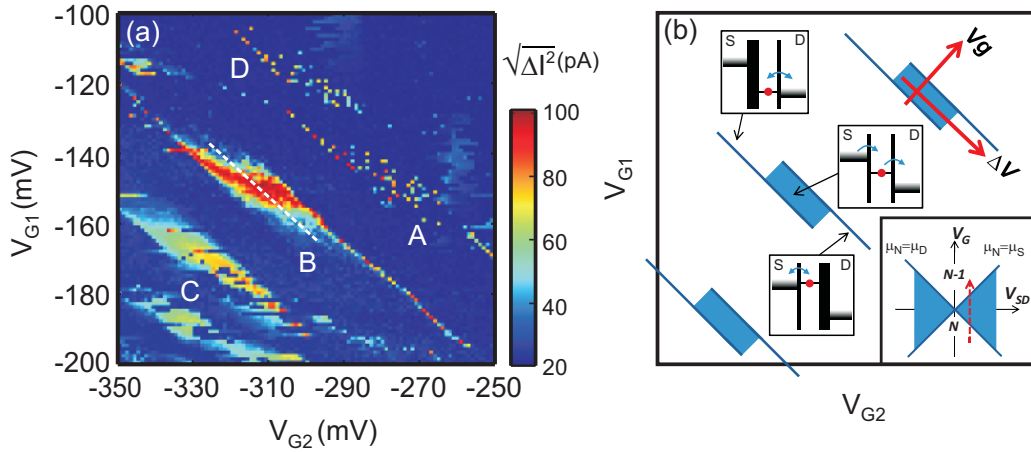


Figure 9.2: (a) The noise (standard deviation) of the detector current as a function of the in-plane gates G1 and G2. The bias over the quantum dot was $700\mu\text{V}$. (b) The schematic of the result with the level scheme of the dot with respect to the electrochemical potential of the leads at various points. The inset shows the constant bias cut through the Coulomb diamond between two charge states in the quantum dot. Two new axes V_g and ΔV can be defined as the symmetric and asymmetric linear combination of V_{G1} and V_{G2} .

Fig. 9.2b shows schematically what we expect to see. Increasing the voltage on the gates causes crossing of the Coulomb diamonds at finite bias (the inset of Fig. 9.2b). This results in parallel stripes in the G1-G2 plane where the dot level μ_N is between the electrochemical potentials of source μ_S and drain μ_D . On each stripe the lower edge corresponds to $\mu_N \sim \mu_D$ and the upper edge to $\mu_N \sim \mu_S$. The in-plane gates also have a lever arm on the tunnel barriers. As a result for example increasing V_{G1} increases the height of the tunnel barrier between the source and the dot, eventually completely closing this barrier. This is shown in Fig. 9.2b. The level scheme of the dot with respect to the source and drain is shown at various points in the figure. At the two stripe tails the noise is expected to be only due to fluctuations in the dot population due to thermal noise of left and right reservoirs. In a short

part of the stripe, the dot is coupled to the source and drain with similar couplings. Inside this stripe, the noise is due to shot noise as a result of uni-directional current flow from source to drain through the dot. Motivated by this schematic we define two new gate axes V_g and ΔV as the symmetric and anti-symmetric combination of V_{G1} and V_{G2} . V_g is used to tune the (electrochemical potential) levels in the dot while ΔV can be used to tune the coupling asymmetry to the source and drain.

The measurement in Fig. 9.2a shows qualitatively similar result. Especially the stripe B is as expected whereas the other stripes are quite different. The reason is that the stripe A is too fast and the stripe C too slow to have a significant effect on the detector current noise due to inevitable influence of V_g on the tunnel barriers. On this plot an anti-crossing of two resonances is visible indicated by D probably due to resonances in the dot/leads.

9.3.2 Telegraph noise

If we look at the detector current at any point inside the stripe B in Fig. 9.2a using a proper filter, the current shows a telegraph noise behaviour as a function of time because of the holes tunneling into and out of the dot. This telegraph noise is shown in Fig 9.3a for a point in the middle of white dashed line for a 200 msec time trace. For this trace an 8th-order software low pass filter with 3 KHz bandwidth was used. The transient time-response of this sharp filter results in some ringing effects due to Gibbs phenomenon [165] at the points the current changes abruptly.

Fig. 9.3b shows the normalized histogram of the current plotted in Fig. 9.3a, indicating that the current switches between two current-level states. The lower current level corresponds to a state where the dot holds one excess hole. The Gaussian distribution of each state is due to the Gaussian noise on the detector current. Using a threshold between the two levels it is possible to identify the state of the quantum dot at any time. The random variables τ_{in} and τ_{out} quantify the time it takes for a hole to tunnel into and out of the dot respectively. We can define the corresponding rates by the inverse of the average of these times

$$\Gamma_{in} = \frac{1}{\langle \tau_{in} \rangle} \quad \Gamma_{out} = \frac{1}{\langle \tau_{out} \rangle} \quad (9.1)$$

The total time of consecutive tunnelling in and out of a hole, the so-called *event time*, is $\tau_{event} = \tau_{in} + \tau_{out}$ and its average is given by

$$\begin{aligned} \langle \tau_{event} \rangle &= \langle \tau_{in} \rangle + \langle \tau_{out} \rangle \\ &= \frac{1}{\Gamma_{in}} + \frac{1}{\Gamma_{out}} \end{aligned} \quad (9.2)$$

motivating the definition of an event rate as

$$\Gamma_{event} = \frac{1}{\langle \tau_{event} \rangle} = \frac{\Gamma_{in}\Gamma_{out}}{\Gamma_{in} + \Gamma_{out}} \quad (9.3)$$

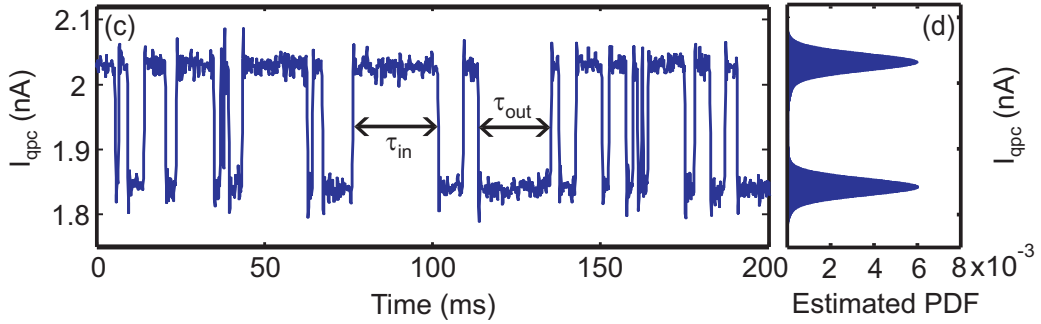


Figure 9.3: (a) The QPC current as a function of time, showing a few holes tunnelling into and out of the quantum dot. The lower current level corresponds to a state when the dot holds one excess hole. The QPC current was filtered with a 3 KHz software filter and re-sampled at a frequency of 14 KHz. The random variables τ_{in} and τ_{out} quantify the time it takes for a hole to tunnel into and out of the dot respectively and are used to calculate the tunnelling rates as explained in the text. (b) the normalized histogram of the detector current showing two distinct current levels corresponding to the two charge state of the dot

The exact distribution of tunnelling times will be discussed later. Note that a time trace like the one shown here does not specify if tunnelling in and out processes happened between the dot and both leads (thus producing a net current and shot noise) or between the dot and only one of the leads (no current and only thermal noise) or a mixed state. This has to be tuned by the gates as discussed with respect to Fig. 9.2a.

9.3.3 Fermi distribution of the leads

Tunnelling rates between the dot and the leads discussed in the previous section depend on the occupancy/availability of the states in the leads. Thus the Fermi distribution of the leads enters the picture

$$\begin{aligned}\Gamma_{\text{in}} &= \Gamma_S f(\epsilon_S) + \Gamma_D f(\epsilon_D) \\ \Gamma_{\text{out}} &= \Gamma_D (1 - f(\epsilon_D)) + \Gamma_S (1 - f(\epsilon_S))\end{aligned}\quad (9.4)$$

where we have defined the bare tunnelling rates of source and drain $\Gamma_{S/D}$ determined by the Fermi-golden rule [1], the Fermi-Dirac distribution $f(\epsilon) = (\exp(\epsilon/k_B T) + 1)^{-1}$ of the leads¹ and the tunnelling energy measured from the electrochemical potentials of the source and drain

$$\epsilon_{S/D} = \mu_N - \mu_{S/D} \quad (9.5)$$

Fig. 9.4 show the number of events in a 200 msec time interval as a function of dot bias and the gate voltage for two different gate configurations, exhibiting

¹Note that $f(-\epsilon) = 1 - f(\epsilon)$

Coulomb diamond pattern. From these diamonds a charging energy of $E_C \approx 2$ meV is extracted. Individual energy levels are not resolved as expected ($T_{hole} \sim 180$ mK that is approximately equal to the expected mean energy spacing).

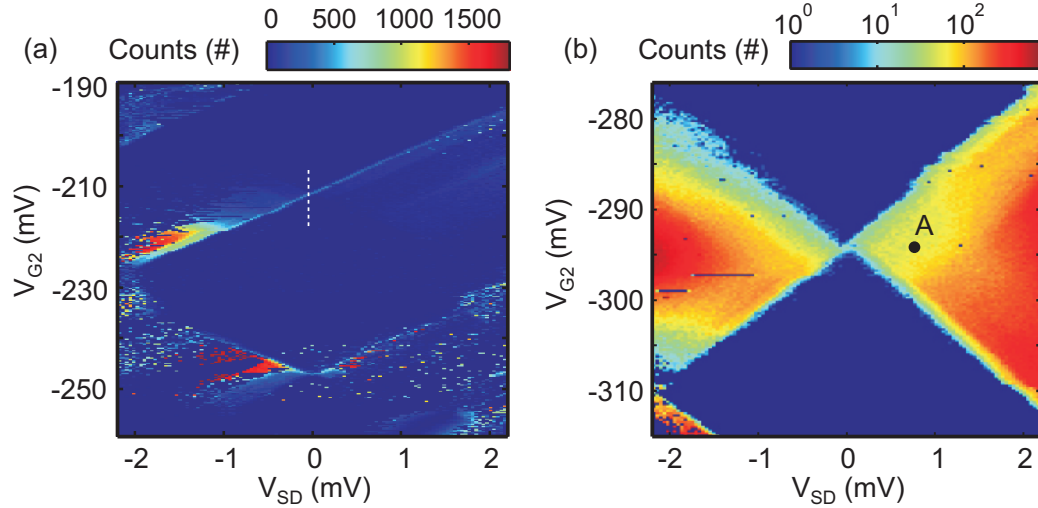


Figure 9.4: The number of charge tunnelling events in a 200 msec-long time interval as a function of the dot bias and the symmetric gate voltage V_g showing a typical Coulomb diamond diagram. The other gate configurations are (a) $V_{G1} = -180$ mV, $V_{QPC} = 167$ mV, $V_{PG} = -371$ mV and (b) $V_{G1} = -140$ mV, $V_{QPC} = 190$ mV, $V_{PG} = -320$ mV. The symbol *A* refers to a point where source and drain levels are $700\mu V$ apart and the dot resonance is in the middle.

Using the balance equation $\Gamma_{event} = p_0\Gamma_{in} = p_1\Gamma_{out}$ the occupancies $p_{0/1}$ are

$$p_1 = \frac{\Gamma_{in}}{\Gamma_{in} + \Gamma_{out}} \quad p_0 = \frac{\Gamma_{out}}{\Gamma_{in} + \Gamma_{out}} \quad (9.6)$$

which are also the average duty cycles of the telegraph noise if written in terms of $\langle \tau_{in/out} \rangle$. For low dot bias $\epsilon_S \sim \epsilon_D$, we get $p_1 \sim f(\epsilon)$ and hence the temperature can be extracted by the amount of time the detector signal spends in the "one"-state. This occupation along the white dashed cut through Fig. 9.4a is shown in Fig. 9.5a where a temperature of 180 mK is extracted from the fit. A fit to the corresponding number of events, plotted in Fig. 9.5b provides the lower temperature limit of 100 mK. This discrepancy is justified given the uncertainties in the latter due to the finite length of the time traces (1 sec each) and the finite bandwidth of the detector (2 KHz).

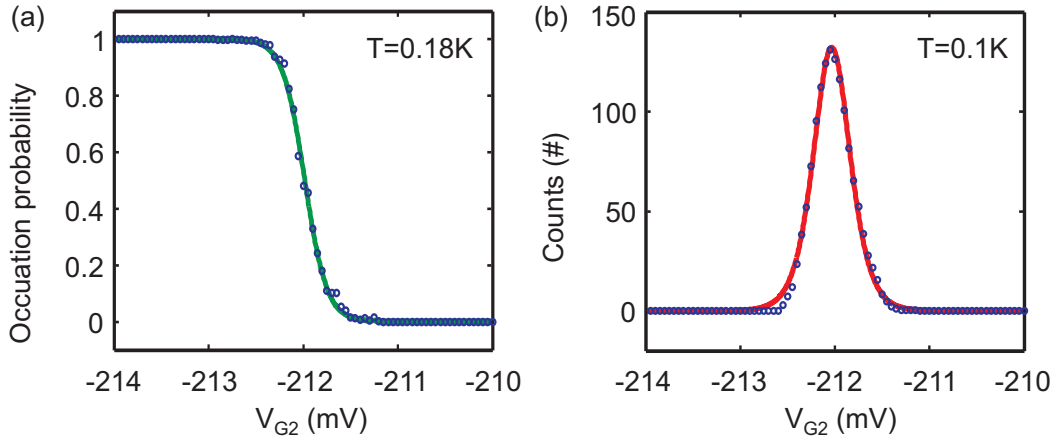


Figure 9.5: The population of the dot and the number of events along the white dashed cut in Fig. 9.4a. (a) Occupation probability of the dot extracted from the duty cycle of time traces together with a Fermi-Dirac distribution fit. (b) Event rate with a thermally broadened fit from which a temperature of 100 mK is extracted.

9.3.4 Tunnel rates

Changing a gate voltage does not only cause an energy shift of the dot levels, but also affects the height of the tunnel barriers connecting the dot to the leads². Fig. 9.6a shows a sketch of the potential landscape of the QD with a bias voltage applied to the source and drain. For elastic tunnelling the holes entering the dot have to tunnel through a potential barrier of height $U_{SB} - \mu_N$ while the holes leaving the dot have to cross a barrier of height $U_{DB} - \mu_N$. Even in WKB (semi-classical) approximation the tunnelling amplitude of holes across a barrier depend not only on the height but also on the width and the exact shape of the potential barrier. These details are of course not known but if we assume that the gate voltage changes only the height of the barrier to first order, for small perturbation to this barrier height δU_{SB} and the dot level $\delta \mu_N$, the tunnelling rate is expected to depend exponentially on the gate voltage [167].

$$\Gamma \sim \Gamma \exp(-\kappa(\delta U_{SB/DB} - \delta \mu_N)) \quad (9.7)$$

The dot levels and potential barrier height depend capacitively on the gates. Changing only δV keeps μ_N constant and only affects $U_{SB/DB}$. Assuming the structure is symmetric this results in $\delta U_{SB/DB} = \mp \gamma_{L/R} \delta(\Delta V)$ and therefore

$$\Gamma_S \sim \exp[+\gamma_S \delta(\Delta V)] \quad \Gamma_D \sim \exp[-\gamma_D \delta(\Delta V)] \quad (9.8)$$

Fig. 9.6b shows how the tunnelling rates Γ_{in} and Γ_{out} change as a function of the asymmetric gate voltage ΔV for the point A in the Coulomb diamond (Fig. 9.4). At this point $\Gamma_{in} = \Gamma_S$ and $\Gamma_{out} = \Gamma_D$. The rates change exponentially in agreement

²This section is written along a similar part from the PhD thesis of S. Gustavson [55] [166]. For example same notation is used.

with the prediction of Eq. 9.8. The solid lines are fits to the data indicating γ_S and γ_D . It is convenient for future references to define a normalized barrier asymmetry parameter a that depends strongly on ΔV

$$a = \frac{\Gamma_{in} - \Gamma_{out}}{\Gamma_{in} + \Gamma_{out}} \quad (9.9)$$

$a = 0$ indicates a symmetric coupling, while $a = \pm 1$ is the asymmetric configuration where one of the rates, either Γ_{in} or Γ_{out} is dominant.

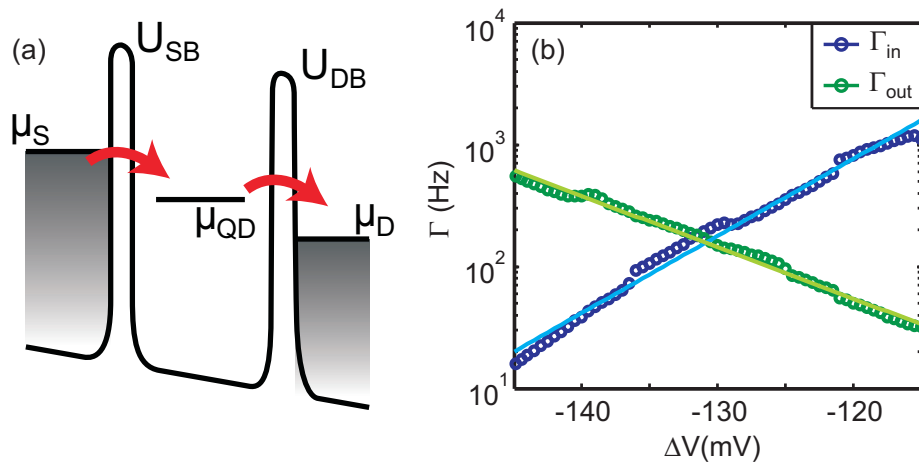


Figure 9.6: The rates for tunnelling into and out of the dot as a function of the asymmetric voltage ΔV on the in-plane gates for the point A indicated in Fig. 9.4b. At this point Γ_{in} and Γ_{out} are the rate of source-dot and dot-drain tunnelling barriers respectively. The rates indeed change exponentially with the asymmetric gate voltage. The solid lines are fits with $\log \Gamma_{in} = +62.3\Delta V + 10.5$ and $\log \Gamma_{out} = -42.2\Delta V - 3.3$.

9.3.5 Time histograms

So far we discussed only in terms of average tunnelling times τ_{in} , τ_{out} and τ_{event} . Fig. 9.7 shows the histogram of these tunnelling times for the two different coupling symmetry configuration (a) ($a = 0$) and (b) ($a = 0.83$). The histograms shown in this figure for τ_{in} and τ_{out} are linear in the logarithmic scale for more than over 4 orders of magnitude. Therefore, it is an experimental observation that these random variables have exponential distribution with the following probability density function (PDF)³

$$p_{in}(t = \tau_{in}) = \Gamma_{in} \exp(-\Gamma_{in}\tau_{in}) \quad p_{out}(t = \tau_{out}) = \Gamma_{out} \exp(-\Gamma_{out}\tau_{out}) \quad (9.10)$$

This is expected as in the weak coupling regime ($h\Gamma \ll k_B T$), the individual tunnelling events are sufficiently separated in time from each other and are thus independent. The stability of the sample is striking, considering that for each of

³For an stream of particles with inter-arrival times given by i.i.d exponential distribution $p(t) = \lambda \exp(-\lambda t)$, the number of arrivals in a $(0, T)$ period is a Poisson distribution $p_T(n) = e^{-\lambda T} (\lambda T)^n / n!$

these plots about two million events over more than 5 hours were taken into account. The key property of the exponential distribution is its being memoryless $P(\tau > t + s | \tau > s) = P(\tau > t)$, justifying the use of Markovian statistics and the rate equation technique to calculate the probabilities. The rate equation for the previous results trivially reads

$$\dot{p}_{in} = -\Gamma_{in}p_{in} \quad \dot{p}_{out} = -\Gamma_{out}p_{out} \quad (9.11)$$

This Markovian statistics property has to be applied with some care. Any extra internal degree of freedom in the dot (e.g. two indistinguishable dot states) that is coupled to the leads, often called *hidden states*, result in some memory effects and the tunnelling time distributions become multi-exponential or totally non-exponential in general [168–171]. In a hole quantum dot with a dense spectrum there are many hidden states with different couplings to the leads that could result in non-Markovian statistics if the relaxation rate is comparable to the tunnel couplings. Therefore we should emphasize that the exponential distribution of the tunnelling times is merely an experimental observation (see appendix G for violation of this assumption).

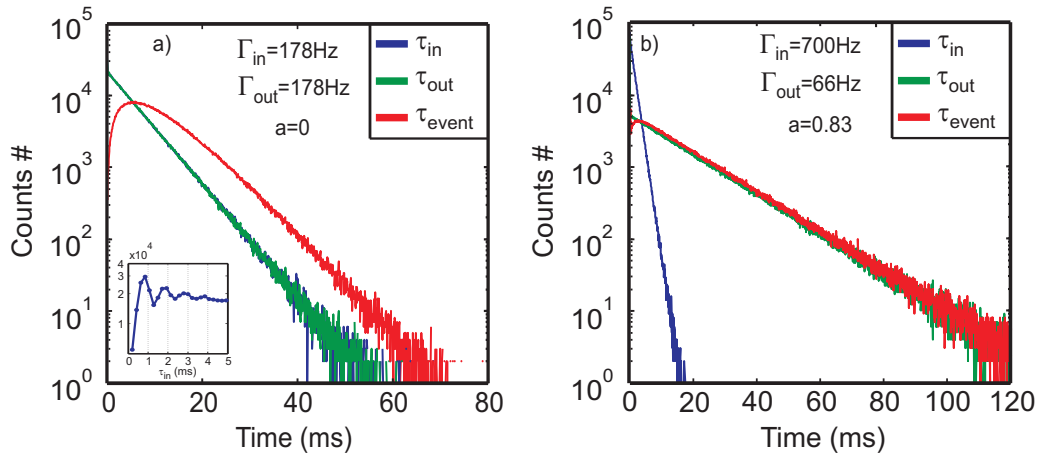


Figure 9.7: The histogram of times a hole needs to tunnel into the dot (blue), tunnel out of the dot (green) and the event time defined as the sum of two consecutive tunneling in and out events (red) for different tunnel barrier asymmetry. (a) Symmetric configuration ($a = 0$). τ_{in} and τ_{out} have the same distribution and the (non-exponential) event time distribution shows a clear anti-bunching effect. The inset shows a zoom into the first 5 msec part of the τ_{in} histogram, showing deviations from Markovian statistics due to memory effects as a result of the transient response of the filter. (b) Asymmetric configuration ($a=0.83$). In this case τ_{in} is ~ 10 times shorter than τ_{out} in average and the quantum dot acts effectively as a single barrier system. The event time distribution is very similar to an exponential distribution corresponding to the bottleneck barrier and the anti-bunching effect is diminished. About two million events accumulated over more than 5 hours were used to calculate the histograms which indicates the stability of the sample.

Another source of memory effects is the low pass filter used to filter the data [172].

This can be seen in the inset of Fig. 9.7a where a zoom into the first 5 msec part of the τ_{in} distribution is shown. At very short times characterized by the inverse bandwidth of the filter, the exponential distribution is suppressed. The non-Markovian behavior of the filter can also be clearly seen. This transient behavior can be ignored if the relevant rates in the system are smaller than the filter bandwidth ($\Gamma \ll \Gamma_D$).

Also shown in this figure is the distribution of event times $\tau_{event} = \tau_{in} + \tau_{out}$. Each event corresponds to a hole being transferred from source to drain. This distribution is clearly non-exponential for the symmetric coupling configuration in Fig. 9.7a. Thus the individual charge transfer effects are not independent. This is a result of Coulomb blockade and manifests itself as the strong suppression of τ_{event} distribution for short times. In other words, the holes have to wait until the previous holes leaves the dot before the new one can enter. This short-time suppression is commonly called *anti-bunching* [55] and is the origin of sub-poissonian shot noise. This is no longer true for the asymmetric coupling configuration in Fig. 9.7b. The anti-bunching effect is (partially) diminished and the τ_{event} distribution resembles more an exponential distribution. In this case $\tau_{event} \approx \tau_{out}$ and the dot behaves effectively like a single-barrier system (note that the fast barrier coupling Γ_{in} is still slower than the bandwidth. A truly single-barrier system would not be countable).

9.3.6 Connection to the queueing theory

In contrast to what it may sound, the anti-bunching effect introduced in this chapter has nothing to do with the fermionic statistics of holes. Similar behavior has been observed for photons in quantum dot single photon sources [173] or the photon blockade effect [174]. In fact any single-capacity classical system would show exactly the same behaviour. Particularly this topic has been studied quite intensively in the 80s and 90s in the framework of queueing theory in connection with the traffic engineering of computer networks [175]. Data packets coming to a network node usually have exponential inter-arrival time (Markovian statistics). In addition due to the variable length of the packets, even if the service rate of a switch/router is constant, the dispatching time becomes a Markovian process. Such a system is usually described by the M/M/1/K model (Markovian input/Markovian output/single server/buffer size K). Of particular interest is the buffer size of the device. A single-packet buffer switch/router exhibits the same statistical properties as a Coulomb blocked quantum dot in the weak coupling regime.

9.4 Fano factor

The current spectral density $S_I(\omega)$ is defined by the expression ⁴

$$S_I^2(\omega) = \int dt e^{i\omega t} \langle\langle I(0)I(t) \rangle\rangle \quad (9.12)$$

⁴For a definition of cumulant average $\langle\langle X \rangle\rangle$ see Chapter 10

The squared current spectral density is proportional to power spectral density (see section 3.3.2). The charge Q transferred from source to drain is $Q(t) = \int_0^t I(\tau) d\tau$. This implies

$$\langle Q \rangle = \langle I \rangle t \quad (9.13)$$

It can be shown [1, 176] from these two definitions (using $\lim_{t \rightarrow \infty} \sin^2 \omega t / \omega^2 t = \pi \delta(\omega)$) that the variance of this charge is given by

$$\langle \langle Q^2 \rangle \rangle = t S_I^2(0) \quad (9.14)$$

On the other hand, Q is the number of transferred charges n times the unit charge q . ($\langle Q \rangle = q \langle n \rangle$ and $\langle \langle Q^2 \rangle \rangle = q^2 \langle \langle n^2 \rangle \rangle$). Combining Eq. 9.13 and 9.14 we get

$$\begin{aligned} S_I^2(0) &= \frac{\langle \langle Q^2 \rangle \rangle}{\langle Q \rangle} \langle I \rangle \\ &= e \frac{q}{e} \frac{\langle \langle n^2 \rangle \rangle}{\langle n \rangle} \langle I \rangle \\ &= eF \langle I \rangle \end{aligned} \quad (9.15)$$

This is the Shockley formula and relates the zero-frequency shot noise power to the average current. Here we have defined the *Fano factor* as $F = q/e \cdot C_2/C_1$ (we use the notation $C_m \equiv \langle \langle n^m \rangle \rangle$). The appearance of charge in this formula enables measuring the charge of carriers using simultaneous noise and average current measurement. This technique has been used to measure the charge of quasi-particles in the fractional quantum Hall regime [177, 178] and quantum dots in the Kondo regime [179, 180] and the double charge of Cooper pairs in superconductors [181]. It is noteworthy that measuring noise with a nearby QPC can only be used to measure C_2/C_1 . Although this is an interesting probe for the correlation between the carriers, measuring the charge of the quasi-particle carriers is not possible with a pure counting experiment.⁵

For a Poissonian process the variance and the mean are the same $C_2 = C_1$ and therefore the Fano factor is equal to unity. Any suppression of the Fano factor below one indicates correlations between the carriers. This quantity is shown in Fig. 9.8 as a function of barrier asymmetry. Note that the Fano factor approaches unity for $a \rightarrow \pm 1$ showing that the statistics is effectively Poissonian for very asymmetric barriers. This goes in parallel with the time histogram in Fig. 9.7b. For the symmetric case the Fano factor drops to 0.5 indicating that the Coulomb blockade regulates the current as was discussed in connection to Fig. 9.7a. The solid line shows the model prediction discussed in chapter 10. The agreement with the model is striking. The figure also shows the so-called skewness which is another statistical property of transport, again discussed in chapter 10.

⁵The charge of holes can be extracted from quantum hall measurements and its equal to the charge of electrons, thus we have $F = C_2/C_1$.

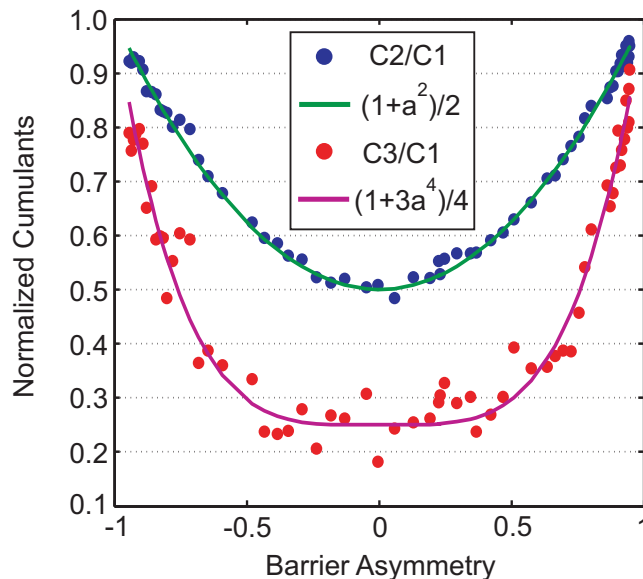


Figure 9.8: The first two normalized cumulants of the statistical distribution of holes traversed the dot as a function of tunnel barrier asymmetry a , calculated from 100 time traces, each 10sec long. The blue points show $C2/C1$ or the Fano factor, and the red points show $C3/C1$ which is the skewness (see chapter 10). The solid lines are the model predictions. While the Fano factor agrees quite well to the model the skewness points are scattered much more due to the limited statistics.

9.5 The excited state spectrum

As discussed in previous chapters, the large effective mass of the holes results in a dense spectra of confined states and therefore hole quantum dots can be considered to be a bridge between electron quantum dots and metallic SETs. This manifests in the fact that it is not possible to resolve the excited states in the diamond measurements like the one shown in Fig. 9.4. Were this resolution possible, we would expect a stepwise increase of the number of events with the steps parallel to the edges of the diamond. Nevertheless we can already see in this figure that the number of events generally increases with increasing dot bias. This can be seen more clearly in Fig. 9.9 where the tunneling rates are shown as a function of the dot bias on resonance ($V_{G2} = -295mV$). It can be seen from this plots that Γ_{in} , Γ_{out} and the event rate Γ_{event} all increase exponentially with the dot bias. More insight into the role of dot spectra in the result is obtained if we look at the Γ_{in} and Γ_{out} diamonds in Fig. 9.10. The equi- Γ lines are parallel to the edges of the diamond. In particular Γ_{in} depends only on the difference in the electrochemical potentials of the source and the dot $\mu_S - \mu_N^0$ (Note that for negative dot bias the role of source and drain changes). This suggests that the number of available (excited) states between these two levels is the cause of the increase in the rate. Provided that they have enough energy, the tunnelling-in holes can occupy any of these states and this increases

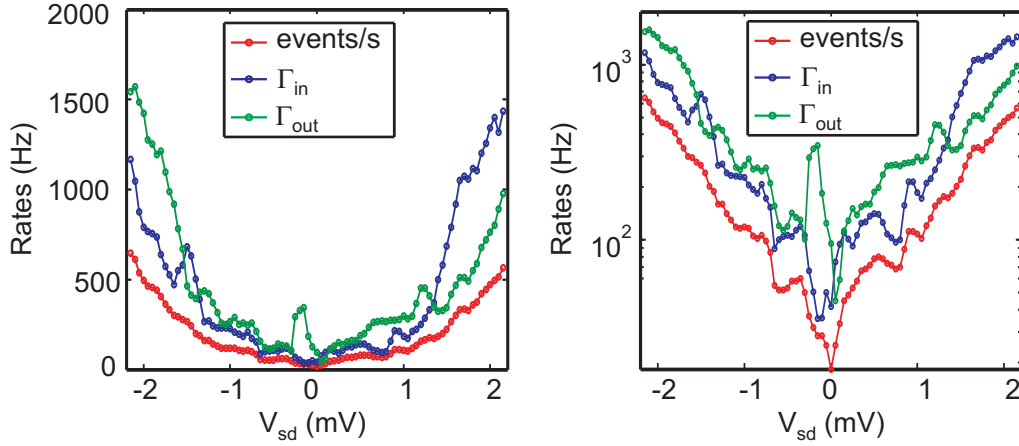


Figure 9.9: The tunnelling rates Γ_{in} , Γ_{out} and the event rate Γ_{event} all increase with the dot bias. This is shown in both linear (a) and logarithmic (b) scales, indicating that the overall dependence is exponential.

the tunnel rate with bias. Similarly Γ_{out} depends only on the difference between the electrochemical potentials of the drain and the dot $\mu_N^0 - \mu_D$, meaning that the number of options also increases with the dot bias for tunnelling-out holes.

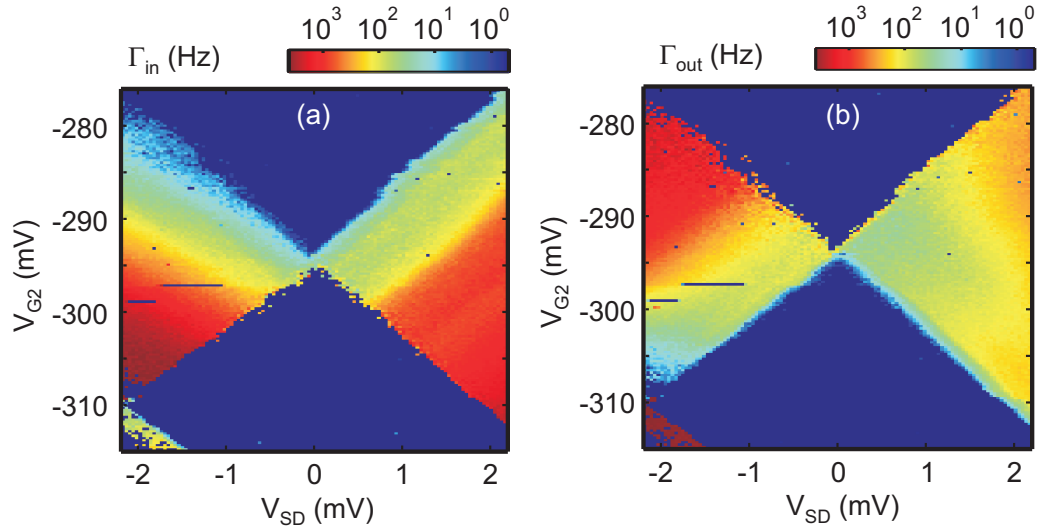


Figure 9.10: The rates of (a) tunnelling into the dot (b) and tunnelling out of the dot measured at the same time as the number of events in Fig. 9.4b.

9.5.1 Possible explanations

The increase in Γ_{in} and Γ_{out} with the dot-bias can be understood in terms of the additional available tunnelling channels in a dense spectrum system. A schematic of the energy spectrum of the dot with $N_0 - 1$, N_0 and $N_0 + 1$ holes inside is shown

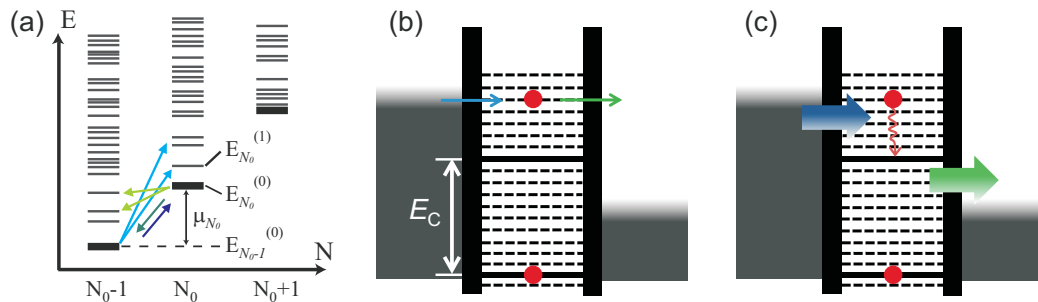


Figure 9.11: (a) Typical energy spectra of a dot with $N_0 - 1$, N_0 and $N_0 + 1$ holes inside (adapted from [1]). Also shown are possible transitions between the $N_0 - 1$ and N_0 charge states. The dark color arrows represent the transition between the ground states while the light color ones represent similar transitions involving the excited states (The thick line of the ground state is just for clarity and does not indicate degeneracy and nor a broader linewidth). (b) and (c) show two possible scenarios for explaining the bias-dependence of the event rate. (b) Strongly energy dependent barriers and no relaxation in the dot. The tunnelling is exponentially enhanced at higher energies. (c) In the case of moderate energy-dependence of barriers, tunnelling into and out of the dot both involves many excited states and the relaxation does not change the qualitative picture.

in Fig. 9.11a. The blue/green arrows show the possible transitions for tunnelling into/out of the N_0 state. The dark color arrows represent the transitions between the ground states while the light color ones represents the transitions involving the excited states. Therefore, for example it is possible for a hole in the ground state of N_0 to tunnel out and leave the dot in the excited state of $N_0 - 1$ charge state. Motivated by these ideas, the level diagram of the dot is represented in Fig. 9.11b,c with excited states above and below the ground state electrochemical potential $\mu_{N_0}^{\pm m}$.

The exponential increase of the tunnelling rates with bias suggests a strong energy-dependence of the barriers. This has two consequences: first, the bias voltage applied to the source and drain will have a gating effect along the same direction discussed in section 9.3.4. As the bias is applied symmetrically this would favor Γ_{out} exponentially against Γ_{in} . Second, since the dot has an almost continuous spectra the holes can tunnel in and out elastically at all energies. Due to a strong energy-dependence of the barriers the higher levels would have exponentially higher rates. Therefore tunnelling happens basically at an energy ϵ_S within a kT window of μ_S optimized by the corresponding Fermi distribution (ϵ_S is measured from μ_S as in Eq. 9.6). If there is no relaxation in the dot, tunnelling out would also happen at the same energy and therefore increase exponentially with the bias in agreement with the data. This scenario is shown schematically in Fig. 9.11b.

However there are two problems with this scenario: first, the relaxation of a hole to the ground state would drastically change this picture and second, in the absence of relaxation the tunnelled-in hole can tunnel back to the source especially if the

drain barrier is higher than the source barrier $\Gamma_S > \Gamma_D$. In this case we can write

$$\Gamma_{in} = \Gamma_S f(\epsilon_S) \quad \Gamma_{out} = \Gamma_S(1 - f(\epsilon_S)) + \Gamma_D \quad (9.16)$$

$$a = \frac{\Gamma_S(2f(\epsilon_S) - 1) + \Gamma_D}{\Gamma_S + \Gamma_D} \quad (9.17)$$

For large asymmetry $\Gamma_S \gg \Gamma_D$ this gives $a \rightarrow 2f(\epsilon_S) - 1$, which is a value around zero and independent of ΔV . This is in contrast with the previous observations that Γ_{in} and Γ_{out} can be tuned as a function of ΔV as plotted in Fig. 9.6 together with the Fano factor measurements of Fig. 9.8. There obviously the barrier asymmetry a takes all the values between ± 1 as a function of ΔV . Also the apparent Fano-factor of the thermal noise is equal to $1/2$ and this is obviously in contrast to the Fano factor measurement results, indicating that the relaxation is much faster than the tunnel barriers (~ 1 KHz in this case).

Another possible explanation assuming a moderate energy-dependence of barriers is that many excited states contribute to both tunnelling in and out rates as shown schematically in Fig. 9.11c. Here Γ_{out} also increases with dot bias even if the relaxation is taken into account.

9.5.2 Complications arising due to QPC back-action

Detecting the charge state of the dot with a nearby QPC is invasive. Besides dephasing of the charge coherence induced by the detector [182, 183] the power consumed by the QPC is emitted as photons and phonons throughout the sample and hence may cause back-actions on the quantum dot either by increasing the effective temperature of the leads [184] or due to photon and phonon-assisted⁶ tunnelling (PAT) [185, 186]. These PAT effects are usually understood in terms of energy transfer between the QPC and the electrons/holes in the dot so that they could overcome Coulomb blockade [187, 188]. Therefore it is characterized by an energy cut-off corresponding to the mean level spacing of the dot, below which this energy transfer does not take place. Identifying the dense spectra of the quantum dot as the source of the peculiar bias dependence of the rates, it is curious if the detector has any back-action on the quantum dot due to PAT and how much does it contribute to the transport and its statistical properties.

Fig. 9.12 shows how the variation of the bias on the detector QPC influences the tunnelling rates in the dot. For large QPC bias ($V_{QPC}^{bias} > 600\mu V$) many fluctuators in the QPC are activated and the overall quality of the signal is degraded. The red shaded area shows the onset this degradation. Fig. 9.12b shows the effect of a symmetric QPC bias on the Fano factor and skewness of the hole transfer distribution. The agreement between the measurements and the model (dashed line) indicates that the effect of the QPC on the dot can be phenomenologically lumped

⁶This effect is sometimes called Boson-assisted tunnelling

into tunnelling rates Γ_{in} and Γ_{out} . While Γ_{out} shown in Fig. 9.12a increases monotonically with the QPC bias, Γ_{in} decreases, suggesting that the influence of QPC on the dot is most probably a simple gating effect. Considering the close proximity of the QPC leads and the dot tunnel barriers in Fig. 9.1a this is not surprising as most of the applied bias voltage drops over the QPC. Therefore the source tunnel barrier increases (decreasing Γ_{in}) and the drain tunnel barrier decreases (increasing Γ_{out}) for positive QPC bias. For all the other experiments the QPC bias is kept at $250\mu V$ unless explicitly mentioned.

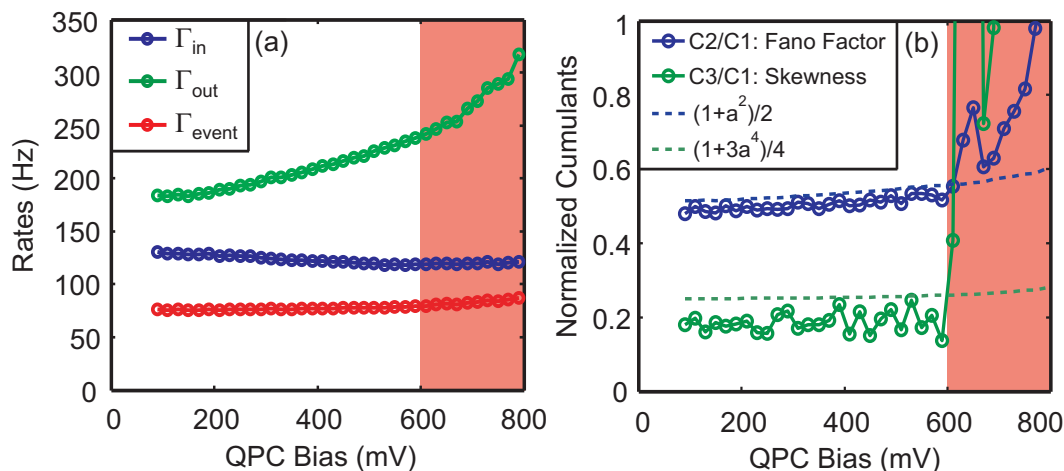


Figure 9.12: (a) Γ_{in} , Γ_{out} and Γ_{event} as a function of the bias voltage on the QPC. The decrease in Γ_{in} and increase in Γ_{out} is most probably due to gating effect. (b) The Fano factor and Skewness as a function of QPC bias show that the statistics of electron transport is not influenced by the emission of energy quanta by the QPC. The dashed lines show the model predictions discussed in the text. The red shaded area shows the onset of the detector signal degradation due to charge fluctuators in the QPC (Counting is not possible for $V_{QPC}^{bias} < 50\mu V$).

9.6 Rate equation simulation

In this section we employ a simple rate equation model to understand the role of the dense spectrum of the quantum dot on the tunnelling rates measured in the experiment. The the number of states of a degenerate (symmetric) two-dimensional harmonic oscillator grows quadratically with energy. However we expect our quantum dot to be far from few hole regime, as discussed before. Therefore a linear spectrum with a constant mean-level spacing is assumed in the following.

9.6.1 Excited states just for Γ_{in}

To verify the ideas developed in the previous section we did some rate equation calculations for a dot with a single state in E_N configuration and few excited states

in the E_{N+1} configuration. All the states in the dot are assumed to be coupled to the leads with a similar tunnelling rate of 100 Hz. This system can be described by

$$\begin{aligned}\dot{p}_N &= \sum_j \left[\Gamma_{N \leftarrow (N+1, j)} p_{N+1}^j - \Gamma_{(N+1, j) \leftarrow N} p_N \right] \\ \dot{p}_{N+1}^i &= \Gamma_{(N+1, i) \leftarrow N} p_N - \Gamma_{N \leftarrow (N+1, i)} p_{N+1}^i + \sum_{j \neq i} \left[W_{i \leftarrow j}^{N+1} p_{N+1}^j - W_{j \leftarrow i}^{N+1} p_{N+1}^i \right]\end{aligned}\quad (9.18)$$

The $W_{i \leftarrow j}^{N+1}$ parameters describe the relaxation of the excited states to the ground state and are non-zero (and independent of i and j) for $i < j$. The tunnelling rates $\Gamma_{in} = \Gamma_{N+1 \leftarrow N}$ and $\Gamma_{out} = \Gamma_{N \leftarrow N+1}$ depend on the gate and the electrochemical potentials of the source and drain as discussed in 9.3.3.

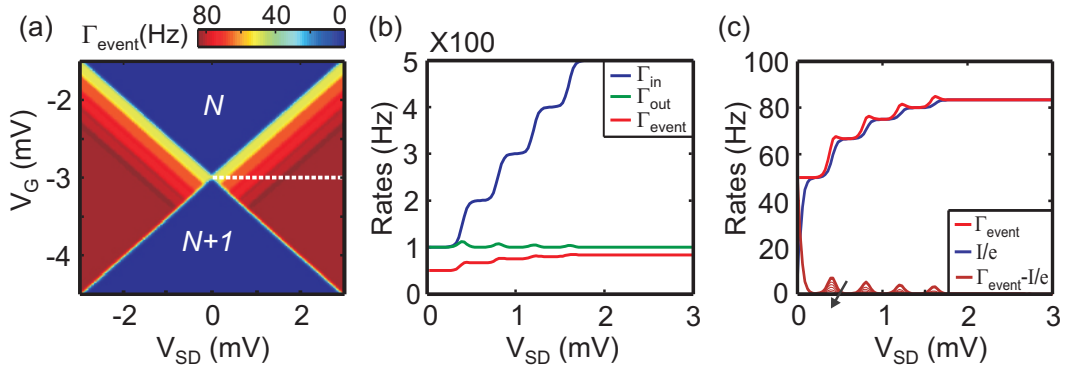


Figure 9.13: Rate equation simulation for a dot with the spectrum of $E_{N+1}^m = \{0, 200, 400, 600, 800\} \mu eV$ in $N + 1$ charge state. (a) The event rate Γ_{event} as a function of bias and the gate voltage. The excited states are parallel to the source electrochemical potential (b) Γ_{in} , Γ_{out} and Γ_{event} along the white dashed cut in a. Γ_{in} increases with 100 Hz increments each time an excited states comes below μ_S , while Γ_{out} mainly stays constant at 100 Hz with short peaks at the bias corresponding to $\mu_S = \mu_N^m$ due to thermal noise with the source. The event rate increases stepwise starting from 50 Hz but tends to saturate at 100 Hz limited by the tunnelling out rate. (c) Comparison of the event rate and the particle current along the white dashed line in a. The difference comes from the thermal fluctuations each time the electrochemical potential of the source aligns with one of the states of the dot. The difference between these two is also shown for increasing the relaxation $\Gamma_\gamma = \{0, 50, 100, 200, 400, 800\}$ Hz in the dot. Except the ground state, the thermal fluctuations of the excited states goes down to zero with increasing the relaxation.

Fig. 9.13a shows the finite bias measurement of event rate calculated by setting the left side of the above equations to zero and finding the steady-state values, using the normalization condition $p_N + \sum_j p_{N+1}^j = 1$. The total tunnelling rates are then calculated using the recipe $\Gamma_{out} = \sum_j \Gamma_{out}^j p_j / \sum_j p_j$ and a similar one for Γ_{in} .

The tunnelling rates along the white dashed line of this figure are shown in Fig. 9.13b. As a function of dot bias, Γ_{in} increases with 100 Hz steps each time

one of the excited states enters the bias window whereas Γ_{out} mainly stays constant at 100 Hz but shows a small peaks each time one of the excited states aligns with μ_S due to thermal noise and back-and-forth tunnelling with this lead. Γ_{event} also increases with the dot bias but the step height decreases so that it tends to saturate at 100 Hz tunnelling out rate as the bottleneck barrier. Fig. 9.13c shows the effect of relaxation on the result. The difference between the event rate and the particle current caused by thermal noise quickly goes to zero as soon as the relaxation rate becomes comparable with the tunnel couplings.

9.6.2 Excited states for Γ_{in} and Γ_{out}

Fig. 9.14 shows the result of similar calculations this time assuming that both N and N+1-hole configurations have each 20 states with equal energy spacing of 100 μV . A temperature of 200 mK is assumed for the leads. Both tunnelling rates Γ_{in} and Γ_{out} depend on the dot bias and the agreement with the measurement data of Fig. 9.10 and the event rate in Fig. 9.4b is remarkable.

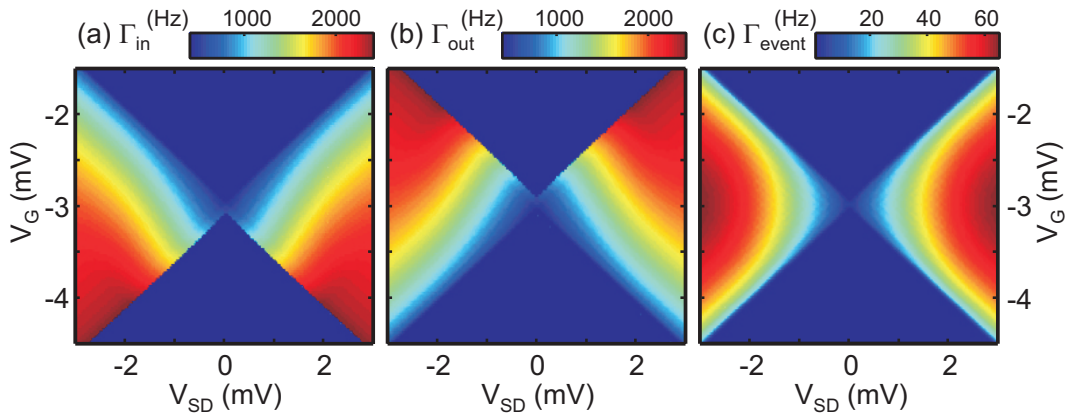


Figure 9.14: Rate equation simulation of a dot with a dense spectra of 100 μV equi-distant energy levels. (a) Γ_{in} in (a) and Γ_{out} in (b) both increase with the dot bias. The equi- Γ_{in} lines and equi- Γ_{out} lines are parallel to source and drain lines respectively. (c) Γ_{event}

9.6.3 Energy-dependence of barriers

Fig. 9.15a shows a horizontal cut through the diamonds of Fig. 9.14 at $V_G = -3\text{mV}$ as a function of the dot bias. The coupling to the source is assumed to be 10% stronger than the drain here so that Γ_{in} and Γ_{out} are not on top of each other.

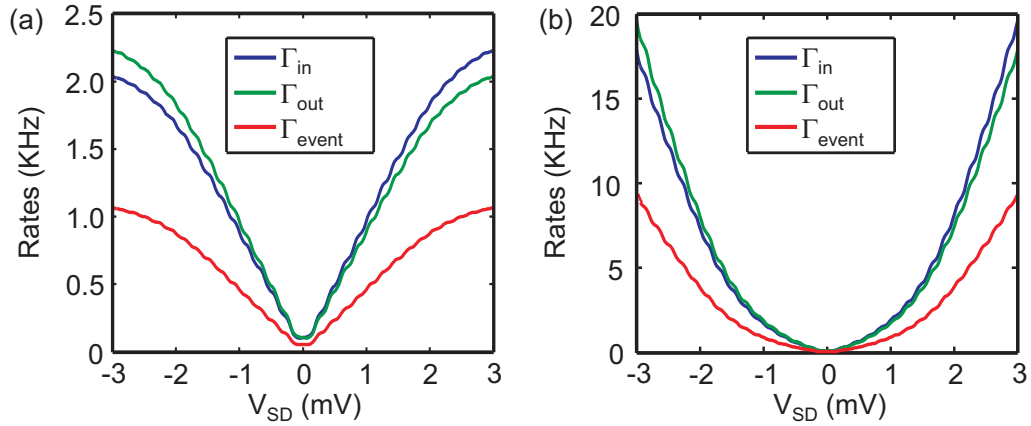


Figure 9.15: The effect of energy dependence of barriers on the tunnelling rates (a) energy-independent barriers, the rates increase linearly with bias. (b) the barriers open up exponentially (0.4 dec/meV) with the energy. The rates follow the same exponential dependence with bias.

9.7 Summary and outlook

In this chapter we have reported on time-resolved charge detection of holes tunnelling into/out of a quantum dot using a nearby charge detector. This time resolution provides the possibility to divide the dot current into a tunnelling in and a tunnelling out rates. Moreover it provides information about the spectrum of excited states and their relaxations in the quantum dot.

The photons emitted from the quantum point contact can trigger excitation and relaxation between different quantum dot states. It is interesting to explore this effect and photon-assisted tunnellings of holes between the dot and the leads in a hole quantum dot with a dense spectrum. Unfortunately this was not possible here due to activation of charge traps by the QPC bias higher than $600 \mu\text{eV}$. As the number of emitted photons is expected to increase with the QPC bias, it would be desirable to study this effect on a new sample.

Chapter 10

Statistics of hole transport

10.1 Introduction

The basic tool in transport experiments is to apply voltage, measure current or vice versa. In the last chapter we saw that the noise of the current opens a new window (that is time) to the experiment revealing more information about the system through statistics. For example we saw that the sub-Poissonian distribution of the particles imply a dot in the coulomb blockade regime without the need to change any external parameter. The question in this chapter is if there is more information contained in the statistics beyond noise that is not available otherwise. Especially if the interactions in the system can show up in the statistics and if the statistics of electrons/holes differ from those of classical particles. This statistics is usually described by the probability distribution function $P(n)$ or alternatively by the generating function obtained from this distribution by $G(z) = \sum_n z^n P(n)$.

The experimental studies of statistics using charge detection with a nearby quantum point contact started by Gustavsson et al. [189, 190] and Fujisawa et al. [191] and was continued by Fricke et al. [192, 193]. All these experiments were performed in quantum dots fabricated in n-GaAs 2DEG. Therefore it is very interesting to compare these results with those obtained in the completely different system of p-GaAs 2DHG quantum dots where the interactions are supposed to be stronger in the dot (if we compare mean level spacing $\Delta E \sim 10\mu\text{eV}$ to the charging energy $E_c \sim 2\text{ meV}$) and in the leads (low Fermi energy $E_F \sim 2\text{ meV}$). *

10.2 Counting experiments

Fig. 10.1a shows a typical counting experiment scenario. The number of particles that pass through the nano-structure within a time $(0, \tau)$ is a random variable $P_\tau(n)$

*Valuable discussions with D. Kambly, Ch. Flindt, F. Hassler, L. Levitov and W. Belzig is appreciated.

and quite generally it can be written [194] as

$$P_\tau(n) = \sum_{N=0}^{\infty} R_\tau(N) Q_\tau(n, N) \quad (10.1)$$

Here $R_\tau(N)$ describes the probability distribution of the number of attempts N during this period. All the information about the interactions and temperature in the leads is contained in $R_\tau(N)$. The distribution $Q_\tau(n, N)$ describes the probability that n out of N attempted particles make it to the drain. For example if the nano-structure is a simple (energy-independent) scatterer we have ($p + q = 1$)

$$P_\tau(n) = \sum_{N=0}^{\infty} R_\tau(N) \binom{N}{n} p^n q^{N-n}$$

Assuming no thermal or quantum fluctuations in the leads in an ideal case, $R_\tau(N) = \delta(N - \langle N \rangle)$ and we have

$$P_\tau(n) = \binom{\langle N \rangle_R}{n} p^n q^{N-n} \quad (10.2)$$

which in the case of weak-coupling ($p \ll 1$) results in a Poisson distribution

$$P_\tau(n) = e^{-\langle N \rangle p} \frac{\langle N \rangle^n p^n}{n!} \quad (10.3)$$

The parameter $\Gamma = \langle N \rangle_{R_\tau} p$ is defined as tunnel coupling. $R_\tau(N)$ is a very narrow distribution and most of the time can be approximated by a delta function. Levitov and Lesovik [194, 195] have calculated this distribution for an ideal Fermi gas at zero temperature

$$\langle N \rangle_{R_\tau} = \frac{2eV\tau}{h} \quad \langle \langle N^2 \rangle \rangle_{R_\tau} = \frac{1}{\pi^2} \log E_F \tau / \hbar \quad (10.4)$$

The mean grows linearly with time but the variance grows only logarithmically in time. Therefore after long enough times, the distribution is very sharp (Fig. 10.1d). Plugging in some realistic numbers: $V > k_B T / e \sim 10 \mu V$ to have uni-directional current flow, $E_F \sim 10 meV$ for a 2DEG in n-GaAs and $\tau \sim 10 \mu sec$ if we were able to look at the nano-structure with a bandwidth of $B \sim 100$ kHz, into these formula we get

$$\langle N \rangle_{R_\tau} \sim 48,000 \quad \langle \langle N^2 \rangle \rangle_{R_\tau} \sim 2 \quad (10.5)$$

This result suggests that the particles from the reservoir will attempt to travel through the nano-structure quite regularly. Note that this picture can change considerably if one considers non-zero temperature, disorder or interactions in the leads. Especially temperature fluctuations also grow linearly with time. Therefore it is not clear what the fluctuations in the number of attempts are in a p-GaAs 2DHG with

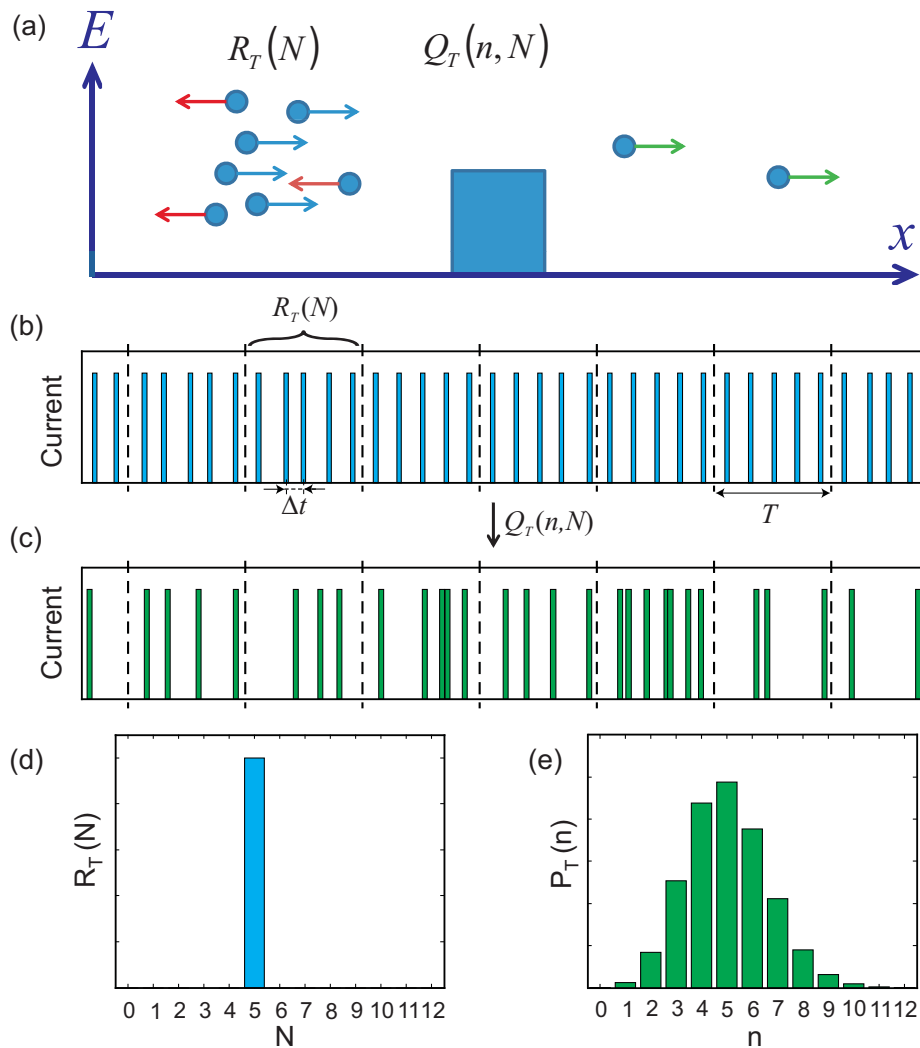


Figure 10.1: (a) Typical counting experiment scenario. The incident particles are scattered at the nano-structure, either transmitted (green) or coherently reflected back (red). The probability distribution function $Q_T(n, N)$ describes the probability that n out of N incident particles are transmitted. The probability distribution of the number of attempts by the incident particles is described by the function $R_T(N)$. (b) The current flow without the scatterer. each spike corresponds to a particle passing through the conductor. The random variable Δt quantifies the time intervals between the particles. For an idealized current this time interval is constant but in reality due to thermal and quantum fluctuations it has a distribution described by $R_T(N)$. (c) The current in presence of the scatterer is modified due to the random nature of scattering process described by $Q_T(n, N)$. Note that the scattering process does not have to be instantaneous and the nano-structure introduces a memory effect. It can hold a particle for a while and then release it. (d) Probability distribution of the number of particles passing the conductor in absence of the scatterer reflects $R_T(N)$ and is a very narrow distribution. (e) The same distribution in presence of the scatterer.

$r_s > 5$. In the absence of the nano-structure this *reservoir noise* is the only source of randomness in the experiment ($P(n) = R_\tau(n)$). This noise has been observed by low-temperature amplification for ballistic and diffusive systems [196].

The current can be schematically represented as shown in Fig. 10.1b and is what happens in a QPC on a plateau or in the edge states of quantum Hall effect. The picture changes dramatically in the presence of the nano-structure (Fig. 10.1c). For example if the nano-structure is a simple scatterer, the reservoir noise can be neglected for [194]

$$p\langle\langle N^2 \rangle\rangle_{R_\tau} \ll q\langle N \rangle_{R_\tau} \quad (10.6)$$

which is safely true especially in the weak-coupling regime ($p \ll 1$). In this case $P(n) = Q(n, \langle N \rangle_{R_\tau})$ and the output becomes random only due to the scatterer (Fig. 10.1e). Please note that the scattering process does not need to be instantaneous. The nano-structure can hold a particle and release it after a while.

Another source of non-trivial interaction effects in the strong-coupling regime is the co-tunnelling effect [1, 197]. Braggio et al. [198] have shown that these higher order tunnelling effects leads to non-Markovian statistics of the charge transfer through the quantum dot. These effects can be neglected in the weak-coupling regime.

10.3 Theory of FCS in the weak coupling regime

It was shown by Bagrets and Nazarov [199] that the information about the number of transferred charges in the weak-coupling regime can be easily captured in the master equation with a slight modification. The usual two states diagram of Fig. 10.2a does not keep this information. To keep track of the number of charges traversed we have to replace it with a chain of two states as shown in Fig. 10.2b. The connection with the two-state system is that $P(n) = p_0(n) + p_1(n)$ and

$$p_0 = \sum_n p_0(n) \quad p_1 = \sum_n p_1(n)$$

A better way to keep track of the number of transferred charges is to separate different transferred charge sectors in the chain by the (red) vertical lines in Fig. 10.2c and multiply the diagonal rate by an auxiliary symbol (for example z) each time the system goes from one charge sector to the next. Attention must be paid that this modification is different than the replacement ($\Gamma_{out} \rightarrow \tilde{\Gamma}_{out} = z\Gamma_{out}$) as it might seem at first sight. Such a replacement would influence the probability of each charge sector by future charge sectors which is not desired.¹

With this modification $p_{0,1}(n)$ becomes proportional to the z in powers of the number of transferred charges $p_{0,1}(n) \rightarrow \tilde{p}_{0,1}(n, z) = z^n p_{0,1}(n)$. Keeping both z and n is redundant and even if we ignore (trace out) the n -dependence by writing

$$\tilde{p}_{0,1}(z) = \sum_n \tilde{p}_{0,1}(n, z) = \sum_n z^n p_{0,1}(n) \quad (10.7)$$

¹Although the notation ($\Gamma_{out} \rightarrow \tilde{\Gamma}_{out} = z\Gamma_{out}$) is used from now on it should not be confusing.

the information about the transferred particles is contained in the power series expansion of $\tilde{p}_0(z)$ and $\tilde{p}_1(z)$. On the diagram this means we do not need to have a chain of two states any more and the system can be represented in the compact form shown in Fig. 10.2d. The sum of the z -dependent two state probabilities is not one any more but the generating function as a power series in the auxiliary symbol!

$$\begin{aligned} \tilde{p}_0(z) + \tilde{p}_1(z) &= \sum_n z^n (p_0(n) + p_1(n)) \\ &= \sum_n z^n P(n) = G(z) \end{aligned} \quad (10.8)$$

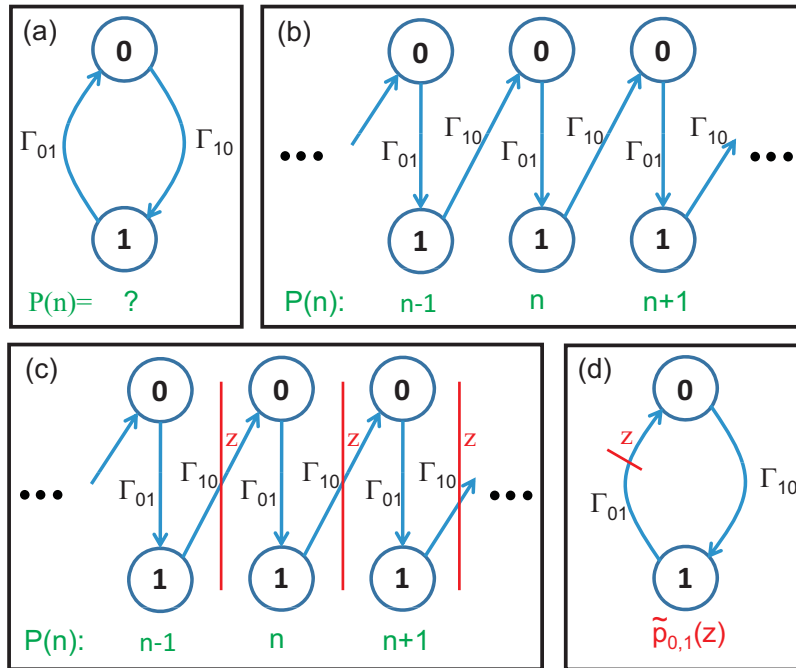


Figure 10.2: The state diagram of a two state system with respect to the number of transferred charge. This information is lost in (a) but it is contained in the index of the 0 and 1 states in (b) and in both the charge index and power of z in (c). The red lines separate different charge sectors and the probability gets a factor of z each time crossing these lines. The state diagram (c) can be condensed to the state diagram (d) after a Z -transform as explained in the text.

This complex-value auxiliary symbol z is commonly called the *counting field*. Mathematically what we did in 10.7 is a Z -transform. The system in Fig. 10.2b can be described as (time-dependence is implicit)

$$\begin{aligned} \dot{p}_0(n) &= -\Gamma_{in} p_0(n) + \Gamma_{out} p_1(n-1) \\ \dot{p}_1(n) &= \Gamma_{in} p_0(n) - \Gamma_{out} p_1(n) \end{aligned} \quad (10.9)$$

which after a Z-transform with respect to n becomes [1]

$$\frac{d}{dt} \begin{pmatrix} \tilde{p}_0(z) \\ \tilde{p}_1(z) \end{pmatrix} = \mathbf{M}(z) \begin{pmatrix} \tilde{p}_0(z) \\ \tilde{p}_1(z) \end{pmatrix} \quad (10.10)$$

$$\mathbf{M}(z) = \begin{pmatrix} -\Gamma_{in} & z\Gamma_{out} \\ \Gamma_{in} & -\Gamma_{out} \end{pmatrix}. \quad (10.11)$$

The time evolution of the state probabilities can be calculated using eigenvalues and eigenvectors of matrix M (Note that M is not symmetric and its right and left eigenvectors $|u_n\rangle$ and $\langle\langle u_n|$ are not necessarily transpose of each other. Nevertheless they satisfy the orthogonality condition $\langle\langle v_n| u_m\rangle\rangle = \delta_{nm}$).

$$|p(z, t)\rangle\rangle = e^{\lambda_1(z)t} |u_1(z)\rangle\rangle \langle\langle v_1(z)| p_0\rangle\rangle + e^{\lambda_2(z)t} |u_2(z)\rangle\rangle \langle\langle v_2(z)| p_0\rangle\rangle \quad (10.12)$$

Having $|p(z, t)\rangle\rangle = \begin{pmatrix} p_0(z) \\ p_1(z) \end{pmatrix}$, the generating function can be calculated as in Eq. 10.8

$$G(z, t) = p_0(z, t) + p_1(z, t)$$

10.3.1 Two-state system

So far our formalism was quite general. Eq. 10.3 and 10.8 can be used for any system. For the two-level system of Fig. 10.2 the eigenvalues are

$$\lambda_{\pm} = -\frac{1}{2}(\Gamma_{in} + \Gamma_{out}) \pm \frac{1}{2}\sqrt{(\Gamma_{in} + \Gamma_{out})^2 - 4\Gamma_{in}\Gamma_{out}(1-z)} \quad (10.13)$$

These can be equivalently written as (using definitions 9.3 and 9.9)

$$\lambda_{\pm} = \frac{2\Gamma_{event}}{1-a^2} \left[-1 \pm \sqrt{1 - (1-a^2)(1-z)} \right] \quad (10.14)$$

Since the only time-dependence of the generating function is in the form of $\lambda_{\pm}t$ and $\Gamma_{event}t = \langle n \rangle$, the probability distribution depends only on the mean event number $\langle n \rangle$ and it will be presented in this way in this chapter. This has the advantage that the statistics becomes universal and will only depend on the asymmetry a .

Moreover at large times, we can only keep the eigenvalue with the smaller real part. This is the eigenvalue that goes to zero with $z \rightarrow 1$. Therefore at large times we have

$$G(z) = \exp[\lambda_+ t] \quad (t \rightarrow \infty) \quad (10.15)$$

For $a \rightarrow \pm 1$ the exponent becomes

$$\lambda_+ t = \Gamma_{event} t (z - 1) \quad (10.16)$$

resulting in $G(z) = \exp[-\langle n \rangle (z - 1)]$ which is the generating function of the Poisson distribution with the mean $\langle n \rangle$ (see Eq. 10.31). For $a \rightarrow 0$ the exponent of Eq. 10.15 becomes

$$\lambda_+ t = 2\Gamma_{event} t (\sqrt{z} - 1) \quad (10.17)$$

The extra factor $1/2$ in the exponent of z leads to the sub-Poissonian value of the Fano factor discussed in chapter 8. The distribution function in this case becomes [200]

$$P(n) = \sum_{N_L, N_R=0}^{\infty} P_P(N_L)P_P(N_R)\delta(n - (N_L + N_R)/2) \quad (10.18)$$

in which $P_P(N_{L/R})$ are the Poisson distributions of left and right barriers.²

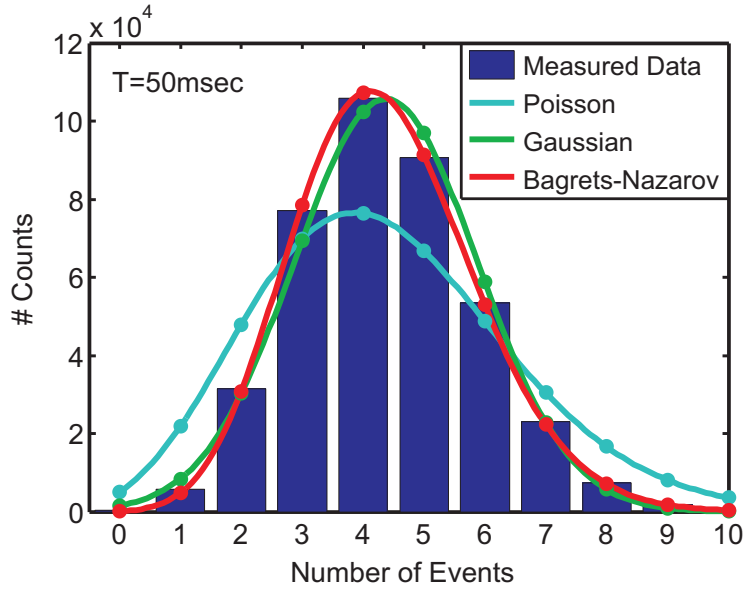


Figure 10.3: The histogram of the number of holes passed through the quantum dot during $T=50$ msec at the point A in Fig. 9.4b with symmetric barriers ($a = 0$). The blue and green lines shows the Poisson and Gaussian distributions respectively, calculated using the mean and variance of the measured data. Please note that all these distributions are discrete and the connecting lines are just guides to the eye. While the Gaussian distribution fits well to the histogram, the data is best fit to the Bagrets-Nazarov distribution with the input parameters Γ_{in} and Γ_{out} .

10.3.2 Charge transfer distribution

The generating function $G(z, t)$ calculated in the previous section is related to the distribution of transferred charge through Eq. 10.20 via a Z-transform. An inverse Z-transform can be used to extract the distribution $P(n)$. However, it is easier to define the characteristic function using

$$F(\chi) = G(e^{i\chi}) = \sum_n P(n, t)e^{i\chi n} \quad (10.19)$$

²Note that this is not a convolution.

which is related to the distribution function with a Fourier transform. The inverse Fourier transform readily gives the distribution. Fig. 10.3 shows the distribution of the number of events detected in the point A in Fig. 9.4b in 50-msec time windows. At this point the $\mu_{S/D}$ are separated by $700\mu\text{V}$ bias with the electrochemical potential of the dot in the middle of them. In the same figure we show the Bagrets-Nazarov model calculated in Eq. 10.15 compared to the best Poissonian and Gaussian distributions calculated from the mean and variance of the data. The agreement of the Bagrets-Nazarov model with the data is striking, while the essence of the distribution is captured by a much simpler Gaussian distribution. The cumulants, introduced in the next section, are the tools that signify the difference between these two distributions.

10.4 Cumulants as non-Gaussian qualifiers

10.4.1 Cumulants

For any discrete and possibly time-dependent distribution $X(t)$ the generating function (GF) is defined as

$$G(z, t) = \langle z^X \rangle = \sum_n z^n P_X(n, t) \quad (10.20)$$

From this generating function, moment generating function (MGF) is defined as:

$$M(z, t) = \langle e^{zX} \rangle = G(e^z, t) \quad (10.21)$$

and the cumulant generating function (CGF) is defined as

$$S(z, t) = \ln[M(z, t)] = \ln[G(e^z, t)] \quad (10.22)$$

Note that the normalization of probability distribution X requires that

$$G(z = 1) = M(z = 0) = 1, \quad S(z = 0) = 1 \quad (10.23)$$

From these two generating functions the (non-central) moments and cumulants are obtained via differentiation

$$\mu_m = \partial_z^m M(z, t)|_{z \rightarrow 0} \quad (10.24)$$

$$C_m = \partial_z^m S(z, t)|_{z \rightarrow 0} \quad (10.25)$$

and are the coefficients of Taylor expansion of the corresponding generating functions. Therefore, knowing either of moments or cumulants specifies the distribution completely. It follows from this definition that the moments of a distribution

$$\mu_m = \langle n^m \rangle = \sum_n n^m P_X(n) \quad (10.26)$$

and the cumulants have the following relation

$$C_n = \langle\langle n^m \rangle\rangle = \mu_n - \sum_{m=1}^{n-1} \binom{n-1}{k-1} C_m \mu_{n-m} \quad (10.27)$$

The first few cumulants are given below in terms of moments

$$\begin{aligned} C_1 &= \mu_1 \\ C_2 &= \mu_2 - \mu_1^2 \\ C_3 &= \mu_3 - 3\mu_2\mu_1 + 2\mu_1^3 \\ C_4 &= \mu_4 - 4\mu_3\mu_1 - 3\mu_2^2 + 12\mu_2\mu_1^2 - 6\mu_1^4 \end{aligned}$$

These are mean, variance, skewness (asymmetry) and kurtosis (sharpness) respectively and are schematically shown for a distribution in Fig. 10.4. Higher order cumulants capture even more subtle details of the distribution function.

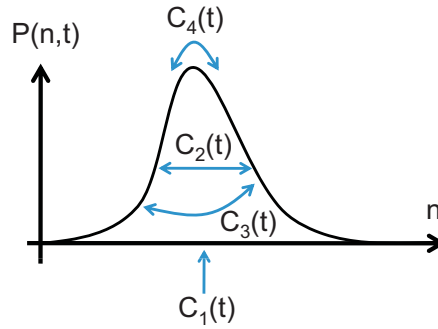


Figure 10.4: The cumulants of a time-dependent distribution depend on time and characterize the details of this distribution. The mean C_1 , the variance C_2 , the skewness (asymmetry) C_3 and the kurtosis (sharpness) C_4 are shown in the figure.

Cumulants have an important property that make them interesting for statistical physics. For a sum of two independent distributions $X = X_1 + X_2$ it can be readily seen from 10.21 and 10.22 that the MGF and CGF of the total X are the product and sum of MGF and CGF of each part respectively. These properties carry on to the moments and cumulants. From this it follows that for any cumulative distribution like the number of charges passed through a conductor, after a certain time within which the charge transfer processes are correlated, all the cumulants grow linearly with time. This is the reason why we will always look at the normalized cumulants C_n/C_1 for ($n > 1$) to study such correlations in this chapter.

Another consequence of this property is that the *cumulant average* of a product $\langle\langle X_1 X_2 \cdots X_n \rangle\rangle$ defined as

$$\langle\langle X_1 X_2 \cdots X_n \rangle\rangle = \partial_{z_1} \partial_{z_2} \cdots \partial_{z_n} \ln \langle e^{\sum z_k X_k} \rangle |_{\vec{z} \rightarrow 0} \quad (10.28)$$

is zero if any subset of the involved random variables X_k is independent of the rest [201]. For example $\langle\langle X_1 X_2 \rangle\rangle = \langle X_1 X_2 \rangle - \langle X_1 \rangle \langle X_2 \rangle$ is obviously zero if X_1 and

X_2 are independent. It implies that for non-zero cumulant average, the random variables must be necessarily connected and this is the reason that the cumulants are called irreducible correlators.

10.4.2 Correlation time

Fig. 10.4.2 shows the auto-correlation $R(\tau)$ of the detector current (with telegraph noise like the one shown in Fig. 9.3) as a function of the shift time at the point A in Fig. 9.4b. The auto-correlation is defined as

$$R(\tau) = \lim_{T \rightarrow \infty} \frac{1}{T} \int_0^T dt I(t) I(t + \tau) \quad (10.29)$$

On the same figure the histogram of the total event time is re-plotted from Fig. 9.7a. Whereas the dip in the event time distribution is given by the time scale $\langle \tau_{event} \rangle = \langle \tau_{in} \rangle + \langle \tau_{out} \rangle = \Gamma_{in}^{-1} + \Gamma_{out}^{-1}$, the fall-off of the auto-correlation function is characterized by the time scale $\tau_{cor} = (\Gamma_{in} + \Gamma_{out})^{-1}$ which is (in the case of symmetric barriers, 4 times) smaller than the average event time. For the present case we obtain $\langle \tau_{event} \rangle \approx 11$ msec and $\tau_{cor} \approx 3$ msec. Using $\Gamma_{event} = 89$ Hz this gives $\langle n \rangle_{cor} \approx 0.25$ as the time-scale for which we expect correlations in the statistics.

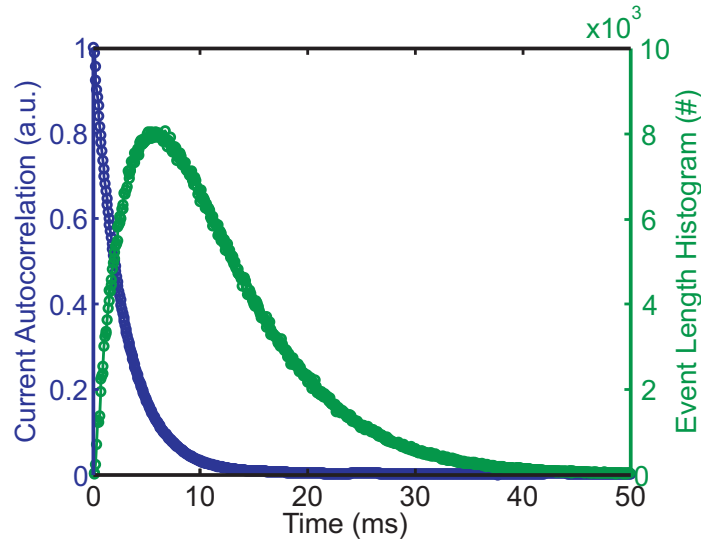


Figure 10.5: Auto-correlation function of the telegraph noise of the detector (blue) and the distribution of the event time duration (green) as a function of time.

10.4.3 Bagrets-Nazarov distribution

The cumulants of the charge transfer can be calculated in the most general case using equations 10.12 and 10.8. In the long-time limit ($t \gg \tau_{cor}$) the CGF is given

by $S(z) = \lambda_+(e^z)t$ where λ_+ is given by Eq. 10.14. Taking the derivatives of this result we obtain

$$\begin{aligned} C_1 &= \langle n \rangle \\ C_2 &= \langle n \rangle (1 + a^2)/2 \\ C_3 &= \langle n \rangle (1 + 3a^4)/4 \end{aligned} \quad (10.30)$$

These cumulants are compared in Fig. 9.8 to the Fano factor and skewness measured in the quantum dot and it fits quite well to the measured data.

10.4.4 Poisson and Gaussian distributions

For a Poissonian distribution the CGF is

$$S_P(z) = \ln \sum_{n=0} e^{nz} \left[e^{-\mu} \frac{\mu^n}{n!} \right] = \mu(e^z - 1) \quad (10.31)$$

and all the cumulants are the same and equal to μ . For a Gaussian distribution only the first two cumulants (mean μ and variance σ^2) are non-zero.

$$S_G(z) = \ln \sum_n e^{nz} \left[\frac{1}{\sqrt{2\pi\sigma}} e^{-\frac{(n-\mu)^2}{2\sigma^2}} \right] = z\mu + \frac{z^2}{2}\sigma^2 \quad (10.32)$$

This means that the central limit theorem can be cast in the statement that the higher order cumulants of sum of i.i.d distributions cancel each other in the limit of many distributions. Therefore any deviation from Gaussian statistics (which for a cumulative distribution is due to correlations) is captured by higher order cumulants. This proves to be a strong tool if for example we look at the distribution of transferred charge through the quantum dot during longer times (here 200msec) in Fig. 10.6a. The Gaussian distribution describes the data as good as the model developed in previous section but a closer look at the logarithmic scale (Fig. 10.6b) shows the differences between the two distributions and shows that the data favours the Bagrets-Nazarov model. All these minor differences are reflected in non-zero higher ($m > 2$) cumulants of the distribution. However, as usual nothing comes for free. It turns out that measuring higher order cumulants of current is in general difficult and requires good signal to noise and enough statistics. In the next section we discuss these issues in the context of our counting experiment.

10.5 Difficulties of measuring cumulants

10.5.1 The problem of limited bandwidth

Measuring cumulants using a counting experiment relies on the fact that the current is either unidirectional or the direction of each charge transfer is identified by some

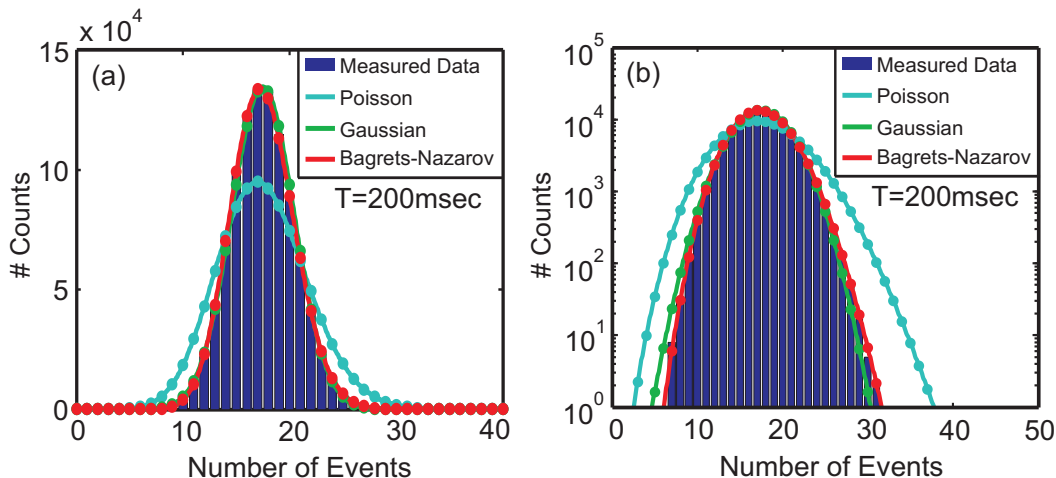


Figure 10.6: The histogram of the number of holes having passed through the quantum dot during $T=200\text{msec}$ in (a) linear and (b) logarithm scales together with Poisson (blue), Gaussian (red) and Bagrets-Nazarov (red) distributions. Increasing the bin size, the data histogram resembles more to the Gaussian distribution (green). However, in logarithm scale the minor differences of the two distribution can be identified and again the measured data favours the Bagrets-Nazarov distribution.

other means (for example using a double dot). This is a safe assumption provided that the bias is sufficiently large $eV_{SD} \gg k_B T$ which is the case here with the bias of $700\mu\text{V}$ and the base temperature of 100 mK . Moreover each time the detector current passes a certain threshold it is assumed to be a sign of change in the charge state of the quantum dot. The latter is the main sources of errors in a counting experiment. In principle many fast events can be missed if two fast tunnel in/out processes are followed by each other within a time faster than the inverse bandwidth. Besides, missing a fast event between two slow events effectively results in the two slow events appear cascaded and therefore having a longer duration [202]. For a Markov process this effects can be systematically taken into account following the ideas by Naaman and Aumentado [202] as shown in the Fig. 10.7. The full state-space of the system+detector is a tensor product of the state-space of each and therefore has 4 states. The state diagram of the full system is shown in the figure with black symbols as the states of the system and the green symbols indicating those of the detector. The detector follows the state transitions in the system with a delay of the order of Γ_D^{-1} . The branch with the counting field z , is the branch at which the detector reports one charge transfer to the drain.

Fig. 10.8 shows the effect of change of bandwidth on the cumulants calculated from the above model (solid lines). In this case $\Gamma_{10}=\Gamma_{01}=178\text{ Hz}$ and the change of the bandwidth does not affect the result as always $\Gamma_D \gg \Gamma_{10/01}$. Similar uncertainties arise when determining of the time of an event due to finite bandwidth, noise and finite sampling rate. However, again if the detector bandwidth and sampling rates are considerably larger than the other rates in the system the finite bandwidth

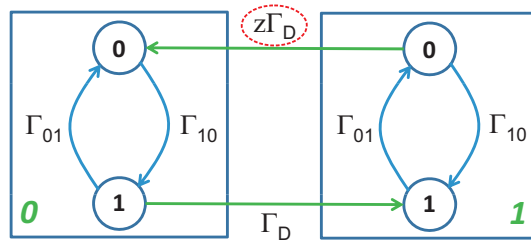


Figure 10.7: The system-detector model used by Naaman and Aumentado [202] to take into account the finite bandwidth corrections. The red dotted circle marks the branch at which the detector reports one charge transfer to the drain.

effects can be neglected.

10.5.2 The problem of limited signal to noise ratio

Another source of error in counting the number of transferred holes are the false counts due to either the noise of the detector [203] or difficulties in setting a proper current threshold for the detector. This issue can be circumvented to some extent by decreasing the bandwidth thus increasing the signal to noise. Fig. 10.8 shows the first few normalized cumulants as a function of mean event number for different detector bandwidths, compared to the cumulants extracted from the model as described in 10.4.3 and using the numerical method introduced by Kambly et al. [204]. At very short time intervals ($\langle n \rangle \sim 10^{-2} \ll 1$) the number of holes passing through the quantum dot is either 0 or 1. The probability p of transmission is so low that the distribution is well described by the Poisson distribution, for which all the cumulants are the same. Therefore the normalized cumulants plotted here all start from 1 at low mean event numbers. At larger times however, there are systematic deviations from the model. These deviations are more dramatic for 7 kHz and 6 kHz bandwidths in Fig. 10.5.1a,b respectively and they decrease with decreasing the bandwidth.

This error source can be taken into account by adding a false count source to the state diagram as shown in Fig. 10.9b. The change with respect to Fig. 10.7 is the introduction of the false count rates denoted by Γ_X and Γ_Y and shown by the red arrows in the figure. The reason for including these rates is schematically shown in Fig. 10.9a.

The false counts simply add to correct counts $N = N_c + N_f$. The important point is that if the false counts are not correlated to the state of the system then the CGFs simply add up $S(z) = S_c(z) + S_f(z)$ and so do the cumulants. In the diagram of Fig. 10.9b, this is the case when $p_0\Gamma_X = p_1\Gamma_Y$.

Fig. 10.10a shows the normalized cumulants calculated from this model for the case when Γ_X and Γ_Y are the same and equal to 0, 20, 60, 120, 220 and 300 Hz. The other parameters of the model are $\Gamma_{10}=\Gamma_{01}=100$ Hz (hence $p_0 = p_1 = 0.5$) and $\Gamma_D=5$ kHz. The false counts in this case have some minor effects on the oscillations and at

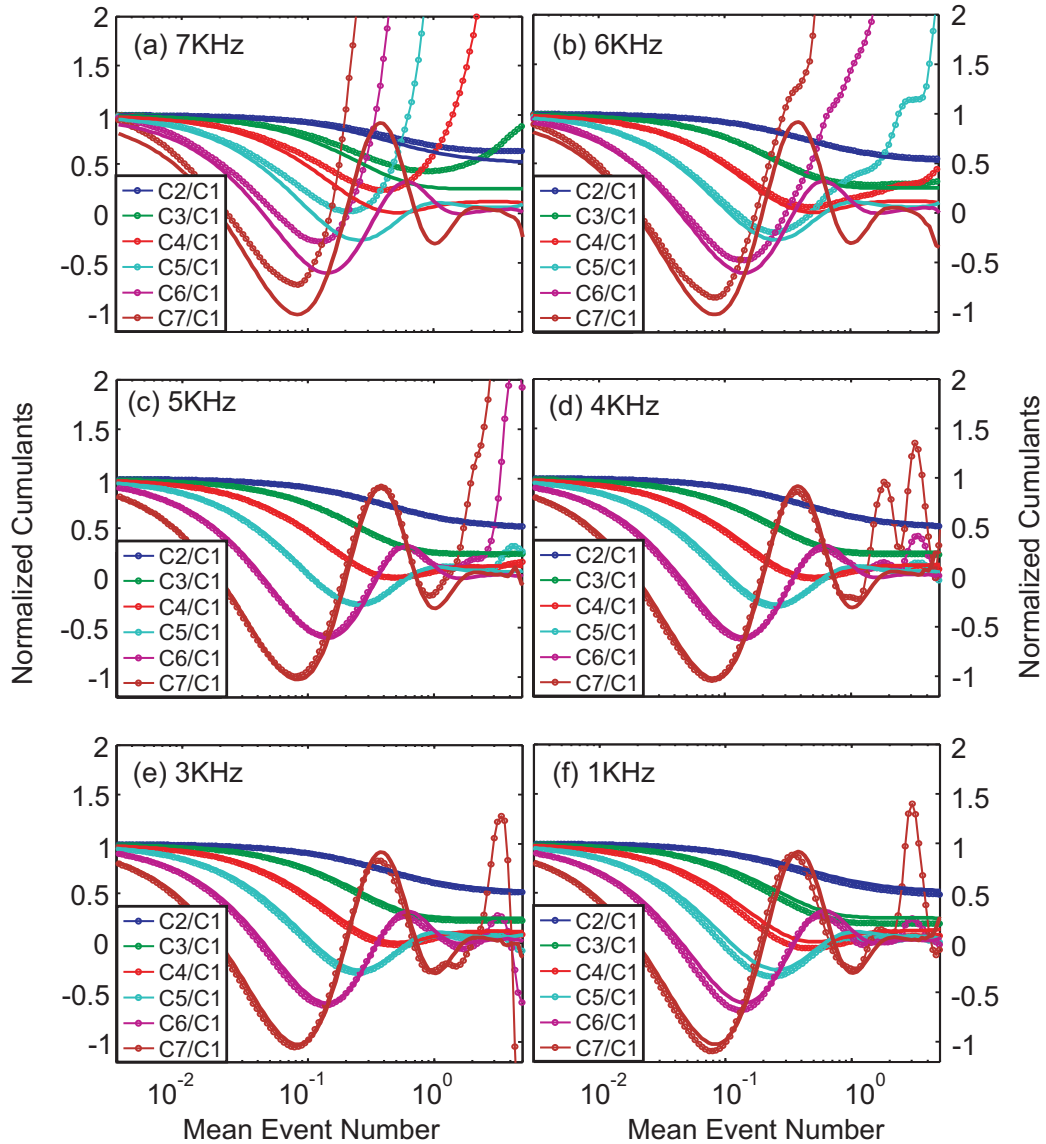


Figure 10.8: The first few normalized cumulants of charge transfer through the dot for the bandwidth of the software filter varied from (a) 7 kHz to (f) 1 kHz. The thin dot-line in each plot is extracted from the measurement while the thick solid line is calculated from the theory. The discrepancy between the measurement and the model decreases by decreasing the filter bandwidth.

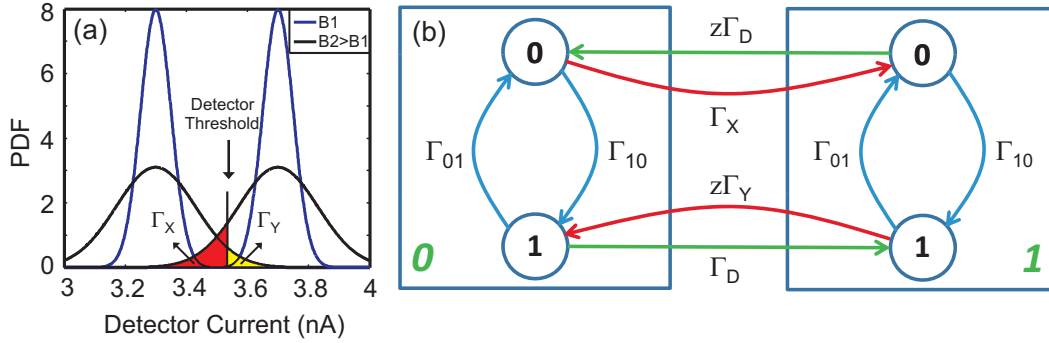


Figure 10.9: (a) The schematic of detector current histogram, showing the source of the false counts and possible asymmetries in them due to position of the current threshold. Lowering the bandwidth decreases the overlap and thus the false count rates. (b) The state diagram of system-detector modified to include the effect of the false counts (red branches) denoted by $\Gamma_{X/Y}$ rates. The detector reports a charge transfer each time the system goes from green state 1 to 0.

large times the normalized cumulants simply get an offset. Fig. 10.10b shows similar results for the case of asymmetric false rates $\Gamma_X \gg \Gamma_Y$. The effect of increasing the false rate Γ_X in this case is much more dramatic. The higher the cumulants, the stronger the oscillations they show and eventually kick out of the calculation range.

This result agrees qualitatively with those obtained from the measurements varying the bandwidth of the detector in Fig. 10.8, supporting the idea that the correlated false counts severely distort the cumulants.

10.5.3 The problem of finite statistics

The last source of errors in calculating cumulants is the finite amount of statistics. For a simple coin-flipping experiment, it requires quite a lot of trails to make any statement about the fairness of a coin, and this is only the mean. The higher cumulants require even more statistics. Since in a counting experiment the event rate is limited basically by the bandwidth, large statistics requires long measurements that are practically limited by the stability of the sample and the patience of the experimentalist.

Fig. 10.5.3 shows the histogram of the transferred charge in 2-sec time intervals, made out of an ensemble of 10,000 data set (about 2 million events). The Bagrets-Nazarov model is plotted in red and the black arrows point to some deviations from this model caused by the finite statistics. For normal moments an N-estimate of the moment is calculated by $\mu_m^N = \frac{1}{N} \sum_{i=1}^N n_i^m$. The hope is that in case of large statistics, these estimates converge to the theoretical ones $\lim_{N \rightarrow \infty} \mu_m^N = \mu_m$. The estimation error due to finite statistics can be easily calculated

$$\Delta \mu_m^N = \sqrt{\frac{\mu_{2m} - \mu_m^2}{N}} \quad (10.33)$$

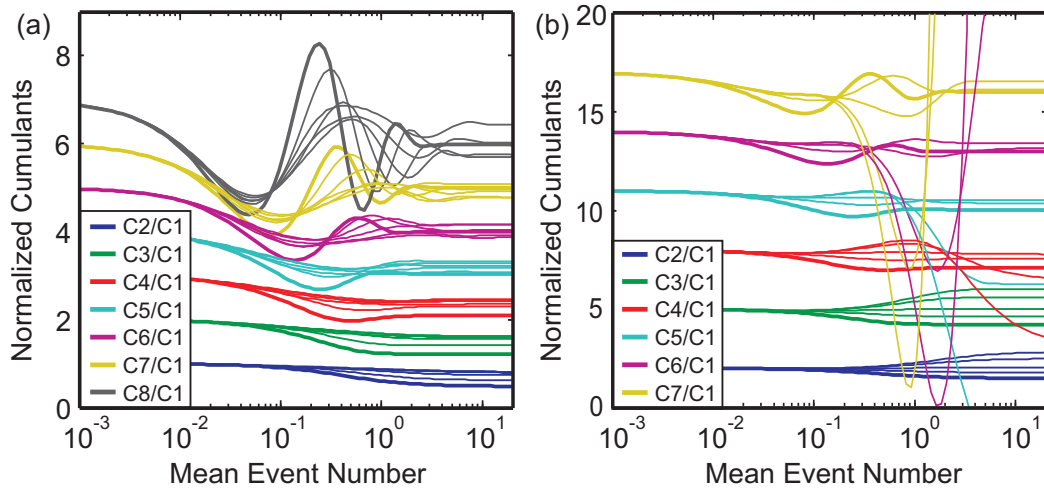


Figure 10.10: Effect of (a) symmetric ($\Gamma_X = \Gamma_Y$) and (b) asymmetric ($\Gamma_X \gg \Gamma_Y$) false count rates on the normalized cumulants calculated from the model of Fig. 10.9 for $\Gamma_X = 0, 20, 60, 120, 220$ and 300 Hz. The thick curve in each color set shows the case of no false counts. Different cumulants are shifted vertically for clarity. While the oscillations are mainly damped in (a), they are enhanced and unstable in the case of correlated false counts of (b).

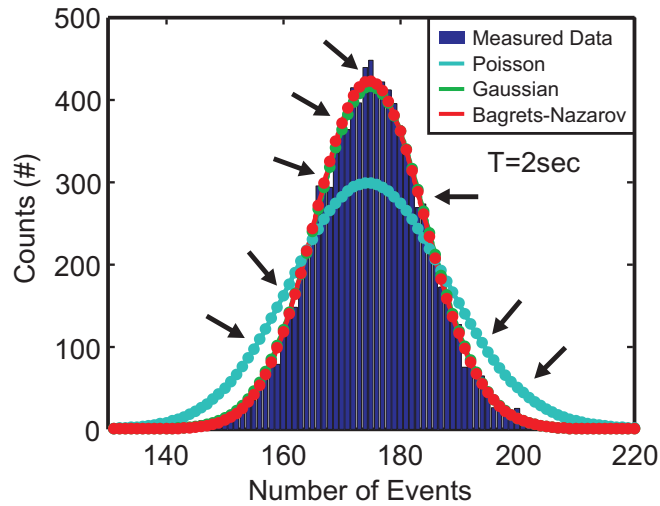


Figure 10.11: The histogram of the transferred charge in 2-sec time intervals, made out of an ensemble of 10,000 data set (about 2 million events). The Bagrets-Nazarov model is plotted in red and the black arrows point to some of deviations from this model caused by the finite statistics.

From these, the errors in the cumulants can be in principle calculated using Eq. 10.27, but this is difficult due to the recursive form of this formula. It can be

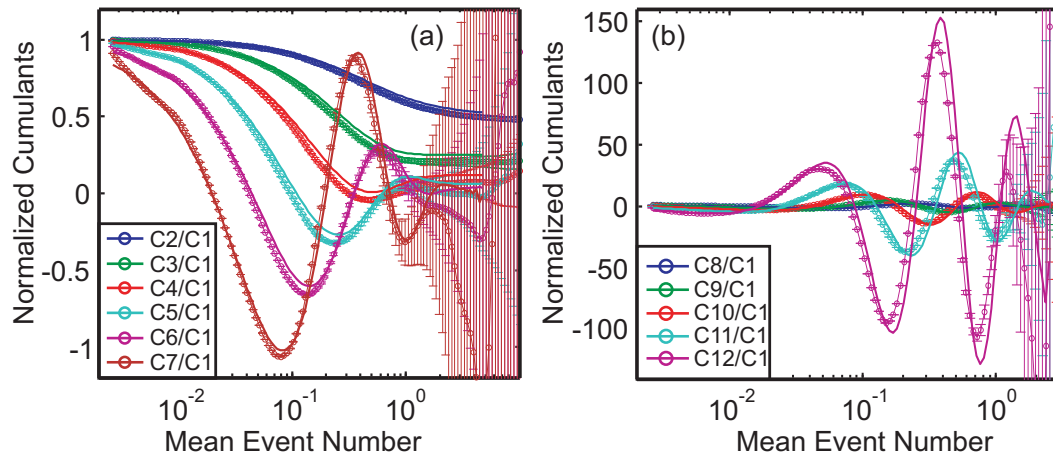


Figure 10.12: The first few cumulants as a function of mean event number for the point A in Fig. 9.4b and symmetric barriers ($a = 0$). The error bars are calculated using Eq. 10.34. Solid lines show the calculations from the model.

shown [205] that the covariance of the cumulants is given by

$$\langle \Delta C_n \Delta C_m \rangle = \frac{m!}{N} \sigma^{2m} \delta_{nm} + O\left(\frac{1}{N^2}\right) \quad (10.34)$$

The error in the cumulants increase factorially with the order of the cumulant.³ Besides that the relative error of consecutive cumulants increase due to power m in the exponent of σ^2 . The N in the denominator signifies the importance of the amount of statistics for reasonable accuracy. If a fixed total number of events K are used to calculate the cumulants as a function of $\langle n \rangle$, then we have $N = K / \langle n \rangle$. Also as argued in 10.4.1, $\sigma^2 = C_2$ eventually grows linearly with $\langle n \rangle$ and therefore the error in the cumulant C_m grows with $\langle n \rangle^{(m+1)/2}$.

10.5.4 Universal oscillations of cumulants

Fig. 10.5.4 shows the first few cumulants as a function of the mean event number that is proportional to time. Error bars in this figure are calculated using Eq. 10.34. The data indicated with small circles agrees very well to the solid lines calculated from the model within the range of error bars.

10.6 Cumulants and interactions

The oscillations of the cumulants do not have any interesting physical origin [204] and can be understood using complex analysis following the ideas of M. Berry [207]. The generating function of a probability distribution can be described by all its zeros

³Note that the cumulants also grow factorially with their order [192, 193, 206].

and poles in the complex z -plane. Assuming that the current flow is uni-directional $P_X(n) = 0$ for $(n < 0)$, this function does not have any pole but only a set of zeros $\{z_n\}$ and possibly some branch points. Since $P_X(n)$ is always positive, the zeros of the GF are all negative. The change in the distribution as a function of any parameter can be represented by the movement of these zeros in the complex plane. Each zero of GF becomes a set of logarithmic singularities (poles) for CGF given by $z_{nm} = \ln z_n = \ln |z_n| + i(2m \pm \angle z_n)$, which are all off real axis. To calculate the cumulants we are interested in the zero-frequency derivatives of the CGF with respect to z , hence the dominant pole(s) are the one(s) close to zero. Assuming a pair of poles are dominant we can approximate the CGF by

$$S(z) \approx \ln(z - z_{00}) + \ln(z - z_{00}^*) \quad (10.35)$$

Calculating the m th cumulant gives [204]

$$C_m = \partial_z^m S(z)|_{z=0} = \frac{2(m-1)!}{|z_{00}|^2} \cos(m\angle z_{00}) \quad (10.36)$$

and oscillates as a function of the argument of the dominant poles ⁴ and any parameter that continuously changes the position of the poles.

10.6.1 Generalized Binomial distributions

Abanov and Ivanov [208] recently showed (see also [209]) that for any non-interacting Hamiltonian (quadratic in fermionic operators) the GF can be written as

$$G(z) = z^{-Q} \prod_i (1 - p_i + zp_i) \quad (10.37)$$

Each term $(1 - p_i + zp_i)$ in this product is the GF of a Binomial distribution with one trial. Therefore the above expression shows that in non-interacting systems the charge transfer statistics can be factored out to effectively independent single-particle events. The pre-factor z^{-Q} corresponds to a deterministic background charge transfer in the opposite direction and can be neglected in uni-directional case [204]. All the zeros of this GF lie on the negative real axis $z_i = (1 - p_i)/p_i < 0$. Interactions in the Hamiltonian *may* displace the zeros off the real axis. It would be interesting to experimentally probe the position of these zeros as a function of parameters of the system, like gates, bias, temperature etc. However, this is not possible by looking at cumulants, since the poles of CGF are off real axis for both interacting and non-interacting systems, resulting in trivial oscillations of the cumulants.

⁴Note that the frequency of oscillation depends on the cumulant order in agreement with the measured data.

10.6.2 Factorial cumulants

Motivated by the above discussion Kambly et al. [204] suggested to use the factorial cumulants as a probe for interactions. The factorial moment generating function

$$M_F(z) = \langle (z+1)^X \rangle = G(z+1, t) \quad (10.38)$$

and the factorial cumulant generating function (FCGF)

$$S_F(z) = \ln [M_F(z)] \quad (10.39)$$

can be used to define the factorial moments and cumulants as

$$\zeta_m = \partial_z^m M_F(z, t)|_{z \rightarrow 0} \quad F_m = \partial_z^m S_F(z, t)|_{z \rightarrow 0} \quad (10.40)$$

Note that $\zeta_m = \langle n(n-1) \cdots (n-m+1) \rangle$ justifying the name factorial moment. Factorial moments and cumulants satisfy the same relation as between ordinary moments and cumulants in Eq. 10.27

$$F_n = \zeta_n - \sum_{m=1}^{n-1} \binom{n-1}{m-1} F_m \zeta_{n-m} \quad (10.41)$$

By writing the power expansion of the $S_F(z) = S(\ln(z+1))$, it can be shown that

$$F_n = \sum_{k=1}^n s(n, k) C_k \quad (10.42)$$

where the $s(k, n)$ are the Stirling numbers of the first kind given by the expansion $[\ln(1+z)^m] = m! \sum_{k=m}^{\infty} s(k, m) z^k / k!$. Eq. 10.41 and 10.42 both can be used to calculate the factorial cumulants from the measurement data. Their importance lies in the fact that in contrast to CGF, FCGF keeps the imaginary part of the position of GF zeros (apart from transforming from zero to pole). Therefore any oscillation the factorial cumulants indicates that the zeros of GF are displaced from the real axis due to interactions. These interactions can be either in the scattering nano-structure or in the reservoirs

$$\begin{aligned} G(z) &= \sum_{n=0}^{\infty} z^n \sum_N R(N) Q(n, N) \\ &= \sum_N R(N) \sum_{n=0}^{\infty} z^n Q(n, N) \end{aligned} \quad (10.43)$$

For the special case of a Poissonian scatterer the GF becomes

$$G(z) = \sum_N R(N) e^{Np(z-1)} = G^R(e^{p(z-1)}) \quad (10.44)$$

and the FCGF is equal to CGF of only the reservoir $S_F(z) = S^R(pz)$ and measuring the statistics directly probes the GF poles of the distribution of reservoir attempts.

10.6.3 Measurement data

Fig. 10.13 shows the first few factorial cumulants, calculated from the ordinary cumulants of Fig. 10.5.4 using Eq. 10.42. In contrast to the latter, the factorial cumulants seem to be monotonic, with alternating sign for different orders.

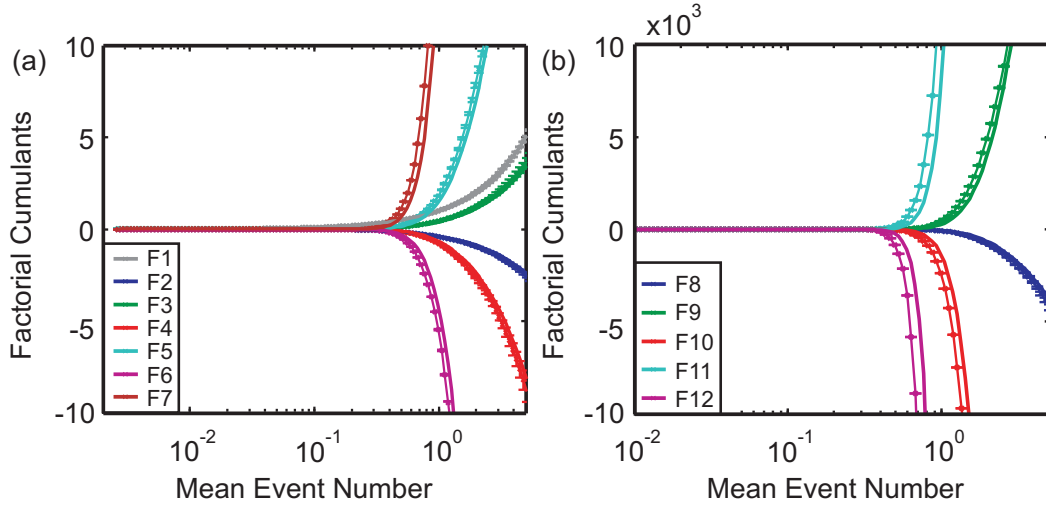


Figure 10.13: Factorial cumulants: (a) F1-F7 and (b) F8-F12 as a function of mean event number. The solid lines shows the theory.

The difficulty with factorial cumulants is that they can show non-trivial features like oscillations at very different scales. These features are best captured in the log-log plot of Fig. 10.14 where the alternating sign of these cumulants for consecutive orders is visible by the blue/red color code. Any zero-crossing oscillation (like the one from Eq. 10.36) reflects as alternative red and blue segments on these curves (see for example those in appendix H). The white arrow in Fig. 10.14a,b point to faint oscillations that are not crossing zero. These oscillations get stronger with increasing the order of the cumulants and at F_{11} and F_{12} start to cross the zero.

So far all the data in this chapter was taken at point A in Fig. 9.4b without changing any experimental parameter e.g. the gate voltages or the source-drain bias. This is a point ($V_{G2} = -295mV$) where the electrochemical potential of dot's ground state lies between those of source and drain, separated by $V_{SD} = 700\mu V$. To check the reliability of the oscillations in the factorial cumulants, we have measured the statistics and calculated the factorial cumulants at the same gate configuration but higher symmetric bias of $V_{SD} = 2.5mV$. As the charging energy of the dot is $E_C = 2mV$ and the dot resonance is in the center of the charging window, there is still only one charging level in the bias window. However, more excited states contribute to the current as discussed in the previous chapter. Γ_{in} and Γ_{out} that were the same at the low bias case and equal to 178 Hz change to different values of 2.8 kHz and 1.1 kHz respectively. As a result the normalized asymmetry a changes from zero in low bias case to $a = 0.44$ at large bias case. Fig. 10.15 shows the log-log plot of the

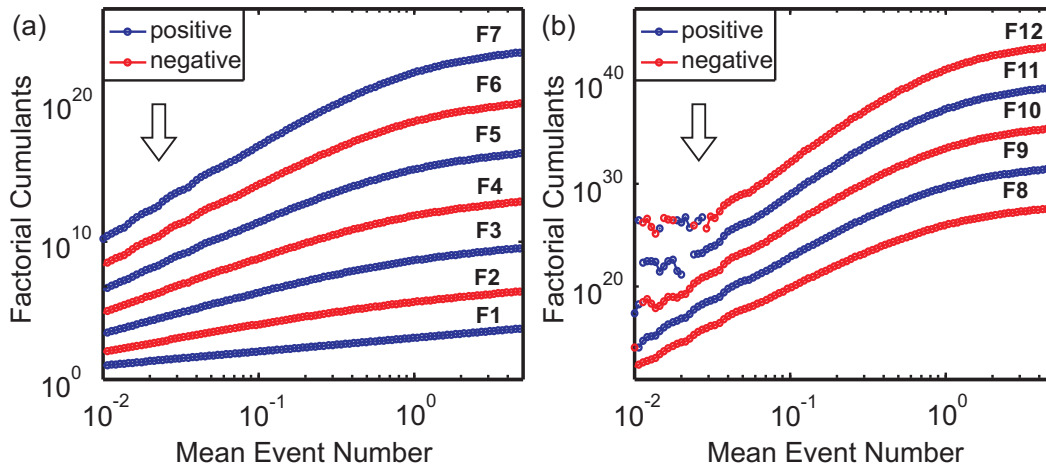


Figure 10.14: The log-log plot of factorial cumulants for $V_{SD}=0.7$ mV : (a) F1-F7 and (b) F8-F12 as a function of mean event number. The positive/negative part of the data is shown in blue/red. The white arrows point to faint oscillations of the cumulants.

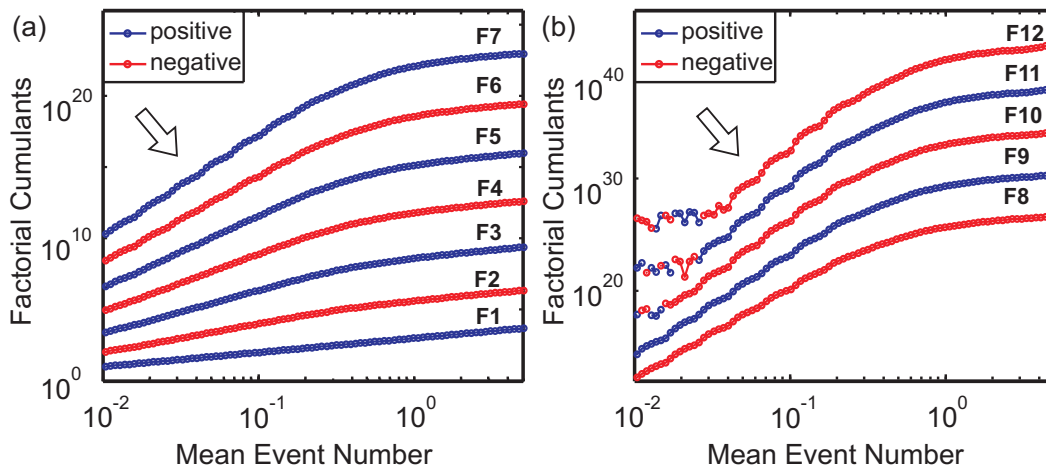


Figure 10.15: The log-log plot of factorial cumulants for $V_{SD}=2.5$ mV : (a) F1-F7 and (b) F8-F12 as a function of mean event number. The positive/negative part of the data is shown in blue/red. The white arrows point to the oscillations of the cumulants.

resulting factorial cumulants in this case. While the general features are very similar to those of Fig. 10.14, the oscillations marked with the white arrow are enhanced.

The event rate Γ_{event} in the low and large-bias cases are 89 Hz and 790 Hz respectively, that is a factor of 9 different. However, the oscillations in the two cases happen at similar time scales and those of the large-bias case tend to happen at even higher times. Moreover, the oscillations seem to be periodic in $\log(t)$ indicating that they are not coming from the response of the filter. In the case of single charge level in bias window, the factorial cumulants are not expected to show any oscillations due

to the nano-structure [204]. Therefore it is interesting if the observed oscillations indicate interactions in the reservoir might be relevant.

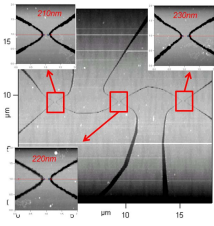
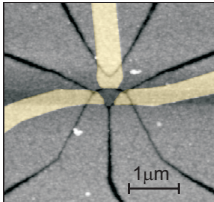
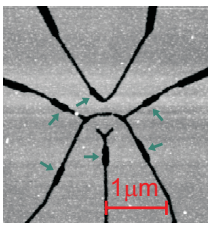
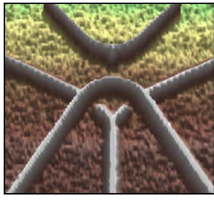
10.7 Summary and outlook

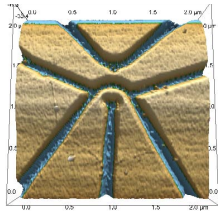
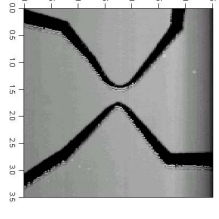
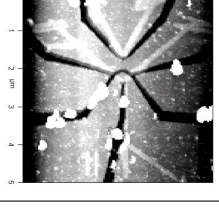
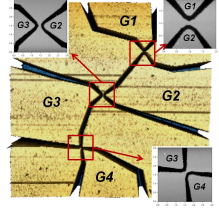
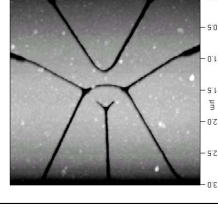
The statistics of hole transfer through the quantum dot is studied. It is shown that this statistics is indeed non-Gaussian and cumulants are introduced which are a set of measures that quantify deviations of a probability distribution from the Gaussian statistics. The cumulants of charge transfer show oscillations as a function of any parameter of the dot including the time. The origin of these oscillations is discussed, the recently proposed factorial cumulants is calculated for our tunnelling statistics to probe the interactions in the dot.

When the bias window is large enough to include more than one charging level, the interaction effects within the dot become significant [204]. Due to large energy-dependence of the barriers in hole quantum dots, two consecutive charging levels have very different couplings to the leads and therefore it is challenging to access to this regime. Attempts to calculate the factorial cumulants for this regime (Appendices G and H) has unfortunately failed in this experiment most probably due to presence of other fluctuators in the vicinity of the quantum dot. This is certainly worth trying again provided that large bias counting regime is available in a similar quantum dot.

Appendices

A List of samples

name	AFM picture	wafer info	processed	structure
A2.1.2		Bochum12029 $p=3.8 \times 10^{15} \text{m}^{-2}$ $\mu=1.2 \times 10^5 \text{cm}^2/\text{Vs}$	03/07/10	Three QPCs used for pre-biased cool down measurements reported in Appendix B.
A2.3		Bochum12029 $p=3.8 \times 10^{15} \text{m}^{-2}$ $\mu=1.2 \times 10^5 \text{cm}^2/\text{Vs}$	14/10/10	A QD defined by chemical etching plus aligned top-gate fingers on top of HfO_2 , discussed in section 3.2.4.
A2.4		Bochum12029 $p=3.8 \times 10^{15} \text{m}^{-2}$ $\mu=1.2 \times 10^5 \text{cm}^2/\text{Vs}$	07/02/11	A QD defined by chemical etching. A second step EBL aligned to the structure was used to correct some under-etched lines.
A2.9.2		Bochum12029 $p=3.8 \times 10^{15} \text{m}^{-2}$ $\mu=1.2 \times 10^5 \text{cm}^2/\text{Vs}$	19/10/07	A small QD made by AFM lithography. This sample is discussed in Chapter 8. The charge detector was too open in this sample.

name	AFM picture	wafer info	processed	structure
<i>A3.10.2</i>		Bochum13127 $p=4\times 10^{15}\text{m}^{-2}$ $\mu=2.0\times 10^5\text{cm}^2/\text{Vs}$	16/04/08	A QD with a charge detector QPC made by AFM lithography followed by HCl dipping. The detector QPC was discussed in Chapter 6. The dot was too dirty.
<i>A3.24.1</i>		Bochum13127 $p=4\times 10^{15}\text{m}^{-2}$ $\mu=2.0\times 10^5\text{cm}^2/\text{Vs}$	07/01/09	Three QPCs one of the QPCs, shown in this picture, exhibited a strong 0.7 anomaly discussed in Chapter 5
<i>A4.2.4</i>		Bochum13127 $p=4\times 10^{15}\text{m}^{-2}$ $\mu=2.0\times 10^5\text{cm}^2/\text{Vs}$	19/11/09	A QD plus detector defined by chemical etching followed by AFM patterning of Ti top-gate layer separated by HfO ₂ . Section 3.2.4.
<i>A4.10.1</i> <i>A4.2.1</i> <i>A4.2.2</i>		Bochum13127 $p=4\times 10^{15}\text{m}^{-2}$ $\mu=2.0\times 10^5\text{cm}^2/\text{Vs}$	17/08/09	Three QPCs fabricated in different orientations by chemical etching used to study the g-factor anisotropy, discussed in Chapter 7 and Appendix F.
<i>A10.8.1</i>		Bochum20122 $p=2.7\times 10^{15}\text{m}^{-2}$ $\mu=0.6\times 10^5\text{cm}^2/\text{Vs}$	15/12/12	A QD plus charge detector QPC fabricated by chemical etching. This sample was discussed in Chapters 9 and 10.

B Pre-biased cool down of p-GaAs nano-structures

Doping GaAs with Si creates impurities with mostly hydrogen-like shallow energy levels below the band edge. Some of these impurities are however linked to local lattice distortions depending on the occupation of the level. These are deep donor levels or DX centers [210] which have energy scales of more than 10 meV. The occupancy of these levels can be controlled via an electric field applied by the top-gate that shifts their potential above or below the Fermi energy at room temperature. Once cooled down below 150 K they are frozen and act as an imprinted top-gate on the two-dimensional electron gas depending on their occupancy. This so-called *pre-biased cooling* technique can be used in combination with split-gates to provide excellent tunability in n-type GaAs nano-structures. Furthermore these nano-structures usually suffer from switching noises known as Flicker noise. It has been shown that charge tunneling between deep donors and the 2DEG is the main origin of these switchings [211] and pre-biased cooling can be used to suppressed them [212]. Not much is known about the spectrum of Carbon acceptors in GaAs and it is not clear if they form deep levels in p-GaAs. In this Appendix we study possible effects of pre-biased cooling on three p-GaAs quantum point contacts fabricated on the sample *A2.1.2*. A linear conductance of these QPCs as a function of in-plane gates was shown in Fig. 3.5c.

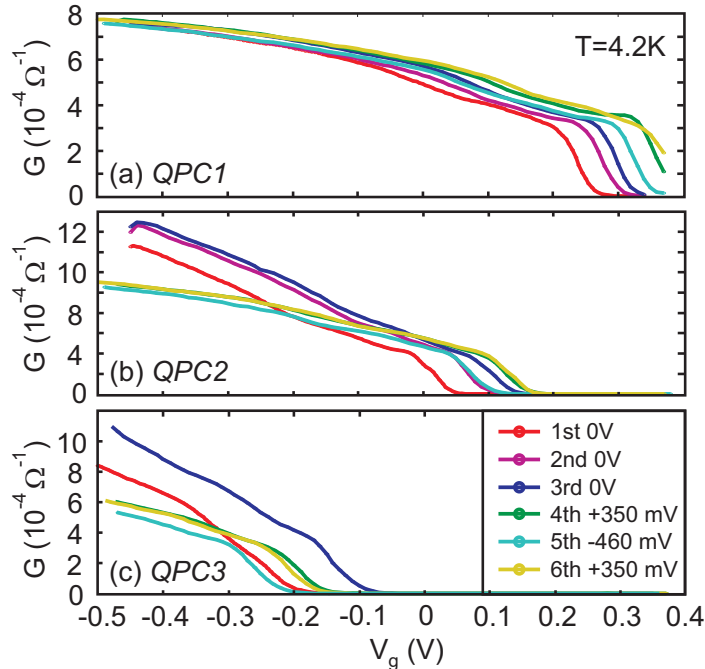


Figure B.1: Effect of pre-biased cool down using in-plane gates on two-terminal conductance of three QPCs in sample *A2.1.2*. The lithographical sizes are 230, 210 and 190 nm for QPC1, QPC2 and QPC3 respectively. The voltages applied to the in-plane gates during 6 cool downs are shown in the inset of (c).

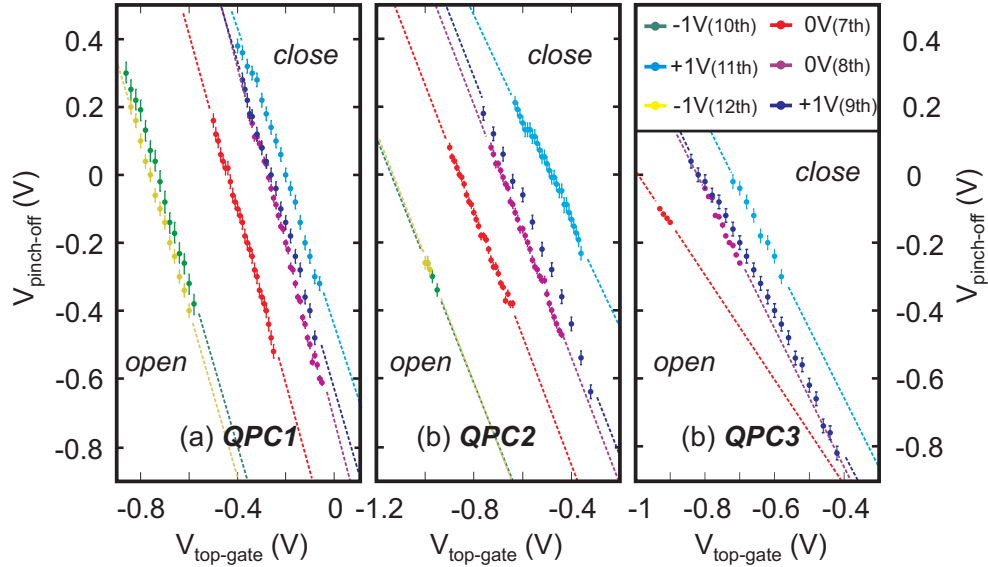


Figure B.2: Pinch-off in-plane gate voltages of the three QPCs as a function of top-gate voltage for different cool downs. The QPCs are open on lower left corner (negative in-plane and top-gate voltages) and closed at upper right corner (positive in-plane and top-gate voltages) of each plot. Dashed lines are guides to the eyes and mark the transition between these two states at each cool down. Measurements range are limited due to in-plane gates leakage that varied at each cool down.

Fig. B.1 illustrates the effect of applying a voltage on the in-plane gates in this (ungated) sample during cool down. The pinch-off value of the in-plane gates hardly changes and there is no significant correlation between the cool down bias and the position of conductance traces in the gate voltage axis. Moreover it seems that several cool downs have increased the series resistance of the QPCs in (b) and (c) presumably due to surface oxidation of the ungated sample.

Later on this sample was covered with a 60 nm thick layer of HfO_2 and an evaporated 10/90 Ti/Au metal film as the top-gate. The sample was cooled down six times with pre-bias voltage values of 0, +1 and -1 V on the top-gate. The cool down bias was alternated between positive and negative values in consecutive cool downs to exclude similar effects that arise from multiple cool downs. The top-gate was leakage free in the regime of $-1 < V_{top-gate} < +1.2$ V with slight variations in each cool down.

The conductance trace of the QPCs were measured as a function of combined top-gate and in-plane gates at each cool down. In order to focus on the relative shift in the QPC potential with respect to the electrochemical potential of the leads and the tunability of the QPC, the in-plane gate voltages at which the QPC opens up $V_{pinch-off}$, defined as the point with the highest transconductance on the conductance trace, are discussed in the following rather than the full linear conductance trace. Fig. B.2 shows how the pinch-off voltage $V_{pinch-off}$ was modified by $V_{top-gate}$

on the three QPCs after each cool down.

These plots can be visualized as 2D plots in which the third axis is the QPC conductance. Toward negative in-plane and top-gate voltages (lower left corner of the plots) the QPCs are open while toward positive in-plane and top-gate voltages (upper right corner of the plots) they are closed. Measured pinch-off voltages, that are extrapolated by the dashed lines as a guide to the eyes, mark the transitions between these two states. While the opening threshold of zero biased cool downs have the highest fluctuations, the biased cool downs have more reproducible thresholds and exhibit a significant shift in the in-plane gate pinch-off value which correlates to the bias during the cool down. Especially in cool downs with negative-biased top-gate, a similar transition is observed on all QPCs (QPC3 was totally closed after negative-biased cool downs). This result can be summarized as the following. Applying a positive (negative) bias on the top-gate during cool down tends to open (close) the QPC. The efficiency of the pre-biased cooling is 0.4 V in the negative case and less than 0.2 V in the positive case.

The pre-biased cool down in n-type quantum wells is understood as the population/depopulation of deep donor centers as discussed before. Observation of similar effects in p-GaAs suggests presence of deep acceptors due to Carbon in AlGaAs. This result can be used to enhance further tunability of p-type nano-structures during cool downs.⁵

⁵The measurements and data analysis presented in this section is adapted from the semester thesis of Daniela Scherer.

C Correction procedure to eliminate the magnetic field-dependent resistance of the leads

Here we discuss the detailed procedure of correcting for a series resistance by which we eliminate the field-dependence of the leads. The procedure is applied to sample *A3.24.1* which was extensively discussed in chapter 5. The corrected conductance is calculated from the raw measured conductance using the formula ⁶

$$G_{corrected}(V_g) = \frac{1}{(G_{raw}(V_g) - G_p)^{-1} - R_{series}} \quad (11.45)$$

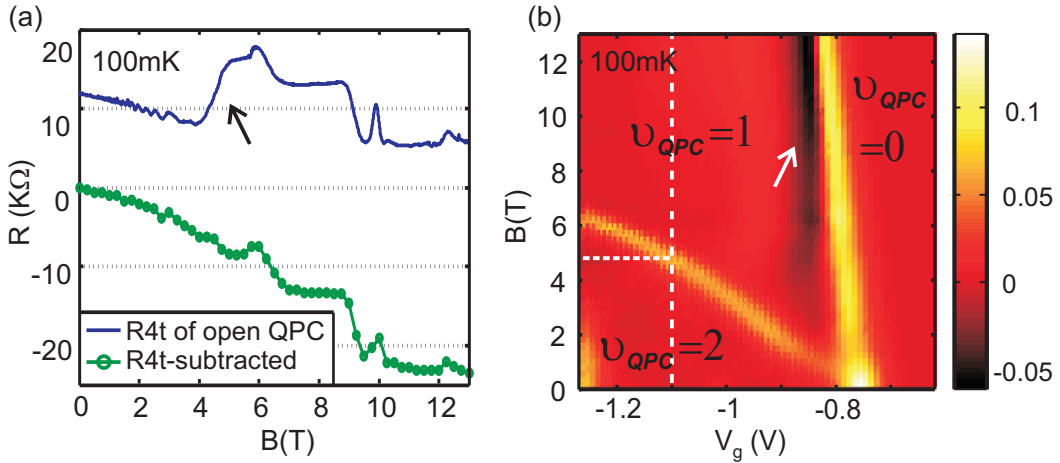


Figure C.3: (a) Comparison between the resistance of the open QPC ($V_g = -1.1V$) (white dashed line in b) with the series resistance *subtracted* from four-terminal resistance of the QPC to keep the conductance of plateaus constant. The black arrow points to the depopulation of the spin down subband. (b) Transconductance (numerical derivative of the raw measured linear conductance with respect to gate voltage) as a function of gate voltage and perpendicular magnetic field. The red areas are plateaus in the conductance whose filling factor is indicated while the high transconductance yellow lines mark the transitions between the plateaus. The white arrow points to the development of a suppressed conductance discussed in the text.

The part G_p comes from the fact that the heterostructure used to fabricate this sample (*A3/Bochum13127*) shows a gate-independent parallel conductance of about $200K\Omega$ which does not depend on the gate voltage and also does not change considerably with the magnetic field without any correlation to SdH oscillations. This parallel conductance can be observed as the non-zero conductance of the QPC in pinch-off in Fig. 5.8a,b. Therefore for the purpose of the high-conductance measurements we are interested in here, it is justified to subtract it from the raw data.

⁶In principle it is also possible to first subtract the resistance and then the conductance. The order of these depends on the circuit model assumed. This formula has the advantage that after removing the parallel conductance the series resistance does not affect the pinch-off resistance.

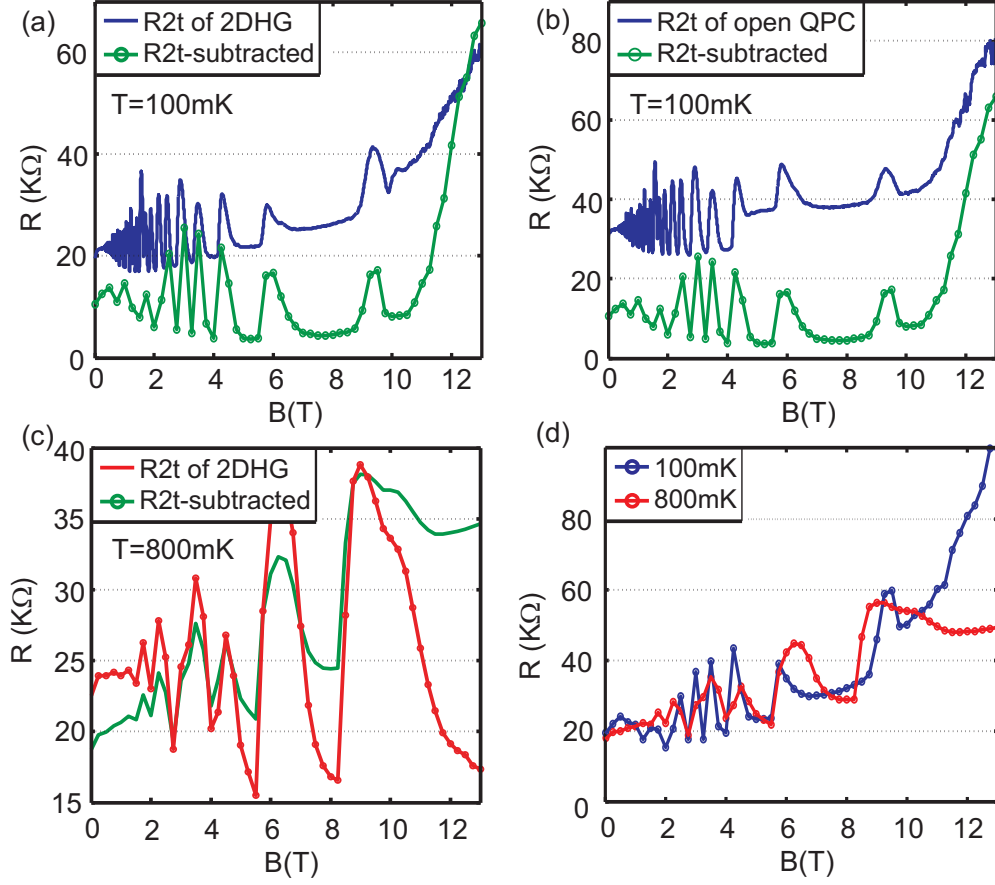


Figure C.4: Comparison of the magnetic field dependence of the series resistance used in the compensation formula 11.45 with the (a) two-terminal resistance of the lead and (b) resistance of the open QPC ($V_g = -1.1\text{V}$), all at 100 mK. (c) shows a similar comparison at 800 mK. Note that the two-terminal resistance of the 2DHG depends on temperature as shown in (d) and so does the series resistance.

Using the Landauer-Buttiker formalism, the four-terminal resistance of the QPC is given by [121, 213, 214]

$$R_{xx} = \frac{h}{e^2} \left(\frac{1}{\nu_{QPC}} - \frac{1}{\nu_0} \right) \quad (11.46)$$

ν_{QPC} and ν_0 are the filling factors inside the QPC and the leads respectively. The former can be extracted from transconductance (derivative of the conductance with respect to the gate voltage) of the QPC as a function of the gate voltage and the perpendicular magnetic field shown in Fig. C.3b. The low transconductance red areas corresponds to plateaus in linear conductance and high transconductance yellow regions are the transitions between the plateaus when the subband energies align with the electrochemical potential of the source and the drain. The 1st subband at $V_g \sim -0.8\text{V}$ at zero field splits linearly to two subbands due to Zeeman splitting (assuming that the gate lever arm is constant). Identifying the filling factor inside the

QPC as shown in the figure, a field-dependent series resistance is subtracted from the measured resistance of the QPC to keep its conductance at the value $\nu_{QPC}(e^2/h)$. Therefore in order to separate the effect of SdH oscillations in the leads from other orbital effects happening in the QPC, it is necessary to *add* a resistance of about

$$R_{added} = -R_{series} = \frac{h}{e^2} \frac{1}{\nu_0} \quad (11.47)$$

to the measured four-terminal resistance of the QPC.

In order to confirm the validity of this procedure, we have plotted in Fig. C.3a the (negative) series resistance used to correct the four-terminal conductance of the QPC as a function of magnetic field in green. On the same plot, the four-terminal resistance of the open QPC (fixed gate voltage $V_g = -1.1V$) is shown in blue. For this particular gate voltage the change in ν_{QPC} from 2 to 1, happens at about 4.5 Tesla (shown by white dashed lines in Fig. C.3b) and this is the reason why the four-terminal resistance of the QPC increases at about $B = 4.5T$ marked with the black arrow in Fig. C.3a.

A similar procedure can be performed for the two-terminal resistance and indeed the same result is obtained. Fig. C.4a compares the serial resistance R_{series} subtracted from the raw two-terminal resistance with the resistance of the leads measured between two independent contacts as a function of B-field. A similar comparison between the subtracted serial resistance R_{series} and the resistance of the open QPC (fixed gate voltage $V_g = -1.1V$) is shown in Fig. C.4b. The fact that the resistance of the leads correlates very well with the subtracted series resistance suggests that indeed what is removed by the correction procedure is the effect of the leads. Note that the SdH oscillations depend on temperature (Fig. C.4c) and therefore different series resistances are used for 100 mK and 800 mK cases. Fig. C.4d compares the series resistance to the two-terminal resistance of the 2DHG at 800 mK.

D Evolution of the finite bias differential conductance at large perpendicular magnetic fields

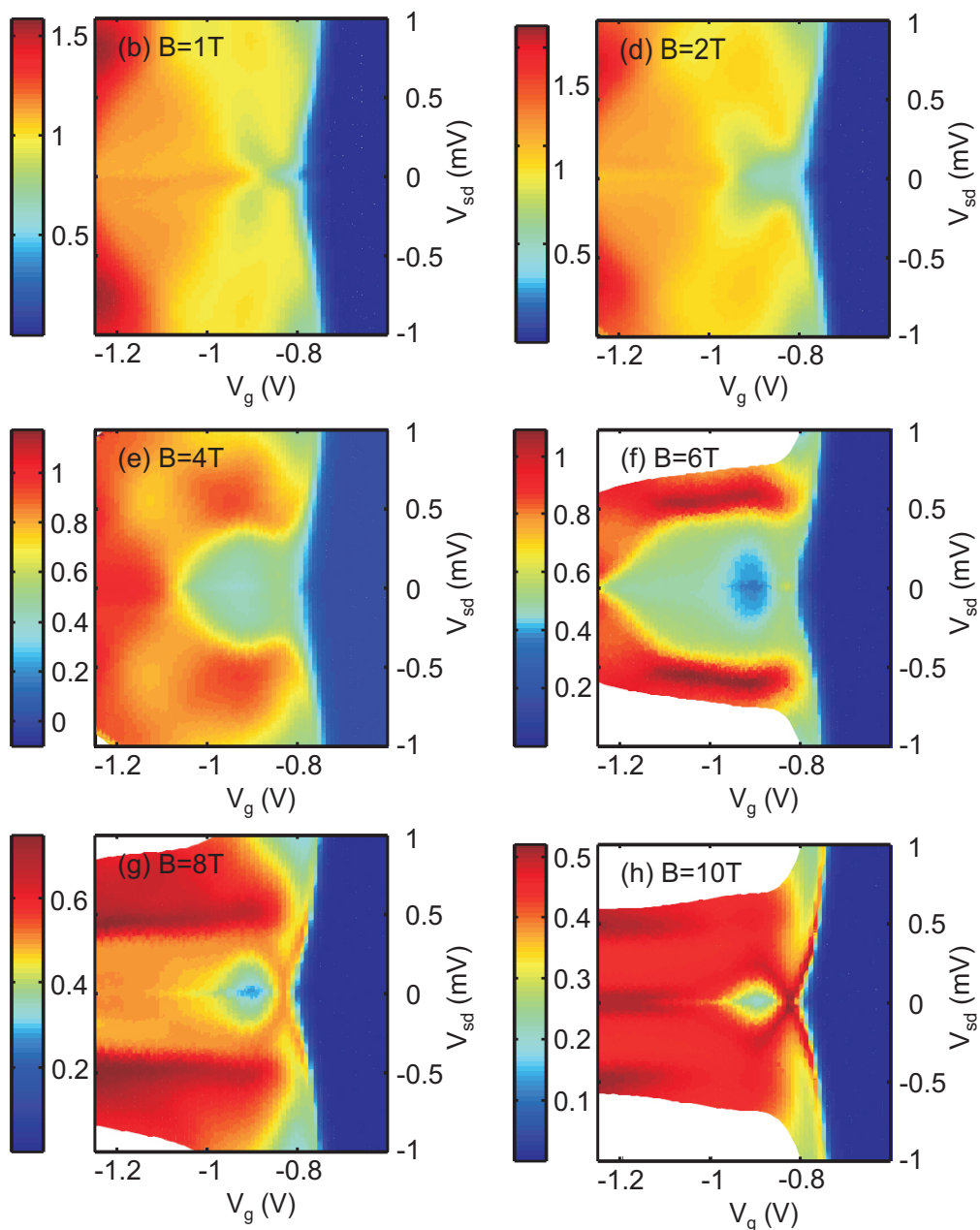


Figure D.5: The evolution of non-linear differential conductance with magnetic field perpendicular to the plane of 2DHG. A region of suppressed conductance in the form of a diamond-like structure is visible in (h).

E Another example of a QPC with 0.7-feature

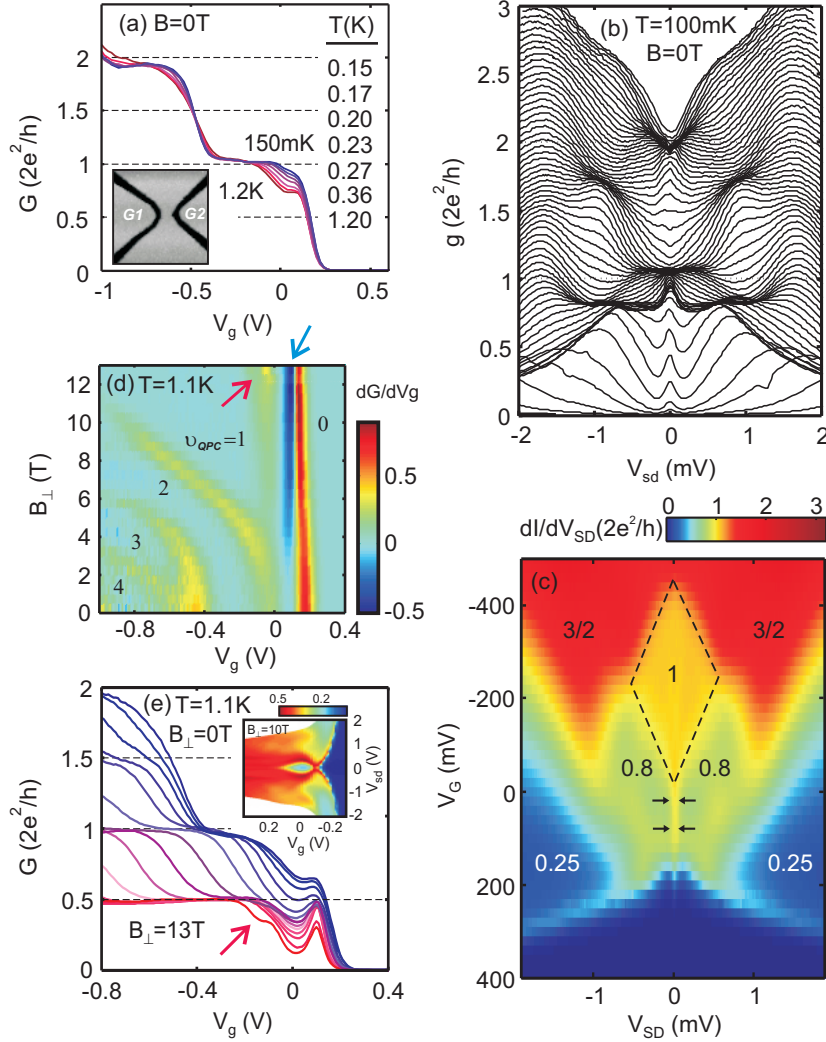


Figure E.6: *A4.10.1/QPC1-10*. (a) Temperature dependence of the linear conductance. The inset shows the AFM micrograph of the sample. (b) and (c) show differential conductance vs. source-drain bias and gate voltage at zero field and base temperature exhibit ZBA. (d) Transconductance as a function of gate voltage and perpendicular magnetic field shows the Zeeman splitting and diamagnetic shift. The blue arrow points to the appearance of the conductance suppression consistent with e. The red arrow points to the appearance of the 2nd peak in the conductance, also shown in e. (e) Effect of perpendicular (to the plane) magnetic field on the linear conductance at the temperature of 1.1 K (a field-dependent series resistance is subtracted). The 0.7-feature gradually transforms to a conductance peak. Inset shows a diamond-like structure on differential conductance at $B_{\perp} = 10$ T.

F Anisotropic Zeeman spin-splitting of hole QPCs

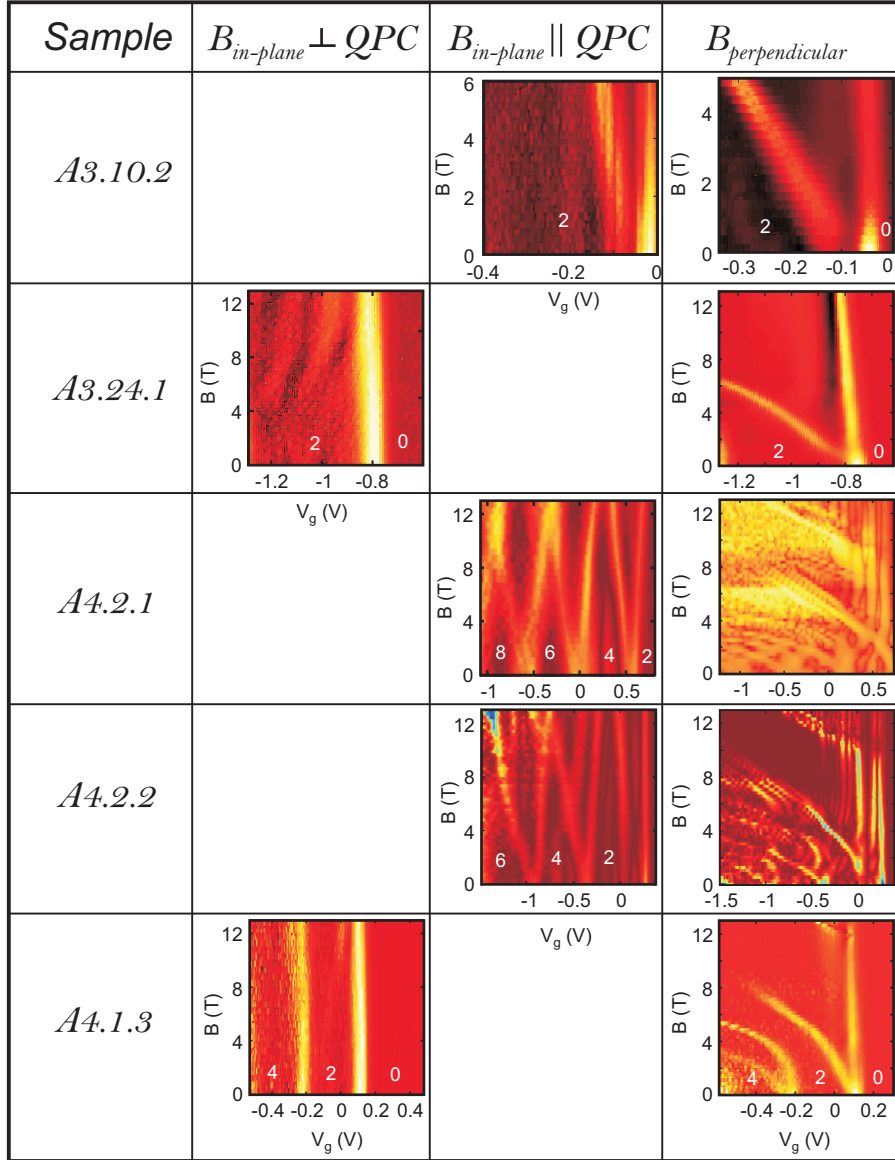


Figure F.7: Transconductance $d^2I/dV_{SD}dV_g$ (a.u.) of quantum point contacts on different samples as a function of gate voltage and magnetic field. The x -axis in all plots are the gate voltage. Magnetic field direction is indicated in the table. The dark red areas are the plateaus conductance of which (or QPC filling factor) is indicated in the plots in units of e^2/h . The bright regions are the transitions between plateaus as the subbands pass the Fermi energy.

G Three charge-state regime

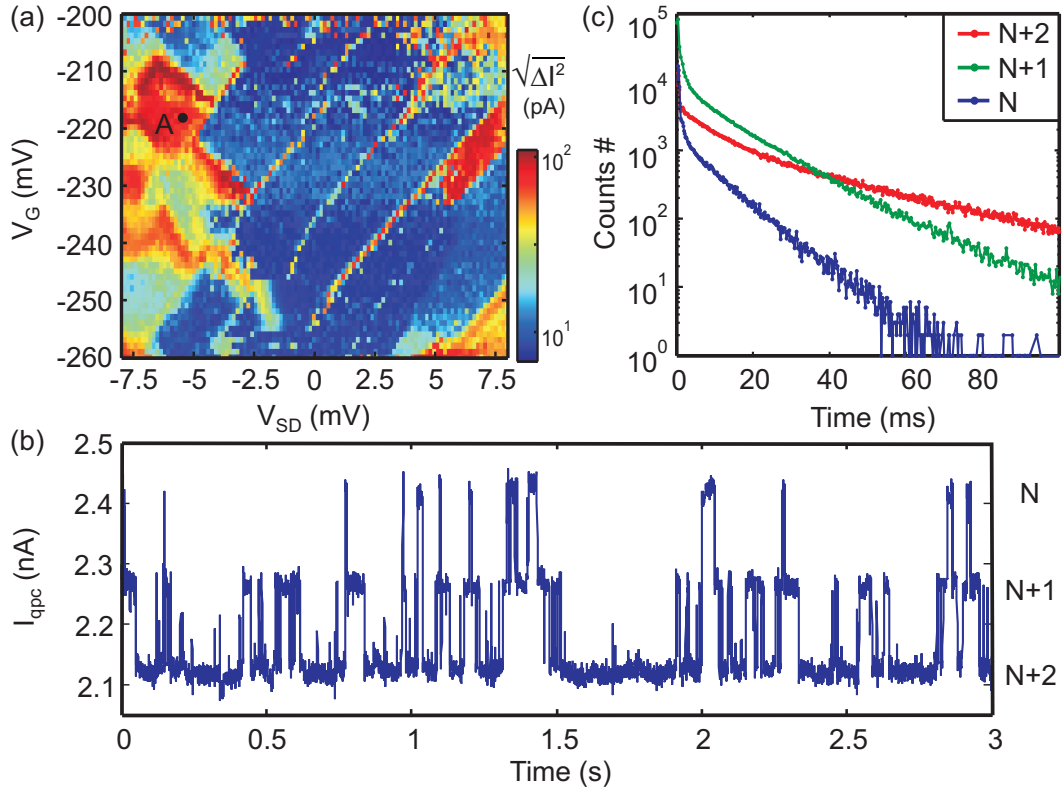


Figure G.8: (a) The detector noise as a function of the dot bias and the symmetric gate voltage. (b) shows the 3-level telegraph noise of the detector current at the point A in (a). The levels correspond to 3 charge state of the dot. (c) the histogram of the times the dot spends in N , $N + 1$ and $N + 2$ charge state, showing non-linearities that suggest non-Markovian statistics in this case.

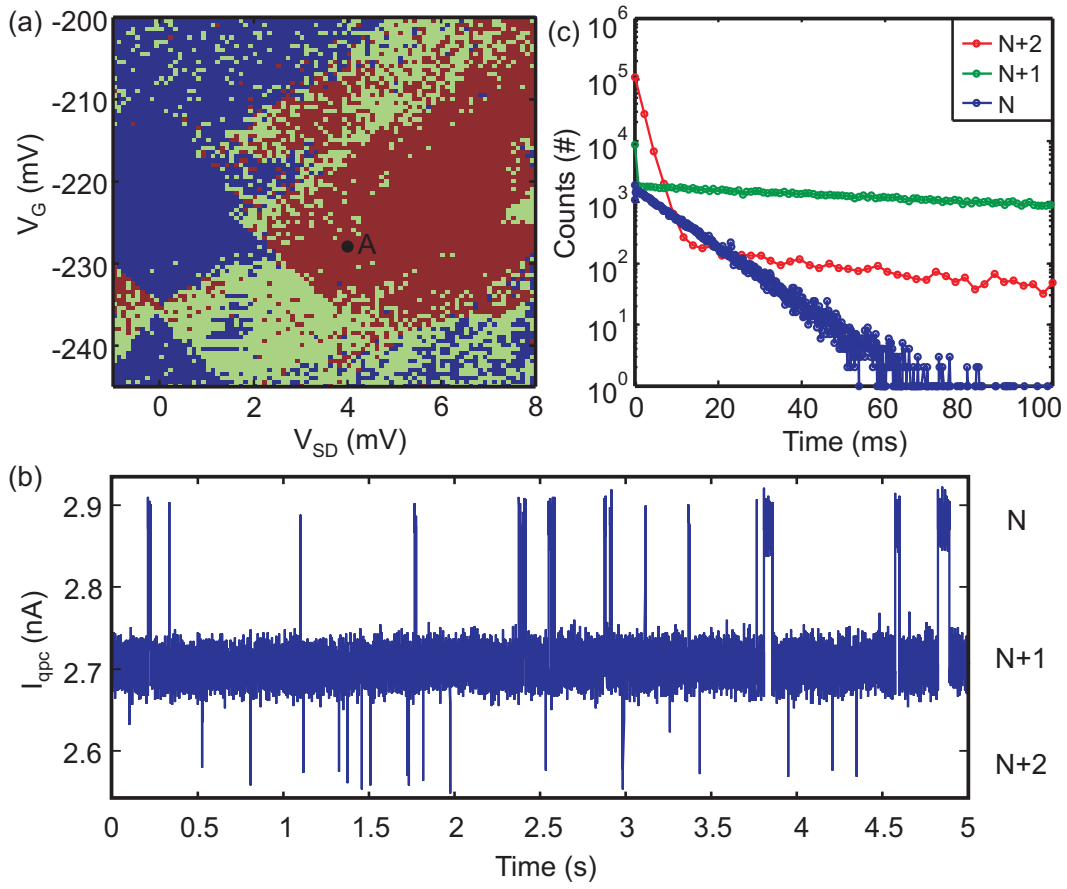


Figure G.9: (a) The number of levels in the detector current as a function of the dot bias and the symmetric gate voltage. (b) shows the 3-level telegraph noise of the detector current at the point A in (a). The levels correspond to 3 charge state of the dot. The dot spends most of the time in the $N + 1$ charge state. (c) the histogram of the times the dot spends in N , $N + 1$ and $N + 2$ charge states. The distribution of the times in $N + 2$ state is clearly double-exponential.

H Cumulants in the three charge-state regime

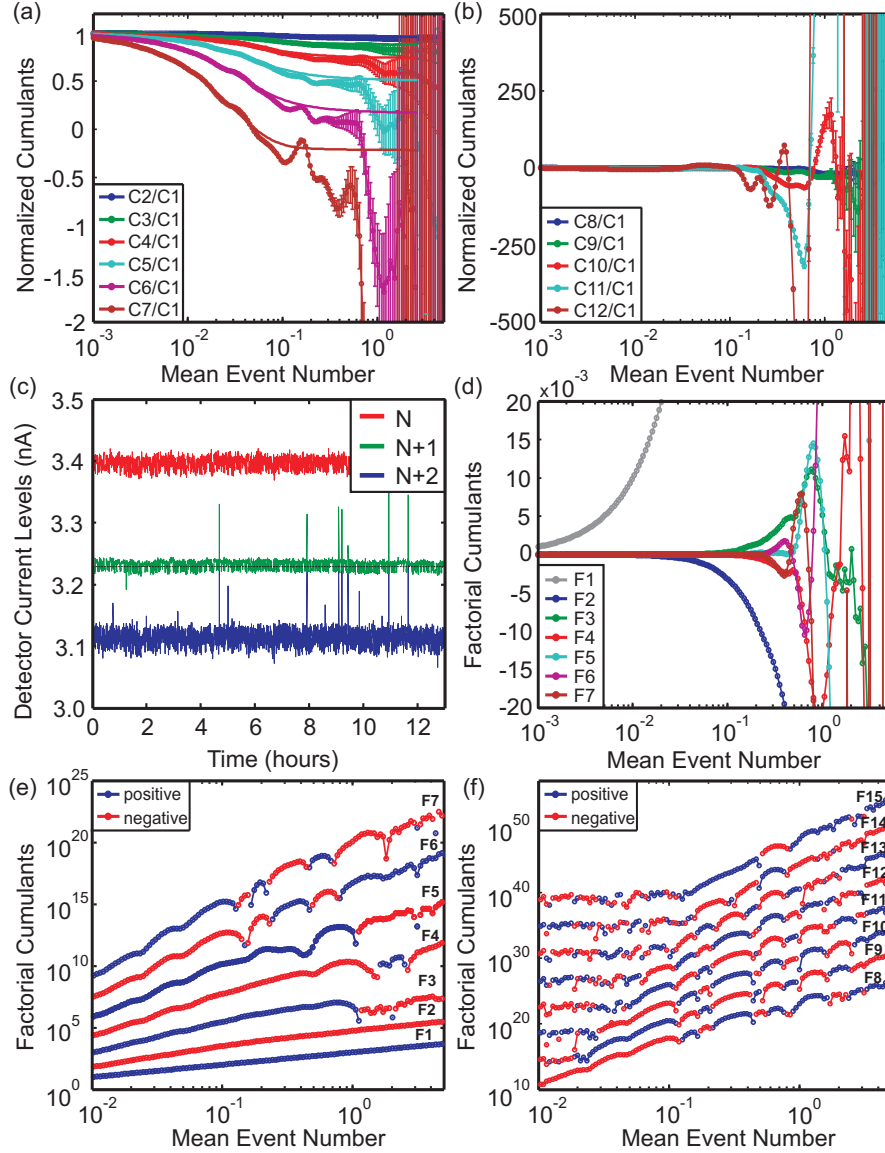


Figure H.10: (a) and (b) show the normalized cumulants measured at the point *A* in Fig. G.9a together with the model calculations (solid lines). The detector current showed fluctuations in the time scale of minutes as shown in (c). Each point is the estimation of the current level of different states from a 10-sec time trace. The calculation of cumulants was only possible if only part of the data, corresponding to the green curve above the black dashed line was kept. (d) First few factorial cumulants calculated from ordinary cumulants show oscillations in all scales along with the predictions of Kambly et al. [204]. (e) and (f) show the factorial cumulants in a log-log plot. The alternation of red and blue segments in each curve indicate zero-crossing oscillations in the cumulants.

Publications

Observation of excited states in a p-type GaAs quantum dot

Y. Komijani, M. Csontos, T. Ihn, K. Ensslin, D. Reuter, A. D. Wieck
Europhys. Lett. **84**, 57004 (2008).

Evidence for localization and 0.7 anomaly in hole quantum point contacts

Y. Komijani, M. Csontos, I. Shurobalko, T. Ihn, K. Ensslin, Y. Meir, D. Reuter, A. D. Wieck
Europhys. Lett. **91**, 67010 (2010).

Nanostructures in p-GaAs with improved tunability

M. Csontos, Y. Komijani, I. Shurobalko, T. Ihn, K. Ensslin, D. Reuter, A. D. Wieck
Appl. Phys. Lett. **97**, 022110 (2010).

Bibliography

- [1] T. Ihn, *Semiconductor Nanostructures: Quantum states and electronic transport* (Oxford University Press, USA, 2010).
- [2] D. Reuter, A. D. Wieck, and A. Fischer, *A compact electron beam evaporator for carbon doping in solid source molecular beam epitaxy*, Review of Scientific Instruments **70**, 3435 (1999).
- [3] A. D. Wieck and D. Reuter, *High electron and hole mobility $Al_{0.3}Ga_{0.7}As$ heterostructures grown in the same standard mbe setup*, Inst. Phys. Conf. Ser. **166**, 51 (2000).
- [4] C. Gerl, S. Schmult, H.-P. Tranitz, C. Mitzkus, and W. Wegscheider, *Carbon-doped symmetric GaAs/AlGaAs quantum wells with hole mobilities beyond 10^6 cm^2/Vs* , Applied Physics Letters **86**, 252105 (pages 3) (2005).
- [5] M. J. Manfra, L. N. Pfeiffer, K. W. West, R. de Picciotto, and K. W. Baldwin, *High mobility two-dimensional hole system in gaas/algaas quantum wells grown on (100) gaas substrates*, Applied Physics Letters **86**, 162106 (pages 3) (2005).
- [6] B. Grbić, Ph.D. thesis, ETH Zurich (2007).
- [7] E. P. D. Poortere, E. Tutuc, S. J. Papadakis, and M. Shayegan, *Resistance spikes at transitions between quantum hall ferromagnets*, Science **290**, 1546 (2000).
- [8] B. Grbić, C. Ellenberger, T. Ihn, K. Ensslin, D. Reuter, and A. D. Wieck, *Magnetotransport in c-doped AlGaAs heterostructures*, Appl. Phys. Lett. **85**, 2277 (2004).
- [9] H. Zhu, K. Lai, D. Tsui, S. Bayrakci, N. Ong, M. Manfra, L. Pfeiffer, and K. West, *Density and well width dependences of the effective mass of two-dimensional holes in (100) gaas quantum wells measured using cyclotron resonance at microwave frequencies*, Solid State Communications **141**, 510 (2007).
- [10] R. Winkler, E. Tutuc, S. J. Papadakis, S. Melinte, M. Shayegan, D. Wasserman, and S. A. Lyon, *Anomalous spin polarization of gaas two-dimensional hole systems*, Phys. Rev. B **72**, 195321 (2005).

- [11] R. Winkler, *Spin polarization of quasi-two-dimensional hole systems*, Phys. Rev. B **71**, 113307 (2005).
- [12] R. Winkler, D. Culcer, S. J. Papadakis, B. Habib, and M. Shayegan, *Spin orientation of holes in quantum wells*, Semiconductor Science and Technology **23**, 114017 (2008).
- [13] B. Grbić, R. Leturcq, T. Ihn, K. Ensslin, D. Reuter, and A. D. Wieck, *Strong spin-orbit interactions and weak antilocalization in carbon-doped p-type GaAs/Al_xGa_{1-x}As heterostructures*, Phys. Rev. B **77**, 125312 (2008).
- [14] A. R. Hamilton, M. Y. Simmons, M. Pepper, E. H. Linfield, and D. A. Ritchie, *Metallic behavior in dilute two-dimensional hole systems*, Phys. Rev. Lett. **87**, 126802 (2001).
- [15] R. Leturcq, D. L'Hôte, R. Tourbot, C. J. Mellor, and M. Henini, *Resistance noise scaling in a dilute two-dimensional hole system in gaas*, Phys. Rev. Lett. **90**, 076402 (2003).
- [16] S. V. Kravchenko and M. P. Sarachik, *Metal-insulator transition in two-dimensional electron systems*, Reports on Progress in Physics **67**, 1 (2004).
- [17] G. A. Csáthy, H. Noh, D. C. Tsui, L. N. Pfeiffer, and K. W. West, *Magnetic-field-induced insulating phases at large r_s*, Phys. Rev. Lett. **94**, 226802 (2005).
- [18] M. J. Manfra, R. de Picciotto, Z. Jiang, S. H. Simon, L. N. Pfeiffer, K. W. West, and A. M. Sergent, *Impact of spin-orbit coupling on quantum hall nematic phases*, Phys. Rev. Lett. **98**, 206804 (2007).
- [19] B. Grbic, R. Leturcq, K. Ensslin, D. Reuter, and A. D. Wieck, *Single-hole transistor in p-article GaAs/AlGaAs heterostructures*, Appl. Phys. Lett. **87**, 232108 (2005).
- [20] O. Klochan, J. C. H. Chen, A. P. Micolich, A. R. Hamilton, K. Muraki, and Y. Hirayama, *Fabrication and characterization of an induced gaas single hole transistor*, Applied Physics Letters **96**, 092103 (pages 3) (2010).
- [21] O. Klochan, W. R. Clarke, R. Danneau, A. P. Micolich, L. H. Ho, A. R. Hamilton, K. Muraki, and Y. Hirayama, *Ballistic transport in induced one-dimensional hole systems*, Appl. Phys. Lett. **89**, 092105 (2006).
- [22] L. P. Rokhinson, L. N. Pfeiffer, and K. W. West, *Spontaneous spin polarization in quantum point contacts*, Phys. Rev. Lett. **96**, 156602 (2006).
- [23] S. P. Koduvayur, L. P. Rokhinson, D. C. Tsui, L. N. Pfeiffer, and K. W. West, *Anisotropic modification of the effective hole g factor by electrostatic confinement*, Phys. Rev. Lett. **100**, 126401 (2008).

- [24] J. Shabani, J. R. Petta, and M. Shayegan, *High-quality quantum point contact in two-dimensional GaAs (311)a hole system*, Appl. Phys. Lett. **93**, 212101 (2008).
- [25] B. Habib, E. Tutuc, and M. Shayegan, *Strong aharonov-bohm oscillations in gaas two-dimensional holes*, Applied Physics Letters **90**, 152104 (pages 3) (2007).
- [26] B. Grbić, R. Leturcq, T. Ihn, K. Ensslin, D. Reuter, and A. D. Wieck, *Aharonov-bohm oscillations in the presence of strong spin-orbit interactions*, Phys. Rev. Lett. **99**, 176803 (2007).
- [27] R. Danneau, W. R. Clarke, O. Klochan, A. P. Micolich, A. R. Hamilton, M. Y. Simmons, M. Pepper, and D. A. Ritchie, *Conductance quantization and the $0.7 \times 2e^2/h$ conductance anomaly in one-dimensional hole system*, Appl. Phys. Lett. **88**, 012107 (2006).
- [28] K. Ensslin, *Quantum point contacts: Pinning down the last spin*, Nature **2**, 587 (2006).
- [29] R. Danneau, O. Klochan, W. R. Clarke, L. H. Ho, A. P. Micolich, M. Y. Simmons, A. R. Hamilton, M. Pepper, and D. A. Ritchie, *0.7 structure and zero bias anomaly in ballistic hole quantum wires*, Phys. Rev. Lett. **100**, 016403 (2008).
- [30] W. A. Harrison, *Elementary Electronic Structure* (World Scientific Pub Co Inc, 2004).
- [31] R. Winkler, *Spin-orbit Coupling Effects in Two-Dimensional Electron and Hole Systems* (Springer, 2003).
- [32] J. M. Luttinger, *Quantum theory of cyclotron resonance in semiconductors: General theory*, Phys. Rev. **102**, 1030 (1956).
- [33] M. Kemerink, Ph.D. thesis, Technische Universiteit Eindhoven (1998).
- [34] G. Dresselhaus, *Spin-orbit coupling effects in zinc blende structures*, Phys. Rev. **100**, 580 (1955).
- [35] J. Nitta, T. Akazaki, H. Takayanagi, and T. Enoki, *Gate control of spin-orbit interaction in an inverted $In_{0.53}Ga_{0.47}As/In_{0.52}Al_{0.48}As$ heterostructure*, Phys. Rev. Lett. **78**, 1335 (1997).
- [36] G. Engels, J. Lange, T. Schäpers, and H. Lüth, *Experimental and theoretical approach to spin splitting in modulation-doped $In_xGa_{1-x}As/InP$ quantum wells for $B \rightarrow 0$* , Phys. Rev. B **55**, R1958 (1997).

- [37] S. Datta and B. Das, *Electronic analog of the electro-optic modulator*, Applied Physics Letters **56**, 665 (1990).
- [38] B. Habib, M. Shayegan, and R. Winkler, *Spin-orbit interaction and transport in GaAs two-dimensional holes*, Semiconductor Science and Technology **24**, 064002 (2009).
- [39] W. Zawadzki and P. Pfeffer, *Spin splitting of subband energies due to inversion asymmetry in semiconductor heterostructures*, Semiconductor Science and Technology **19**, R1 (2004).
- [40] D. Loss and D. P. DiVincenzo, *Quantum computation with quantum dots*, Phys. Rev. A **57**, 120 (1998).
- [41] A. V. Khaetskii, D. Loss, and L. Glazman, *Electron spin decoherence in quantum dots due to interaction with nuclei*, Phys. Rev. Lett. **88**, 186802 (2002).
- [42] F. Koppens, C. Buizert, K. Tielrooij, I. Vink, K. Nowack, T. Meunier, L. Kouwenhoven, and L. Vandersypen, *Driven coherent oscillations of a single electron spin in a quantum dot*, Nature **442**, 766 (2006).
- [43] J. R. Petta, A. C. Johnson, J. M. Taylor, E. A. Laird, A. Yacoby, M. D. Lukin, C. M. Marcus, M. P. Hanson, and A. C. Gossard, *Coherent manipulation of coupled electron spins in semiconductor quantum dots*, Science **309**, 2180 (2005).
- [44] J. Fischer, W. A. Coish, D. V. Bulaev, and D. Loss, *Spin decoherence of a heavy hole coupled to nuclear spins in a quantum dot*, Phys. Rev. B **78**, 155329 (2008).
- [45] P. Fallahi, S. T. Yilmaz, and A. Imamoglu, *Observation of heavy-hole hyperfine interaction in quantum dots*, ArXiv e-prints **1009.0181** (2010).
- [46] N. W. Ashcroft and N. D. Mermin, *Solid State Physics* (Brooks Cole, 1976).
- [47] H. Bruus and K. Flensberg, *Many-body quantum theory in condensed matter physics: an introduction*, Oxford graduate texts in mathematics (Oxford University Press, 2004), ISBN 9780198566335.
- [48] G. Giuliani and G. Vignale, *Quantum Theory of the Electron Liquid* (Cambridge University Press, 2005).
- [49] R. Shankar, *Theories of the fractional quantum Hall effect*, arXiv based on Cargese Lectures (2001), http://arxiv.org/PS_cache/cond-mat/pdf/0108/0108271v1.pdf.

- [50] B. J. van Wees, H. van Houten, C. W. J. Beenakker, J. G. Williamson, L. P. Kouwenhoven, D. van der Marel, and C. T. Foxon, *Quantized conductance of point contacts in a two-dimensional electron gas*, Phys. Rev. Lett. **60**, 848 (1988).
- [51] D. A. Wharam, T. J. Thornton, R. Newbury, M. Pepper, H. Ahmed, J. E. F. Frost, D. G. Hasko, D. C. Peacock, D. A. Ritchie, and G. A. C. Jones, *One-dimensional transport and the quantisation of the ballistic resistance*, Journal of Physics C: Solid State Physics **21**, L209 (1988).
- [52] B. J. van Wees, L. P. Kouwenhoven, E. M. M. Willems, C. J. P. M. Harmans, J. E. Mooij, H. van Houten, C. W. J. Beenakker, J. G. Williamson, and C. T. Foxon, *Quantum ballistic and adiabatic electron transport studied with quantum point contacts*, Phys. Rev. B **43**, 12431 (1991).
- [53] I. Aleiner, P. Brouwer, and L. Glazman, *Quantum effects in coulomb blockade*, Physics Reports **358**, 309 (2002).
- [54] M. Pustilnik and L. Glazman, *Kondo effect in quantum dots*, Journal of Physics: Condensed Matter **16**, R513 (2004).
- [55] S. Gustavsson, Ph.D. thesis, ETH Zurich (2008).
- [56] I. Zailer, J. E. F. Frost, C. J. B. Ford, M. Pepper, M. Y. Simmons, D. A. Ritchie, J. T. Nicholls, and G. A. C. Jones, *Phase coherence, interference, and conductance quantization in a confined two-dimensional hole gas*, Phys. Rev. B **49**, 5101 (1994).
- [57] A. J. Daneshvar, C. J. B. Ford, A. R. Hamilton, M. Y. Simmons, M. Pepper, and D. A. Ritchie, *Enhanced g factors of a one-dimensional hole gas with quantized conductance*, Phys. Rev. B **55**, R13409 (1997).
- [58] J. R. Waldrop, *Schottky-barrier height of ideal metal contacts to GaAs*, Appl. Phys. Lett. **44**, 1002 (1984).
- [59] E. I. Rashba, *Properties of semiconductors with an extremum loop .1. cyclotron and combinational resonance in a magnetic field perpendicular to the plane of the loop*, Sov. Phys. Solid. State **2**, 1109 (1960).
- [60] A. Dorn, Ph.D. thesis, ETH Zurich (2004).
- [61] R. Williams, *Modern GaAs Processing Methods* (Artech House, 1990).
- [62] J. A. Dagata, *Device fabrication by scanned probe oxidation*, Science **270**, 1625 (1995).

- [63] R. Held, T. Vancura, T. Heinzel, K. Ensslin, M. Holland, and W. Wegscheider, *In-plane gates and nanostructures fabricated by direct oxidation of semiconductor heterostructures with an atomic force microscope*, Appl. Phys. Lett. **73**, 262 (1998).
- [64] L. Rokhinson, D. Tsui, L. Pfeiffer, and K. West, *AFM local oxidation nanopatterning of a high mobility shallow 2d hole gas*, Superlattices and Microstructures **32**, 99 (2002).
- [65] R. E. Held, Ph.D. thesis, ETH Zurich (2000).
- [66] D. Graf, M. Frommenwiler, P. Studerus, T. Ihn, K. Ensslin, D. C. Driscoll, and A. C. Gossard, *Local oxidation of Ga[Al]As heterostructures with modulated tip-sample voltages*, **99**, 053707 (2006).
- [67] J. Robertson, *High dielectric constant oxides*, The European Physical Journal - Applied Physics **28**, 265 (2004).
- [68] M. Ritala and M. Leskelä, *Atomic layer epitaxy - a valuable tool for nanotechnology?*, Nanotechnology **10**, 19 (1999).
- [69] M. Ritala, *High k Gate Dielectrics* (Taylor & Francis, 2003).
- [70] G. D. Wilk, R. M. Wallace, and J. M. Anthony, *High- κ gate dielectrics: Current status and materials properties considerations*, Appl. Phys. Lett. **89**, 5243 (2001).
- [71] M. Büttiker, *Quantized transmission of a saddle-point constriction*, Phys. Rev. B **41**, 7906 (1990).
- [72] M. Sigrist, Ph.D. thesis, ETH Zurich (2006).
- [73] U. A. Gasser, Ph.D. thesis, ETH Zurich (2011).
- [74] J. F. Keithley, *Low Level Measurements Handbook* (John Yeager and Mary Anne Hrusch-Tupta, 1998).
- [75] H. B. Callen and T. A. Welton, *Irreversibility and generalized noise*, Phys. Rev. **83**, 34 (1951).
- [76] F. Pobel, *Matter and Methods at Low Temperatures* (Springer; 2nd edition, 2002).
- [77] C. L. Kane and M. P. A. Fisher, *Transmission through barriers and resonant tunneling in an interacting one-dimensional electron gas*, Phys. Rev. B **46**, 15233 (1992).

- [78] D. L. Maslov and M. Stone, *Landauer conductance of luttinger liquids with leads*, Phys. Rev. B **52**, R5539 (1995).
- [79] A. P. Micolich, *What lurks below the last plateau: experimental studies of the $0.7 \times 2e^2/h$ conductance anomaly in one-dimensional systems*, Journal of Physics: Condensed Matter **23**, 443201 (2011).
- [80] A. Graham, Ph.D. thesis, University of Cambridge (2003).
- [81] K. J. Thomas, J. T. Nicholls, M. Y. Simmons, M. Pepper, D. R. Mace, and D. A. Ritchie, *Possible spin polarization in a one-dimensional electron gas*, Phys. Rev. Lett. **77**, 135 (1996).
- [82] A. Kristensen, H. Bruus, A. E. Hansen, J. B. Jensen, P. E. Lindelof, C. J. Marckmann, J. Nygård, C. B. Sørensen, F. Beuscher, A. Forchel, et al., *Bias and temperature dependence of the 0.7 conductance anomaly in quantum point contacts*, Phys. Rev. B **62**, 10950 (2000).
- [83] S. M. Cronenwett, H. J. Lynch, D. Goldhaber-Gordon, L. P. Kouwenhoven, C. M. Marcus, K. Hirose, N. S. Wingreen, and V. Umansky, *Low-temperature fate of the 0.7 structure in a point contact: A kondo-like correlated state in an open system*, Phys. Rev. Lett. **88**, 226805 (2002).
- [84] F. Sfgakis, Ph.D. thesis, University of Cambridge (2005).
- [85] T. Rejec, A. Ramšak, and J. H. Jefferson, *Spin-dependent resonances in the conduction edge of quantum wires*, Phys. Rev. B **62**, 12985 (2000).
- [86] K. A. Matveev, *Conductance of a quantum wire at low electron density*, Phys. Rev. B **70**, 245319 (2004).
- [87] A. M. Lunde, A. D. Martino, A. Schulz, R. Egger, and K. Flensberg, *Electron-electron interaction effects in quantum point contacts*, New Journal of Physics **11**, 023031 (2009).
- [88] G. Seelig, K. A. Matveev, and A. V. Andreev, *Phonon-induced resistivity of electron liquids in quantum wires*, Phys. Rev. Lett. **94**, 066802 (2005).
- [89] K.-F. Berggren, P. Jaksch, and I. Yakimenko, *Effects of electron interactions at crossings of zeeman-split subbands in quantum wires*, Phys. Rev. B **71**, 115303 (2005).
- [90] A. Graham, K. Thomas, M. Pepper, M. Simmons, D. Ritchie, K.-F. Berggren, P. Jaksch, A. Debnarova, and I. Yakimenko, *0.7 analogue structures and exchange interactions in quantum wires*, Solid State Communications **131**, 591 (2004).

- [91] K. F. Berggren and I. I. Yakimenko, *Effects of exchange and electron correlation on conductance and nanomagnetism in ballistic semiconductor quantum point contacts*, Phys. Rev. B **66**, 085323 (2002).
- [92] D. J. Reilly, T. M. Buehler, J. L. O'Brien, A. R. Hamilton, A. S. Dzurak, R. G. Clark, B. E. Kane, L. N. Pfeiffer, and K. W. West, *Density-dependent spin polarization in ultra-low-disorder quantum wires*, Phys. Rev. Lett. **89**, 246801 (2002).
- [93] D. J. Reilly, *Phenomenological model for the 0.7 conductance feature in quantum wires*, Phys. Rev. B **72**, 033309 (2005).
- [94] E. Lieb and D. Mattis, *Theory of ferromagnetism and the ordering of electronic energy levels*, Phys. Rev. **125**, 164 (1962).
- [95] N. D. Mermin and H. Wagner, *Absence of ferromagnetism or antiferromagnetism in one- or two-dimensional isotropic heisenberg models*, Phys. Rev. Lett. **17**, 1133 (1966).
- [96] I. V. Zozoulenko and S. Ihnatsenka, *Handbook of Nanophysics: Nanotubes and Nanowires, Chapter 38, Quantum Point Contact in Two-Dimensional Electron Gas* (CRC Press, Taylor & Francis, 2010).
- [97] Y. Meir, *The theory of the '0.7 anomaly' in quantum point contacts*, Journal of Physics: Condensed Matter **20**, 164208 (2008).
- [98] O. P. Sushkov, *Restricted and unrestricted hartree-fock calculations of conductance for a quantum point contact*, Phys. Rev. B **67**, 195318 (2003).
- [99] A. A. Starikov, I. I. Yakimenko, and K.-F. Berggren, *Scenario for the 0.7-conductance anomaly in quantum point contacts*, Phys. Rev. B **67**, 235319 (2003).
- [100] Y. Meir, K. Hirose, and N. S. Wingreen, *Kondo model for the '0.7 anomaly' in transport through a quantum point contact*, Phys. Rev. Lett. **89**, 196802 (2002).
- [101] S. M. Cronenwett, Ph.D. thesis, Stanford University (2001).
- [102] T. Rejec and Y. Meir, *Magnetic impurity formation in quantum point contacts*, Nature **442**, 900 (2006).
- [103] W. Kohn and L. J. Sham, *Self-consistent equations including exchange and correlation effects*, Phys. Rev. **140**, A1133 (1965).
- [104] H. Bruus, V. V. Cheianov, and K. Flensberg, *The anomalous 0.5 and 0.7 conductance plateaus in quantum point contacts*, Physica E: Low-dimensional Systems and Nanostructures **10**, 97 (2001).

- [105] D. J. Reilly, *The 0.7 conductance feature above the kondo temperature*, Proc. 2nd Quantum Transport Nano-Hana International Workshop **IPAP Conf. Series 5**, 7 (2004).
- [106] D. Reilly, Y. Zhang, and L. DiCarlo, *Phenomenology of the 0.7 conductance feature*, Physica E: Low-dimensional Systems and Nanostructures **34**, 27 (2006).
- [107] S. Ihnatsenka and I. V. Zozoulenko, *Conductance of a quantum point contact based on spin-density-functional theory*, Phys. Rev. B **76**, 045338 (2007).
- [108] I. V. Zozoulenko and S. Ihnatsenka, *Electron interaction and spin effects in quantum wires, quantum dots and quantum point contacts: a first-principles mean-field approach*, Journal of Physics: Condensed Matter **20**, 164217 (2008).
- [109] D. Goldhaber-Gordon, H. Shtrikman, D. Mahalu, D. Abusch-Magder, U. Meirav, and M. A. Kastner, *Kondo effect in a single-electron transistor*, Nature **391**, 156 (1998).
- [110] Y. Meir, N. S. Wingreen, and P. A. Lee, *Low-temperature transport through a quantum dot: The anderson model out of equilibrium*, Phys. Rev. Lett. **70**, 2601 (1993).
- [111] A. Ghosh, M. H. Wright, C. Siegert, M. Pepper, I. Farrer, C. J. B. Ford, and D. A. Ritchie, *Zero-bias anomaly and kondo-assisted quasiballistic 2d transport*, Phys. Rev. Lett. **95**, 066603 (2005).
- [112] T. A. Sedrakyan, E. G. Mishchenko, and M. E. Raikh, *Zero-bias tunneling anomaly in a clean 2d electron gas caused by smooth density variations*, Phys. Rev. Lett. **99**, 206405 (2007).
- [113] F. Sfigakis, C. J. B. Ford, M. Pepper, M. Kataoka, D. A. Ritchie, and M. Y. Simmons, *Kondo effect from a tunable bound state within a quantum wire*, Phys. Rev. Lett. **100**, 026807 (2008).
- [114] S. Sarkozy, F. Sfigakis, K. Das Gupta, I. Farrer, D. A. Ritchie, G. A. C. Jones, and M. Pepper, *Zero-bias anomaly in quantum wires*, Phys. Rev. B **79**, 161307 (2009).
- [115] T.-M. Chen, A. C. Graham, M. Pepper, I. Farrer, and D. A. Ritchie, *Non-kondo zero-bias anomaly in quantum wires*, Phys. Rev. B **79**, 153303 (2009).
- [116] Y. Ren, W. W. Yu, S. M. Frolov, J. A. Folk, and W. Wegscheider, *Zero-bias anomaly of quantum point contacts in the low-conductance limit*, Phys. Rev. B **82**, 045313 (2010).

- [117] T.-M. Liu, B. Hemingway, A. Kogan, S. Herbert, and M. Melloch, *Magnetic splitting of the zero-bias peak in a quantum point contact with a tunable aspect ratio*, Phys. Rev. B **84**, 075320 (2011).
- [118] A. R. Hamilton, R. Danneau, O. Klochan, W. R. Clarke, A. P. Micolich, L. H. Ho, M. Y. Simmons, D. A. Ritchie, M. Pepper, K. Muraki, et al., *The 0.7 anomaly in one-dimensional hole quantum wires*, Journal of Physics: Condensed Matter **20**, 164205 (2008).
- [119] P. E. Lindelof and M. Aagesen, *Measured deviations from the saddle potential description of clean quantum point contacts*, Journal of Physics: Condensed Matter **20**, 164207 (2008).
- [120] K.-F. Berggren and I. I. Yakimenko, *Nature of electron states and symmetry breaking in quantum point contacts according to the local spin density approximation*, Journal of Physics: Condensed Matter **20**, 164203 (2008).
- [121] R. W. Giannetta, T. A. Olheiser, M. Hannan, I. Adesida, and M. R. Melloch, *Conductance quantization and zero bias peak in a gated quantum wire*, Physica E **27**, 270 (2005).
- [122] P. L. McEuen, B. W. Alphenaar, R. G. Wheeler, and R. N. Sacks, *Resonant transport effects due to an impurity in a narrow constriction*, Surf. Sci. **229**, 312 (1990).
- [123] J. U. Nöckel and A. D. Stone, *Resonance line shapes in quasi-one-dimensional scattering*, Phys. Rev. B **50**, 17415 (1994).
- [124] T. Heinzel, G. Salis, R. Held, S. Lüscher, K. Ensslin, W. Wegscheider, and M. Bichler, *Shifting a quantum wire through a disordered crystal: Observation of conductance fluctuations in real space*, Phys. Rev. B **61**, R13353 (2000).
- [125] M. E. Rensink, *Modification of friedel oscillations by a magnetic field*, Phys. Rev. **174**, 744 (1968).
- [126] O. Klochan, A. P. Micolich, L. H. Ho, A. R. Hamilton, K. Muraki, and Y. Hirayama, *The interplay between one-dimensional confinement and two-dimensional crystallographic anisotropy effects in ballistic hole quantum wires*, New Journal of Physics **11**, 043018 (2009).
- [127] L. I. Glazman and A. V. Khaetskii, *Nonlinear quantum conductance of a lateral microconstraint in a heterostructure*, EPL (Europhysics Letters) **9**, 263 (1989).
- [128] L. Martin-Moreno, J. T. Nicholls, N. K. Patel, and M. Pepper, *Non-linear conductance of a saddle-point constriction*, Journal of Physics: Condensed Matter **4**, 1323 (1992).

- [129] K.-F. Berggren and M. Pepper, *Electrons in one dimension*, Philosophical Transactions of the Royal Society A: Mathematical, Physical and Engineering Sciences **368**, 1141 (2010).
- [130] L. G. G. V. Dias da Silva, N. P. Sandler, K. Ingersent, and S. E. Ulloa, *Zero-field kondo splitting and quantum-critical transition in double quantum dots*, Phys. Rev. Lett. **97**, 096603 (2006).
- [131] L. G. G. V. Dias da Silva, K. Ingersent, N. Sandler, and S. E. Ulloa, *Finite-temperature conductance signatures of quantum criticality in double quantum dots*, Phys. Rev. B **78**, 153304 (2008).
- [132] L. G. G. V. Dias da Silva, N. P. Sandler, K. Ingersent, and S. E. Ulloa, *Transmission in double quantum dots in the kondo regime: Quantum-critical transitions and interference effects*, Physica E: Low-dimensional Systems and Nanostructures **40**, 1002 (2008).
- [133] T.-F. Fang and H.-G. Luo, *Tuning the kondo and fano effects in double quantum dots*, Phys. Rev. B **81**, 113402 (2010).
- [134] W.-z. Wang, *Kondo effect and continuous quantum phase transitions in double quantum dots with on-site and interdot repulsion and magnetic field*, Phys. Rev. B **83**, 075314 (2011).
- [135] A. Wong, W. B. Lane, L. G. G. V. D. da Silva, K. Ingersent, N. Sandler, and S. E. Ulloa, *Signatures of entanglement and quantum phase transitions in parallel quantum dots*, arXiv:1109.3696v1 (2011).
- [136] C.-H. Chung, G. Zarand, and P. Wölfle, *Two-stage kondo effect in side-coupled quantum dots: Renormalized perturbative scaling theory and numerical renormalization group analysis*, Phys. Rev. B **77**, 035120 (2008).
- [137] R. Žitko, *Fano-kondo effect in side-coupled double quantum dots at finite temperatures and the importance of two-stage kondo screening*, Phys. Rev. B **81**, 115316 (2010).
- [138] R. M. Potok, I. G. Rau, H. Shtrikman, Y. Oreg, and D. Goldhaber-Gordon, *Observation of the two-channel kondo effect*, Nature **446**, 167 (2007).
- [139] L. M. Roth, B. Lax, and S. Zwerdling, *Theory of optical magneto-absorption effects in semiconductors*, Phys. Rev. **114**, 90 (1959).
- [140] T. Englert, D. Tsui, A. Gossard, and C. Uihlein, *g-factor enhancement in the 2d electron gas in GaAs/AlGaAs heterojunctions*, Surface Science **113**, 295 (1982).

- [141] R. Danneau, O. Klochan, W. R. Clarke, L. H. Ho, A. P. Micolich, M. Y. Simmons, A. R. Hamilton, M. Pepper, D. A. Ritchie, and U. Zülicke, *Zeeman splitting in ballistic hole quantum wires*, Phys. Rev. Lett. **97**, 026403 (2006).
- [142] J. C. H. Chen, O. Klochan, A. P. Micolich, A. R. Hamilton, T. P. Martin, L. H. Ho, U. Zülicke, D. Reuter, and A. D. Wieck, *Observation of orientation- and k -dependent zeeman spin-splitting in hole quantum wires on (100)-oriented AlGaAs/GaAs heterostructures*, New Journal of Physics **12**, 033043 (2010).
- [143] D. Csontos, U. Zülicke, P. Brusheim, and H. Q. Xu, *Landé-like formula for the g factors of hole-nanowire subband edges*, Phys. Rev. B **78**, 033307 (2008).
- [144] D. Csontos, P. Brusheim, U. Zülicke, and H. Q. Xu, *Spin- $\frac{3}{2}$ physics of semiconductor hole nanowires: Valence-band mixing and tunable interplay between bulk-material and orbital bound-state spin splittings*, Phys. Rev. B **79**, 155323 (2009).
- [145] T. Ando, A. B. Fowler, and F. Stern, *Electronic properties of two-dimensional systems*, Rev. Mod. Phys. **54**, 437 (1982).
- [146] K. J. Thomas, J. T. Nicholls, N. J. Appleyard, M. Y. Simmons, M. Pepper, D. R. Mace, W. R. Tribe, and D. A. Ritchie, *Interaction effects in a one-dimensional constriction*, Phys. Rev. B **58**, 4846 (1998).
- [147] H. W. van Kesteren, E. C. Cosman, W. A. J. A. van der Poel, and C. T. Foxon, *Fine structure of excitons in type-ii GaAs/AlAs quantum wells*, Phys. Rev. B **41**, 5283 (1990).
- [148] V. F. Sapega, M. Cardona, K. Ploog, E. L. Ivchenko, and D. N. Mirlin, *Spin-flip raman scattering in GaAs/ $Al_xGa_{1-x}As$ multiple quantum wells*, Phys. Rev. B **45**, 4320 (1992).
- [149] S. A. Wolf, D. D. Awschalom, R. A. Buhrman, J. M. Daughton, S. von Molnár, M. L. Roukes, A. Y. Chtchelkanova, and D. M. Treger, *Spintronics: A spin-based electronics vision for the future*, Science **294**, 1488 (2001).
- [150] L. P. Kouwenhoven, T. H. Oosterkamp, M. W. S. Danoesastro, M. Eto, D. G. Austing, T. Honda, and S. Tarucha, *Excitation Spectra of Circular, Few-Electron Quantum Dots*, Science **278**, 1788 (1997).
- [151] J. R. Petta, A. C. Johnson, C. M. Marcus, M. P. Hanson, and A. C. Gossard, *Manipulation of a single charge in a double quantum dot*, Phys. Rev. Lett. **93**, 186802 (2004).
- [152] A. Kogan, S. Amasha, D. Goldhaber-Gordon, G. Granger, M. A. Kastner, and H. Shtrikman, *Measurements of kondo and spin splitting in single-electron transistors*, Phys. Rev. Lett. **93**, 166602 (2004).

- [153] R. Hanson, L. P. Kouwenhoven, J. R. Petta, S. Tarucha, and L. M. K. Vandersypen, *Spins in few-electron quantum dots*, Rev. Mod. Phys. **79**, 1217 (2007).
- [154] F. Cavaliere, U. D. Giovannini, M. Sassetti, and B. Kramer, *Transport properties of quantum dots in the wigner molecule regime*, New Journal of Physics **11**, 123004 (2009).
- [155] P. Schneider, J. Kainz, S. D. Ganichev, S. N. Danilov, U. Rössler, W. Wegscheider, D. Weiss, W. Prettl, V. V. Bel'kov, M. M. Glazov, et al., *Spin relaxation times of two-dimensional holes from spin sensitive bleaching of intersubband absorption*, Appl. Phys. Lett. **96**, 420 (2004).
- [156] D. V. Bulaev and D. Loss, *Spin relaxation and decoherence of holes in quantum dots*, Phys. Rev. Lett. **95**, 076805 (2005).
- [157] B. D. Gerardot, D. Brunner, P. A. Dalgarno, P. Ohberg, S. Seidl, M. Kroner, K. Karrai, N. G. Stoltz, P. M. Petroff, and R. J. Warburton, *Optical pumping of a single hole spin in a quantum dot*, Nature **451**, 441 (2008).
- [158] V. N. Golovach, A. Khaetskii, and D. Loss, *Phonon-induced decay of the electron spin in quantum dots*, Phys. Rev. Lett. **93**, 016601 (2004).
- [159] C. W. J. Beenakker, *Theory of coulomb-blockade oscillations in the conductance of a quantum dot*, Phys. Rev. B **44**, 1646 (1991).
- [160] S. De Franceschi, S. Sasaki, J. M. Elzerman, W. G. van der Wiel, S. Tarucha, and L. P. Kouwenhoven, *Electron cotunneling in a semiconductor quantum dot*, Phys. Rev. Lett. **86**, 878 (2001).
- [161] M. Field, C. G. Smith, M. Pepper, D. A. Ritchie, J. E. F. Frost, G. A. C. Jones, and D. G. Hasko, *Measurements of coulomb blockade with a noninvasive voltage probe*, Phys. Rev. Lett. **70**, 1311 (1993).
- [162] L. M. K. Vandersypen, J. M. Elzerman, R. N. Schouten, L. H. W. van Beveren, R. Hanson, and L. P. Kouwenhoven, *Real-time detection of single-electron tunneling using a quantum point contact*, **85**, 4394 (2004).
- [163] J. M. Elzerman, R. Hanson, V. L. H. Willems, B. Witkamp, L. M. K. Vandersypen, and L. P. Kouwenhoven, *Single-shot read-out of an individual electron spin in a quantum dot.*, Nature **430**, 431 (2004).
- [164] R. Schleser, E. Ruh, T. Ihn, K. Ensslin, D. C. Driscoll, and A. C. Gossard, *Time-resolved detection of individual electrons in a quantum dot*, **85**, 2005 (2004).
- [165] A. V. Oppenheim and R. W. Schaffer, *Digital Signal Processing* (Prentice Hall, 1975).

- [166] M. C. Rogge, B. Harke, C. Fricke, F. Hohls, M. Reinwald, W. Wegscheider, and R. J. Haug, *Coupling symmetry of quantum dot states*, Phys. Rev. B **72**, 233402 (2005).
- [167] K. MacLean, S. Amasha, I. P. Radu, D. M. Zumbühl, M. A. Kastner, M. P. Hanson, and A. C. Gossard, *Energy-dependent tunneling in a quantum dot*, Phys. Rev. Lett. **98**, 036802 (2007).
- [168] W. Belzig, *Full counting statistics of super-poissonian shot noise in multilevel quantum dots*, Phys. Rev. B **71**, 161301 (2005).
- [169] S. Gustavsson, R. Leturcq, B. Simovič, R. Schleser, P. Studerus, T. Ihn, K. Ensslin, D. C. Driscoll, and A. C. Gossard, *Counting statistics and super-poissonian noise in a quantum dot: Time-resolved measurements of electron transport*, Phys. Rev. B **74**, 195305 (2006).
- [170] C. Flindt, T. c. v. Novotný, A. Braggio, M. Sasseti, and A.-P. Jauho, *Counting statistics of non-markovian quantum stochastic processes*, Phys. Rev. Lett. **100**, 150601 (2008).
- [171] C. Flindt, T. c. v. Novotný, A. Braggio, and A.-P. Jauho, *Counting statistics of transport through coulomb blockade nanostructures: High-order cumulants and non-markovian effects*, Phys. Rev. B **82**, 155407 (2010).
- [172] C. Flindt, A. Braggio, and T. Novotný, *Non-markovian dynamics in the theory of full counting statistics*, AIP Conference Proceedings **922**, 531 (2007).
- [173] P. Michler, A. Kiraz, C. Becher, W. V. Schoenfeld, P. M. Petroff, L. Zhang, E. Hu, and A. Imamoglu, *A quantum dot single-photon turnstile device*, Science **290**, 2282 (2000).
- [174] A. Boca, R. Miller, A. D. Boozer, T. E. Northup, and H. J. Kimble, *Photon blockade in an optical cavity with one trapped atom*, Nature **436**, 87 (7 July 2005)).
- [175] L. Kleinrock, *Queueing Systems. Volume 1: Theory* (Wiley-Interscience, 1975).
- [176] Y. M. Blanter and M. Büttiker, *Shot noise in mesoscopic conductors*, Physics Reports **336**, 1 (2000).
- [177] R. de Picciotto, M. Reznikov, M. Heiblum, V. Umansky, G. Bunin, and D. Mahalu, *Direct observation of a fractional charge*, Nature **389**, 162 (1997/09/11).
- [178] L. Saminadayar, D. C. Glattli, Y. Jin, and B. Etienne, *Observation of the $e/3$ fractionally charged Laughlin quasiparticle*, Phys. Rev. Lett. **79**, 2526 (1997).

- [179] O. Zarchin, M. Zaffalon, M. Heiblum, D. Mahalu, and V. Umansky, *Two-electron bunching in transport through a quantum dot induced by kondo correlations*, Phys. Rev. B **77**, 241303 (2008).
- [180] Y. Yamauchi, K. Sekiguchi, K. Chida, T. Arakawa, S. Nakamura, K. Kobayashi, T. Ono, T. Fujii, and R. Sakano, *Evolution of the kondo effect in a quantum dot probed by shot noise*, Phys. Rev. Lett. **106**, 176601 (2011).
- [181] X. Jehl, M. Sanquer, R. Calemczuk, and D. Mailly, *Detection of doubled shot noise in short normal-metal/ superconductor junctions*, Nature **405**, 50 (2000/05/04).
- [182] E. Buks, R. Schuster, M. Heiblum, D. Mahalu, and V. Umansky, *Dephasing in electron interference by a “which-path” detector*, Nature **391**, 871 (1998/02/26).
- [183] D. V. Averin and E. V. Sukhorukov, *Counting statistics and detector properties of quantum point contacts*, Phys. Rev. Lett. **95**, 126803 (2005).
- [184] U. Gasser, S. Gustavsson, B. Küng, K. Ensslin, T. Ihn, D. C. Driscoll, and A. C. Gossard, *Statistical electron excitation in a double quantum dot induced by two independent quantum point contacts*, Phys. Rev. B **79**, 035303 (2009).
- [185] L. P. Kouwenhoven, S. Jauhar, K. McCormick, D. Dixon, P. L. McEuen, Y. V. Nazarov, N. C. van der Vaart, and C. T. Foxon, *Photon-assisted tunneling through a quantum dot*, Phys. Rev. B **50**, 2019 (1994).
- [186] S. Gustavsson, M. Studer, R. Leturcq, T. Ihn, K. Ensslin, D. C. Driscoll, and A. C. Gossard, *Frequency-selective single-photon detection using a double quantum dot*, Phys. Rev. Lett. **99**, 206804 (2007).
- [187] R. Aguado and L. P. Kouwenhoven, *Double quantum dots as detectors of high-frequency quantum noise in mesoscopic conductors*, Phys. Rev. Lett. **84**, 1986 (2000).
- [188] G.-L. Ingold and Y. V. Nazarov, *Charge Tunneling Rates in Ultrasmall Junctions*, ArXiv Condensed Matter e-prints (2005), [arXiv:cond-mat/0508728](https://arxiv.org/abs/cond-mat/0508728).
- [189] S. Gustavsson, R. Leturcq, B. Simovič, R. Schleser, T. Ihn, P. Studerus, K. Ensslin, D. C. Driscoll, and A. C. Gossard, *Counting statistics of single electron transport in a quantum dot*, Phys. Rev. Lett. **96**, 076605 (2006).
- [190] S. Gustavsson, R. Leturcq, T. Ihn, K. Ensslin, M. Reinwald, and W. Wegscheider, *Measurements of higher-order noise correlations in a quantum dot with a finite bandwidth detector*, Phys. Rev. B **75**, 075314 (2007).

- [191] T. Fujisawa, T. Hayashi, R. Tomita, and Y. Hirayama, *Bidirectional counting of single electrons*, Science **312**, 1634 (2006).
- [192] C. Flindt, C. Fricke, F. Hohls, T. Novotný, K. Netočný, T. Brandes, and R. J. Haug, *Universal oscillations in counting statistics*, Proceedings of the National Academy of Sciences **106** (25), 10116 (2009).
- [193] C. Fricke, F. Hohls, C. Flindt, and R. J. Haug, *High cumulants in the counting statistics measured for a quantum dot*, Physica E: Low-dimensional Systems and Nanostructures **42**, 848 (2010), 18th International Conference on Electron Properties of Two-Dimensional Systems.
- [194] L. G. B. Levitov L. S., *Charge distribution in quantum shot noise*, JETP Lett. **58** (3), 230 (1993).
- [195] L. S. Levitov, H. Lee, and G. B. Lesovik, *Electron counting statistics and coherent states of electric current*, J. Math. Phys. **37**, 4845 (1996).
- [196] M. Henny, S. Oberholzer, C. Strunk, and C. Schönberger, *1/3-shot-noise suppression in diffusive nanowires*, Phys. Rev. B **59**, 2871 (1999).
- [197] Y. V. Nazarov and Y. M. Blanter, *Quantum Transport: Introduction to Nanoscience* (Cambridge University Press, 2009).
- [198] A. Braggio, J. König, and R. Fazio, *Full counting statistics in strongly interacting systems: Non-markovian effects*, Phys. Rev. Lett. **96**, 026805 (2006).
- [199] D. A. Bagrets and Y. V. Nazarov, *Full counting statistics of charge transfer in coulomb blockade systems*, Phys. Rev. B **67**, 085316 (2003).
- [200] D. Bagrets, Y. Utsumi, D. Golubev, and G. Schön, *Full counting statistics of interacting electrons*, Fortschritte der Physik **54**, 917 (2006).
- [201] R. Kubo, *Generalized cumulant expansion method*, Journal of Physical Society of Japan **17**, 1100 (1962).
- [202] O. Naaman and J. Aumentado, *Poisson transition rates from time-domain measurements with a finite bandwidth*, Phys. Rev. Lett. **96**, 100201 (2006).
- [203] S. Gustavsson, R. Leturcq, M. Studer, I. Shorubalko, T. Ihn, K. Ensslin, D. Driscoll, and A. Gossard, *Electron counting in quantum dots*, Surface Science Reports **64**, 191 (2009).
- [204] D. Kambly, C. Flindt, and M. Büttiker, *Factorial cumulants reveal interactions in counting statistics*, Phys. Rev. B **83**, 075432 (2011).
- [205] P. G. Ferreira, J. a. Magueijo, and J. Silk, *Cumulants as non-gaussian qualifiers*, Phys. Rev. D **56**, 4592 (1997).

- [206] C. Fricke, F. Hohls, N. Sethubalasubramanian, L. Fricke, and R. J. Haug, *High-order cumulants in the counting statistics of asymmetric quantum dots*, **96**, 202103 (2010).
- [207] M. Berry, *Universal oscillations of high derivatives*, Proceedings of the Royal Society A: Mathematical, Physical and Engineering Science **461**, 1735 (2005).
- [208] A. G. Abanov and D. A. Ivanov, *Factorization of quantum charge transport for noninteracting fermions*, Phys. Rev. B **79**, 205315 (2009).
- [209] F. Hassler, Ph.D. thesis, ETH Zurich (2009).
- [210] P. M. Mooney, *Deep donor levels (DX centers) in III/V semiconductors*, J. Appl. Phys. **67**, R1 (1990).
- [211] M. Pioro-Ladrière, J. H. Davies, A. R. Long, A. S. Sachrajda, L. Gaudreau, P. Zawadzki, J. Lapointe, J. Gupta, Z. Wasilewski, and S. Studenikin, *Origin of switching noise in GaAs/Al_xGa_{1-x}As lateral gated devices*, Phys. Rev. B **72**, 115331 (2005).
- [212] C. Buizert, F. H. L. Koppens, M. Pioro-Ladrière, H.-P. Tranitz, I. T. Vink, S. Tarucha, W. Wegscheider, and L. M. K. Vandersypen, *insitu reduction of charge noise in GaAs/Al_xGa_{1-x}As schottky-gated devices*, Phys. Rev. Lett. **101**, 226603 (2008).
- [213] R. J. Haug, A. H. MacDonald, P. Streda, and K. von Klitzing, *Quantized multichannel magnetotransport through a barrier in two dimensions*, Phys. Rev. Lett. **61**, 2797 (1988).
- [214] M. Büttiker, *Absence of backscattering in the quantum hall effect in multiprobe conductors*, Phys. Rev. B **38**, 9375 (1988).

Acknowledgements

First of all, I am grateful to Prof. Klaus Ensslin for giving me the opportunity to do a PhD in his group. This was surely a big step in my life and I appreciate him for his trust. And that while my project went through many ups and downs along the way, he never stopped his support. His door was always open and I was always welcome for a discussion. Apart from great intuition for physics, the fact that he is a true manager is the main secret for the pleasant atmosphere in the group. I would also like to thank him for his warm supports regarding my crazy future career plans.

I would like to thank Prof. Thomas Ihn for his excellent lecture and his book which became sort of a Bible in our group long before getting published. I appreciate many helpful discussions with him, from which I always learned new things, and the great example of a physicist that he set in my mind with his analytical approach to physics. Special thanks to Prof. Wolfgang Belzig for accepting to be a member of the exam committee. It was an honor to have him as a co-examiner of my exam. I also appreciate him for inviting me to visit and present my work in his group.

It was pleasant to work with Miklos Csontós who was “my” post doc during most of this project. His great mastery of wire-bonding artwork, his talent in writing fluent papers and his meticulous attention to all possible details that I often missed is very much appreciated. The fact that he travelled thousands of kilometers just to be there during our defense is another thing for which I feel indebted. Boris Grbić, my predecessor in p-type project, spent plenty of time to tell me many stories about *holes* and mentor me in FIRST. I have to say that no matter how hard we tried, it was never possible to beat the standard that he set in the project. I owe a lot to Ivan Shorubalko who brought his magical skills to the project and initiated the wet chemical-etching technique for the fabrication of p-type nano-structures. The fine tuning of the chemical etching was done together with Fabrizio Nichele who is my successor in the p-type project. I wish him all the best with his PhD, especially with the part which is related to *holes*.

This project would have never been finished without major selfless contributions from Theodore Choi. While very busy with his own project, he spent lots of time and effort to help re-establishing the chemical etching technique and fabricating quantum dots. Besides being a great friend, his proficiency of electron beam lithography and his experience with counting electrons were crucial in watching *holes* jump around. I want to use this opportunity to say: Thank you, Theo!

Paul Studerus’ expertise in electronics and Cecil Barengo’s vital support with

mechanical and low-temperature equipments were essential for this project. Paul never minded to explain me how things work and always had a "box" for new measurements and Cecil never refused to fix a broken sample holder again and again. I would like to appreciate Claudia Vinzens for both being a running companion and her perfect support with administrative procedures. Klaus once said that "I wish we were as good physicists as Claudia, Paul and Cecil are in their jobs". I could not agree more. They also brought new perspectives to our narrow physicist view which I enjoyed very much. I would also like to thank Brigitte Abt for her administrative support when I started my PhD.

Apart from having fun whenever there was a chance, I learned many things from discussing with Bruno Küng and Thomas Müller. When I was lost in the myriad of official steps toward the end, it was reassuring to follow Thomas step by step and benefit from his fresh experiences. They also did their best to make me familiar with the Swiss culture which I appreciate.

I really enjoyed the company of Françoise Molitor, Susanne Dröscher and Arnhild Jacobson among many other officemates in E4 and Tobias Frey in E11. Moreover, I would like to thank all the other members of Nanophysics group who created a pleasant atmosphere in the office and the lab during many years: Sarah Hellmüller, Domonik Bischoff, Stephan Baer, Peter Leek, Clemens Rössler, Pauline Simonet, Anastasia Varlet, Clément Barraud, Tobias Krähenmann, Julien Basset, Aleksey Kozikov, Nikola Pascher, Peter Märki, Matthias Studer, Simon Gustavsson, Lena Hüfner, Stephan Schnez, Renaud Leturcq, Lorenz Meier, Elisabeth Ruth, Slavo Kicin, Davy Graf, Urszula Gasser, Arnd Gildemeister and Andreas Pfund.

I would like to acknowledge supports from all the FIRST staff, without whom this project would not be possible. Hansrudi Scherere and his team's collaboration for the contact metallization of Ohmic contacts and Isabelle Altorfer's flexible supply of liquid Helium is very much appreciated.

The PhD study by its own is not always a sweet thing. I would like to thank many friends including Preden Rolleau, Morteza Moazzami Goudarzi, Sanaz Sadati, Jafar Amiri Parian, Chloé Crowther-Alwyn and Ajit Srivastava who, by their cheerful and motivating support, made this time delightful.

I am deeply indebted to my parents for their endless love, unconditional support and continuous encouragement. That they have always wise advice when I ask for it and at the same time accept and support my own decisions in every respect. I appreciate my brother and sister for their sympathy in hard times and I hope all the best for them and wish that their sweetest dreams come true.

Finally, I would like to express sincere thanks to my beautiful girlfriend, Maria Alexandrova. Her contributions to this thesis are countless, with the design of the cover being only one of them. As I look back and see how lovely colors you have brought to my life, and how hope and enthusiasm has returned to me with you, I can only say, with the greatest humility, Thank you!

Curriculum Vitae

Name: Yashar Komijani
Born: Sept. 14, 1980 in Tehran
citizen of Iran
Parents: Mohammad Komijani and Roohangiz Mahvi

Education:

2007- Ph.D in Physics, ETH Zurich, Switzerland
Group: Prof. Klaus Ensslin

2003-2006 M.Sc. Electrical/Communication Engineering,
University of Tehran, Tehran, Iran

1998-2003 B.Sc Electrical/Communication Engineering,
University of Tehran, Tehran, Iran

1992-1997 Dehkhoda and Khajeh Nasir High schools, Semnan, Iran

Work experience:

10/2003-07/2004 Information center of University of Tehran, Tehran, Iran
Network traffic and quality of service engineering

04/2002-06/2003 Ashna Net Imen, Co., Tehran, Iran
Traffic engineering, product testing

05/2000-09/2002 Andisheh Negar, Co., Tehran, Iran
LAN/Wireless/VoIP networks design and implementation